An approach to using novel 3d, 4f, and 3d-4f systems captured by lacunary Polyoxometalates for PRE (Paramagnetic Resonance Enhancement) and electrocatalysis on small molecules

Zur Erlangung des akademischen Grades eines

DOKTORS DER NATURWISSENSCHAFTEN

(Dr. rer. nat.)

von der KIT-Fakultät für Chemie und Biowissenschaften

des Karlsruher Instituts für Technologie (KIT)



genehmigte

DISSERTATION

von

M.Sc., M.Tech. Aiswarya Chalikunnath Venu

1. Referentin: Prof. Dr. Annie K. Powell
2. Referent: PD Dr. Dr. Michael Hirtz

Tag der mündlichen Prüfung: 29.10.2025



This document is licensed under a Creative Commons Attribution-NonCommercial-ShareAlike 4.0 International License (CC BY-NC-SA 4.0):
https://creativecommons.org/licenses/by-nc-sa/4.0/deed.en

I. Eidesstattliche Erklärung

Eidesstattliche Versicherung gemäß § 13 Absatz 2 Ziffer 3 der Promotionsordnung des Karlsruher Instituts für Technologie für die KIT-Fakultät für Chemie und Biowissenschaften:

1. Bei der eingereichten Dissertation zu dem Thema

An approach to using novel 3d, 4f, and 3d-4f systems captured by lacunary Polyoxometalates for PRE (Paramagnetic Resonance Enhancement) and electrocatalysis on small molecules

handelt es sich um meine eigenständig erbrachte Leistung.

2. Ich habe nur die angegebenen Quellen und Hilfsmittel benutzt und mich keiner unzulässigen Hilfe Dritter bedient. Insbesondere habe ich wörtlich oder sinngemäß aus anderen Werken übernommene Inhalte als solche kenntlich gemacht.

3. Die Arbeit oder Teile, davon habe ich bislang nicht an einer Hochschule des In- oder Auslands als Bestandteil einer Prüfungs- oder Qualifikationsleistung vorgelegt.

4. Die Richtigkeit der vorstehenden Erklärungen bestätige ich.

5. Die Bedeutung der eidesstattlichen Versicherung und die strafrechtlichen Folgen einer unrichtigen oder unvollständigen eidesstattlichen Versicherung sind mir bekannt.

Ich versichere an Eides statt, dass ich nach bestem Wissen die reine Wahrheit erklärt und nichts verschwiegen habe.

……

Ort und Datum

……

Unterschrift

II. Note

Atoms and ions shown in illustrations are not to scale. Organic hydrogen atoms, as well as solvent molecules, are often not shown for clarity.

Numerical quantities, such as bond lengths and angles, are given with their standard uncertainties in parentheses after the respective values and refer to the last digits.

This thesis was prepared from 1st of July 2020, to 16th of September 2025, at the Institute of Inorganic Chemistry (AOC), Faculty of Chemistry and Biosciences of the Karlsruhe Institute of Technology (KIT) under the supervision of Prof. Dr. Annie K. Powell.

To my daughter, ***Liya Karadhka Shankara****, born during this PhD, who gave me new love, strength, and purpose.*

Abbreviations

B_0	External magnetic field
B_1	Secondary magnetic field
CO_2RR	Carbon dioxide Reduction Reaction
CPMG	Carr-Purcell-Meiboom-Gill pulse sequence
CV	Cyclic Voltammetry
DLS	Dynamic Light Scattering
DMA	N, N-dimethylacetamide
E_{Pa}	Oxidation peak potential
E_{Pc}	Reduction peak potential
EPG	Edge Plane Pyrolytic Graphite
EPR	Electron Paramagnetic Resonance
E_R	Reverse potential
ESI-MS	Electron Spray Ionisation Mass Spectrometry
FID	Free Induction Decay signal
ATR-FTIR	Attenuated Total Reflectance Fourier Transform Infrared Spectroscopy
HER	Hydrogen Evolution Reaction
I_N	Normalised current values
IS	Inner sphere mechanism
IR	Inversion Recovery pulse
Ln	Lanthanides
M_0	Bulk magnetisation
MRI	Magnetic Resonance Imaging
M_{xy}	Transverse component
NMR	Nuclear Magnetic Resonance
NMRD	Nuclear Magnetic Resonance dispersion
NRR	Nitrogen Reduction Reactions
OER	Oxygen Evolution Reaction
ORR	Oxygen Reduction Reaction
PM-POMs	Paramagnetic Metal Ion-Containing POMs
POM	Polyoxometates
POMOFs	POM-based Metal-Organic Frameworks
POMos	Polyoxomolybdates
POTs	Polyoxotungstate
PRE NMR	Paramagnetic Relaxation Enhancement NMR
PSR	Progressive Saturation Recovery pulse
PXRD	Powder X-ray Diffraction
SCE	Saturated Calomel Electrode
SCXRD	Single-Crystal X-ray Diffraction
SHE	Standard hydrogen electrode
SMM	Single Molecular Magnets
SNR	Signal-to-Noise Ratio
T_1	Longitudinal relaxation
T_2	Transverse relaxation
TM	Transition Metal

TMSPs	Transition Metal Substituted POMs
UV-Vis	Ultraviolet-Visible spectroscopy
WOCs	Water Oxidation Catalysts
ZFS	Zero-Field Splitting
Z-pot	Zeta Potential
τ	Delay
C	Concentration
μ_s	Electronic spin moment
T_{ele}	Electronic relaxation times
μ_B	Bohr magneton
γ_1	Nuclear gyromagnetic ratio
r_2	Transverse relaxivity
R_1	Longitudinal relaxation rate
I	Nuclear spins
r_1	Longitudinal relaxivity
μ_I	Nuclear spin moment
S	The electron spins
R_2	Transverse relaxation rate
OS	Outer sphere mechanism
T	Temperature

Abstract

Polyoxometalates (POMs) are inorganic anionic metal–oxygen clusters known for their rich structural diversity. Their lacunary derivatives serve as versatile inorganic ligands, capable of hosting a wide range of 3d, 4f, and mixed 4d-4f metal ions. These hybrid POM clusters are remarkable materials due to their structural complexity and versatile applications in fields such as magnetism, catalysis, and imaging.

Inspired by these characteristics, the aim of this thesis was to develop and study multifunctional POM-based metal clusters by incorporating suitable transition metal ions, including 3d and 4f ions, for two main applications: (i) high-field magnetic resonance imaging (MRI) contrast agents, and (ii) redox electrocatalysts. This approach allows the investigation of how metal ion incorporation influences NMR relaxivity, particularly under ultra-high magnetic fields, as well as the catalytic performance in multi-electron/proton transfer reactions.

During this thesis work, new POMs were synthesised using a one-pot method: the 3d metal-containing clusters $[Cs_8(W_{10}M_2GeO_{38})_6]^{40-}$ (where M = Ni or Co), referred to as **Ni_{12}-GeW_{10}** and **Co_{12}-GeW_{10}** respectively; the iron-based cluster $[\{W_{10}Fe_2PO_{37}\}_4\{Fe_4(PO_4)_4\}]^{12-}$, abbreviated as **$Fe_{12}$-$PW_{10}$**; and the 3d-4f heterometallic clusters of the general formula $[(W_9GeO_{34})_2(WO_3)_4(PO_4)_6Co_6(Ln_x^{3+}/Na_{1-x})(Co_y^{2+}/Na_{1-y})]^{n-}$ (where Ln^{3+} = Dy^{3+}, Gd^{3+}, Y^{3+}, Eu^{3+}, Ho^{3+}, Tb^{3+}), which are denoted as **$Co_7Ln_xNa_{1-x}$-GeW_9**. The synthesised compounds were characterised using several techniques, including single-crystal X-ray diffraction (XRD), Attenuated Total Reflectance Fourier Transform Infrared (ATR-FTIR) spectroscopy, and elemental analysis. Electrospray ionisation mass spectrometry (ESI-MS) was also measured for **Co_{12}-GeW_{10}**, **Ni_{12}-GeW_{10}**, and **$Co_7Dy_{0.3}Na_{0.7}$-GeW_9**. Additionally, powder X-ray diffraction (PXRD) analysis was performed on **Co_{12}-GeW_{10}** and **Ni_{12}-GeW_{10}** to confirm their phase purity.

Although these compounds were synthesised using one-pot methods, obtaining pure products in good yield required careful optimisation of reaction parameters such as pH, reactant concentration, temperature, reaction time, and ionic strength. Adjusting these conditions was essential to overcome challenges in crystallisation and isolation of pure POM clusters from aqueous solutions.

Paramagnetic Relaxation Enhancement NMR (PRE-NMR) was used to assess how effectively a paramagnetic compound increases the relaxation rates of nearby nuclei, and in particular water protons. This is of crucial importance for developing new MRI contrast agents. PRE-NMR analysis was conducted on a range of POMs, including previously reported 3d- and 4f-based systems (**Mn_{16}-SiW_9**, **Co_{16}-PW_9**, **Ni_{16}-PW_9**, **Dy-W_{11}**, **Er-W_{11}**, **Er_2-W_{34}**, **Er_2-W_{22}**, **Gd_2-W_{22}** and **Dy_2-W_{22}**) as well as newly synthesised 3d-4f heterometallic POMs prepared during this PhD work (**$Co_7Gd_{0.1}Na_{0.9}$-GeW_9**, **$Co_7Dy_{0.3}Na_{0.7}$-GeW_9** and **$Co_7Dy_{0.3}Na_{0.7}$-GeW_9**). Relaxivity studies were conducted across magnetic fields from 20 MHz to 1.4 GHz using various NMR instruments equipped with permanent magnets (20 MHz, 80 MHz), superconducting magnets (300 MHz, 400 MHz), and resistive magnets (870 MHz,

1050 MHz, 1200 MHz, and 1400 MHz). These experiments were carried out in collaboration with Prof. Dr. Gisela Guthausen (KIT) and Dr Steffen Krämer (LNCMI). Measurements at low and intermediate fields using permanent and superconducting magnets were performed internally at KIT, while high-field studies using resistive magnets were conducted in collaboration with LNCMI Grenoble. These short-term scientific missions to Grenoble were financially supported by EMFL and the ISABEL project through secondment grants.

The electrochemical characterisation and electrocatalytic properties of the 3d-POMs (**Co_{12}-GeW_{10}, Ni_{12}-GeW_{10}, Fe_{12}-PW_{10}** and 3d-4f **($Co_7Dy_{0.3}Na_{0.7}$-GeW_9, $Co_7Gd_{0.1}Na_{0.}$-GeW_9, $Co_7Y_{0.3}Na_{0.7}$-GeW_9, $Co_7Eu_{0.1}Na_{0.9}$-GeW_9, $Co_7Ho_{0.1}Na_{0.9}$-GeW_9, $Co_7Tb_{0.2}Na_{0.8}$-GeW_9** were evaluated using cyclic voltammetry (CV) experiments. The stability of the materials in the buffer solutions was analysed using UV-vis spectroscopy and cyclic voltammetry (CV). The electrocatalytic oxidation properties of these newly synthesised materials were of interest in terms of their water splitting capabilities. These were evaluated through water oxidation reactions. **Co_{12}-GeW_{10}** also exhibited reduction of O_2, NO_2^- and H_2O_2. **Ni_{12}-GeW_{10}** showed catalytic behaviour specifically for the reduction of NO_2^- at the tungsten centre. Similarly, **Fe_{12}-PW_{10}** demonstrated catalytic activity toward O_2, NO_2^- and H_2O_2 reduction. All 3d-4f-POM metal clusters displayed similar electrochemical behaviour. This is attributed to the 3d rather than the 4f metal ions. These materials demonstrated significant catalytic activity for the reduction of NO_2^-. These studies were conducted with collaborators at CNRS, Université Paris-Saclay, and funded by a KHYS Travel grant.

This thesis is organised into seven chapters.

Chapter 1 discusses the motivation and objectives of this doctoral thesis research. Chapter 2 provides an introduction to POMs, covering their historical development, properties, types, and isomers. It also addresses multidentate POM-based ligands, functionalization, and their significant applications. Chapter 3 details the synthesis, structural characterisation, and challenges in isolating pure 3d-POMs and 3d-4f heterometallic POM clusters. This chapter also discusses structural disorder observed in these materials. Chapter 4 introduces the nuclear magnetic relaxation (NMR) technique with emphasis on relaxivity measurements at ultra-high magnetic fields. It includes studies on 3d-, 4f-, and 3d-4f-POMs, as well as experimental details and descriptions of the magnets used, including those at LNCMI Grenoble. Chapter 5 focuses on the electrochemical characterisation and electrocatalytic studies of 3d- and 3d-4f-POMs, including an additional 3d-POM cluster, **Fe_4-GeW_{10}**. The relevant experimental procedures are also provided. Chapter 6 presents the conclusions and outlook based on the findings of the previous chapters. Chapter 7 outlines the synthetic procedures for preparing precursor POM ligands and describes the experimental methods and instruments used for the characterisation of the POM clusters.

Kurzzusammenfassung

Polyoxometallate (POMs) sind anorganische anionische Metall-Sauerstoff-Cluster, die für ihre große strukturelle Vielfalt bekannt sind. Ihre lakunären Derivate dienen als vielseitige anorganische Liganden, die eine Vielzahl von 3d-, 4f- und gemischten 4d-4f-Metallionen aufnehmen können. Diese hybriden POM-Cluster sind aufgrund ihrer strukturellen Komplexität und vielseitigen Anwendungsmöglichkeiten in Bereichen wie Magnetismus, Katalyse und Bildgebung bemerkenswerte Materialien.

Inspiriert von diesen Eigenschaften war es das Ziel dieser Arbeit, multifunktionale POM-basierte Metallcluster zu entwickeln und zu untersuchen, indem geeignete Übergangsmetallionen, einschließlich 3d- und 4f-Ionen, für zwei Hauptanwendungen integriert wurden: (i) Kontrastmittel für die Hochfeld-Magnetresonanztomographie (MRT) und (ii) Redox-Elektrokatalysatoren. Dieser Ansatz ermöglicht die Untersuchung des Einflusses von Metallionen auf die NMR-Relaxivität insbesondere unter sehr hohen Magnetfeldern und auf die katalytische Leistung in Elektronen/Protonen-Transferreaktionen.

Im Rahmen dieser Doktorarbeit wurden folgende neue POMs unter Verwendung einer „One-Pot-Synthese“ hergestellt. Die 3d-metallhaltigen Cluster $[Cs_8(W_{10}M_2GeO_{38})_6]^{40-}$ (M^{II} = Ni oder Co) **Ni_{12}-GeW_{10}** bzw. **Co_{12}-GeW_{10}** ; der eisenbasierte Cluster $[\{W_{10}Fe_2PO_{37}\}_4\{Fe_4(PO_4)_4\}]^{12-}$ **Fe_{12}-PW_{10}** und die 3d-4f-heterometallischen Cluster $[(W_9GeO_{34})_2(WO_3)_4(PO_4)_6Co_6(Ln_x^{3+}/Na_{1-x})(Co_y^{2+}/Na_{1-y})]^{n-}$ (where Ln^{3+} = Dy^{3+},Gd^{3+},Y^{3+},Eu^{3+},Ho^{3+},Tb^{3+}), bezeichnet als **$Co_7Ln_xNa_{1-x}$-GeW_9**, wurden mittels Einkristall-Röntgenbeugung (XRD), Fourier-Transform-Infrarotspektroskopie mit abgeschwächter Totalreflexion (ATR-FTIR) und Elementaranalysen charakterisiert. Zusätzlich wurden für **Co_{12}-GeW_{10}, Ni_{12}-GeW_{10}** und **$Co_7Dy_{0.3}Na_{0.7}$-GeW_9** Elektrospray-Ionisations-Massenspektrometrien (ESI-MS) durchgeführt. Mittels Pulver-Röntgenbeugungsanalyse (PXRD) wurde die Phasenreinheit von **Co_{12}-GeW_{10}** und **Ni_{12}-GeW_{10}** bestätigt. Obwohl diese Verbindungen mittels „One-Pot-Synthese“ hergestellt wurden, erforderte die Gewinnung reiner Produkte in guter Ausbeute eine Optimierung der Reaktionsparameter wie pH-Wert, Reaktantenkonzentration, Temperatur, Reaktionszeit und Ionenstärke. Die Anpassung dieser Bedingungen war unerlässlich, um die Kristallisation und Isolierung reiner POM-Cluster aus wässrigen Lösungen zu erzielen.

Mit Hilfe der paramagnetischen Relaxationsverstärkung NMR (PRE-NMR) wurde untersucht, wie effektiv eine paramagnetische Verbindung die Relaxationsraten benachbarter Kerne, insbesondere von Wasserprotonen, erhöht. Dies ist von entscheidender Bedeutung für die Entwicklung neuer MRT-Kontrastmittel. Die PRE-NMR-Analyse wurde an einer Reihe von POMs durchgeführt, darunter bereits zuvor beschriebene 3d- und 4f-basierte Systeme (**Mn_{16}-SiW_9**, **Co_{16}-PW_9**, **Ni_{16}-PW_9**, **Dy-W_{11}**, **Er-W_{11}**, **Er_2-W_{34}**, **Er_2-W_{22}**, **Gd_2-W_{22}** und **Dy_2-W_{22}**) sowie neu synthetisierte 3d-4f-heterometallische POMs, die im Rahmen dieser Doktorarbeit hergestellt wurden **($Co_7Gd_{0.1}Na_{0.9}$-GeW_9**, **$Co_7Dy_{0.3}Na_{0.7}$-GeW_9** und **$Co_7Dy_{0.3}Na_{0.7}$-GeW_9**). Die Relaxivitätsuntersuchungen wurden in Magnetfeldern von 20 MHz bis 1,4 GHz mit verschiedenen NMR-Geräten durchgeführt, die mit Permanentmagneten (20

MHz, 80 MHz), supraleitenden Magneten (300 MHz, 400 MHz) und Widerstandsmagneten (870 MHz, 1050 MHz, 1200 MHz und 1400 MHz) ausgestattet waren. Diese Experimente wurden in Zusammenarbeit mit Prof. Dr. Gisela Guthausen (KIT) und Dr. Steffen Krämer (LNCMI) durchgeführt. Messungen bei niedrigen und mittleren Feldern mit Permanent- und supraleitenden Magneten wurden intern am KIT durchgeführt, während Hochfeldstudien mit resistiven Magneten in Zusammenarbeit mit dem LNCMI Grenoble durchgeführt wurden. Diese „Short-term scientific missions“ nach Grenoble wurden finanziell durch EMFL und das ISABEL-Projekt mittels Entsendungszuschüssen unterstützt.

Die elektrochemische Charakterisierung und die elektrokatalytischen Eigenschaften der 3d-POMs (**Co_{12}-GeW_{10}**, **Ni_{12}-GeW_{10}**, **Fe_{12}-PW_{10}**) und 3d-4f POMs (**$Co_7Dy_{0,3}Na_{0,7}$-GeW_9**, **$Co_7Gd_{0,1}Na_{0,9}$-GeW_9**, **$Co_7Y_{0,3}Na_{0,7}$-GeW_9**, **$Co_7Eu_{0,1}Na_{0,9}GeW_9$**, **$Co_7Ho_{0,1}Na_{0,9}$-$GeW_9$**, **$Co_7Tb_{0,2}Na_{0,8}$-$GeW_9$** wurden mittels Cyclovoltammetrie (CV) untersucht. Die Stabilität der Materialien in den Pufferlösungen wurde mittels UV-Vis-Spektroskopie und CV untersucht. Hierbei waren die elektrokatalytischen Oxidationseigenschaften dieser neuartigen Materialien waren von Interesse. Ihre Wasseraufspaltungsfähigkeiten wurden durch Wasseroxidationsreaktionen bewertet. **Co_{12}-GeW_{10}** zeigte auch eine Reduktion von O_2, NO_2^- und H_2O_2 . **Ni_{12}-GeW_{10}** zeigte das beste katalytische Fähigkeit zur Reduktion von NO_2^- am Wolframzentrum. In ähnlicher Weise präsentierte **Fe_{12}-PW_{10}** eine katalytische Aktivität bezüglich der Reduktion von O_2, NO_2^- und H_2O_2. Alle 3d-4f-POM-Metallcluster zeigten ein ähnliches elektrochemisches Verhalten, welches primär auf die 3d-Metallionen zurückzuführen ist. Diese Materialien offenbarten eine signifikante katalytische Aktivität für die Reduktion von NO_2^-. Diese Studien wurden in Zusammenarbeit mit dem CNRS, der Université Paris-Saclay und mit finanzieller Unterstützung durch das KHYS-Reisestipendium durchgeführt.

Diese Dissertation ist in sieben Kapiteln gegliedert. Kapitel 1 befasst sich mit der Motivation und den Zielen dieser Doktorarbeit. Kapitel 2 bietet eine Einführung in POMs und behandelt deren historische Entwicklung, Eigenschaften, Typen und Isomere. Außerdem werden mehrzähnige POM-basierte Liganden, Funktionalisierungen und ihre bedeutenden Anwendungen behandelt. Kapitel 3 beschreibt die Synthese, strukturelle Charakterisierung und Herausforderungen bei der Isolierung reiner 3d-POMs und 3d-4f-heterometallischer POM-Cluster. In diesem Kapitel werden auch strukturelle Fehlordnungen diskutiert, die in diesen Materialien beobachtet wurden. Kapitel 4 stellt die Kernspinresonanzspektroskopie (NMR) vor, wobei der Schwerpunkt auf Relaxivitätsmessungen bei sehr hohen Magnetfeldern liegt. Es umfasst Studien zu 3d-, 4f- und 3d-4f-POMs sowie experimentelle Details und Beschreibungen der verwendeten Magnete, darunter auch diejenigen am LNCMI Grenoble. Kapitel 5 beschreibt die elektrochemische Charakterisierung und elektrokatalytische Untersuchungen von 3d- und 3d-4f-POMs, einschließlich eines zusätzlichen 3d-POM-Clusters, **Fe_4-GeW_{10}**. Die entsprechenden experimentellen Details werden ebenfalls vorgestellt. Kapitel 6 präsentiert die Schlussfolgerungen und Ausblicke auf der Grundlage der Ergebnisse der vorangegangenen Kapitel. Kapitel 7 skizziert die Synthesen zur Herstellung von POM-Precursor-Liganden und beschreibt die experimentellen Methoden und Instrumente, die zur Charakterisierung der POM-Cluster verwendet wurden.

Table of Contents

1. Motivation and Objective **1**

2. Introduction **3**

2.1. Polyoxometalates: Evolution and Development **3**

2.2. Types of Polyoxometalates **4**

2.3. Lacunary Derivatives of Keggin ion **6**

2.4. Formation and Synthetic Strategies of Polyoxometalates **8**

2.5. Functionalisation of POMs **9**

2.6. General Properties of Polyoxometalates **11**

2.7. Applications of Polyoxometalates **14**

3. Functionalisation of Polyoxometalates **20**

3.1. Introduction **20**

3.2. Synthesis and Structural Features of Transition Metal -Substituted POMs (TM-SPs) **23**

3.2.1. **Co_{12}-GeW_{10}** and **Ni_{12}-GeW_{10}** 24

3.2.2. **Fe_{12}-PW_{10}** 33

3.2.3. **Fe_4-GeW_{10}** 36

3.3. Synthesis and Structural Features of 3d-4f Heterometallic Substituted Polyoxometalates (HMPOMs) **39**

3.3.1. **$Co_7Ln_xNa_{1-x}$-GeW_9** 40

3.4. Conclusion and Summary **47**

4. NMR Relaxivities of Paramagnetic Metal Ion Containing POMs (PM-POMs) **49**

4.1. Introduction **49**

4.2. NMR Relaxation Measurements ($\mathbf{T_1}$ and T_2) **49**

4.2.1. $\mathbf{T_1}$ Relaxation-Logitudinal Relaxation 50

4.2.2. T_2 Relaxation (Transverse / Spin–Spin Relaxation) 51

4.3. Relaxation rates and relaxivity **52**

4.4. Paramagnetic Relaxation Enhancement NMR (PRE NMR) **52**

4.4.1. Mechanism of PRE 54

4.4.2. Factors Influencing the Relaxivity of Paramagnetic Metal-Containing Molecules 57

4.4.3. Electronic relaxation of a paramagnetic ion in solution 60

4.5. Application of PRE **61**

4.6. PM-POM Clusters as MRI Contrast Agents **61**

4.7. NMR Relaxivity Measurements of POM Clusters at Ultra-High Fields.....66

4.8. NMR Relaxivities of Paramagnetic POMs Investigated during this PhD Work 68

Experimental determination of PRE 68

4.8.1. NMR Relaxivities of 3d Metal-Containing POMs.....68

4.8.2. NMR Relaxivities of 4f-metal Containing POMs.....74

4.8.3. NMR Relaxivities of Heterometallic 3d-4f Containing POMs.....85

4.8.4. Ageing and Structural Changes of Lanthanide Containing-POM Affecting NMR Relaxivity 89

4.9. Conclusion and Outlook.....93

4.10. Experimental Section.....96

4.10.1. Resistive Magnet.....98

5. Electrochemistry and Electrocatalytic Behaviour of POMs.....104

5.1. Introduction.....104

5.2. Fundamentals of Electrochemical Analysis.....106

5.3. Electrocatalysis of POM Systems.....108

5.3.1. Electrocatalytic Water Oxidation by Transition Metal-Substituted POMs.....110

5.3.2. Electrocatalytic Reduction of NOx by Transition Metal-Substituted POMs.....112

5.3.3. Electrocatalytic Reduction of Dioxygen and Hydrogen Peroxide.....113

5.4. Results and Discussion.....114

5.4.1. Electrochemical Characterisation of **Co_{12}-GeW_{10}** 114

5.4.2. Electrochemical Characterisation of the **Ni_{12}-GeW_{10}**.....131

5.4.3. Electrochemical Characterisation of **Fe_{12}-PW_{10}** 134

5.4.4. Electrochemical Characterisation of **Fe_4-GeW_{10}** 140

5.4.5. Electrochemical Characterisation of **$Co_7Ln_XNa_{1-X}$-GeW_9** 143

5.5. Conclusion and Outlook.....148

5.6. Experimental Section.....150

6. Overall Conclusion and Outlook.....152

7. Experimental 154

8. Reference 163

Additional Information

Curriculum Vita

Acknowledgements

1. Motivation and Objective

This thesis focuses on the development of multifunctional POM metal clusters for use as contrast agents in high-field magnetic resonance imaging (MRI) and in electrocatalysis. POMs are attractive due to their chemical stability, tunable structure, and ability to incorporate different metal ions. These features make them ideal candidates for creating advanced materials with dual functionality. In this work, POM-based systems are designed to serve as effective MRI contrast agents at very high magnetic fields, offering a safer alternative to conventional Gd-based agents. At the same time, their metal-rich structures are explored for electrocatalytic applications.

Nuclear magnetic resonance (NMR) is a powerful technique used to probe molecular structures, dynamics, and local chemical environments. One of its most well-known applications is magnetic resonance imaging (MRI), which is widely used in clinical diagnostics. Contrast agents are compounds containing paramagnetic ions that enhance MRI signals by accelerating the relaxation of nearby water protons. Beyond medicine, MRI is increasingly being applied in non-clinical fields such as materials science, process monitoring, and environmental studies, despite its broad utility. However, MRI has inherently low sensitivity. This limitation can be overcome by employing higher magnetic fields, which enhance the signal-to-noise ratio and improve resolution. However, these advances also demand contrast agents that remain effective under high applied fields. The effect, known as Paramagnetic Relaxation Enhancement (PRE), arises from hyperfine interactions between the electronic magnetic moments of the paramagnetic centres and the nuclear magnetic moments of solvent protons. Clinical contrast agents are typically based on gadolinium (Gd^{3+}) complexes, but these show reduced relaxivity at higher fields and raise concerns due to the toxicity of free Gd^{3+} ions. Thus, there is a pressing need for safer and more effective alternatives that can perform reliably under high magnetic fields. In this context, the design of POM-based systems incorporating paramagnetic metal centres offers a promising strategy for developing next-generation contrast agents for both clinical and non-medical MRI applications. The research presented here focuses on developing MRI contrast agents based on paramagnetic metal-containing POMs (PM-POMs) that can be utilised at very high magnetic fields, in particular for non-human applications. Lacunary POM ligands, where some $(WO_X)_n$ units are removed from the plenary POM, are analogous to organic ligands and can incorporate paramagnetic 3d and 4f metals.

This thesis describes relaxivity measurements of PM-POMs containing various paramagnetic ions (3d, 4f, and 3d-4f) under applied NMR magnetic fields from 20 MHz to

1.4 GHz. Measurements were performed using NMR instruments with permanent, superconducting, and resistive magnets, including high-field experiments performed at LNCMI Grenoble.

POM clusters also provide redox-active frameworks that can be tuned by incorporating various 3d or 3d-4f metal ions. Their unique electron-rich structures and ability to reversibly store and transfer multiple electrons make them ideal “electron sponges” for redox processes. This work aims to explore the electrocatalytic potential of newly synthesised hybrid POMs by evaluating their redox behaviour and catalytic activity in both oxidative and reductive reactions. Given their structural robustness and multiple accessible redox states, these materials are promising candidates for noble-metal-free electrocatalysts in energy-related applications.

2. Introduction

2.1. Polyoxometalates: Evolution and Development

Polyoxometalates (POMs) are a significant class of inorganic metal oxide clusters which consist of oxygen and early transition metals belonging to either group V or VI at their highest oxidation states (Mo^{6+}, W^{6+}, Nb^{5+}, V^{5+}, Nb^{5+}). These anionic metal clusters also include other heteroatoms such as P, As, Si and Ge. The chemistry of polyoxometalates is gaining importance due to their structural diversity and wide range of applications in fields such as catalysis, magnetism, medicine, and analytical chemistry.[1–10]

Polyoxometalates have a long history dating back to 1783 when Scheele discovered reduced molybdenum salts, known today as molybdenum blue. Their crystal structure and composition were unknown until the discovery of the [Mo_{154}] cluster in 1995. The very first polyoxometalates were invented by Berzelius in 1826.[11] He noted the formation of a yellow precipitate (heteropolyanion) by the reaction of ammonium molybdate and ortho-phosphoric acid. The isolated yellow product was later named ammonium 12 phosphomolybdate, $(NH_3)_4[PMo_{12}O_{40}]\cdot Aq$.[12] The composition and structure of this compound were unknown until 1862, when the first polytungstosilicic acids were discovered and characterised using elemental analysis and description of their crystal morphology by Marignac.[1] The field of polyoxometalates has flourished rapidly, with hundreds of such new compound discoveries, and many of the polyoxometalate scientists have contributed remarkable progress at that time.[12] In 1909, German scientist Alfred Werner suggested the structure for this species as an edge and face-sharing polyhedral.[13] In 1929, Pauling proposed structural details of these species, according to which the central XO_4 (X= P, As, Si and Ge) units were surrounded by twelve corners shared MO_6 octahedra; this structure was closer to the fundamental structures suggested at that time. In 1933, J. F Keggin determined the first structure of heteropoly acids $[H_3PW_{12}O_{40}].6H_2O$ by powder X-ray diffraction and confirmed the presence of four edge-shared triads, W_3O_{13} units, connected via corner-sharing. These types of structures are named Keggin ions.[14] Subsequently, in 1948, the second structure of heteropoly anion $[TeMo_6O_{24}]^{6-}$ (Anderson-Evans structure) was proposed[15,16] and in 1953, the third structure of heteropoly anion $[P_2W_{18}O_{62}]^{6-}$ named Wells-Dawson was reported. [17] Lindqvist reported the $[Nb_6O_{19}]^{8-}$ structure, named the Lindqvist structure.[1] In 1968, Lindqvist structures of $[Mo_6O_{19}]^{2-}$ and $[W_6O_{19}]^{2-}$ were communicated by Jahr and Fuchs. The real structural history of polyoxometalates is very long, and these four are the important structural variations of POMs.[18,19]

Further development of single-crystal X-ray crystallographic techniques, multinuclear NMR, and new analytical techniques advanced POM chemistry, as evidenced by the increasing number of research articles related to polyoxometalates published every year.[20]

2.2. Types of Polyoxometalates

The structural framework of polyoxometalates contains addenda atoms, central hetero atoms and oxo ligands. Addenda atoms (M) are the metal atoms involved in the primary building blocks of the POMs. The heteroatoms (X) are the central metal-oxygen clusters of the polyanion, which are mostly $[PO_4]^{2-}$, $[SO_4]^{2-}$, $[AsO_4]^{2-}$, $[SiO_4]^{2-}$, etc.[7,21] However, in addition to these metals, over 70 elements from all groups of the periodic table are incorporated and reported as heteroatoms. The addition of heteroatoms provides structural stability to the framework and also contributes to the overall charge of the cluster.[21,22]

Depending on the types of atoms involved in the structure, polyoxometalates can be broadly divided into two categories: Isopolyanions (IPAs) and heteropolyanions (HPAs). The Isopolyanion (IPA) of the general formula $[MmO_y]^{p-}$, is formed by the condensation of identical metal oxide ions $[MOx]^{n-}$. In contrast, in HPAs, the condensation takes place around the central heteroatom (X), and it gives rise to a heteropoly anion represented as $[X_sM_nO_m]^{q-}$.[23]

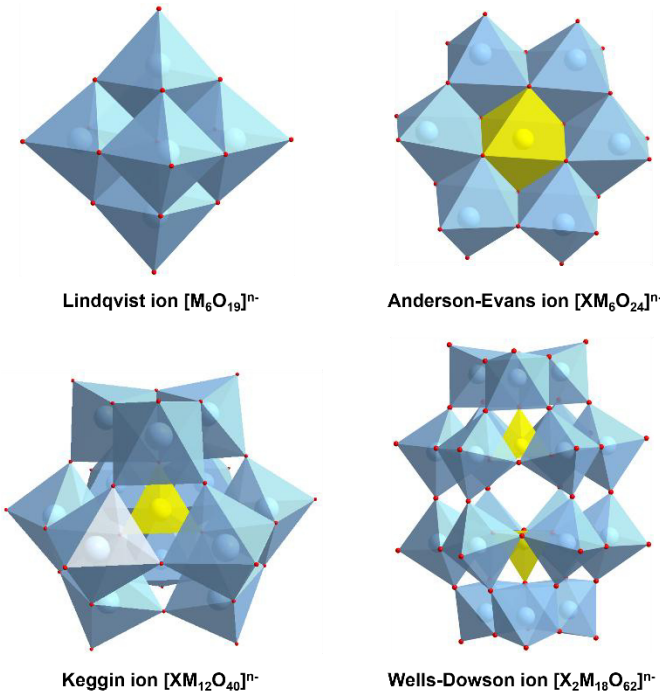


Figure 2.1 Important structural types of polyanions.

The most important structural types of polyoxometalates include the Keggin, Wells-Dawson, Anderson-Evans, and Lindqvist anions. The Keggin ion $[XM_{12}O_{40}]^{n-}$, Wells-Dawson ion

$[X_2M_{18}O_{62}]^{n-}$ and Anderson-Evans $[XM_6O_{24}]^{n-}$ belong to the heteropolyanion class, and Lindqvist $[M_6O_{19}]^{n-}$ belongs to the Isopolyanion structural type class (Figure **2.1**). Among these structural types, Keggin and Wells-Dawson structures are extensively studied due to their charge distribution, variety of isomers, ability to form lacunary derivatives, diverse compositions and redox properties.[24]

Structural overview of Keggin POMs

The Keggin and Wells-Dawson structures are well-established, with detailed information on their structures, isomers, derivatives, and stability under various conditions. This thesis focuses on the Keggin-based POM structure; therefore, the primary emphasis will be on the discussion of Keggin ion species.

The Keggin ion of the general formula $[XM_{12}O_{40}]^{n-}$, consists of one central tetrahedra of heteroatoms at the centre and is surrounded by four oxygen atoms (XO_4). The addenda atom (M) is in the centre of a distorted octahedra of six oxygen ligands (MO_6). Altogether, the coordinated structure consists of one central tetrahedra (XO_4), which is surrounded by twelve distorted octahedra (MO_6) linked by shared oxygens. These twelve octahedra are arranged into four groups, and each group of metal triads (M_3O_{13}) consists of three octahedra. The terminal O^{2-} ligand, through $p\pi - d\pi$ interaction, forms a double bond with the metals. The Keggin structure has the overall symmetry of the T_d point group.[25]

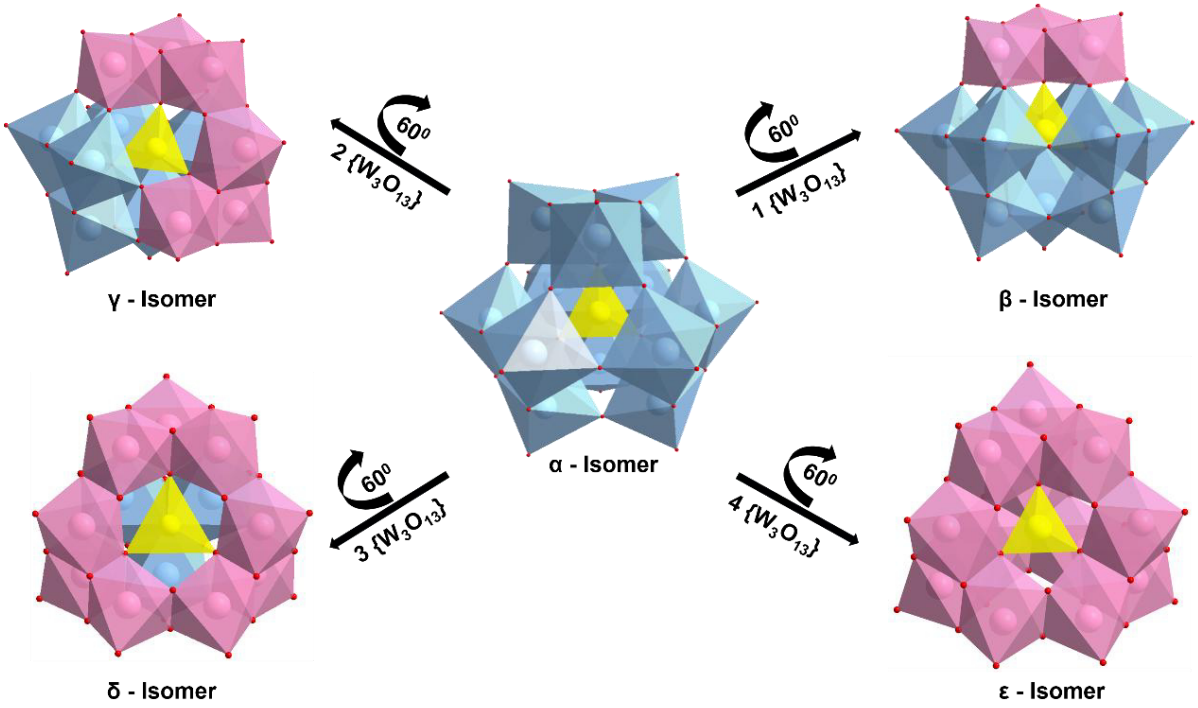


Figure 2.2 Polyhedral representation of five Keggin Isomers.

In the regular Keggin structure, all the metal triads (M_3O_{13}) are equivalent. Apart from this structure, four more Keggin structures are also proposed by Baker and Figgis.[26]

Therefore, a total of five rotational structural isomers ($\alpha, \beta, \gamma, \delta, \varepsilon$) were obtained by the 60° rotations of basic M_3O_{13} units Figure **2.2**. Some of these isomers ($\gamma, \delta, \varepsilon$) are unstable and form in situ. They are found as part of the transition metal-substituted derivatives, making it challenging to study their individual properties. This is in contrast to the stable α and β isomers, which can be studied more easily.[27–29] In the case of ($\gamma, \delta, \varepsilon$) isomers, the twelve vertex linkages are replaced by one to six shared edge linkers, which will considerably reduce the distance between two adjacent W atoms. This increases the Coulombic repulsion so that the stability decreases with the number of rotations.[30]

2.3. Lacunary Derivatives of Keggin ion

Controlled hydrolysis of the complete (plenary) Keggin structure leads to the cleavage of metal-oxygen bonds, resulting in the selective removal of MO_x octahedral units. This process gives rise to more reactive derivatives known as lacunary species. Depending on the number of MO_6 units removed, these species are classified as mono-, di-, or trilacunary derivatives (Figure **2.3**). The formation of lacunary species significantly enhances their reactivity, allowing them to coordinate with a wide range of metal atoms. This versatility makes them valuable for the synthesis of novel compounds with diverse catalytic, structural, and electronic properties.

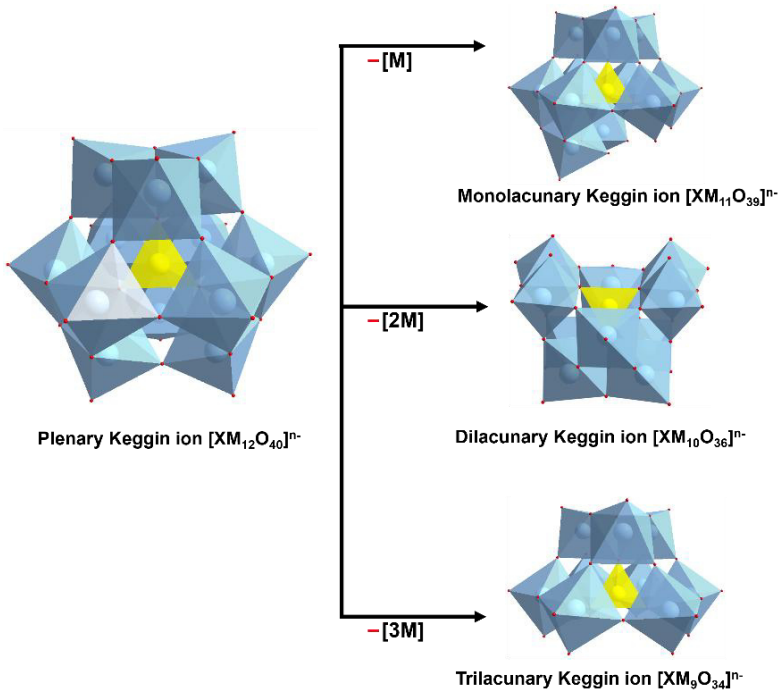


Figure 2.3 Polyhedral representation of three lacunary species of α -Keggin species.

Monolacunary derivatives

Monolacunary Keggin POMs are formed by selectively removing one (MO_x) unit from the parent Keggin structure $[XM_{12}O_{40}]^{n-}$ resulting in $[XM_{11}O_{39}]^{(n-4)-}$. This process creates a vacancy (lacuna) while maintaining the overall framework, making the structure reactive and useful for catalysis, material design, and functionalisation.[31,32]

Dilacunary derivatives

The dilacunary Keggin structure is exclusively observed in silico- and germanotungstates. These compounds, with the general formula $[\gamma\text{-}XM_{10}O_{36}]^{n-}$ (where X = Si or Ge), are formed by the removal of two tungsten-oxo units from the parent Keggin structure $[XM_{12}O_{40}]^{n-}$, creating two adjacent vacancies. The gamma isomer is the only configuration that has been successfully isolated and characterised for dilacunary silico- and germanotungstates. Other isomers, such as the alpha (α) isomer, have not been obtained in their pure form, highlighting the unique stability and structural preference of the gamma isomer in these systems.[33]

Trilacuanry derivatives

Trilacunary derivatives of the general formula $[XW_9O_{34}]^{z-}$ are formed by the removal of three metal-oxo units from the parent Keggin structure and are classified into A-type and B-type based on the arrangement of the vacancies (Figure **2.4**). In A-type species, the removed M_3 group involves corner-shared octahedra, preserving a more connected structure, while in B-type species, the removal involves edge-shared octahedra, resulting in a more open framework with one oxygen from the central tetrahedron pointing outward. Notably, trilacunary anions with a central pyramidal heteroatom bearing a lone pair, such as $[As^{3+}W_9O_{33}]^{9-}$ and $[Sb^{3+}W_9O_{33}]^{9-}$, exclusively adopt the B-type configuration due to steric and electronic repulsion from the lone pair, preventing further condensation. This contrasts with other trilacunary species like $[GeW_9O_{34}]^{10-}$ or $[PW_9O_{34}]^{9-}$, which can undergo further functionalisation. The structural and chemical differences between A- and B-type trilacunary species highlight their diverse reactivity and flexibility.[34–36]

The more reactive lacunary species derived from the parent Keggin polyoxometalate structure serve as multidentate inorganic ligands, facilitating the incorporation of metal-oxo clusters and the formation of high-nuclearity molecules. Similarly, the Wells-Dawson structure can also generate lacunary species, which enable the construction of high-nuclearity metal-oxo assemblies based on the Wells-Dawson framework.[7]

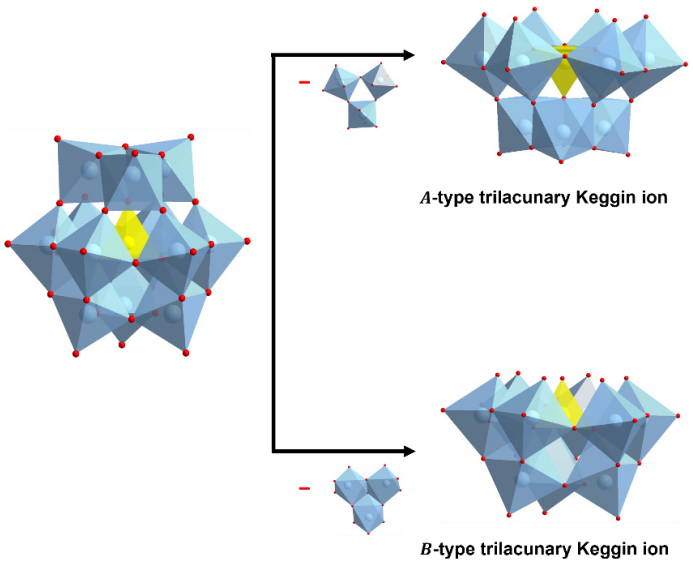


Figure 2.4 Two types (*A*-type and *B*-type) of trilacunary POMs.

2.4. Formation and Synthetic Strategies of Polyoxometalates

The primary building block of POMs is MO_6 octahedral units; here, the M represents the addenda atom. Only a few of the metals from groups 5 and 6, usually Mo, W and V, less frequently Nb and Tb can act as addenda atoms. The one which can increase the coordination number to sixfold when the polymerisation takes place to form MO_6 linkers.[7] Another important property of the addenda metal atom is the size, which should be in the octahedral ionic range from 0.65 to 0.80 Å and a high positive charge to form the bond between oxygen ligands. The metal should act as an excellent π acceptor to form $p\pi - dp$ (M-O) interaction.[37] These metal oxide units are connected by the sharing of oxygen atoms. The most stable bonding modes between octahedral structures are edge-sharing and corner-sharing, while face-sharing is the least stable. These are the basic building blocks of POM clusters, which then self-assemble together or with the additional heteroatom to form the POM species. The systematic way of formation of the Keggin species from tetrahedral metal oxide is shown in Figure **2.5**.

Polyanions are formed by the polycondensation of metal oxide ions ($[MO_4]^{n-}$) under appropriate conditions. The synthetic methods for POMs are straightforward, primarily involving one-pot reactions (Figure **2.6**). Additionally, synthetic techniques for polyoxometalates vary widely, ranging from one-pot synthesis to sophisticated flow systems. A set of synthetic parameters influences the synthesis of polyoxometalates. In addition to conventional simple chemical reactions, methods such as hydrothermal, microwave, and reflux methods are also employed to synthesise polyoxometalates.

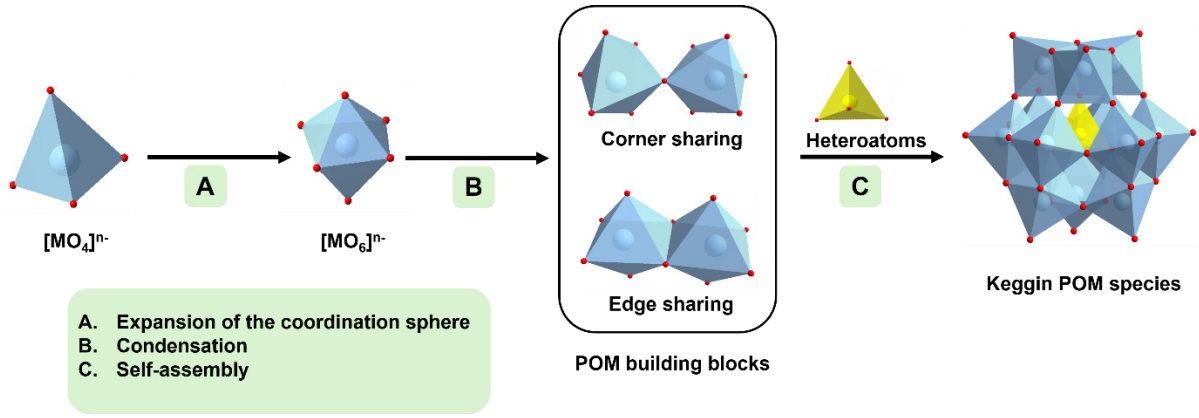


Figure 2.5 Illustration of the expansion of $[MO_4]^{n-}$ into octahedral $[MO_6]^{n-}$ undergoes acidic condensation and formation of POM building blocks, and further interaction with heteroatoms to form Keggin POM species by the process known as self-assembly.

The mechanism by which acidic condensation of metal oxide clusters forms complex polyoxometalate structures is unknown. This is referred to as the self-assembly of metal-oxygen clusters. This entirely depends on the external reaction conditions, like the concentration of the starting materials, pH, presence of other ligands, temperature, ionic strength, etc. The reaction conditions are precise for every polyoxometalate.[38]

The outcome of the formation behaviour of POMs from aqueous solution explains that at a certain pH, many polyoxometalate species coexist. As a result, one species, which is crystallised or isolated from the solution, does not need to be the one which is dominant in the solution, but a less soluble one corresponds to the added countercations.

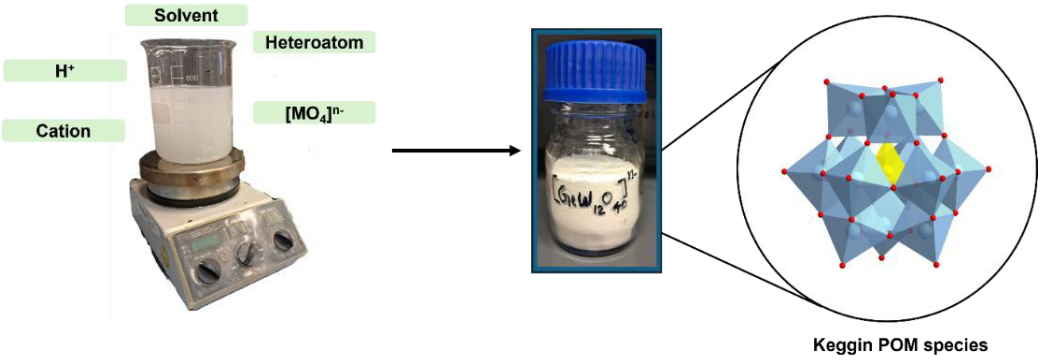


Figure 2.6 Representation of one-pot synthesis of polyoxometalates with multiple parameters affecting the synthesis and isolation of polyoxometalates.

2.5. Functionalisation of POMs

The functionalisation of POM is preceded by self-assembly of the active lacunary POM ligand with the cationic entities (transition metal ion (3d), lanthanides (4f), heterometallic (3d-4f) and organic groups).[39,40] The clusters formed by the incorporation of metal ions with POM ligands derive the multifunctional POM-based system. Depending on the metal ions, the POM metal clusters are used in various fields of application. The general scheme of

coordination of 3d, 4f and 3d-4f metal ions with the lacuanry POM ligands is represented in Figure **2.7**.

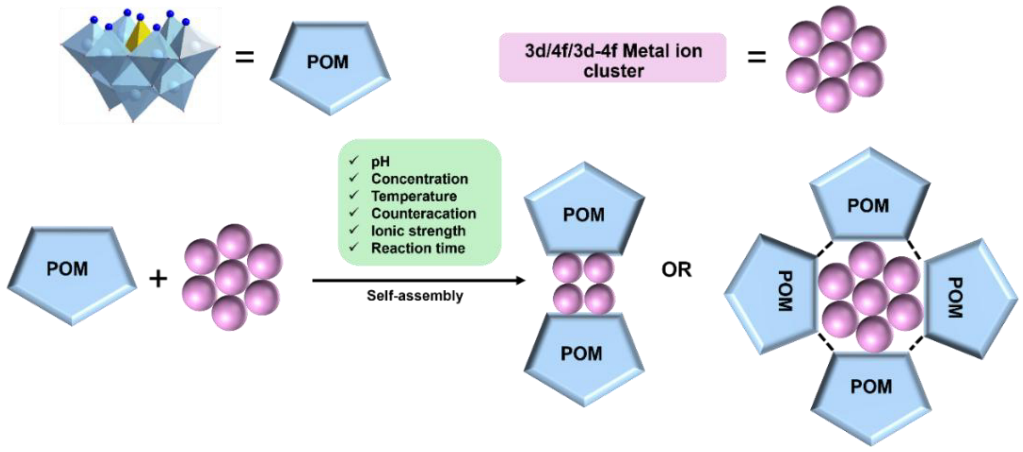


Figure 2.7 Schematic representation of 3d, 4f, and 3d-4f metal cluster-containing POMs via a self-assembly process.

In addition to metal ion and hetero metal ion clusters, substitution of organic ligand with the lacunary POM species is an effective way of functionalisation of inorganic POM species with organic ligand to form a POM hybrid material. This is an effective way to control the electronic properties, stability and extent of the field of applications of POM species.[41,42]

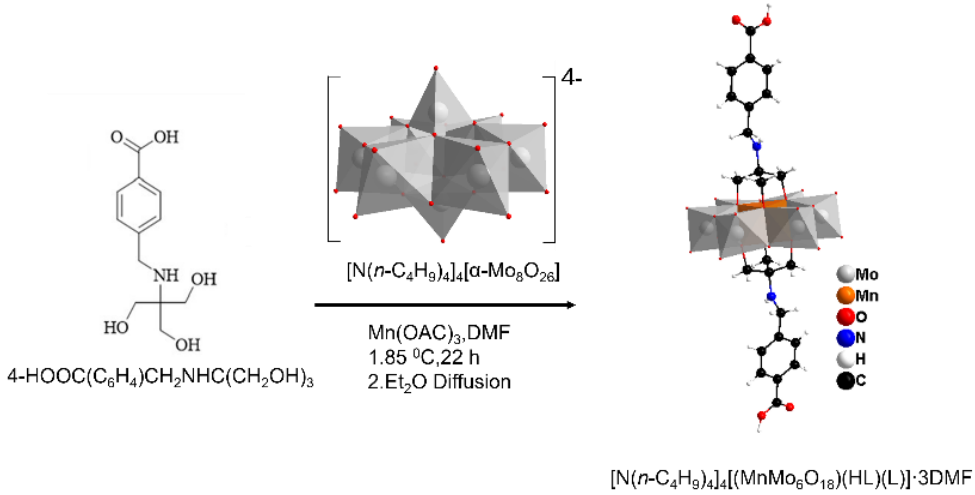


Figure 2.8 Synthesis of $MnMo_6$-Tris-C_4H_9.[43]

Anderson-Evans type POMs are fascinating compounds that have garnered significant interest for their versatile grafting strategies. These compounds can be functionalised with an array of multidentate alkoxy ligands, notably the elegant tris-ligands of the form $RC(CH_2OH)_3$. The variety of substituents R, which can include groups like $–NH_2$, –OH, $–CH_3$, and others, allows for a rich palette of chemical interactions and modifications, making these POMs invaluable in advanced materials science and coordination chemistry.[44,45]

Figure **2.8** shows a molecular structure of Mn^{2+}centred single-sided tris-functionalised Anderson-type polyoxometalates.[43]

2.6. General Properties of Polyoxometalates

Polyoxometalates show various properties depending on the diversity of their composition, counter ions, total charge, preparation medium, structure and structural arrangement. The POMs exhibit some common properties despite their diverse structure (Figure **2.9**).

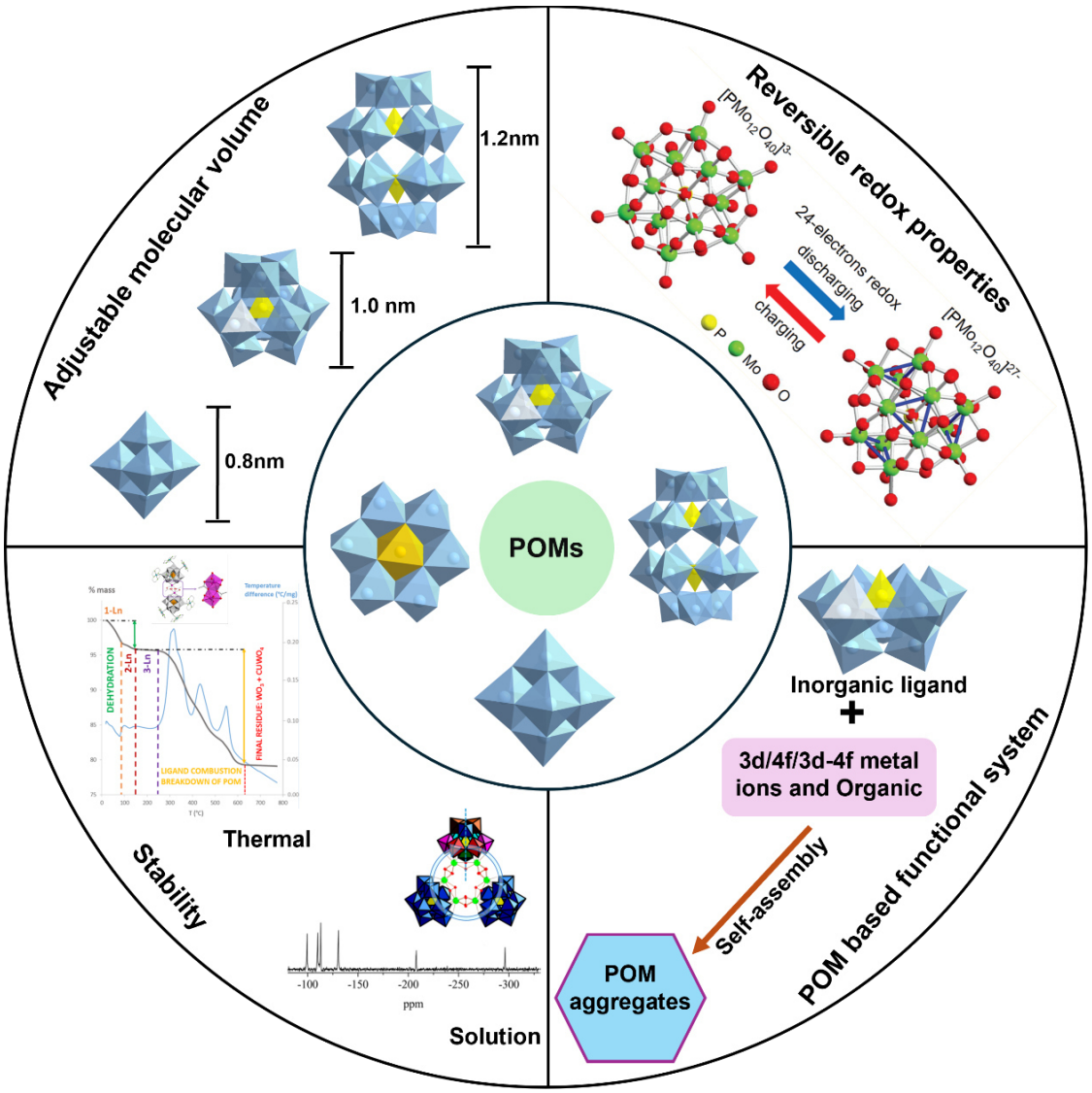


Figure 2.9 Important properties of polyoxometalates.

Stability

Most polyoxometalates exhibit remarkable stability in both solution and solid states, even when exposed to air and high temperatures. They generally maintain their structural integrity when dissolved in solution, making them suitable for various applications. Their thermal stability has been extensively studied using thermogravimetric analysis (TGA),

which reveals that many POMs can withstand high temperatures before undergoing decomposition.[46]

The extent of their stability depends on factors such as the type of addenda atom, counterions, and overall structural framework. To assess their stability in solution, various analytical techniques are employed. Nuclear Magnetic Resonance (NMR) spectroscopy provides insight into the structural integrity and dynamic behaviour of POMs in solution, while Electrospray Ionisation Mass Spectrometry (ESI-MS) helps determine molecular composition and detect possible degradation. Ultraviolet-Visible (UV-Vis) spectroscopy is useful for monitoring electronic transitions and potential aggregation, and Cyclic Voltammetry (CV) evaluates redox stability and electrochemical properties. These techniques collectively help confirm whether POMs maintain their structural framework under different environmental conditions, which is essential for their applications in catalysis, energy storage, and biomedical fields.[7,12,47–49]

Solubility

The degree of solubility of POMs depends on the solvents and, most importantly, the nature of the cation present. The polyoxometalates, which contain group 5 or 6 metal atoms like (V, Mo, W), can show excellent aqueous solubility in the presence of small alkali metals like Li or Na; however, they exhibit poor solubility when Cs ions are present in the solution. The application of these polyanions in chemistry largely depends on their solubility. The influence of cations on POM species is crucial for adjusting their properties, as some applications require solubility while others benefit from insoluble characteristics. The general solubility trends of POM with different counter cations are illustrated in Figure **2.10**.[50]

The solubility of inorganic-organic hybrid POMs is also primarily influenced by the type of countercations present. Due to their low surface charge density, POMs can dissolve in organic solvents with varying polarities, such as dimethyl sulfoxide and benzene, when suitable countercations are included. The solubility of POMs in organic solvents is further enhanced by the presence of large organic countercations like alkylammonium (e.g., tetraethylammonium or tetrabutylammonium) and alkylphosphonium (e.g., tetraethylphosphonium or tetrabutylphosphonium). These countercations consist of organic alkyl groups attached to nitrogen (in the case of alkylammonium) or phosphorus (in the case of alkylphosphonium) atoms. The large, hydrophobic nature of these countercations increases the interaction between POMs and organic solvents, thereby improving their solubility in non-aqueous environments.[47,51]

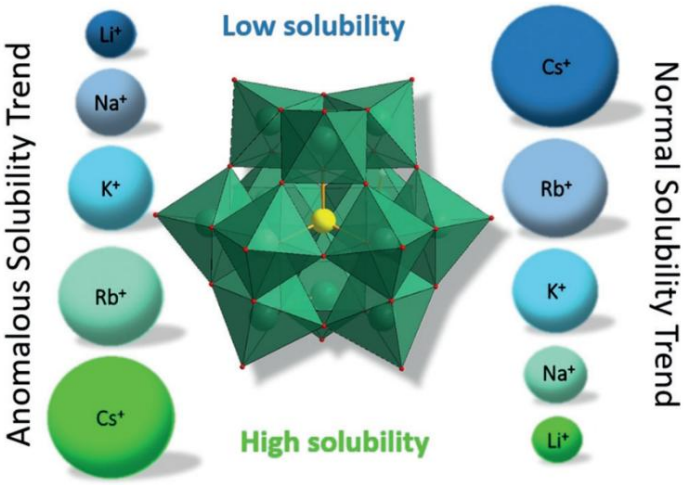


Figure 2.10 Solubility trends for Keggin ion POM species with alkali metal ion counter-cations. Blue represents the least soluble, and green represents the most soluble cations.[50]

Redox behaviour and electron-sponge properties of POMs

The electrochemical properties of POMs are based on the electron transfer behaviour within the POM system. Most POM structures, especially Keggin and Wells-Dawson structures, are redox active.[52] These structures can undergo a multielectron redox process without significant changes to their structure or degradation. The extra electrons added to the system are delocalised over the metal centres, which promotes faster electron transfer to the system. Electron transfer due to the redox process of POMs is always coupled to proton and cation transfer; mostly, the edge-sharing oxygen atoms are heavily protonated, resulting in faster electron transfer without changing the total structure of the cluster and total charge. Usually, biological systems involve this kind of electron transfer. Due to the structural stability of polyoxometalates upon redox reaction, POM species are reported as cathode materials of high-capacity lithium-ion batteries.

The reduced form of polyoxometalates (Polyoxomolybdates (POMos) and Polyoxotungstate (POTs)) carries an intense blue colour due to the intense d-d transition and intervalence charge transfer, which is known as blue or brown POMs. Usually, reduced POMs are stable enough that they will reoxidise to form oxidised POMs, which can accept or release electrons without altering the original structure. This reversible electrochemical property of POMs is well-explored in the field of electrocatalysis.[52–54]

The electron-sponge property of POMs is important in several applications, including catalysis, energy storage, electrochemical sensing, environmental remediation, and molecular electronics. In catalysis, their ability to reversibly accept and release electrons enhances efficiency in oxidation and reduction reactions (Figure **2.11**). In energy storage,

POMs are used in supercapacitors and batteries for efficient charge/discharge cycles. Additionally, their redox properties are key in electrochemical sensors and environmental processes such as water purification. Overall, this unique property makes POMs highly versatile for energy and catalytic applications.[56]

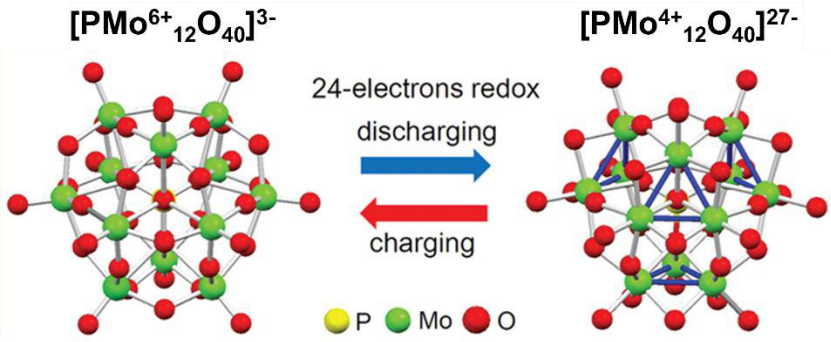


Figure 2.11 X-ray absorption near-edge structure analyses reveal that all 12 Mo^{6+} ions in $[PMo_{12}O_{40}]^{3-}$ are reduced to Mo^{4+} during the discharging process. This reduction leads to the formation of a super-reduced state of the POM, specifically $[PMo_{12}O_{40}]^{27-}$, which can store 24 electrons.[55]

2.7. Applications of Polyoxometalates

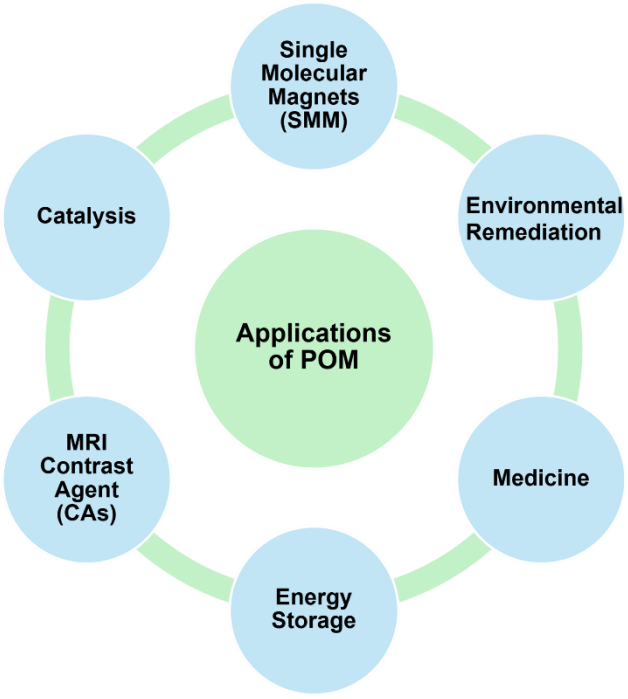


Figure 2.12 Important applications of polyoxometalates.

The applications of POMs are vast and mainly focus on the unique properties of these materials, which are explained in the previous section. These properties include flexible and diverse structures with controllable size and shape, thermal stability, proton transfer, and electron sponge properties. The structural robustness in solution and high Bronsted acidity of POMs make them interesting for solution-based applications. The range of POM

applications is extensive, with several notable uses summarised in Figure **2.12**. This section highlights some of the key applications of POMs.

Magnetism

The mono-, di-, and tri-lacunary polyoxometalate ligands are excellent polydentate oxygen donors for incorporating 3d and 4f spin-coupled magnetic centres with different spin ground states. These materials can exhibit ferromagnetic and antiferromagnetic interactions. In addition to that, the magnetic isolation of this paramagnetic centre within the diamagnetic POM ligand is also beneficial to understanding the magnetic properties, such as slow magnetic relaxation dynamics and quantum tunnelling of magnetisation.[57]

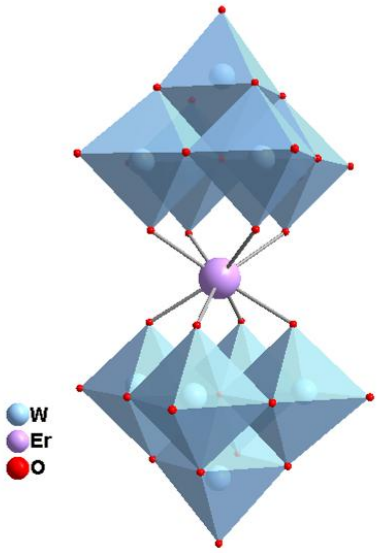


Figure 2.13 $[ErW_{10}O_{36}]^{9-}$ is the first polyoxometalate identified to behave as a single-molecular magnet (SMM).[58]

One of the most interesting features of these POM-based magnetic materials is that some of them show single-molecular magnetic (SMM) behaviour and magnetic stability. Single molecular magnets (SMM) are molecules that are magnetised in magnetic fields and show slow relaxation when the magnetic field is removed. SMMs are promising for application in quantum computing, high-density storage devices, molecular spintronics and quantum computing. The POM-based SMM demonstrates remarkable structural stability for surface deposition, enabling the fabrication of next-generation molecular devices and enhancing intrinsic magnetism. In comparison to organic ligand-based SMMs, inorganic POM ligand-based SMMs exhibit superior structural stability.[59,60]

$[ErW_{10}O_{36}]^{9-}$ is the first POM-based SMM that was reported by M. A. AlDamen et al. in 2008. The molecular structure consists of one Er^{3+} ion (4f) sandwiched between two anionic $[W_5O_{18}]^{6-}$ moieties (Figure **2.13**). The SMM behaviour observed for this lanthanide ion (4f)

substituted POM species is strongly dependent on the coordination geometry around the metal ion in the crystal structure.[58]

Tetrameric 36-tungsto-8-phosphate $[\{Co_4(OH)_3PO_4\}_4(PW_9O_{34})_4]^{28-}$(Figure **2.14**) is the 3d-POM SMM reported by M. Ibrahim et al,. This polyanionic species, containing a 16-metal-oxo cluster as the central magnetic core, is stabilised by four trilacunary $[PW_9O_{34}]^{9-}$ POM units.[61]

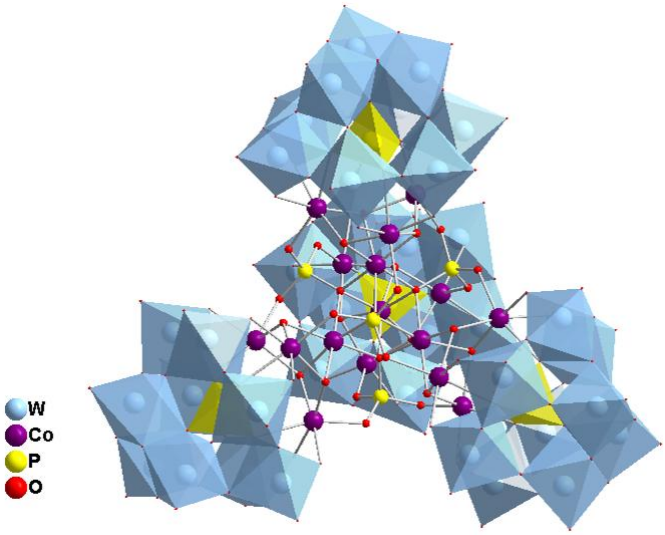


Figure 2.14 $[\{Co_4(OH)_3PO_4\}_4(PW_9O_{34})_4]^{28-}$: 3d-POM species exhibiting SMM behaviour.

Polyanion $[Dy_{30}Co_8Ge_{12}W_{108}O_{408}(OH)_{42}(H_2O)_{30}]^{56-}$ is the first all-inorganic heterometallic POM to exhibit SMM behaviour (Figure **2.15**). This complex features a unique combination of 3d-4f and 4f aggregates encapsulated by $[A\text{-}\alpha\text{-}GeW_9O_{34}]^{10-}$ ligands. Notably, it contains the largest number of 4f ions ever reported in a POM and is the first to incorporate two distinct 3d-4f and 4f coordination cluster assemblies within the same POM framework.[62]
Another important application of paramagnetic metal-containing POMs is their use as contrast agents for Magnetic Resonance Imaging (MRI). This application will be discussed in detail in Chapter **4** of this thesis.

Medicine and biotechnology

Several polyoxometalates have been identified and characterised as materials used in medicine. The practical utilisation of this pure inorganic ligand as a medicine is still in the initial stages. The unique size, wide range of length and shape, easy and economical synthetic procedure, stable structure even in the physiological pH, easily soluble in water and electron acceptor nature make POM an ideal candidate to consider as a biocompatible material.[63] Many POM-based materials have been shown to be more effective than existing organic drugs. The antiviral, antimicrobial and anticancer activities of POM are the most

significant medicinal applications. In 1971, Raynaud noticed the antiviral activities of tungstosilicate anion on the inhibition of murine leukaemia sarcoma virus. Later, several other viruses like polio, rubella, Rauscher leukaemia, etc. $(NH_4)_{17}Na[NaSb_9W_{21}O_{86}]$, also known as HPA-23, is the first POM which is administered to humans for the treatment of HIV in France.[64] However, the use of this drug was discontinued after three years because of its severe side effects. Anticancer activity was first mentioned by Mukherjee, who first administered the in vivo application of a mixture of $H_3[PW_{12}O_{40}]$, $H_3[PMo_{12}O_{40}]$, and caffeine to a cancer patient, and this effective drug completely killed the tumour cells.[65]

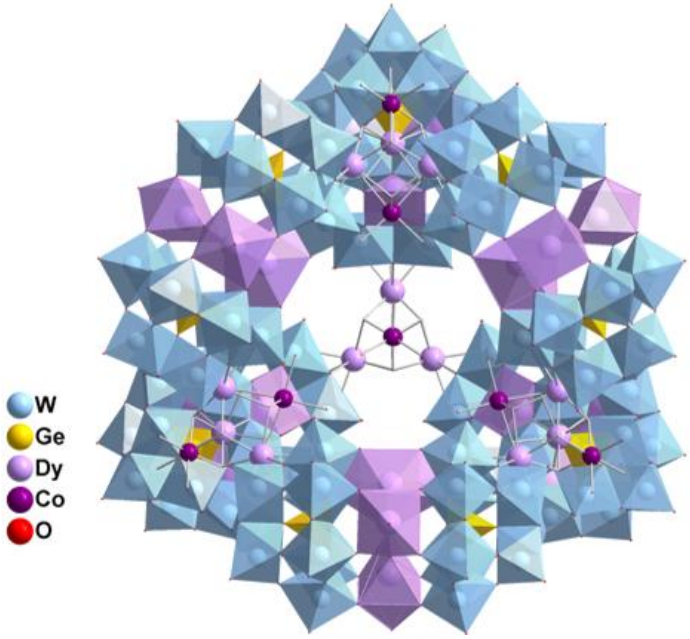


Figure 2.15 Molecular structure of $[Dy_{30}Co_8Ge_{12}W_{108}O_{408}(OH)_{42}(H_2O)_{30}]^{56-}$.[62]

Despite this good result, clinical application is very limited because of serious drawbacks, such as most of the POMs are highly toxic, some structures are not stable enough in the physiological pH, the interaction of POM as a drug with the biomolecules is not clear and the selectivity of POM with the proteins are very low, the naked POM possess low cell penetration. However, the properties of POMs are still valuable to consider as a bioactive agent. The encapsulated POM with nanostructure or other polymers functions as a less toxic and more effective alternative to the original POM. This requires further studies and clear evidence in the future to be applied as a bioactive material.[66,67]

Role of Polyoxometalates in catalysis

Polyoxometalates and their metal-substituted derivatives play a significant role in catalysis. Their unique properties make them suitable for various catalytic processes, including oxidation, acid and base catalysis, reduction reactions, polymerisation, and electrocatalysis.[68] The multifunctional nature, redox activity, and structural diversity of

POMs make them highly effective catalysts. Most POMs exhibit Lewis basicity due to the abundance of surface oxygen atoms, which can donate electrons to electron-acceptor species.[69] At the same time, the vacant orbital in the metal centres of the POMs accepts electrons from the electron-rich species and acts as a Lewis acid. Hence, the POMs can exhibit Lewis acid and Lewis base properties under different applied conditions. Polyoxometalates can collectively be regarded as electron sponges due to their ability to accept and donate electrons without undergoing structural alterations.

Additionally, the polyoxometalate framework, its constituent elements, and chemical behaviour can be easily tailored using various synthetic strategies. Another key property of POMs is their exceptional thermal stability, with most structures remaining stable at very high temperatures. Notably, the Keggin structure exhibits greater thermal stability than the Wells-Dawson structure, and the choice of countercations also significantly influences the thermal stability of POMs. Owing to their high thermal stability, POMs serve as excellent heterogeneous catalysts.[7] Polyoxometalates are widely used in both homogeneous and heterogeneous catalysis due to their unique properties. In homogeneous catalysis, their solubility in water and organic solvents is crucial for maintaining the homogeneous phase. POMs with larger countercations tend to have limited solubility in these solvents. To address this, ion exchange with appropriate cations is employed to enhance their solubility, enabling efficient catalytic reactions in various solvents.[70–72]

In heterogeneous catalysis, POMs offer significant advantages, particularly in recovery and recyclability. Additionally, POMs can be immobilised onto solid supports such as silica, metal oxides, or polymers. This immobilisation not only enhances their stability but also facilitates easier separation and reuse in catalytic processes, making POM-based catalysts more efficient and sustainable. This approach is particularly beneficial in large-scale applications where catalyst recovery and reusability are critical for reducing costs and environmental impact.[73]

The POMs exhibit remarkable sensitivity to light and electricity, enabling them to function as both photocatalysts and electrocatalysts. In photocatalysis, light energy activates the ground state of the POM molecule, initiating catalytic reactions. Due to the excitation by light, charge transfer takes place internally from the oxygen (O^{2-}) to the vacant d^0 orbital of the metal ions. As a result of this process, an electron-deficient hole site of the O^- and an electron-captured metal centre (M^{n+1}) couple is formed. This excited form of POM can perform better as an electron acceptor than the ground state. The well-defined HOMO-LUMO energy band hinder the recombination of the electron-hole pairs when the irradiation of light energy is higher than or equal to their energy band. Due to this property, the

photogenerated electrons and holes can initiate the photooxidative and photo-reductive reactions, respectively.[68,74]

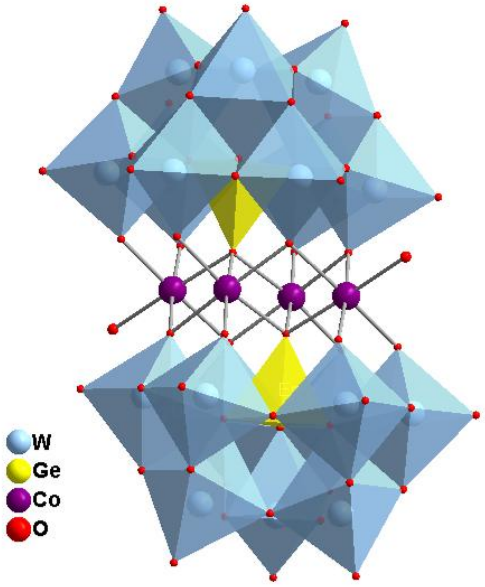


Figure 2.16 X-ray crystallographic structure of $[Co_4(H_2O)_2(PW_9O_{34})_2]^{10-}$.[75]

Transition metal-containing POMs (particularly with Mn, Fe, and Co) have been explored as catalysts for water oxidation, a key reaction for sustainable energy production. The first significant report on POM-catalysed water oxidation was published by C. Hill, where he demonstrated the potential of POMs, specifically the Keggin-type POM $[Co_4(H_2O)_2(PW_9O_{34})_2]^{10-}$ (Figure **2.16**) to catalyse the oxygen evolution reaction (OER). This discovery highlighted the ability of POMs to efficiently mediate water oxidation under mild conditions, setting the foundation for further research into their applications in clean energy technologies, such as artificial photosynthesis. Hill's pioneering work led to the development of POM-based catalysts with enhanced activity and stability for water splitting [75]

Further details about electrocatalysis will be discussed in Chapter **5** of this thesis.

3. Functionalisation of Polyoxometalates

3.1. Introduction

This chapter presents the synthesis and characterisation of three novel 3d transition metal-substituted POMs and six heterometallic 3d-4f-based POM molecules. The incorporation of transition metals, lanthanides, and mixed-metal clusters into the POM framework enhances both structural diversity and functional versatility. Lacunary POMs, formed through the selective removal of metal-oxo units from plenary POMs, serve as robust inorganic ligands enabling coordination of various metal cations. These vacant frameworks allow the selective incorporation of transition metals, lanthanides, or their combinations, leading to high-nuclearity, multifunctional hybrid clusters. Such systems exhibit promising properties for applications in catalysis, molecular magnetism, optical sensing, energy storage, and biomedical imaging, including their use as MRI contrast agents.[76–82]

Table 3.1 Cobalt-containing high nuclearity polyoxometalates.

POM Cluster	Nuclearity	Ref.
$[\{Co_3(B\text{-}\alpha\text{-}SiW_9O_{33}(OH))(B\text{-}\alpha\text{-}SiW_8O_{29}(OH)_2)\}_2]^{22-}$	6	[83]
$[\{(B\text{-}\beta\text{-}SiW_9O_{33}(OH))(\beta\text{-}SiW_8O_{29}(OH)_2)Co_3(H_2O)\}_2Co(H_2O)_2]^{20-}$	6	[84]
$[Co_3O(H_2O)(A\text{-}\alpha\text{-}PW_9O_{34})_2]^{14-}$	6	[85]
$[Co_2(H_2O)_{10}Co_4(H_2O)_2(B\text{-}\alpha\text{-}GeW_9O_{34})_2]^{8-}$	6	[86]
$\{Co_{1.5}(H_2O)_{5.5}\}[Co_{11}(OH)_5(H_2O)_5(W_6O_{24})(PW_9O_{34})_3]^{19-}$	8	[87]
$[Co_9(OH)_3(H_2O)_6(PO_4)_2(B\text{-}\alpha\text{-}GeW_9O_{34})_3]^{21-}$	9	[88]
$[Co_9(H_2O)_6(OH)_3(HPO_4)_2(PW_9O_{34})_3]^{16-}$	9	[89]
$[\{Co_4(OH)_3(H_2O)(PW_9O_{34})\}_2\{K\subset(H_2W_{12}O_{41})_2\}\{Co(H_2O)_4\}_2]^{17-}$	12	[87]
$[Co_6(H_2O)_{30}\{Co_9Cl_2(OH)_3(H_2O)_9(\beta\text{-}SiW_8O_{31})_3\}]^{5-}$	15	[90]
$[\{Co_4(OH)_3PO_4\}_4(A\text{-}\alpha\text{-}PW_9O_{34})_4]^{28-}$	16	[91]
$[\{Co_4(OH)_3PO_4\}_4(A\text{-}\alpha\text{-}SiW_9O_{34})_4]^{32-}$	16	[92]
$[\{Co_4(OH)_3PO_4\}_4(A\text{-}\alpha\text{-}GeW_9O_{34})_4]^{32-}$	16	[92]
$\{[Co_8(\mu_2\text{–}OH)(\mu_3\text{–}OH)_2(H_2O)_2(Co(H_2O)GeW_6O_{26})(B\text{-}\alpha\text{-}GeW_9O_{34})_2][BO(OH)_2][Co_{12}(\mu_2\text{–}OH)(\mu_3\text{–}OH)_5(H_2O)_3(Co(H_2O)GeW_6O_{26})(GeW_6O_{26})(B\text{-}\alpha\text{-}GeW_9O_{34})]\}^{31-}$	20	[93]
$[Co(H_2O)_6]_2\{[Na(H_2O)_4]_2[Na(H_2O)_2]_2[Co(H_2O)_3]_2[Co_{21}(H_2O)_4(OH)_{12}](SiW_{10}O_{37})_6\}^{18-}$	25	[94]
$\{Co^{III}(H_2O)_6\}_4\{[Co^{II}_4(\mu_3\text{-}OH)_3(PO_4)]_4(A\text{-}\alpha\text{-}GeW_9O_{34})_4\}_2^{52-}$	40	[95]

Previously reported high-nuclearity cobalt, nickel and iron-containing polyoxometalates are listed in Tables **3.1**, **3.2**, and **3.3.**

Table 3.2 Nickel-containing high nuclearity polyoxometalates.

POM Cluster	Nuclearity	Ref.
$[\{Ni_6(H_2O)_4(\mu_2\text{-}H_2O)_4(\mu_3\text{-}OH)_2\}(x\text{-}SiW_9O_{34})_2]^{10-}$	6	[96]
$[Na_3\subset\{Ni(H_2O)_4\}_6\{WO(H_2O)\}_3(P_2W_{12}O_{48})_3]^{15-}$	6	[97]
$[(SiW_8O_{31})_2Ni_7(H_2O)_4(OH)_6]^{12-}$	7	[98]
$[Ni_7(OH)_4(H_2O)(CO_3)_2(HCO_3)(A\text{-}\alpha\text{-}SiW_9O_{34})(\beta\text{-}SiW_{10}O_{37})]^{10-}$	7	[96]
$[Na\{(A\text{-}\alpha\text{-}SiW_9O_{34})Ni_4(CH_3COO)_3(OH)_3\}_2]^{15-}$	8	[99]
$[Na\{(A\text{-}\alpha\text{-}SiW_9O_{34})Ni_4(CH_3COO)_3(OH)_2(N_3)\}_2]^{15-}$	8	[99]
$[Ni_9(OH)_3(H_2O)_6(HPO_4)_2(PW_9O_{34})_3]^{16-}$	9	[100]
$[(A\text{-}\alpha\text{-}SiW_9O_{34})_2Ni_9(OH)_6(H_2O)_6(CO_3)_3]^{14-}$	9	[99]
$[Ni_{12}(OH)_9\text{-}WO_4(W_7O_{26}(OH))(PW_9O_{34})_3]^{25-}$	12	[101]
$[Ni_{12}(OH)_9(CO_3)_3(PO_4)(SiW_9O_{34})_3]^{24-}$	12	[102]
$[Ni_{13}(H_2O)_3(OH)_9(PO_4)_4(SiW_9O_{34})_3]^{25-}$	13	[102]
$[Ni_{14}(OH)_6(H_2O)_{10}(HPO_4)_4(P_2W_{15}O_{56})_4]^{34-}$	14	[103]
$[\{Ni_4(OH)_3AsO_4\}_4(B\text{-}\alpha\text{-}PW_9O_{34})_4]^{28-}$	16	[104]
$[Ni_{16}(H_2O)_{15}(OH)_9(PO_4)_4(A\text{-}\alpha\text{-}SiW_9O_{34})_3]^{19-}$	16	[105]
$[Ni_{25}(H_2O)_2OH)_{18}(CO_3)_2(PO_4)_6(SiW_9O_{34})_6]^{50-}$	25	[102]
$[Ni_{36}(H_2O)_{36}(OH)_{18}(SiW_9O_{34})_6]^{6-}$	36	[106]

Table 3.3 Iron-containing high nuclearity polyoxometalates.

POM Cluster	Nuclearity	Ref.
$[Fe_4(H_2O)_2(FeW_9O_{34})_2]^{10-}$	6	[107]
$[(\alpha\text{-}SiFe_3W_9(OH)_3O_{34})_2(OH)_3]^{11-}$	6	[108]
$[(\alpha\text{-}Si(FeOH_2)_2FeW_9(OH)_3O_{34})_2]^{8-}$	6	[108]
$Cs_4Na_7[Fe_6(OH)_3(A\text{-}\alpha\text{-}GeW_9O_{34}(OH)_3)_2]^{11-}$	6	[109]
$[Fe_4(H_2O)_2(FeW_9O_{34})_2]^{16-}$	6	[110]
$[(Fe_4W_9O_{34}(H_2O))_2\ (FeW_6O_{26})]^{19-}$	6	[111]
$[Fe_6Se_6W_{34}O_{124}(OH)_{16}]^{18-}$	6	[112]
$[H_4P_2W_{12}Fe_9O_{56}(OAc)_7]^{6-}$	9	[113]
$[Rb_9Cs_4H_{37}Fe_{10}O_{34}(A\text{-}\alpha\text{-}PW_9O_{31})_3(OH)_3]^{6-}$	10	[114]
$[Fe_{11}(H_2O)_{14}(OH)_2(W_3O_{10})_2(\alpha\text{-}SbW_9O_{33})_6]^{27-}$	11	[115]
$[KFe_{12}(OH)_{18}(a\text{-}1,2,3\text{-}P_2W_{15}O_{56})_4]^{29-}$	12	[116]
$[Fe^{III}_{13}P_8W_{60}O_{227}(OH)_{15}(H_2O)_2]^{30-}$	13	[117]
$[Fe^{III}_{13}P_8W_{60}O_{224}(OH)_{12}(PO_4)_4]^{33-}$	13	[117]
$[H_3Rb_3Fe_{14}(OH)_{12}(PO_4)_6(B\text{-}\alpha\text{-}PW_9O_{34})_2]^{9-}$	14	[114]
$[Na_2Fe_{14}(OH)_{12}(PO_4)_4(A\text{-}\alpha\text{-}XW_9O_{34})_4]^{20-}$, X = Si, Ge	14	[118]

$[NaFe_{15}(OH)_{12}(PO_4)_4\ (A\text{-}\alpha\text{-}SiW_9O_{34})_4]^{21-}$	15	[119]
$[P_8W_{48}O_{184}Fe_{16}(OH)_{28}(H_2O)_4]^{20-}$	16	[120]
$[H_{55}P_8W_{49}Fe_{27}O_{248}]^{26-}$	27	[121]
$[H_{56}P_8W_{48}Fe_{28}O_{248}]^{28-}$	28	[121]
$[((W^{VI})W_5^{VI}O_{21}(SO_4)_{12})((Fe(H_2O))_{30})(SO_4)_{13}(H_2O)_{34}]^{42-}$	30	[122]
$[Fe_{48}(OH)_{76}(H_2O)_{16}(HP_2W_{12}O_{48})_8]^{36-}$	48	[123]

The primary methods for synthesising such hybrid materials generally involve straightforward one-pot synthesis techniques and hydrothermal processes.[124–126] In recent developments, microwave-assisted synthesis is also used as a fast and efficient method to produce polyoxometalates, helping to reduce reaction times.[127] [128]

In the synthesis of POM-based hybrid systems, self-assembly governs the organisation of POM units with metal cations or metal oxo-clusters. Although the exact mechanism is not yet fully understood, factors such as temperature, pH, concentration, and ionic strength significantly influence the outcome of the assembly process.[129–132]

Compared to 3d metals, lanthanide ions are harder to incorporate into POMs' skeleton due to their larger size and variable coordination numbers. They often lead to extended structures, acting as linkers between POM units.[133]

Whereas the incorporation of either 3d or 4f metal ions into POMs is well established, the construction of heterometallic 3d-4f POM clusters remains challenging. These clusters benefit from the synergistic properties of both metal types, enhancing their magnetic, luminescent, and catalytic features. However, reactions involving lacunary POM ligands with 3d and 4f metal ions often result in amorphous precipitates rather than well-defined crystalline materials.[134] Additionally, the strong oxophilic nature of 4f ions can impede the formation of 3d-4f aggregates and their coordination with the POM ligands, complicating the synthesis process.[135–137] Table **3.4** lists all previously reported all-inorganic 3d-4f heterometallic POM clusters.

Table 3.4 All inorganic 3d-4f-POM metal clusters.

POM Cluster	Ln/3d	Ref.
$[\{(GeW_9O_{34})_2Dy^{3+}{}_3(\mu_2\text{-}OH)_3(H_2O)_2\}_6\{Co^{2+}{}_2Dy^{3+}{}_3(\mu_3\text{-}OH)_6(OH_2)_6\}_4]^{56-}$	Dy_{30}/Co_8	[138]
$[K\subset\{FeCe(AsW_{10}O_{38})(H_2O)_2\}_3]^{13-}$	Ce_3/Fe_3	[139]
$[\{\alpha\text{-}P_2W_{15}O_{56}\}_6\{Ce_3Mn_2(\mu_3\text{-}O)_4(\mu_2\text{-}OH)_2\}_3(\mu_2\text{-}OH)_2(H_2O)_2(PO_4)]^{47-}$	Ce_6/Mn_6	[140]
$[\{Ce(H_2O)_2\}_2Mn_2(B\text{-}R\text{-}GeW_9O_{34})_2]^{8-}$	Ce_2/Mn_2	[141]
$[\{Ce^{4+}(OAc)\}Cu^{2+}{}_3(H_2O)(B\text{-}R\text{-}GeW_9O_{34})_2]^{11-}$	Ce/Cu_3	[142]
$[Dy_6Fe_6(H_2O)_{12}(SiW_{10}O_{38})_6]^{26-}$ Ln= Dy, Tb	Ln_6/Fe_6	[143]

$[Fe_{16}O_2(OH)_{23}(H_2O)_9P_8\ W_{49}O_{189}Ln_4(H_2O)_{19}]^{11-}$, Ln = Eu, Gd	Ln_4/Fe_{16}	[144]
$[\{Dy^{3+}Mn^{3+}{}_4(\mu_3\text{-}O)_2(\mu_2\text{-}OH)_2(H_2O)(CO_3)\}(\beta\text{-}SiW_8O_{31})_2]^{13-}$	Dy/Mn_4	[145]
$[Ln_2Fe_2(B\text{-}\alpha\text{-}FeW_9O_{34})_2]^{10-}$, Ln = Dy, Ho,Y	Ln_2/Fe_2	[146]
$[Ln\{PZn_2W_{10}O_{38}(H_2O)_2\}_2]^{11-}$, Ln = Nd, Sm, Eu, Gd, Tb, Dy, Ho, Er, Tm, Yb, and Lu	Ln/Zn_4	[147]
$Na_{21}K_2[LaNi_{12}W_{35}Sb_3P_3O_{139}(OH)_6]^{23-}$	La/Ni_{12}	[148]
$Na_{70}K_4H_{12}[La_{10}Ni_{48}W_{140}Sb_{16}P_{12}O_{568}(OH)_{24}(H_2O)_{20}]^{96-}$	La_{10}/Ni_{48}	[148]
$[Dy_3(H_2O)_6Ni(H_2O)(W_3O_{11})(B\text{-}\alpha\text{-}SbW_9O_{33})_3]^{20-}$	Dy_3/Ni	[149]
$[Cr_6Ln_6(H_2O)_{12}(\alpha\text{-}GeW_{10}O_{38})_6]^{36-}$, Ln = Dy, Tb	Ln_6/Cr_6	[150]
$[HoCo_7Si_3W_{29}O_{108}(OH)_5(H_2O)_4]^{18-}$	Ho/Co_7	[151]
$[\{Dy(H_2O)_6\}_2Mn_4P_4W_{30}O_{112}(H_2O)_2]^{10-}$	Dy_2/Mn_4	[152]
$[Ln_3(H_2O)_5Ni^{2+}(H_2O)_3(Sb_4O_4)(SbW_9O_{33})_3(Ni^{2+}W_6O_{24})(WO_2)_3(CH_3COO)]^{17-}$, Ln = La, Pr, Nd	Ln_3/Ni_6	[153]
$[Ln_3(H_2O)_3Ni^{2+}{}_3(H_2O)_6(SbW_9O_{33})_3(WO_4)(CO_3)]^{16-}$, Ln = La, Pr, Nd	Ln_3/Ni_3	[153]
$[Ln(H_2O)_5\{Ni(H_2O)\}_2As_4W_{40}O_{140}]^{21-}$, Ln = Y, Ce, Pr, Nd, Sm, Eu, Gd	Ln/Ni_2	[154]
$[((VO)_2Dy\ (H_2O)_4K_2(H_2O)_2Na(H_2O)_2)(a\text{-}B\text{-}AsW_9O_{33})_2]^{8-}$	Dy/V_2	[155]
$[Ce_3Mn_2O_6(OAc)_6(H_2O)_9]_2\ [Mn_2P_2W_{16}O_{60}]_3$	Ce_3/Mn_2	[156]
$[Ln\{PCo_2W_{10}O_{38}(H_2O)_2\}_2]^{11-}$, Ln = Sm, Eu, Gd, Tb, Dy, Ho, Er, Tm, Yb, Lu	Ln/Co_4	[157]
$[Ln_3(H_2O)_5Ni^{2+}(H_2O)_3(Sb_4O_4)(SbW_9O_{33})_3(Ni^{2+}W_6O_{24})\text{-}(WO_2)_3(CH_3COO)]^{17-}$, Ln = La, Pr, Nd	Ln_3/Ni_2	[158]
$[Ln_3(H_2O)_3Ni^{2+}{}_3(H_2O)_6(SbW_9O_{33})_3(WO_4)(CO_3)]^{16-}$, Ln = La, Pr, Nd	Ln_3/Ni_3	[158]
$[Ln_3Ni^{2+}{}_9(\mu_3\text{-}OH)_9(SbW_9O_{33})_2(PW_9O_{34})_3(CH_3COO)_3]^{30-}$, Ln = Dy, Er	Ln_3/Ni_9	[158]
$[HoCo_7Si_3W_{29}O_{108}(OH)_5(H_2O)_4]^{18-}$	Ho/Co_7	[159]
$[Cr_6Ln_6(H_2O)_{12}(\alpha\text{-}GeW_{10}O_{38})_6]^{36-}$, Ln =Dy,Ho	Ln_6/Cr_6	[160]

3.2. Synthesis and Structural Features of Transition Metal - Substituted POMs (TM-SPs)

This section presents the synthesis, characterisation, and crystal structure analysis of three transition metal-substituted polyoxotungstate complexes (excluding **Fe_4-GeW_{10}**).

1. $Na_{36}CoCs_2[Cs_8(W_{10}Co_2GeO_{38})_6]\cdot 120\ H_2O$ **(Co_{12}-GeW_{10})**
2. $Na_{37}Cs_3[Cs_8\{W_{10}Ni_2GeO_{38}\}_6]\cdot 160\ H_2O$ **(Ni_{12}-GeW_{10})**
3. $K_{12}(OH_2)_{24}[\{W_{10}Fe_2PO_{37}\}_4\{Fe_4(PO_4)_4\}]\cdot 30\ H_2O$ **(Fe_{12}-PW_{10})**
4. $K_{14}[Fe^{3+}{}_4(\mu\text{-}O)_2(\mu\text{-}OH)_2\{W_{10}GeO_{37}\}_2]\cdot 34\ H_2O$ **(Fe_4-GeW_{10})**

These polyanions were synthesised through simple one-pot reactions in aqueous media. Their solid-state structures were characterised using single-crystal X-ray diffraction, ATR-

FTIR spectroscopy, PXRD, and elemental analysis. Additionally, ESI-MS studies were performed to evaluate the stability of these clusters in solution.

3.2.1. Co_{12}-GeW_{10} and Ni_{12}-GeW_{10}

Synthetic procedure

$Na_{30.5}K1.5[\{Co_4(OH)_3PO_4\}_4(A\text{-}\alpha\text{-}GeW_9O_{34})_4]\cdot 116H_2O$(**$Co_{16}$-$GeW_9$**) and $Na_{37}Cs_3[Cs_8(W_{10}Ni_2GeO_{38})_6]\cdot 120H_2O$ **(Ni_{12}-GeW_{10})** were synthesised via a simple one-pot reaction in aqueous medium. The reactions involved mixing $CoCl_2\cdot 6H_2O$ or $Ni(NO_3)_2\cdot 6H_2O$ with the trilacunary precursor $Na_{10}[A\text{-}\alpha\text{-}GeW_9O_{34}]\cdot 18H_2O$ and $Y(NO_3)_3\cdot 5H_2O$ in sodium phosphate buffer (pH 8.6–8.8), followed by heating at 80°C. CsCl was added dropwise after the reaction to aid crystallisation. **Co_{12}-GeW_{10}** formed purple elongated crystals after two days, while pale green crystals of **Ni_{12}-GeW_{10}** appeared within three to four days.

The addition of $Y(NO_3)_3\cdot 5H_2O$ was found to be crucial for the formation and crystallisation of the **Co_{12}-GeW_{10}** and **Ni_{12}-GeW_{10}** polyanions. Although Y^{3+} was not detected in the final crystal structure by single-crystal X-ray diffraction or elemental analysis, its presence in the reaction mixture likely played a key role in stabilising intermediate species or influencing the crystallisation environment. Similar effects have been observed with other lanthanide ions, suggesting that various Ln^{3+} salts could serve the same purpose as $Y(NO_3)_3\cdot 5H_2O$ in this synthetic system. Importantly, in the absence of Y^{3+}, the target POM clusters were not obtained; instead, reported or undesired POM species were formed, highlighting the essential role of Y^{3+} in directing the synthesis toward the desired products.

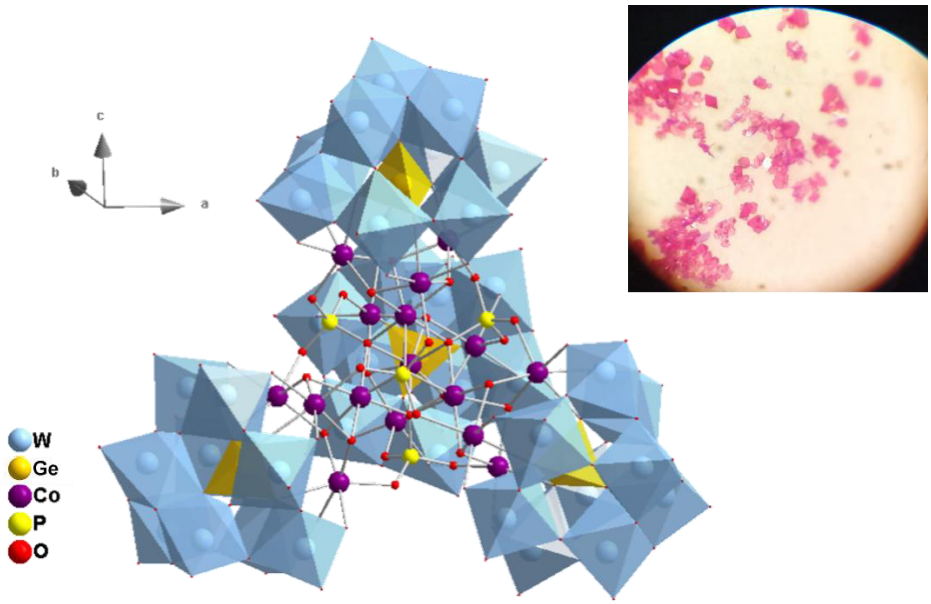


Figure 3.1 Combined ball and stick and polyhedral representation of **Co_{16}-GeW_9**, image of a microscopic view of maroon square-shaped crystals of **Co_{16}-GeW_9** (upper right).

The successful synthesis of pure **Co_{12}-GeW_{10}** and **Ni_{12}-GeW_{10}** with high yields depends on two main factors. First, controlling the concentration of cobalt and nickel ions precisely, maintaining an optimal metal salt to POM precursor ratio of 1:3, is essential. Using lower metal ion concentrations typically leads to the formation of mixed products instead of the desired pure phases. Second, the POM precursor must be prepared without the final NaCl washing step. When these conditions are not met, the reaction produces a mixture of crystals, including the desired purple, elongated **Co_{12}-GeW_{10}** crystals along with denser, maroon-coloured, square-shaped crystals (Figure **3.1**).

Further analysis using ATR-FTIR spectroscopy and single-crystal X-ray diffraction confirmed that the maroon crystals correspond to $Na_{30.5}K_{1.5}[\{Co_4(OH)_3PO_4\}_4(A\text{-}\alpha\text{-}GeW_9O_{34})_4]\cdot 116\ H_2O$ (**Co_{16}-GeW_9**), identified as the previously reported structure.[91] The ATR-FTIR spectrum of this mixture displays a prominent peak at 1200 cm^{-1}, indicating the presence of phosphate ions within the structure (Figure **3.2**). The proportion of **Co_{16}-GeW_9** decreases with the addition of excess cobalt chloride during the synthesis process. This is supported by the reduced intensity of the phosphate peak in the ATR-FTIR spectrum and the noticeable decline in the number of denser red crystals in the final product. Achieving an optimal amount of 1.6 mmol of cobalt chloride results in the formation of 100% pure purple **Co_{12}-GeW_{10}** crystals, as confirmed by microscopic examination of the final dry crystals (Figure **3.3**). This finding was further validated by ATR-FTIR spectroscopy, which showed no phosphate peak, indicating the absence of unwanted products.

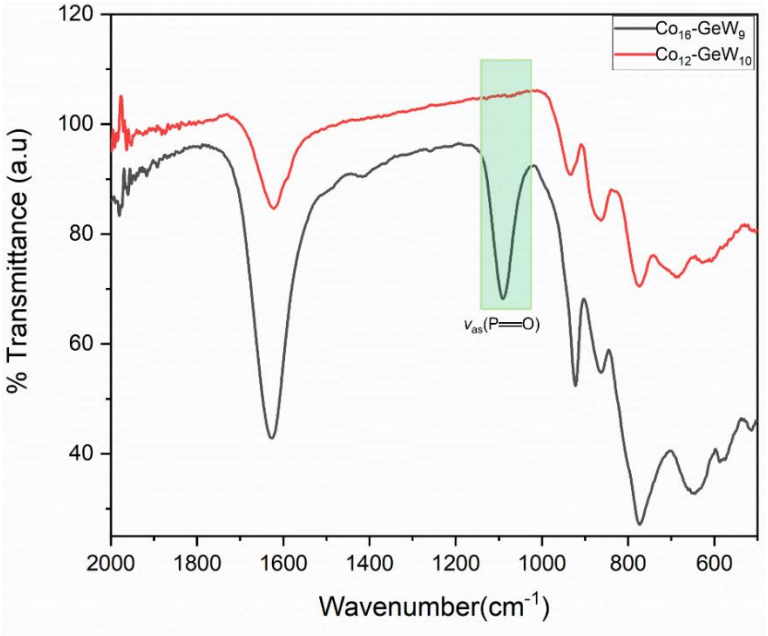


Figure 3.2 The ATR-FTIR spectra of **Co_{12}-GeW_{10}** and **Co_{16}-GeW_9** show that the phosphate peak at approximately 1200 cm^{-1} differentiates the two structures.

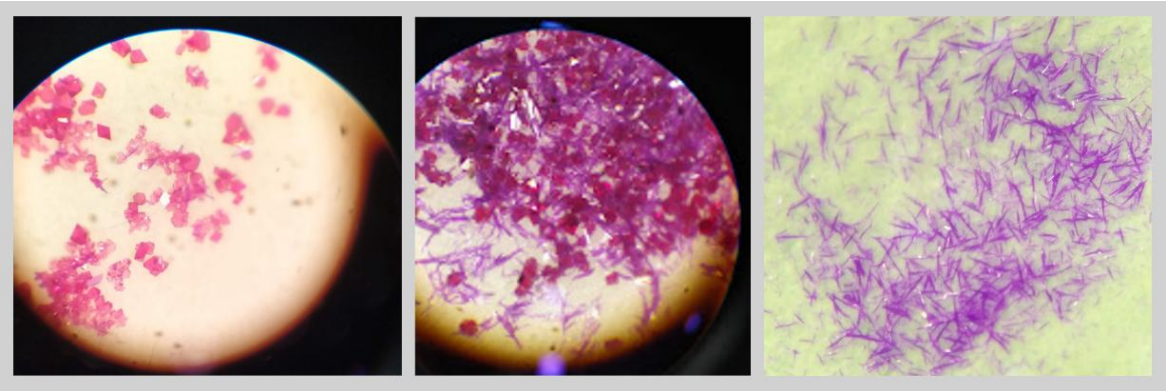


Figure 3.3 Microscopic view of maroon coloured square-shaped crystals **Co_{16}-GeW_9** (left), a mixture of crystals (middle), pure purple coloured elongated **Co_{12}-GeW_{10}** crystals (right).

Ni_{12}-GeW_{10} was prepared following the same procedure as **Co_{12}-GeW_{10}**. However, unlike **Co_{12}-GeW_{10}**, the **Ni_{12}-GeW_{10}** crystals exhibited instability after formation. The initially obtained yellowish-green crystals gradually transformed into a sticky, oily substance when left in the mother liquor for an extended period after crystallisation (Figure **3.4**). ATR-FTIR analysis (Figure **3.5**) revealed significant differences between the freshly formed crystals and the transformed material, indicating a change in the structural framework. To prevent this transformation, it is essential to filter the crystals from the mother liquor immediately after crystallisation or seal the reaction vessels once crystal formation is complete.

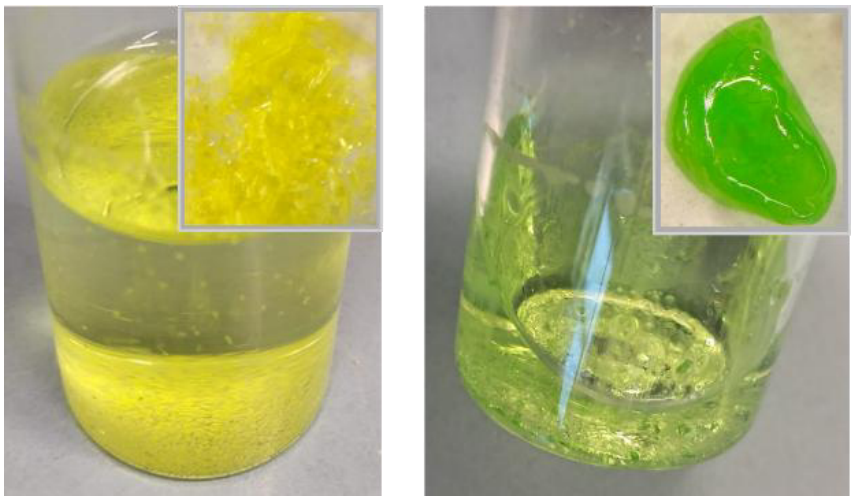


Figure 3.4 Pure yellowish green coloured **Ni_{12}-GeW_{10}** (left). Dry yellowish green crystals of **Ni_{12}-GeW_{10}** are shown on the upper side. The pure **Ni_{12}-GeW_{10}** crystals transformed to a green oily sticky substance (right) when exposed to air. The green oily sticky substance is shown on the upper side.

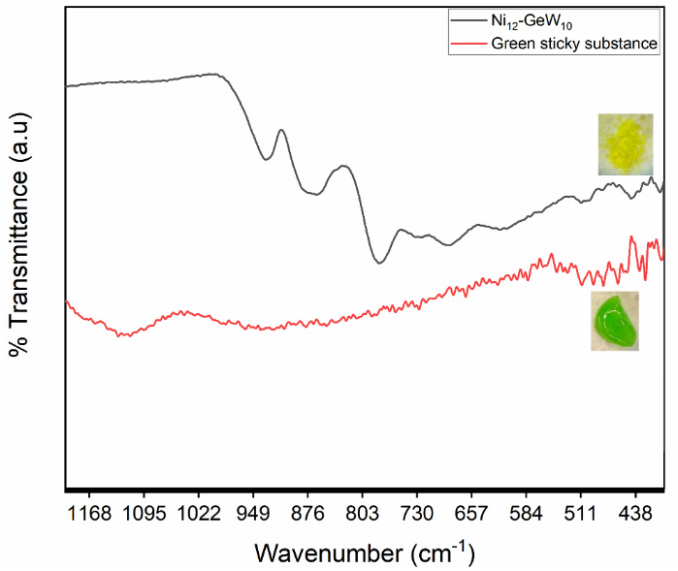


Figure 3.5 ATR-FTIR spectra of **Ni_{12}-GeW_{10}** and the transformed green sticky substance. The difference in the IR spectral patterns indicates the disruption of the **Ni_{12}-GeW_{10}** material.

Crystal structure

X-ray diffraction studies reveal that both polyoxotungstate complexes of Co_{12} containing $Na_{36}CoCs_2[Cs_8(W_{10}Co_2GeO_{38})_6]\cdot 120H_2O$ (**Co_{12}-GeW_{10}**) and Ni_{12} containing $Na_{37}Cs_3[Cs_8\{W_{10}Ni_2GeO_{38}\}_6]\cdot 160H_2O$ (**Ni_{12}-GeW_{10}**) are isostructural (Figures **3.6** and **3.7**); therefore, only the crystal structure of **Co_{12}-GeW_{10}** will be discussed in detail.

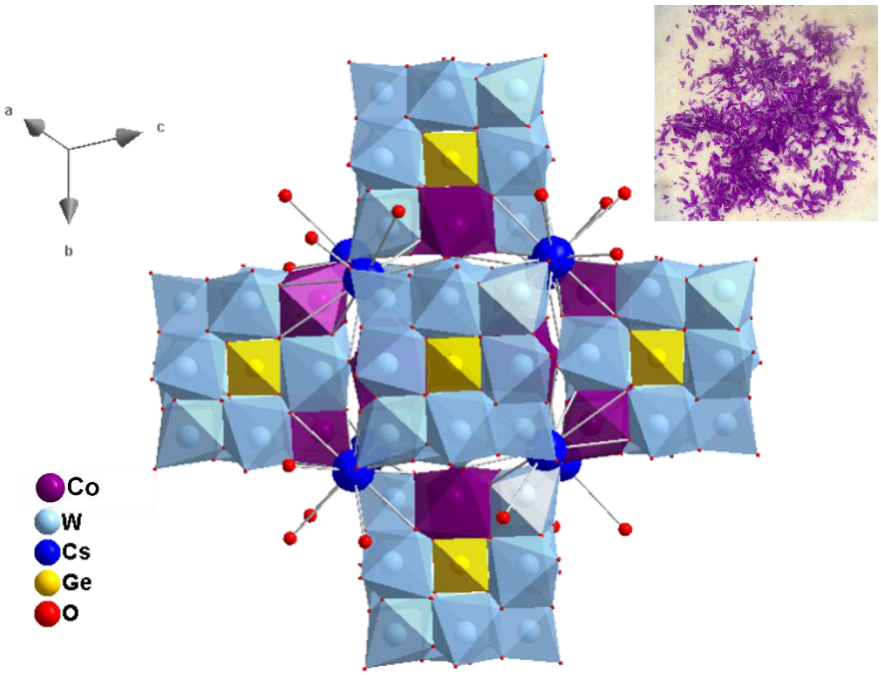


Figure 3.6 Molecular structure of **Co_{12}-GeW_{10}** with Cs ions as linkers. The pure purple coloured **Co_{12}-GeW_{10}** crystals are shown in the upper right.

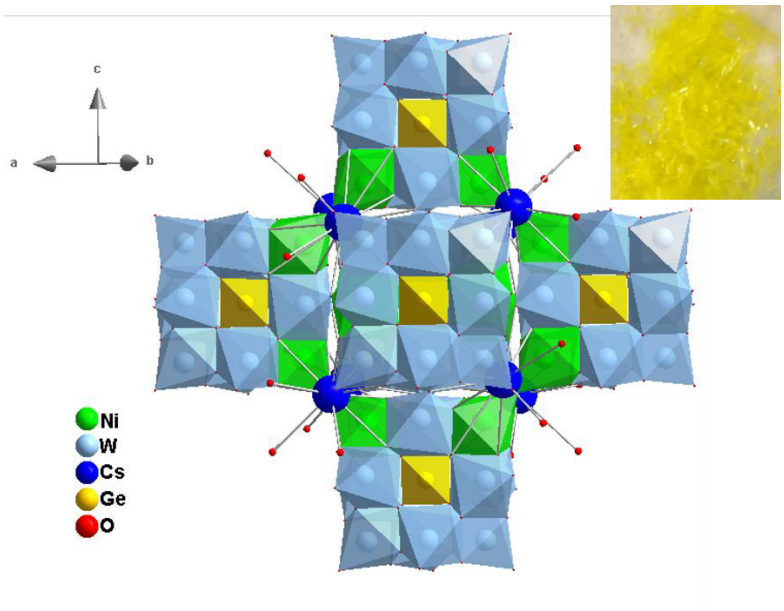


Figure 3.7 Molecular structure of **Ni_{12}-GeW_{10}** with Cs ions as linkers. The pure yellowish green coloured **Ni_{12}-GeW_{10}** crystals are shown in the upper right.

Co_{12}-GeW_{10} crystallised in the triclinic system with space group C12/c1. The crystal structure consists of six dicobalt-substituted dilacunary Keggin units, formulated as $\{GeW_{10}Co_2O_{38}\}]^{8-}$, which are connected by Cs^+ ions acting as linkers between the building blocks (Figure **3.8**).

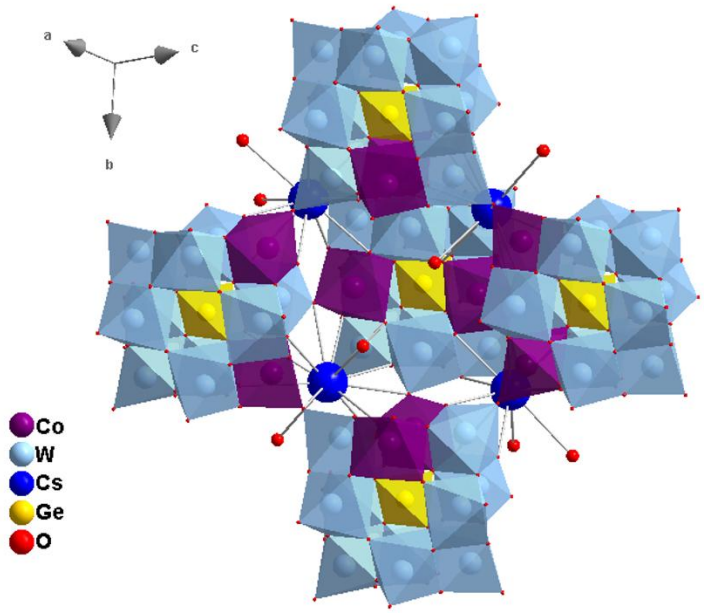


Figure 3.8 One $\{GeW_{10}Co_2O_{38}\}^{8-}$ building block and four Cs atoms removed, the inner part of the molecule is viewed through the C4 axis.

To enhance our understanding of the structure, the Keggin units are regarded as cobalt-disubstituted building blocks, as illustrated in Figure **3.9**. Each dilacunary Keggin-type POM building unit in the structure can be formulated as $\{GeW_{10}Co_2O_{38}\}^{8-}$, where the lacunary

nature of the POM unit arises from the absence of two of the twelve addenda tungsten atoms typically found in a complete Keggin structure ($\{GeW_{12}O_{40}\}^{4-}$). These two vacant sites are occupied by metal cations W/Co, which are incorporated into the interior cavities of the dilacunary structure, resulting in a stabilised configuration with octahedral coordination environments.

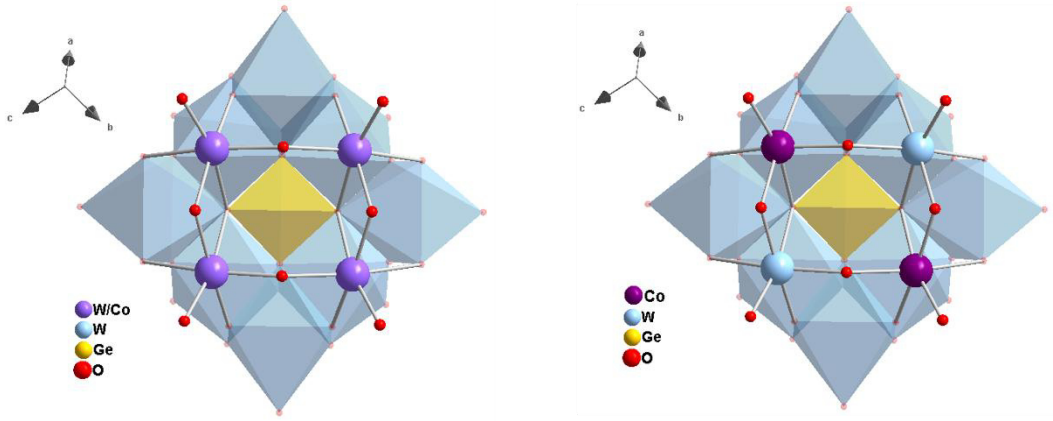


Figure 3.9 In the **Co_{12}-GeW_{10}** structure, the POM building blocks exhibit four metal-binding positions within each Keggin unit that were occupied with a 50:50 disorder between Co and W atoms (left). The electron density corresponding to cobalt is distributed over two alternative positions within the Keggin building blocks, indicating positional disorder consistent with the observed crystallographic data (right).

Crystallographic analysis reveals that the four potential metal-binding positions within each POM unit exhibit partial occupancy disorder. Specifically, these sites are shared between Co^{2+} and W^{6+} ions in an approximate 1:1 ratio, leading to a statistical occupancy of 50% for each metal. Importantly, this Co/W disorder is consistently observed across all such Keggin-based building units within the structure.

Each $\{GeW_{10}Co_2O_{38}\}^{8-}$ unit shares four oxido oxygen atoms to connect with each adjacent di-cobalt substituted Keggin unit. The Co and W cations on opposite corners of the Keggin square form Co-O-W or W-O-Co bonds to connect with the adjacent Keggin unit (Figure **3.10**).

It is essential to note that the reaction began with a trilacunary ligand precursor, $\{GeW_9O_{34}\}^{10-}$, which underwent a transformation during the synthesis. Under the reaction conditions, an additional tungsten atom was incorporated into the structure, resulting in the formation of the dilacunary species $\{GeW_{10}O_{34}\}^{8-}$. Although the exact mechanism of this conversion remains unclear, such behaviour corresponds to the well-documented flexibility of POM clusters, which are known to undergo rearrangements, fragmentation, or reassembly in solution. Conditions such as alkaline pH and the presence of metal cations may have facilitated this transformation. This structural evolution highlights the dynamic

nature of the ligand framework and its sensitivity to the surrounding chemical environment during crystallisation.[161–163]

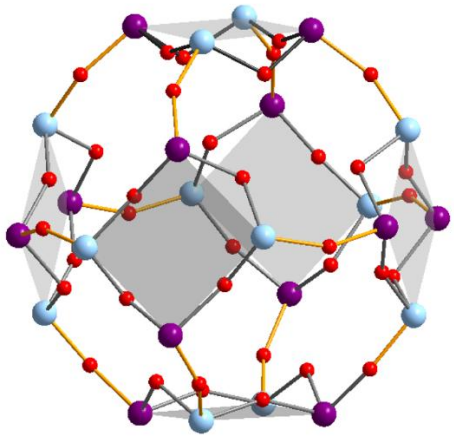


Figure 3.10 The ball-and-stick representation illustrates the central core of the **Co_{12}-GeW_{10}** cluster, which contains Co_{12} without Keggin units and cesium ions. This structure consists of six W_2Co_2 squares (highlighted in grey), each containing two cobalt ions at opposite corners, and two tungsten (W) ions. The Co-O-W bonds, which connect each of the square units, are indicated with yellow bonds.

The eight Cs^+ ions act as linkers between the $\{GeW_{10}Co_2O_{34}\}^{8-}$ units (Figure **3.8**). Each Cs^+ ion is coordinated to the polyoxometalate framework through Cs-O=W and/or Cs-O-Co interactions. All Co^{2+} centres exhibit distorted octahedral geometry, with Co-O bond lengths ranging from 2.00(3) to 2.38(3) Å, and O-Co-O bond angles varying between 73.02(1)° and 168.44(1)°.

In **Ni_{12}-GeW_{10}**, the Ni-O bond lengths range from 1.7607(0) to 2.1718(0) Å, and the O-Ni-O bond angles range from 119.856(1)° to 143.350(1)°.The total charge of the **Co_{12}-GeW_{10}** compound was balanced by 36 sodium, two cesium and one cobalt countercations, whereas for **Ni_{12}-GeW_{10}**, 37 sodium and three cesium countercations were responsible for the charge balance. Elemental analysis was used to confirm the complete composition of both compounds, including the countercations and crystal water content.

Attenuated Total Reflectance-Fourier Transform Infrared Spectroscopy (ATR-FTIR)

ATR-FTIR spectra of the **Co_{12}-GeW_{10}** and **Ni_{12}-GeW_{10}** and precursor POM ligands $Na_{10}[GeW_9O_{34}]$ are shown in Figure **3.11**. ATR-FTIR spectra were recorded in the fingerprint region (1200–400 cm^{-1}), which is characteristic of POM frameworks. Prominent absorption bands observed at 930–935 cm^{-1} and 870–875 cm^{-1} are attributed to the asymmetric stretching vibrations of terminal W=O bonds ($\nu_{as}(W{=}O_t)$) and bridging W–O–W bonds involving corner/vertex-sharing octahedra ($\nu_{as}(W{-}O_v{-}W)$), respectively. Additional bands

appearing at 775 cm^{-1} and 687 cm^{-1} are assigned to W–O–W vibrations associated with edge-sharing octahedra (ν(W–O_e–W)). The observed shifts in vibrational bands for **Co_{12}-GeW_{10}** and **Ni_{12}-GeW_{10}** compared to the free ligand spectra reflect the coordination of the transition metal ions, confirming the successful formation of the transition metal-substituted POM structures.

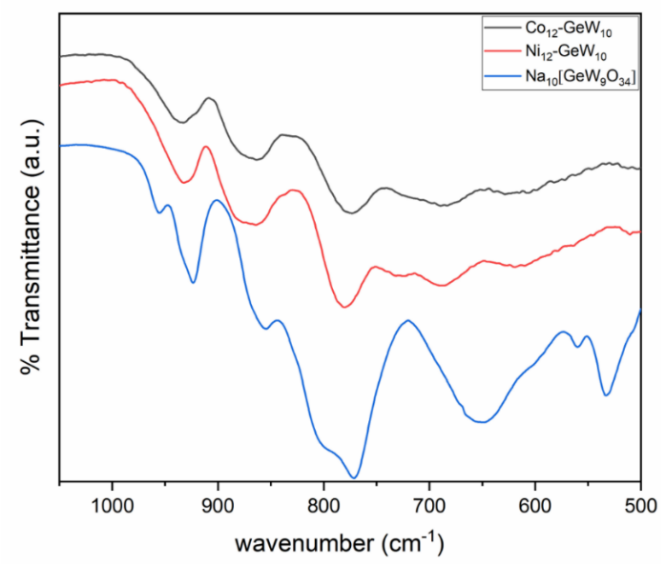


Figure 3.11 ATR-FTIR spectra of $Na_{10}[GeW_9O_{34}]$, **Co_{12}-GeW_{10}** and **Ni_{12}-GeW_{10}**.

Powder X-ray Diffraction (PXRD)

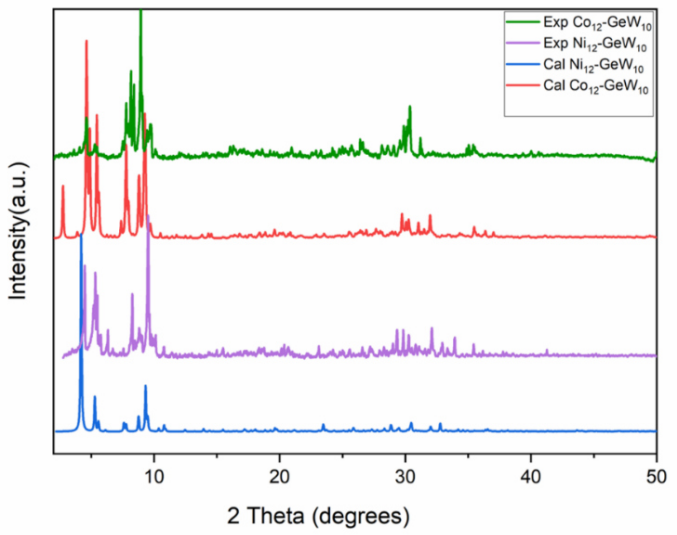


Figure 3.12 Experimental PXRD patterns of **Co_{12}-GeW_{10}** and **Ni_{12}-GeW_{10}**, compared with the simulated patterns calculated from their respective single-crystal X-ray diffraction structures.

PXRD was used to assess the phase purity of **Co_{12}-GeW_{10}** and **Ni_{12}-GeW_{10}**. The observed PXRD patterns closely match the simulated patterns generated from single-crystal X-ray

diffraction (SCXRD) data collected at 180 K, indicating good phase purity. Some minor differences in peak intensity and 2θ values suggest slight changes in crystallinity, likely due to the loss of lattice water during the room temperature PXRD measurements. These findings confirm the successful synthesis of phase-pure products (Figure **3.12**).

Electron Spray Ionisation Mass Spectrometry (ESI-MS)

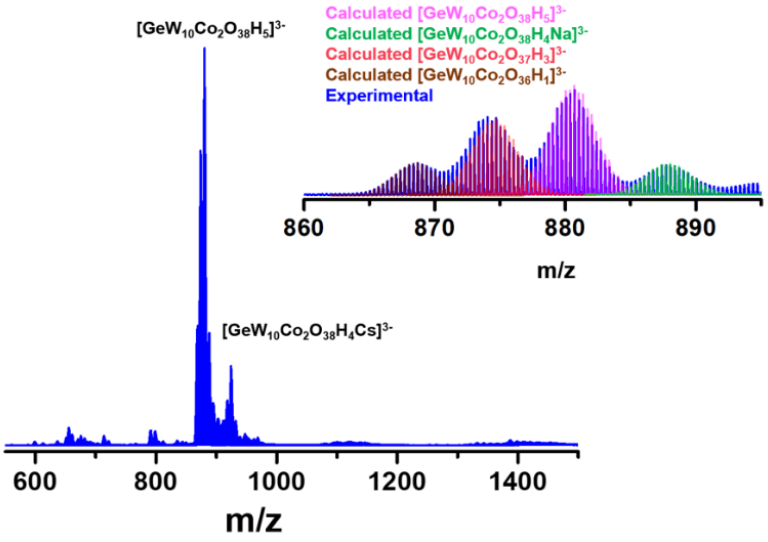


Figure 3.13 ESI MS of **Co_{12}-GeW_{10}** showing two sets of peaks at mass ranges for m/z 860-870 and 930-940 corresponding to 3^- charge state. The strongest peak at m/z 860-870 is expanded in the inset.

Electrospray ionisation mass spectrometry (ESI-MS) was used to investigate the solution-phase behaviour of **Co_{12}-GeW_{10}**. A small amount of its crystalline form was dissolved in a 1:1 (v/v) mixture of water and acetonitrile and analysed in negative ion mode.

During the ionisation process, the intact molecular ion of **Co_{12}-GeW_{10}** was not observed. Instead, signals corresponding to fragmented building block units were detected, indicating partial dissociation of the cluster under ESI conditions. A dominant signal was observed at m/z 870, assigned to the trianionic species $[GeW_{10}Co_2O_{38}H_5]^{3-}$, and a peak at m/z 930 was attributed to $[GeW_{10}Co_2O_{38}H_4Cs]^{3-}$ (Figure **3.13**). These fragments reflect the presence of a stable di-cobalt-substituted dilacunary Keggin-type unit, which likely originates from the decomposition of the **Co_{12}-GeW_{10}.** These results suggest that under ESI-MS conditions, **Co_{12}-GeW_{10}** does not remain intact, but instead breaks down into stable subunits.

A comparable fragmentation pattern was observed when **Ni_{12}-GeW_{10}** was analysed under identical ESI-MS conditions (Figure **3.14**). Similar to **Co_{12}-GeW_{10}**, the mass spectrum

displayed strong signals corresponding to the di-nickel-substituted di-lacunary Keggin-type units. The most intense peaks appeared at m/z 870 and m/z 930, which were assigned to $[GeW_{10}Co_2O_{38}H_5]^{3-}$ and $[GeW_{10}Ni_2O_{38}H_4Cs]^{3-}$, respectively.

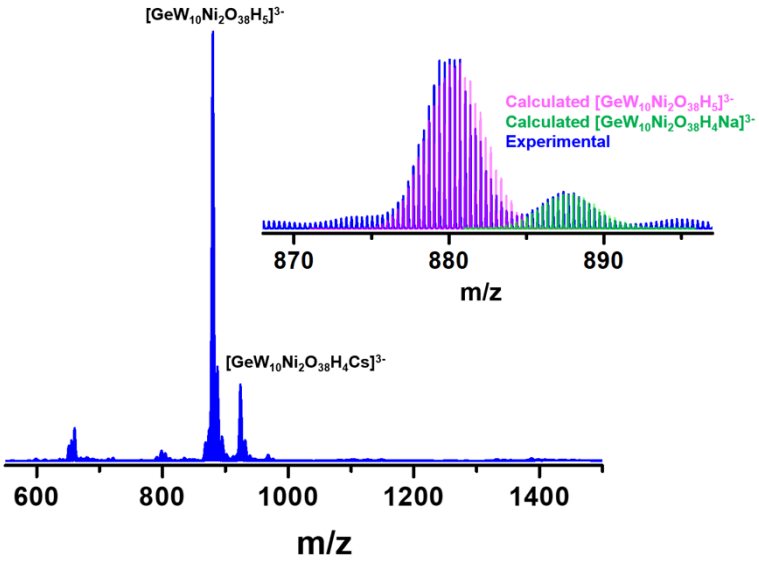


Figure 3.14 ESI MS of **Ni_{12}-GeW_{10}** showing two sets of peaks at mass ranges for m/z 880-900 and 940-960 corresponding to 3^- charge state. The strongest peak at m/z 880-900 is expanded in the inset.

These results collectively suggest that although the whole parent clusters are not preserved during ionisation, their core building blocks remain intact and detectable, highlighting the robustness of the metal-substituted lacunary POM structures.

3.2.2. Fe_{12}-PW_{10}

Synthetic procedure

The 12 Fe^{3+} containing $K_{12}(OH_2)_{24}[\{W_{10}Fe_2PO_{37}\}_4\{Fe_4(PO_4)_4\}]\cdot 30H_2O$ (**Fe_{12}-PW_{10}**) was synthesised in a one-pot reaction of trilacunary polyanion $Na_{10}[PW_9O_{34}]\cdot 18H_2O$ precursor with $FeCl_3\cdot 6H_2O$ in KCl solution. After two weeks, dark yellow coloured **Fe_{12}-PW_{10}** crystals were observed on the walls of the reaction vessels. During this time, the solution transitioned to a turbid yellow hue. The turbid solution was subsequently separated through centrifugation, resulting in a clear supernatant. The **Fe_{12}-PW_{10}** crystals obtained were then washed multiple times to remove any residual yellow precipitate using a clear supernatant solution. Finally, the purified crystals were allowed to air dry.

Crystal structure

Fe_{12}-PW_{10} was crystallised as a hydrated potassium salt in the cubic space group I-43 m (217), as confirmed by single-crystal X-ray diffraction (Figure **3.15**). Single-crystal X-ray diffraction analysis reveals that the polyanion adopts a highly symmetric, self-assembled

structure composed of four $\{Fe_2PW_{10}O_{37}\}$ units surrounding a central $\{Fe_4(PO_4)_4\}$ tetrahedral core (Figure **3.16**). Structurally, the central core of **Fe_{12}-PW_{10}** consists of a cubane-type $\{Fe_4O_4\}$ cluster in which the four Fe^{3+} ions are connected via four μ_3-oxo atoms and further stabilised by four tetrahedral phosphate (PO_4^{3-}) linkers. The $\{Fe_4(PO_4)_4\}$ unit acts as a rigid, tetrahedral scaffold within the structure (Figure **3.17**). However, the central Fe_4O_4 cubane core exhibits occupancy disorder involving the Fe^{3+} ions, which has prevented complete structural refinement. This disorder suggests that further crystallographic analysis is required to more accurately represent the distribution of Fe^{3+} ions within the core. Each $\{Fe_2PW_{10}O_{37}\}$ unit is based on a dilacunary Keggin-type $[PW_{10}O_{36}]^{7-}$ ligand, functionalised with two Fe^{3+} ions that coordinate to the vacant lacunary sites. Each vertex of the tetrahedral $\{Fe_4(PO_4)_4\}$ core is capped by $[\{Fe_2PW_{10}O_{37}\}]$ fragment, resulting in a tetrahedral supramolecular architecture with idealised Td symmetry. The bridging between the central cubane core and the POM units is mediated through coordination of the PO_4 oxygen atoms to Fe centres, with each phosphate ligand connecting to three of the $\{Fe_2PW_{10}O_{37}\}$ fragments via Fe–O–P bridges.

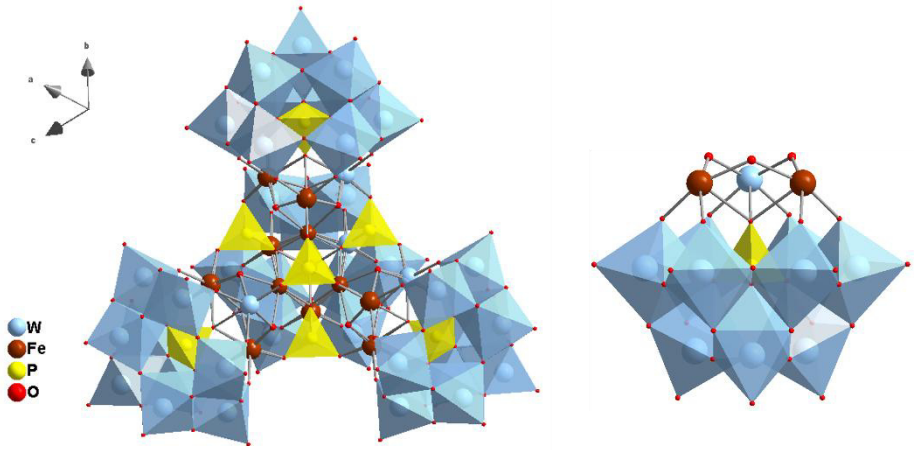


Figure 3.15 Combined polyhedral and ball-and-stick representation of **Fe_{12}-PW_{10}**. (left). The Keggin unit $\{Fe_2PW_{10}O_{37}\}$ (right).

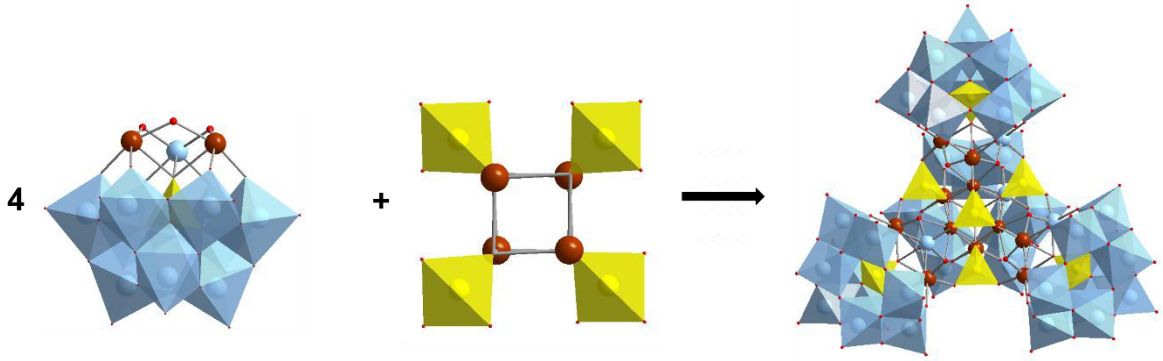


Figure 3.16 Polyhedral and ball-and-stick representation of various building blocks of the **Fe_{12}-PW_{10}**. Colour code: WO_6 (light blue), PO_4 (yellow), Fe (brown).

During the formation of **Fe_{12}-PW_{10},** the trilacunary POM precursor undergoes an in-situ transformation into a dilacunary derivative, which facilitates the assembly of the final Fe-substituted Keggin-type framework. This transformation underscores the high reactivity and structural adaptability of the trilacunary species under the applied synthetic conditions.

In the resulting structure, a mixed occupancy (W/Fe disorder) was observed in all four $\{Fe_2PW_{10}O_{37}\}$ units at specific metal sites, where Fe^{3+} ions are statistically distributed with tungsten atoms. This indicates a dynamic metal exchange process occurring during self-assembly or crystallisation. Such disorder is frequently encountered in metal-substituted dilacunary POMs, reflecting the flexibility of these frameworks in accommodating heterometals at vacant sites.

Their overall self-assembled structure **Fe_{12}-PW_{10}** highlights the ability of transition-metal-functionalised POM building blocks to organise into complex, multi-metallic architectures through controlled coordination chemistry and templating effects.

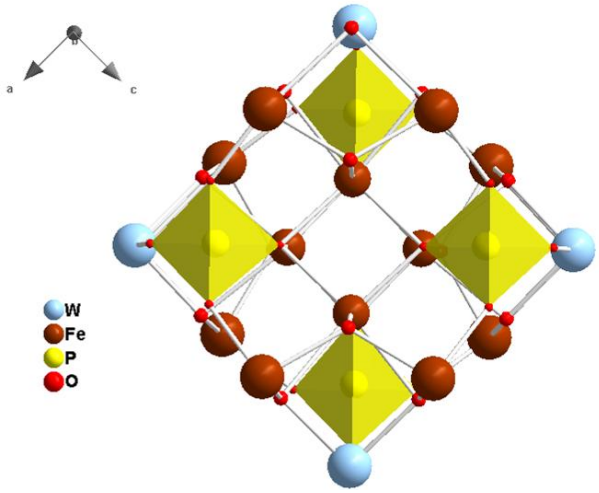


Figure 3.17 Ball and stick representation of the metal central core $[\{WFe_2\}_4\{Fe_4(PO_4)_4\}]$.

Attenuated Total Reflectance Fourier Transform Infrared Spectroscopy (ATR-FTIR)

ATR-FTIR spectra of **Fe_{12}-PW_{10}** and its precursor POM ligand $Na_9[PW_9O_{34}]$ are shown in Figure **3.18**. The spectra were recorded in the fingerprint region (1200–400 cm^{-1}), which contains characteristic vibrational modes of the POM framework.

Both spectra display a prominent band at approximately 1180 cm^{-1}, which is assigned to the asymmetric stretching vibration of phosphate groups ($\nu_{as}PO_4^{3-}$). In the spectrum of $Na_9[PW_9O_{34}]$, prominent bands are observed in the range of 930–935 cm^{-1} and 870–875 cm^{-1}, which correspond to the asymmetric stretching vibration of the terminal tungsten-oxo

bonds ($\nu_{as}W{=}O_t$) and the asymmetric stretching of corner/vertex-sharing (bridging) tungsten–oxygen–tungsten bonds (ν_{as} W–O_V–W), respectively. Additional bands appear at 775 cm^{-1} and 687 cm^{-1}, which are assigned to the stretching vibrations of edge-sharing tungsten–oxygen–tungsten bonds (νW–O_e–W) within the Keggin-type framework.

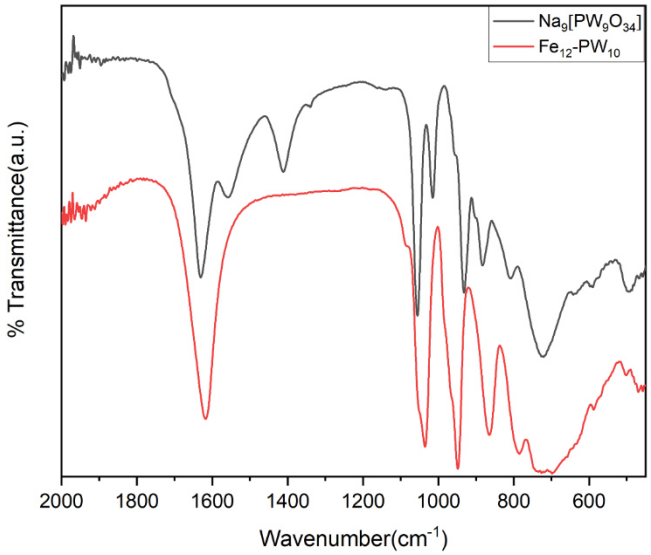


Figure 3.18 ATR-FTIR spectrum of **Fe_{12}-PW_{10}** and $Na_{10}[PW_9O_{34}]$ POM precursor.

Upon formation of **Fe_{12}-PW_{10}**, noticeable shifts in these vibrational bands are observed, particularly in the regions associated with $W{=}O_t$ and W–O–W stretches. These shifts reflect changes in the local bonding environment resulting from the incorporation of Fe^{3+} ions into the vacant sites of the trilacunary POM. These spectral changes provide strong evidence for the successful coordination of Fe^{3+} ions, confirming the transformation of the trilacunary precursor into the Fe-substituted Keggin-type cluster **Fe_{12}-PW_{10}**.

3.2.3. Fe_4-GeW_{10}

Synthetic procedure

The reaction of $FeCl_3{\cdot}6H_2O$ with $Na_{10}[GeW_9O_{34}]{\cdot}18H_2O$ in an aqueous 0.5 M KCl solution led to the formation of a clear, dark yellow-brown solution. This solution was left undisturbed to allow slow crystallisation. After one week, yellow crystals of the iron-containing polyoxometalate $K_{14}[Fe^{3+}{}_4(\mu O)_2(\mu\text{-}OH)_2\{W_{10}GeO_{37}\}_2]{\cdot}34H_2O$ (**Fe_4-GeW_{10}**) were obtained. The crystals were collected by filtration and air-dried at room temperature.

Crystal structure

Single-crystal X-ray diffraction analysis reveals that **Fe_4-GeW_{10}** crystallises as a hydrated potassium salt in the monoclinic crystal system, space group P121/c1(14) (Figure **3.19**). The polyanion features a $\{Fe_4(\mu\text{-}O)_2(\mu\text{-}OH)_2\}$ bridging core linking two equivalent

$\{W_{10}GeO_{37}\}$ lacunary Keggin-type fragments, forming a dimeric assembly stabilised by oxo and hydroxo bridges. Four Fe^{3+} ions are symmetrically sandwiched between the two di-lacunary Keggin units. Each $\{GeW_{10}O_{36}\}$ unit contains two Fe^{3+} ions bridged by a μ_2-oxygen atom, creating a Fe–O–Fe linkage that constitutes the fundamental building block Fe_2O-$GeW_{10}O_{36}$. Two such units were interconnected by additional bridging oxygen atoms. The Fe^{3+} centres adopt distorted octahedral coordination, bonded to four oxide ligands from the Keggin units and two bridging oxygen atoms. Bond valence sum calculations confirm Fe oxidation states near +3 (3.13 and 3.10 for Fe(11) and Fe(12)). The bridging oxygens are assigned as hydroxide (O(28), OH^-) and oxide (O(29), O^{2-}) ligands (Figure **3.20**).

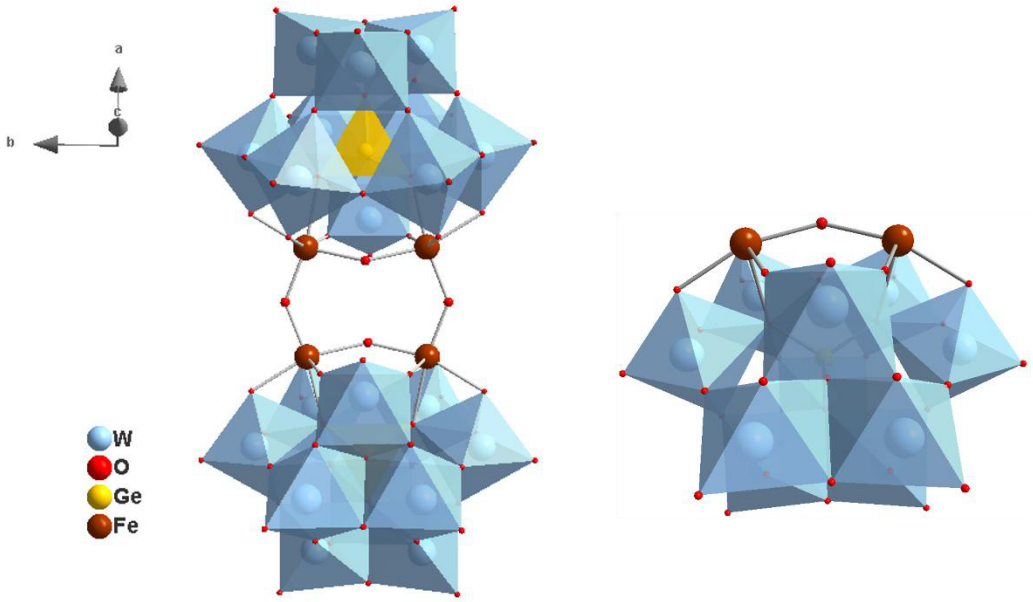


Figure 3.19 Combined polyhedral and ball-and-stick representation of **Fe_4-GeW_{10}** (left), **Fe_2-GeW_{10}** unit (right).

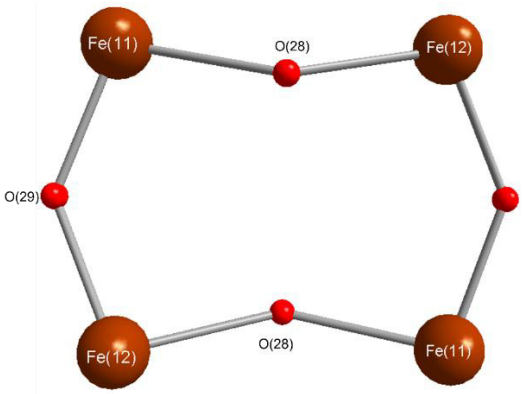


Figure 3.20 Ball and stick representation of $Fe^{3+}{}_4$ core with bridging oxygens.

This compound's crystal structure and fundamental characterisation have been reported previously in the literature.[164] Therefore, a detailed discussion of its crystallographic and structural properties will not be included here. Instead, Section **5.4.4** will focus on insights

derived from electrocatalytic studies related to this material. Elemental analysis further confirmed the chemical composition and counterions, consistent with the proposed formula.

Attenuated Total Reflectance Fourier Transform Infrared Spectroscopy (ATR-FTIR)

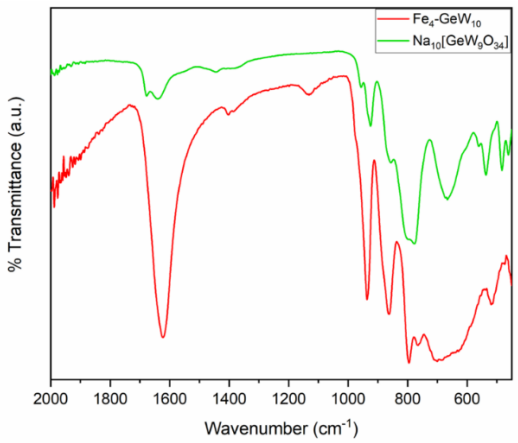


Figure 3.21 ATR-FTIR spectrum of **Fe_4-GeW_{10}** and $Na_{10}[GeW_9O_{34}]$ POM precursor.

ATR-FTIR spectra of **Fe_4-GeW_{10}** and its precursor POM ligand $Na_{10}[GeW_9O_{34}]$ are shown in Figure **3.21**. The measurements were conducted in the fingerprint region (1200–400 cm^{-1}), which contains the characteristic vibrational modes of POMs.

In the spectrum of the precursor, strong bands observed at 930–935 cm^{-1} and 870–875 cm^{-1} are attributed to the asymmetric stretching vibrations of terminal W=O_t bonds (ν_{as} W=O_t) and corner/vertex-sharing W–O_v–W bridges (ν_{as} W–O_v–W), respectively. Additional bands at 775 cm^{-1} and 687 cm^{-1} are assigned to edge-sharing W–O_e–W vibrations, which are typical of the Keggin-type structure.

In the case of **Fe_4-GeW_{10},** small shifts in the position of these bands are observed relative to the precursor, indicating modifications in the local bonding environment due to the incorporation of Fe^{3+} ions into the lacunary sites of the Keggin fragment. These spectral changes support the formation of the Fe-substituted dimeric cluster and reflect the structural reorganisation around the tungsten–oxygen framework upon Fe coordination.

Electron Spray Ionisation Mass Spectrometry (ESI-MS)

The ESI-MS spectrum of the compound $K_{14}[Fe^{3+}_4(\mu\text{-}O)_2(\mu\text{-}OH)_2\{W_{10}GeO_{37}\}_2]\cdot 34H_2O$ shows a series of peaks corresponding to different charge states and adducts of the intact or partially fragmented POM cluster (Figure **3.22**). In the low m/z range (~900), a signal is assigned to a monomeric fragment $[Fe_2Ge_1W_{10}O_{38}]^{3-}$, likely representing half of the sandwich-type dimer. The main cluster appears around m/z 1070-1105 as

$K_mH_n[Fe_4(O)_2(OH)_2\{W_{10}GeO_{37}\}_2]^{5-}$ and around m/z 1340-1390 in its 4^- charge state, with multiple peaks reflecting various combinations of potassium and proton adducts (e.g., K_3H_7, K_4H_6, etc.). At higher m/z (1830-1880), the intact molecular ion $[Fe_4Ge_3W_{20}O_{78}]^{3-}$ is detected, confirming the preservation of the complete sandwich-type architecture in the gas phase. These observations validate the composition and stability of the Fe_4-based POM cluster and demonstrate typical multi-charged ion behaviour and adduct formation common in large anionic metal-oxide frameworks under ESI-MS conditions.

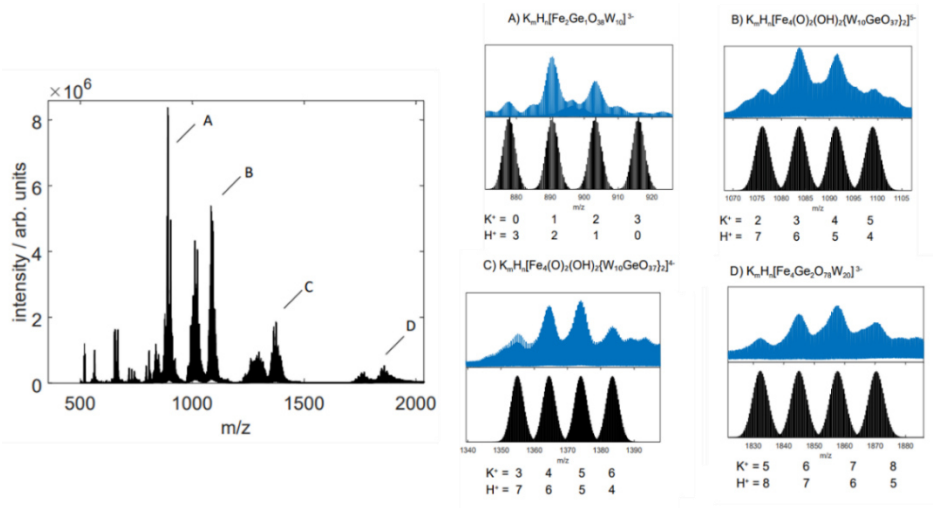


Figure 3.22 ESI MS of **Fe_4-GeW_{10}** showing four sets of peaks at mass ranges of 880-920 and 1830-1880 m/z correspond to 3^- charge state, and 1340-390 and 1070-11105 m/z correspond to 4^- and 5^- charge states.

3.3. Synthesis and Structural Features of 3d-4f Heterometallic Substituted Polyoxometalates (HMPOMs)

In this section, the synthesis, crystal structure analysis, and characterisation of the following isolated 3d-4f heterometallic polyoxotungstate complexes will be discussed.

1. $Na_{21.5}Cs_{1.3}[(W_9GeO_{34})_2(WO_3)_4(PO_4)_6Co_6(Dy_{0.3}/Na_{0.7})(Co_{0.6}/Na_{0.4})]\cdot 75H_2O$
   ($Co_7Dy_{0.3}Na_{0.7}$-GeW_9)
2. $Na_{21.7}Cs_{1.7}[(W_9GeO_{34})_2(WO_3)_4(PO_4)_6Co_6(Gd_{0.1}/Na_{0.9})(Co_{0.5}/Na_{0.5})]\cdot 75H_2O$
   ($Co_7Gd_{0.1}Na_{0.9}$-GeW_9)
3. $Na_{21.65}Cs_{1.5}[(W_9GeO_{34})_2(WO_3)_4(PO_4)_6Co_6(Y_{0.3}/Na_{0.7})(Co_{0.25}/Na_{0.75})]\cdot 75H_2O$
   ($Co_7Y_{0.3}Na_{0.7}$-GeW_9)
4. $Na_{21.6}Cs_{1.7}[(W_9GeO_{34})_2(WO_3)_4(PO_4)_6Co_6(Eu_{0.1}/Na_{0.9})(Co_{0.4}/Na_{0.6})]\cdot 75H_2O$
   ($Co_7Eu_{0.1}Na_{0.9}$-GeW_9)
5. $Na_{21.7}Cs_{1.5}[(W_9GeO_{34})_2(WO_3)_4(PO_4)_6Co_6(Ho_{0.1}/Na_{0.9}Co_{0.6}/Na_{0.4})]\cdot 75H_2O$
   ($Co_7Ho_{0.1}Na_{0.9}$-GeW_9)
6. $Na_{21.6}Cs_{1.5}[(W_9PO_{34})_2Co_6(PO_4)_6(WO_3)_4(Tb_{0.2}/Na_{0.8})(Co_{0.5}/Na_{0.5})]\cdot 75H_2O$
   ($Co_7Tb_{0.2}Na_{0.8}$-GeW_9)

These polyanions were synthesised via simple one-pot reactions in aqueous media. Their solid-state structures were characterised using single-crystal X-ray diffraction, ATR-FTIR spectroscopy, powder X-ray diffraction (PXRD), and elemental analysis. Additionally, ESI-MS studies were performed to evaluate the stability of these clusters in solution.

3.3.1. $Co_7Ln_xNa_{1-x}$-GeW_9

Synthetic procedure

The heterometallic **$Co_7Ln_xNa_{1-x}$-GeW_9** polyanions (Ln = Dy^{3+}, Gd^{3+}, Y^{3+}, Eu^{3+}, Ho^{3+}, Tb^{3+}) were synthesised by reacting $CoCl_2{\cdot}6H_2O$, $Na_{10}[A\text{-}\alpha\text{-}GeW_9O_{34}]{\cdot}18H_2O$, and a lanthanide ($Ln^{3+}$) salt in 1 M sodium phosphate buffer at pH 8.6, with the addition of CsCl to promote crystallisation. This procedure was consistently applied for all analogues in the **$Co_7Ln_xNa_{1-x}$-GeW_9** series. The conditions were initially optimised using the synthesis of **$Co_7Dy_{0.3}Na_{0.7}$-GeW_9.**

During the crystallisation of **$Co_7Dy_{0.3}Na_{0.7}$-GeW_9**, which required about four weeks in phosphate buffer, significant water evaporation occurred. As a result, unwanted colourless sodium phosphate crystals formed alongside the desired purple **$Co_7Dy_{0.3}Na_{0.7}$-GeW_9** crystals. To address this issue, several modifications to the reaction conditions were explored.

One approach involved reducing the buffer concentration from 1 M to 0.5 M. This change led to the formation of a different compound, $Na_{30.5}K_{1.5}[\{Co_4(OH)_3PO_4\}_4(A\text{-}\alpha\text{-}GeW_9O_{34})_4]{\cdot}116H_2O$ (**Co_{16}-GeW_9**), shown in Figure **3.23**. Further reducing the buffer concentration to 0.1 M produced another compound, $Na_{30.5}K_{1.5}[\{Co_4(OH)_3PO_4\}_4(A\text{-}\alpha\text{-}GeW_9O_{34})_4]{\cdot}116H_2O$(**$Co_{16}$-$GeW_9$**), also presented in Figure **3.23**.

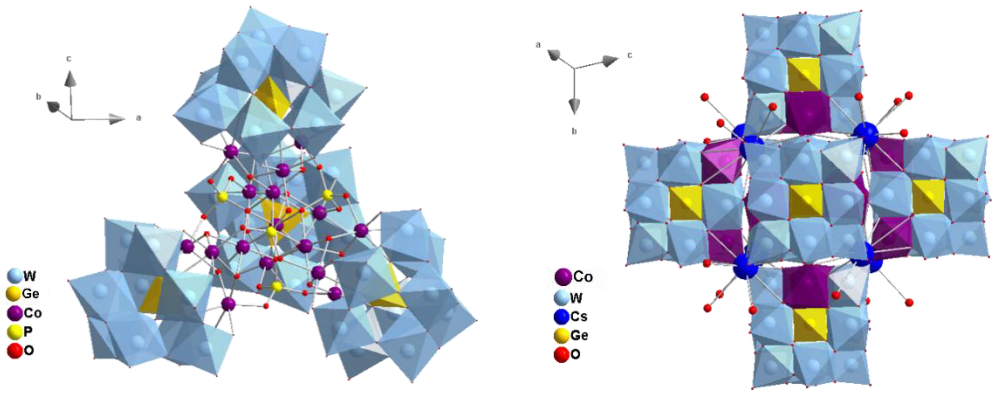


Figure 3.23 Molecular structure of **Co_{16}-GeW_9** (left)[91] and **Co_{12}-GeW_{10}** (right).

Additional experiments were conducted by replacing CsCl with N, N-dimethylacetamide (DMA) or by omitting any added counter cation. Both approaches led to the formation of a distinctive banana-shaped cobalt cluster containing six cobalt atoms, identified as the reported polyoxometalate $[((CoOH_2)Co_2GeW_9O_{34})_2(GeW_6O_{26})]^{20-}$ (**Co_6-GeW_9**), shown in Figure **3.24**.

The trials conducted indicate that the successful formation of the desired **$Co_7Dy_{0.3}Na_{0.7}$-GeW_9** crystals necessitates the use of a 1M sodium phosphate buffer along with the presence of CsCl as counter cations. However, the highly concentrated buffer solution tends to lead to the excessive formation of phosphate crystals, which complicates the isolation of the target purple crystals. As a result, both types of crystals frequently coexist in the reaction vials, making separation challenging. One proposed method for isolating the desired crystals involves washing the mixed crystal sample with cold distilled water; however, this washing process has been observed to adversely impact the yield of the desired **$Co_7Dy_{0.3}Na_{0.7}$-GeW_9**.

All the other POMs obtained during these trials to optimise the reaction conditions were previously reported compounds.[165]

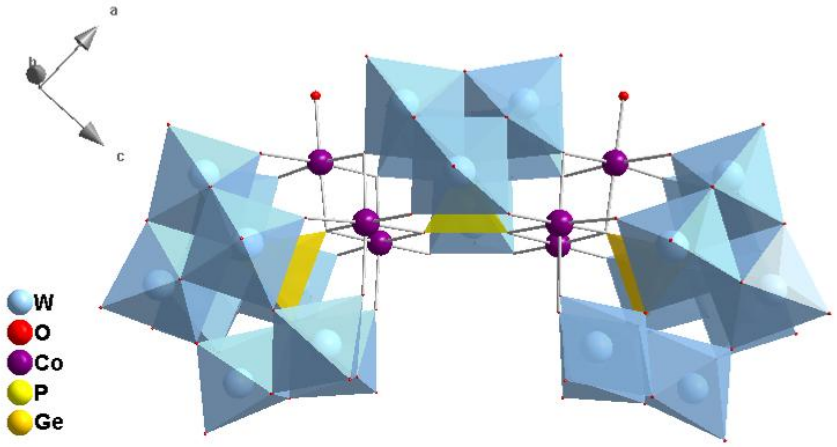


Figure 3.24 The molecular structure of 6 cobalt-containing polyoxometalates **(Co_6-GeW_9)**.[165]

In addition to the single crystal analysis, the ATR-FTIR spectrum provides valuable insights into the molecules generated during the optimisation of reaction conditions. Specifically, it allows for differentiation in the phosphate peak region, highlighting shifts and variations in position. Figure **3.25** illustrates a comparative analysis of the ATR-FTIR spectra of all potential products formed throughout the reactions.

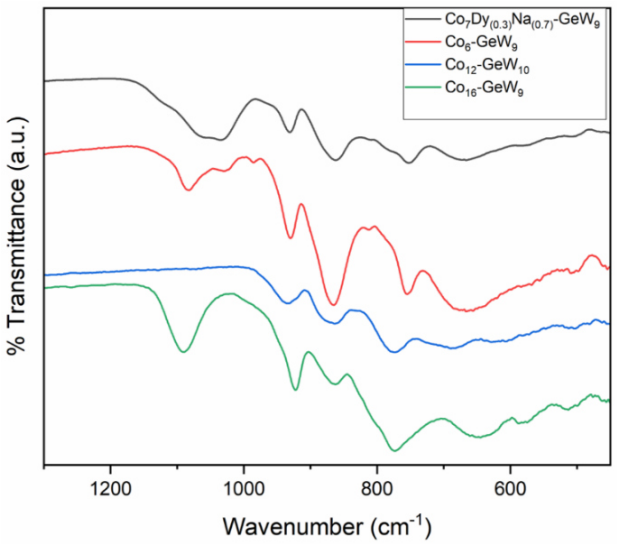


Figure 3.25 Comparison of the ATR-FTIR spectra of the expected products obtained during optimisation of the reaction conditions.

Crystal structure

Compound $Na_{21.5}Cs_{1.3}[(W_9GeO_{34})_2(WO_3)_4(PO_4)_6Co_6(Dy_{0.3}/Na_{0.7})(Co_{0.6}/Na_{0.4})]\cdot 75H_2O$ **($Co_7Dy_{0.3}Na_{0.7}$-GeW_9)** crystallises in the monoclinic system with the C12/c1 space group. X-ray crystal analysis of all six 3d-4f heterometallic **$Co_7Ln_xNa_{1-x}$-GeW_9** polyanions (Ln = Dy, Gd, Y, Eu, Ho, Tb) reveals that they are isostructural. The structural description was therefore applicable to all compounds containing different lanthanide ions. Consequently, **$Co_7Dy_{0.3}Na_{0.7}$-GeW_9** was selected as a representative example for detailed discussion.

A single unit of the **$Co_7Dy_{0.3}Na_{0.7}$-GeW_9** polyanion is shown in Figure **3.26**. Due to Na/Ln disorder at the central site, the position is occupied by varying proportions of sodium and lanthanide metals The central metal site in this structure comprises a mixture of sodium and dysprosium, with a Dy:Na occupancy ratio of 30:70. The corresponding occupancy ratios for the other analogues are 10:90 (Gd), 30:70 (Y), 10:90 (Eu), 10:90 (Ho), and 20:80 (Tb). The mixed Dy/Na site is coordinated by eight oxygen atoms derived from phosphate groups. In this environment, the Na–O bond lengths average approximately 2.35 Å, while the Dy–O bonds are slightly longer, around 2.45 Å.

The central $Dy/Na(PO_4)_6$ unit is further linked to six cobalt ions. These cobalt centres are contributed by two trilacunary Keggin POM building blocks, as well as by two additional cobalt cations connected through four tungsten atoms. Notably, one of these additional cobalt cations, designated Co(4), acts as a bridging site between two polyanion units. This bridging cobalt is shared between two clusters, so there is effectively only one Co(4) per **$Co_7Dy_{0.3}Na_{0.7}$-GeW_9** unit (Figure **3.27** and Figure **3.28**).

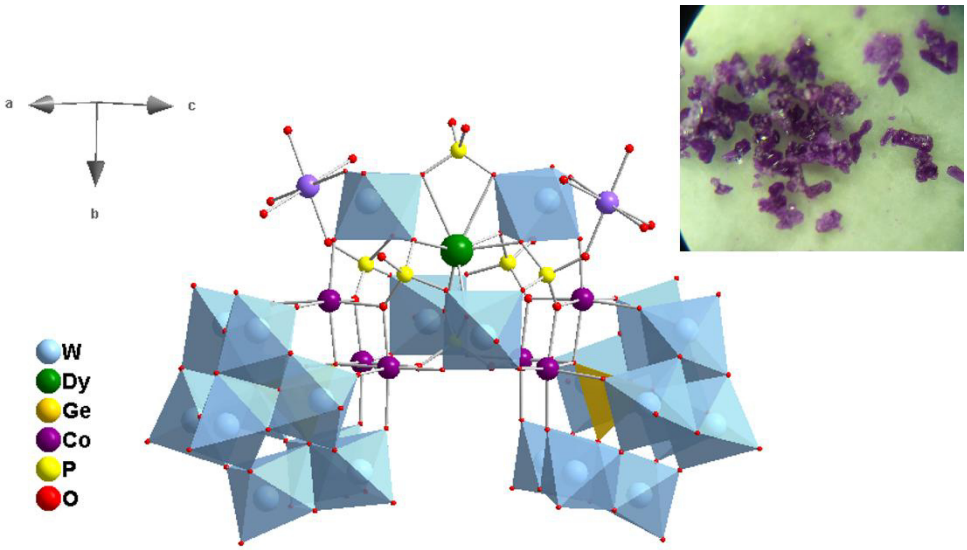


Figure 3.26 Molecular structure of **$Co_7Dy_{0.3}Na_{0.7}$-GeW_9**, two cobalt atoms shown in the lavender colour linking this single unit with the other unit to form an ID chain structure. The microscopic view of the purple coloured **$Co_7Dy_{0.3}Na_{0.7}$-GeW_9** crystals (upper right).

Overall, the single unit consists of two tricobalt-substituted trilacunary $\{Co_3GeW_9O_{34}\}$ Keggin units, and a central fragment containing one disordered Dy/Na site, six phosphate ions, four tungsten oxide units, and two Co/Na disordered linker cations bridging the structure (Figure **3.27**).

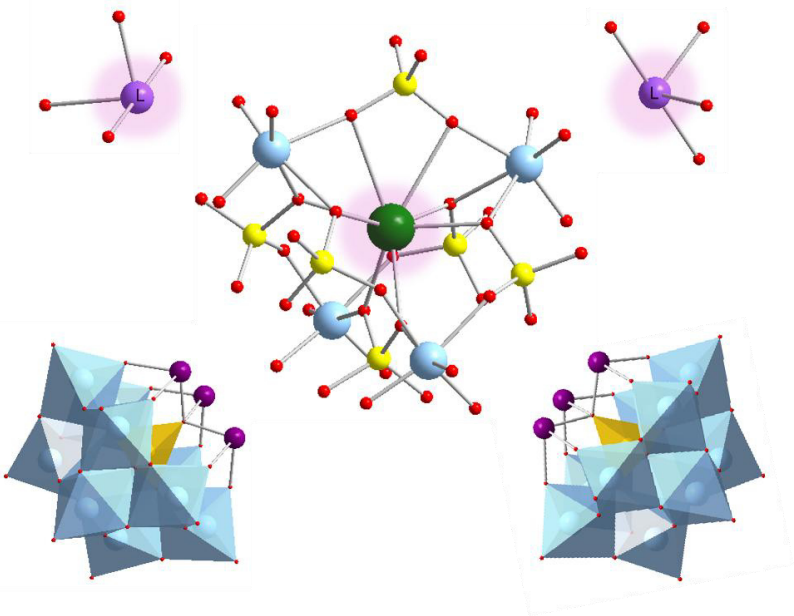


Figure 3.27 Fragmented view of a single unit of the **$Co_7Dy_{0.3}Na_{0.7}$-GeW_9** crystal structure. Disordered positions are highlighted in pink.

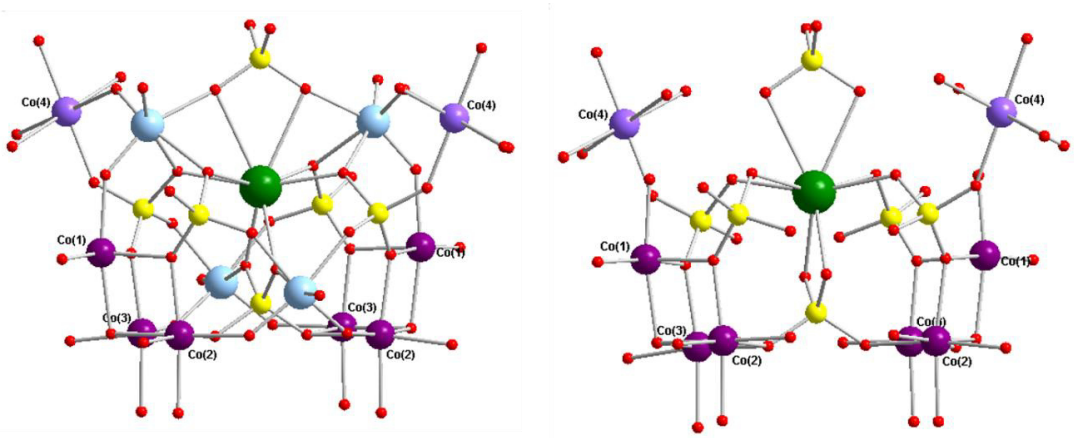


Figure 3.28 The central metal core of **$Co_7Dy_{0.3}Na_{0.7}$-GeW_9** without the trilacunary Keggin ions (left) and the central metal core without four tungsten atoms (right). The cobalt cation at position 4 is in the bridging position, which is shared with the adjacent single units.

The occupancy of the cobalt cation in the bridging position displays disorder, with a 50:50 ratio between cobalt (Co) and sodium (Na). Therefore, each bridging position can be occupied by either a linear O–Co–O configuration or a nonlinear O–Na–O configuration. Figure **3.29** illustrates the occupancy of the octahedral bridging position, which contains two Na^+ ions and one Co^{2+} ion. Due to the larger ionic radii or the distortions in the crystal structure, the Na^+ octahedra are positioned slightly above or below the linear arrangement of the Co^{2+} octahedra. This structural arrangement highlights the complexity and versatility of the coordination environment within the cluster.

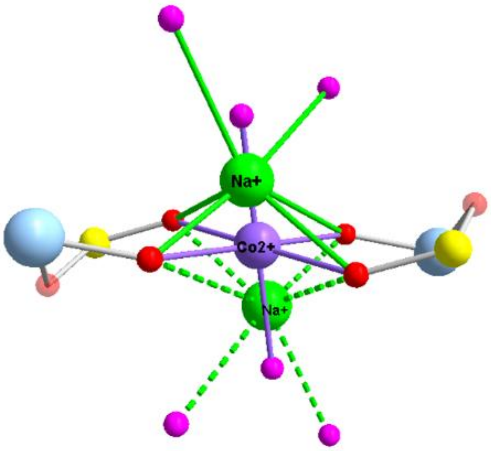


Figure 3.29 The figure illustrates the positional disorder of the linker Co^{2+} with two Na^+ ions. Due to their larger ionic radii, the Na^+ octahedra can be positioned slightly differently compared to the linear octahedron position of Co^{2+}. In either case, the four coordinated oxygen atoms are linked to one tungsten (W) atom and phosphate ions in the central unit, while the other two valencies are satisfied by two coordinated water molecules. Colour code: Bridging Co lavender, Na bright green, H_2O pink, O red, P yellow, W pale blue.

Each 3d-4f single unit, **$Co_7Dy_{0.3}Na_{0.7}$-GeW_9**, is interconnected through bridging cobalt cations, resulting in the formation of a one-dimensional (1D) chain structure, as illustrated

in Figure **3.30**. In this arrangement, the cobalt ions serve as key linker sites that connect the discrete polyoxometalate units, facilitating extended structural propagation along a single dimension.

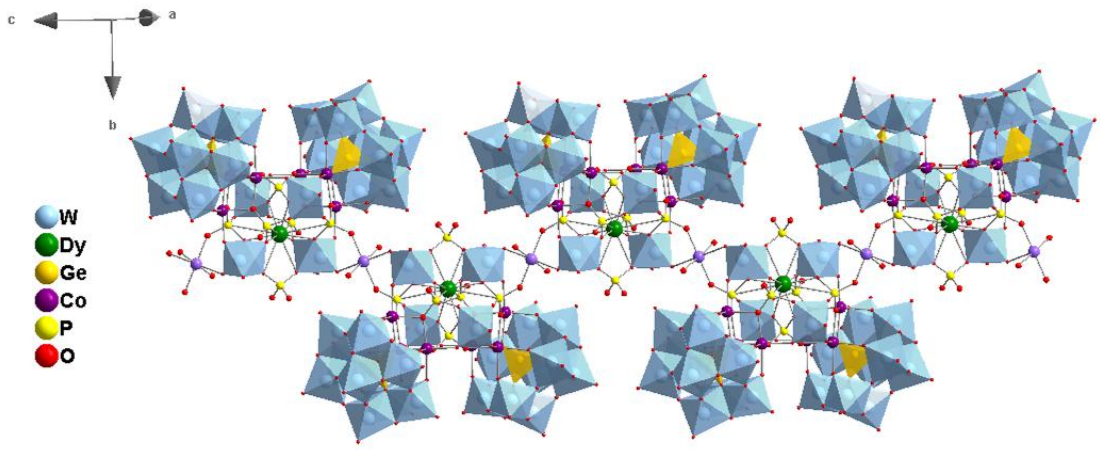


Figure 3.30 The ID chain structure of **$Co_7Dy_{0.3}Na_{0.7}$-GeW_9**. The bridging cobalt is shown as lavender coloured balls.

Attenuated Total Reflectance Fourier Transform Infrared Spectroscopy (ATR-FTIR)

The ATR-FTIR spectrum of **$Co_7Dy_{0.3}Na_{0.7}$-GeW_9,** synthesised using the $Na_9[GeW_9O_{34}]$ polyoxometalate (POM) precursor ligand, is presented in Figure **3.31**. Notable shifts in the IR absorption bands compared to the precursor indicate the successful formation of a 3d-4f metal cluster. In particular, the distinct phosphate-related peak observed around 1300 cm^{-1} confirms the presence of six phosphate groups within the metal cluster, distinguishing it from the precursor spectrum.

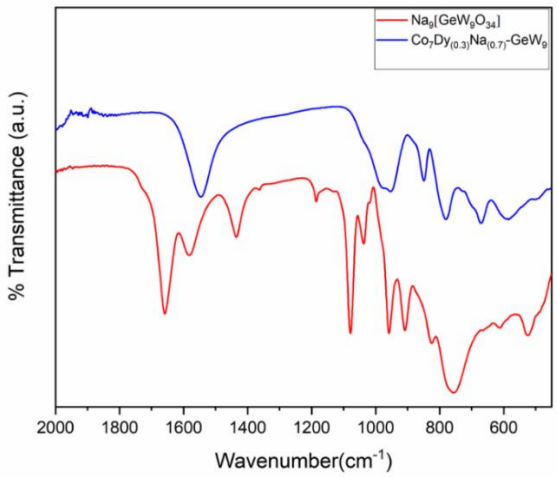


Figure 3.31 ATR-FTIR spectrum of **$Co_7Dy_{0.3}Na_{0.7}$-GeW_9** with $Na_9[GeW_9O_{34}]$ POM precursor ligand.

Figure **3.32** displays the ATR-FTIR spectra of isostructural **$Co_7Ln_xNa_{1-x}$-GeW_9** clusters, where Ln corresponds to various lanthanides, including Dy, Gd, Eu, Ho, Tb, and Y. The consistent peak positions and spectral features across all lanthanide analogues suggest that these metal clusters share a similar structural framework regardless of the specific lanthanide ion incorporated.

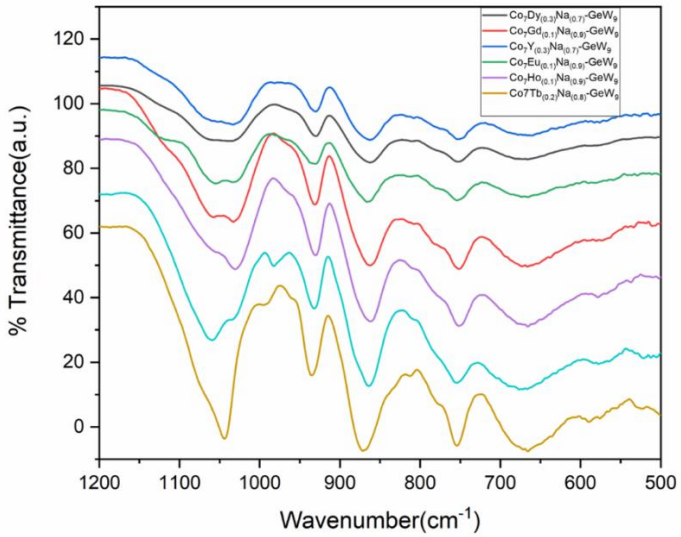


Figure 3.32 ATR-FTIR spectrum of **$Co_7Ln_xNa_{1-x}$-GeW_9** , where Ln = Dy, Gd, Eu, Ho, Tb, and Y with GeW_9O_{34} POM precursor ligand. The similarity of the peak regions indicates the structural similarities of the analogous 3d-4f metal clusters.

Electron Spray Ionisation Mass Spectrometry (ESI-MS)

ESI-MS is useful in determining the intact POM core, as it generally possesses a high inherent negative charge. The few crystals of **$Co_7Dy_{0.3}Na_{0.7}$-GeW_9** were dissolved in water diluted with acetonitrile at a 50:50 volume ratio. ESI-MS was performed to confirm the composition and structural integrity of the polyanionic cluster $Na_{21.5}Cs_{1.3}[(W_9GeO_{34})_2(WO_3)_4(PO_4)_6Co_6(Dy_{0.3}/Na_{0.7})(Co_{0.6}/Na_{0.4})]\cdot 75H_2O$. The spectrum shows a dominant distribution of peaks in the range of *m/z* 1000-1100, corresponding to the multiply charged species **$[Na_{17-x}Cs_xM\cdot nH_2O]^{5-}$**, where M represents the polyanion. The expanded region of the spectrum (inset) displays decent agreement between experimental and simulated isotopic patterns for species with varying sodium and cesium content (x = 0-3), confirming the presence of a statistical mixture of alkali metal-substituted clusters in solution under ESI conditions. These results collectively support the proposed molecular formula and confirm the stability of the intact polyanion in solution (Figure **3.33**).

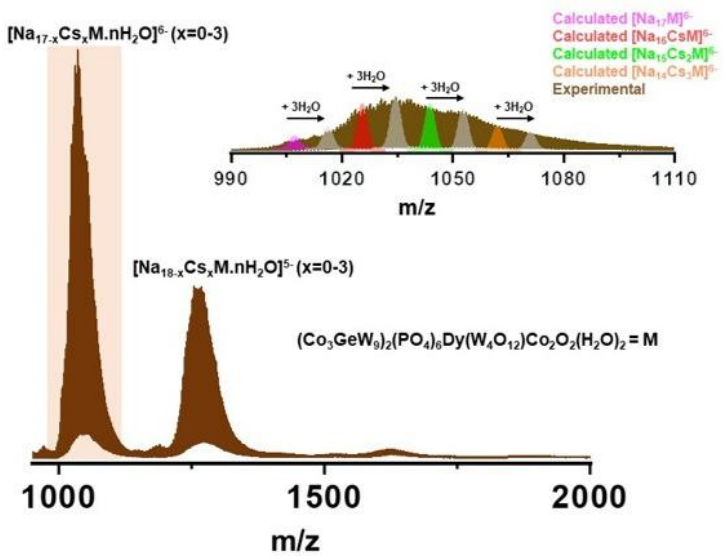


Figure 3.33 ESI MS of **$Co_7Dy_{0.3}Na_{0.7}$-GeW_9** showing two sets of peaks at mass ranges for m/z 1100 and 1350 corresponding to 6^- and 5^- charge states. The strongest peak at m/z 1100 is expanded in the inset. Different sodium-exchanged peaks were observed, and the mass envelope was compared with 4 possible compositions, with their calculated isotope distribution patterns overlaid.

3.4. Conclusion and Summary

In this chapter, three novel high-nuclearity 3d metal-containing POMs were synthesised using a simple one-pot aqueous method. Two analogous clusters containing twelve Co^{2+} and twelve Ni^{2+} ions, namely **Co_{12}-GeW_{10}** and **Ni_{12}-GeW_{10},** were successfully obtained and characterised by ATR-FTIR spectroscopy, powder X-ray diffraction (PXRD), elemental analysis, and electrospray ionisation mass spectrometry (ESI-MS). Single-crystal X-ray diffraction revealed structural details and positional disorder between the 3d metal centres and tungsten atoms within the polyanion framework.

Additionally, POMs containing twelve Fe^{3+} cations, referred to as **Fe_{12}-PW_{10}**, were synthesised and characterised using X-ray crystallography, elemental analysis and ATR-FTIR spectroscopy. The positional disorder of tungsten with Fe^{3+} was also analysed using X-ray crystallographic techniques. The **Fe_4-GeW_{10}** POM was fully characterised after isolation, including structural analysis. However, during the preparation of this thesis, it was identified that the crystal structure had already been reported in earlier literature. Therefore, the characterisation data were briefly presented here to provide a foundation for the electrochemical studies, which are discussed in detail in the electrochemistry chapter. Furthermore, six analogous compounds, **$Co_7Ln_xNa_{1-x}$-GeW_9** (where Ln = Dy^{3+}, Gd^{3+}, Eu^{3+}, Ho^{3+}, Tb^{3+}, and Y^{3+}), were synthesised using a one-pot reaction approach. The materials were characterised by ATR-FTIR spectroscopy, ESI-MS, and elemental analysis. Powder X-ray diffraction (PXRD) patterns did not provide conclusive information due to partial loss of crystallinity in the bulk samples; therefore, PXRD data are not included in this thesis. X-

ray crystallographic analysis revealed positional disorder at both the central lanthanide site and the cobalt linker positions, with partial occupancy by sodium ions in each case.

The findings in this chapter lay a strong foundation for understanding the relationship between structure and function in these complex POM systems. Lacunary POMs are suitable ligands for obtaining such complex structures. These compounds are further investigated in the following chapters with respect to their electrochemical behaviour and potential applications in catalysis.

4. NMR Relaxivities of Paramagnetic Metal Ion Containing POMs (PM-POMs)

4.1. Introduction

Nuclear Magnetic Resonance (NMR) spectroscopy is a technique used to determine the structure of molecules in various fields such as chemistry, biology, and materials science.[166] NMR spectroscopy is based on the interaction of radiofrequency waves with the NMR active nuclei of atoms immersed in an external magnetic field (B_0). The most commonly used NMR active abundant nuclei are ^{1}H, ^{13}C, ^{15}N, ^{19}F, ^{29}Si (all with spin I=1/2).

In B_0, these nuclei behave like tiny magnets and precess around the field direction (z-axis). At equilibrium, the bulk magnetisation M_0 is aligned along the z-axis (longitudinal component M_z), with the transverse component M_{xy} lying in the xy-plane.

An NMR experiment starts with an RF pulse applied to the nuclei as a pulse (τ_p time in μs) at the Larmor frequency ω_0, which depends on the nucleus and the strength of B_0. This pulse produces a secondary magnetic field B_1 perpendicular to B_0, tipping M_0 away from the z-axis by a defined flip angle. A 90° ($\frac{\pi}{2}$) pulse moves M_0 into the xy-plane, while a 180° (π) pulse inverts it along the –z direction (**Figure 4.1**).[167] [168]

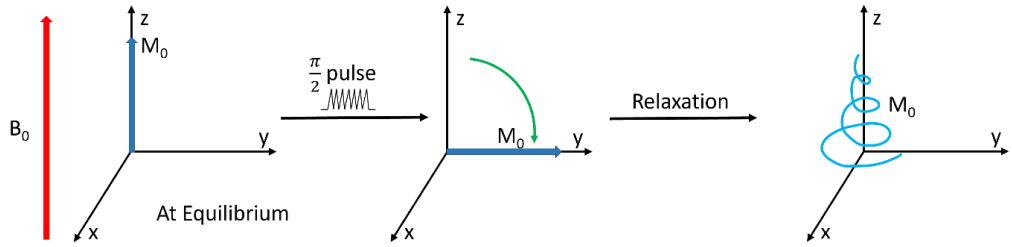


Figure 4.1 Representation of the nuclear spin relaxation process after $\frac{\pi}{2}$ pulse. At equilibrium (left), new equilibrium (middle), relaxation along the z axis (right).

4.2. NMR Relaxation Measurements (T_1 and T_2)

When the pulse ends, B_1 disappears and M_0 returns to equilibrium, a process called relaxation. This occurs through two mechanisms:

- T_1 **(longitudinal/spin–lattice) relaxation** – recovery of M_z via energy exchange with the surrounding lattice.
- T_2 **(transverse/spin–spin) relaxation** – loss of phase coherence of M_{xy}.

During relaxation, the precessing transverse magnetisation induces a voltage in the detection coil, producing the Free Induction Decay (FID) signal, which gradually decays to zero (Figure **4.2**).

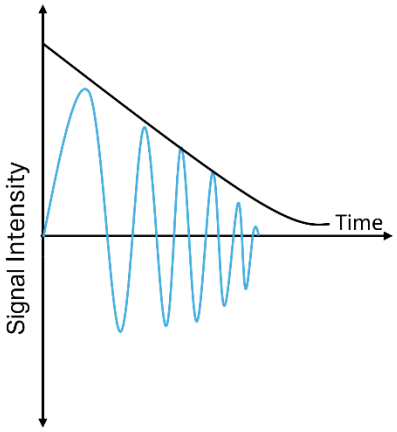


Figure 4.2 Shape of the Free Induction Decay (FID) pulse sequence.

4.2.1. T_1 Relaxation (Longitudinal Relaxation)

T_1 relaxation is the process by which the magnetisation along the z-axis (M_z) comes back to normal after being pushed away by the pulse. This happens because the spinning nuclei exchange energy with their environment (called the lattice). As time passes, M_z slowly recovers until it reaches its original level, as shown in the figure. (Figure **4.3**).

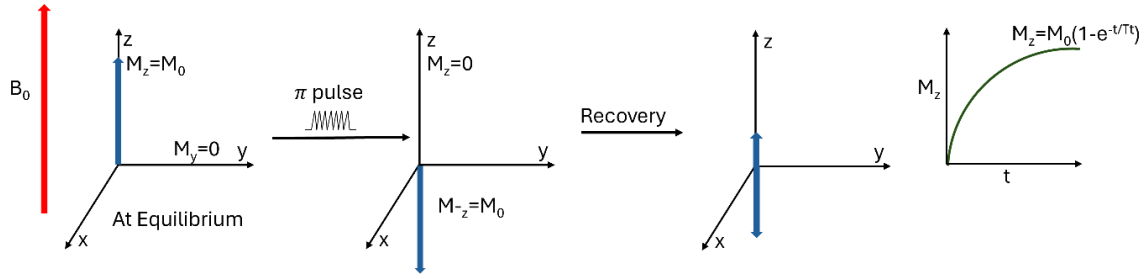


Figure 4.3 Illustration of T_1 relaxation process and its exponential curve.

This process can be described by an exponential equation, i.e.,

$$M_z = M_0(1 - e^{-t/T_1}) \tag{4.1}$$

The T_1 relaxation time constant was calculated by the following equation,

$$M_z(\tau) = M_0 \left(1 - exp\left(\frac{-\tau}{T_1}\right)\right) \tag{4.2}$$

For the current T_1 relaxation studies, two pulse sequences are commonly used:

a. Inversion Recovery (IR) pulse

This sequence includes a π pulse followed by a delay (τ) and then a $\frac{\pi}{2}$ pulse that generates the FID signal ($\pi - \tau - \frac{\pi}{2}$ FID signal). The initial π pulse flips the equilibrium magnetisation completely upside down, inverting it from the +z axis to the -z axis. During the delay τ, the magnetisation gradually recovers towards its original equilibrium along the +z axis. Before full recovery, a $\frac{\pi}{2}$ pulse is applied to rotate the magnetisation into the xy plane, producing the FID signal used to measure how much magnetisation has returned. By varying τ, the recovery curve can be traced and T_1 determined.[169]

b. Progressive Saturation Recovery (PSR) pulse

In this method, many $\frac{\pi}{2}$ pulses (called saturation pulses) are applied one after another to keep the magnetisation from recovering. Because the pulses come quickly, the magnetisation can't return to equilibrium. After this series, a waiting time allows the magnetisation to relax back toward its original state. Then, a final $\frac{\pi}{2}$ pulse is applied to move the magnetisation into the xy plane, producing an FID signal. By measuring how the signal changes with different waiting times, we can determine the T_1 relaxation time.[169]

4.2.2. T_2 Relaxation (Transverse / Spin–Spin Relaxation)

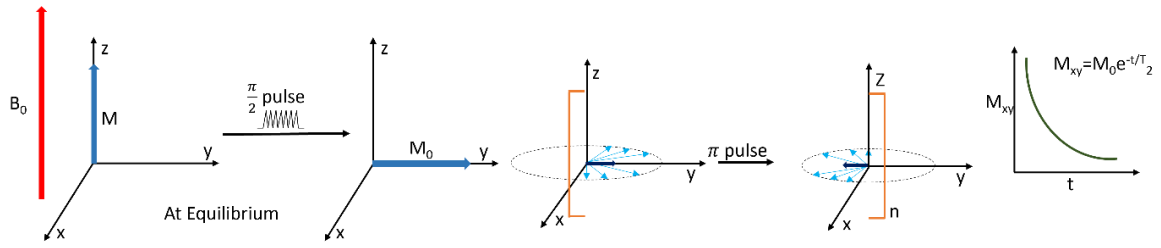


Figure 4.4 Illustration of T_2 relaxation process and its exponential curve.

In an NMR experiment, transverse magnetisation (M_{xy}) gradually decays because the individual spins lose phase coherence with each other. This loss of synchrony/harmony, called *dephasing*, happens due to interactions between spins and small variations in the local magnetic field. As a result, the overall magnetisation in the xy-plane decreases over time (Figure **4.4**). The time constant describing this decay is called T_2 relaxation or transverse relaxation.

T_2 relaxation is described by the exponential equation (4.3),

$$M_{xy} = M_0 e^{-\tau/T_2} \tag{4.3}$$

The T_2 relaxation time constant was calculated by the following equation,

$$M_{xy}(\tau) = M_0 \, exp\left(\frac{-\tau}{T_2}\right) \quad (4.4)$$

a. CPMG pulse sequence

For the current T_2 relaxation measurements, the Carr-Purcell-Meiboom-Gill (CPMG) pulse sequence was used. The application of the CPMG reduces the interference of the inhomogeneous external magnetic field (B_0) during the T_2 relaxation measurements.[170] The CPMG pulse is given as: $\frac{\pi}{2} - (\tau - \pi - \tau)_n$ echo, where τ is the waiting time or delay. The $\frac{\pi}{2}$ excitation pulse flipped the magnetisation to the y axis and followed the delay; during this time, the magnetisation started to dephase. After this dephasing process, the subsequent π pulse refocused the dephased magnetisation and flipped to an 180^0 angle, then during the second waiting time, the spins dephased automatically. The resultant echo signal is detected by an NMR spectrometer.

4.3. Relaxation rates and relaxivity

The longitudinal relaxation rate (R_1) and transverse relaxation rate (R_2) are the inverses of their respective relaxation times (T_1 and T_2), and are expressed in s^{-1}.

$$R_1 = \frac{1}{T_1} \quad \text{and} \quad R_2 = \frac{1}{T_2} \quad (4.5)$$

Longitudinal relaxivity (r_1) and transverse relaxivity (r_2) describe how effectively a substance can enhance the relaxation rates (R_1 and R_2) of water protons per millimole of the agent. Relaxivity values are essential for evaluating the performance of contrast agents in imaging applications, and are reported in millimolar per second unit ($mM^{-1}s^{-1}$).

$$r_1 = \frac{R_1}{C} \quad \text{and} \quad r_2 = \frac{R_2}{C} \quad (4.6)$$

Here, c is the concentration of the contrast agent in mM. Relaxivity depends on factors such as the applied magnetic field strength, the corresponding Larmor frequency, and the properties of paramagnetic molecules. These effects are discussed in the following sections.[171–173]

4.4. Paramagnetic Relaxation Enhancement NMR (PRE NMR)

A paramagnetic ion, which has one or more unpaired electrons, strongly influences the NMR behaviour of a molecule. The electron spins (S) of these ions interact closely with the nearby nuclear spins (I). This interaction affects the NMR spectra in two main ways. First, the magnetic moments of the electrons cause significant changes in chemical shifts, about ±100 ppm for lighter nuclei like ^{1}H, and over ±1000 ppm for heavier nuclei like ^{13}C or ^{15}N. Second, it speeds up both the longitudinal (R_1) and transverse (R_2) relaxation rates.[174] The increase

in the relaxation rates of solvent nuclei caused by the presence of a paramagnetic solute is known as NMR Paramagnetic Relaxation Enhancement (NMR-PRE). This is due to the fluctuating hyperfine interaction of magnetic moments of electron spins (μ_s) with the magnetic moment of the nucleus (μ_I) (Figure **4.5**). Usually, the electron spin magnetic moments are larger than the nuclear magnetic moments.[175] A small amount of paramagnetic solute is enough to provide a noticeable PRE for the nuclear spins in a sample.

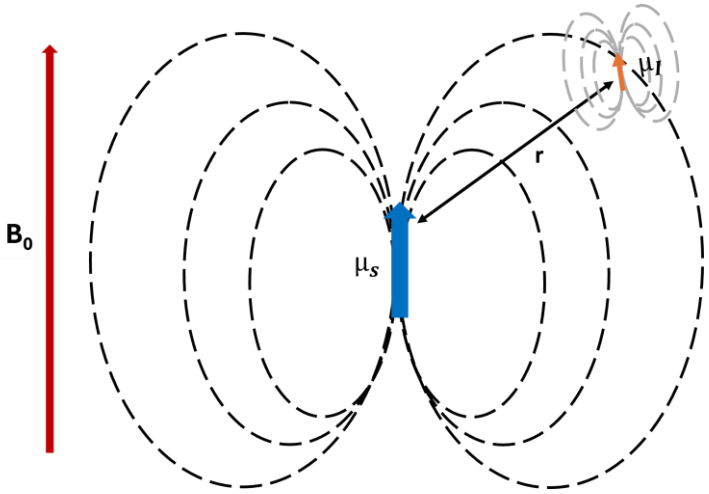


Figure 4.5 Illustration of the interaction between μ_s and μ_I in an external magnetic field, r represents the distance between μ_s and μ_I.

Two significant processes which control the PRE process are dipole-dipole (DD) interaction and Curie spin (C) contribution. The dipole-dipole interaction is the strong interaction between the electronic spin magnetic moment (μ_s) and the nuclear spin magnetic moment (μ_I). This depends on the distance (r) between the magnetic moments (μ_s and μ_I), electronic spin (s) and the orientation of the magnetic moment.

The dipole-dipole (DD) contribution in PRE is given by,

$$R_{DD} \propto C_{DD}^2 J(\omega, \tau_C) \tag{4.7}$$

J : total electronic spin quantum number.

ω : nuclear and electronic Larmor frequencies at a given magnetic field.

τ_C : Correlation time (Includes rotational and exchange relaxation time as well as electronic correlation time).

C_{DD}, The first part of the equation (4.7) which contributes to the electronic momentum of the dipole-dipole interactions,

Therefore,

$$C_{DD} \propto \frac{\mu_e}{r^3} \tag{4.8}$$

where μ_e = electronic moment and r = distance between the electronic and nuclear magnetic moment.

The second part corresponds to the dynamics, which is represented in terms of spectral densities, i.e., $J\ (\omega, \tau_c)$

$$J\ (\omega, \tau_c) \propto \frac{\tau_c}{1 + \omega^2\, \tau_c^2} \tag{4.9}$$

Curie spin relaxation is another important mechanism involved in the relaxation process. Also called the average electronic spin, Curie spin relaxation becomes stronger as the external magnetic field increases and is directly related to the magnetic moment of the molecule. This relaxation mechanism is especially significant for lanthanide ions such as Dy^{3+}, Er^{3+}, Ho^{3+}, and Tb^{3+} (but not Gd^{3+}), which have high magnetic moments and short electronic relaxation times due to their anisotropic electronic configurations. Curie spin relaxation mainly affects the T_2 relaxation process at high magnetic fields, particularly when the rotational motion of the molecule is fast (i.e., low rotational correlation times).[176–178]

Curie's term is given by,

$$R_C \propto < \frac{\mu_e^2\, B}{T r^3} \tag{4.10}$$

Both dipole-dipole interaction and Curie spin relaxation contribute to the inner and outer sphere relaxation mechanisms. The main effect depends on the paramagnetic ion's electronic features, magnetic strength, and its structure.

4.4.1. Mechanism of PRE

The introduction of paramagnetic molecules in the solvent improves the longitudinal as well as transverse relaxation processes of the solvent nuclei. The resultant relaxation (R^{total}) of the solvent nuclei is the sum of the paramagnetic (R^{para}) and diamagnetic (R^{dia}) relaxation contributions of the solvent molecules. R^{para} and R^{dia} represent the relaxation rates of solvent molecules with and without paramagnetic metals present, respectively.

$$R^{total} = Ri^{para} + Ri^{dia};\ i = 1{,}2 \tag{4.11}$$

Several factors, such as the size of the molecule and the total electronic spin, influence hyperfine interactions, which in turn affect the relaxation processes of solvent molecules.[179]

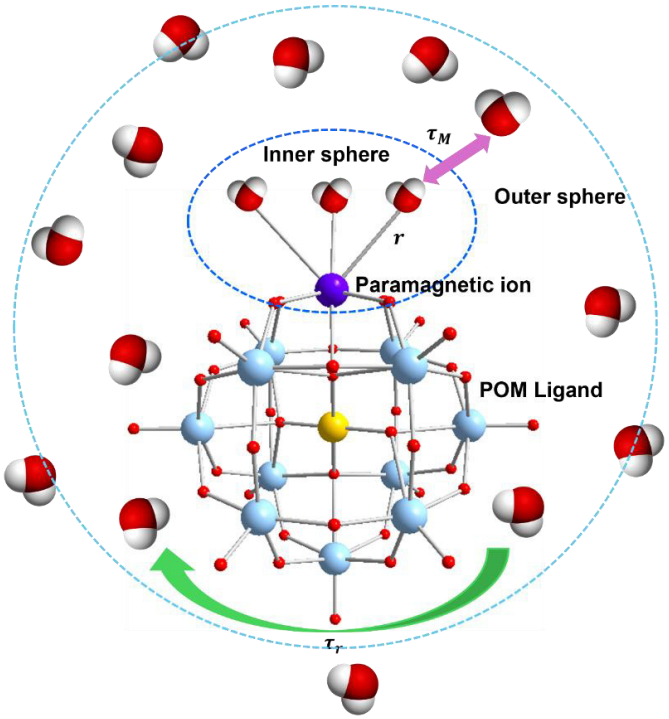


Figure 4.6 Illustration of the PRE process and various parameters involved in the PRE mechanism between paramagnetic ion-containing POM (PM-POM) and surrounding water molecules.

Two main interaction mechanisms determine the relaxation behaviour of solvent molecules. These mechanisms and the factors influencing relaxation are illustrated in Figure **4.6**. The inner sphere (IS) mechanism occurs when solvent molecules are directly coordinated to the paramagnetic centre. In contrast, the outer sphere (OS) mechanism involves interactions between the paramagnetic molecule and nearby solvent molecules that are not directly bound.[180]

The overall paramagnetic relaxation rate is the sum of both inner sphere and outer sphere contributions.

$$R^{para} = Ri^{IS} + Ri^{OS}; i = 1,2 \tag{4.12}$$

Inner sphere mechanism

In the case of the inner sphere mechanism, the water molecule is directly coordinated to a vacant site of the paramagnetic metal ions. The inner sphere relaxation is described by the Solomon–Bloembergen–Morgan theory, equation (4.13)

$$R^{IS} = fq \frac{1}{T_{1,M} + \tau_M} \tag{4.13}$$

Here R^{IS} Innersphere relaxation, f The ratio of concentrations of the paramagnetic compound and the solvent, q : The number of water-binding sites, $T_{1,M}$: longitudinal relaxation time of the coordinated water molecules and τ_M : the residence time of the coordinated water molecules exchanging with the bulk.

Eq (4.13) is the sum of dipolar-dipolar and Curie spin contributions given in equations 4.14 and 4.15

The dipolar contribution $R^{IS,DD}$ is given by,

$$R^{IS,DD} \propto \gamma_1^2 \mu_B^2 g_j^2 J(j+1) \frac{1}{r^6} [3J(\omega_1, \tau_C) + 7J(\omega_1, \tau_C)] \quad (4.14)$$

Where γ_1 : nuclear gyromagnetic ratio, μ_B : Bohr magneton, g_j : The Landé factor, J: total electronic spin quantum number, r the distance between observed nuclei and the paramagnetic species.

The Curie spin contribution for the outersphere mechanism is,

$$R^{IS,C} \propto \gamma_1^2 B_0^2 \mu_B^4 g_j^4 J^2 (J+1)^2 \frac{1}{r^6} \frac{1}{(3K_B T)^2} 3J(\omega_1, \tau_{CC}) \quad (4.15)$$

Where,

τ_{CC}: Curie correlation time, $K_B T$: constant,(K_B; Boltzmann constant, T; temperature).

Outer sphere mechanism

The outer sphere mechanism addresses the relaxation contributions of water molecules in the bulk, near the paramagnetic centre, without any direct coordination. This relaxation model focuses on the electronic properties of the paramagnetic molecules and the intermolecular distance between the paramagnetic molecules and the water proton. The main parameters which influence this mechanism are the electronic properties of the paramagnetic centre (S), the distance between the paramagnetic centre and the water molecules (r) and the corresponding diffusion coefficient (D).[180]

The outersphere contribution is also the sum of dipole-dipole and the Curie spin contributions.

The dipolar contribution for the outersphere mechanism is,

$$R^{OS,DD} \propto \frac{\gamma_1^2 \mu_B^2 g_j^2 N_A [C]}{aD} \Big[6 \left(J(J+1) S_c coth \left(\frac{B_0 \mu_B g_j}{2K_B T} \right) S_C^2 \right) J(\omega_1, \tau_s, \tau_D) + 7\, S_c coth \left(\frac{B_0 \mu_B g_j}{2K_B T} \right) J(\omega_1, \tau_s, \tau_D) \Big] \quad (4.16)$$

N_A : Avogadro number, $[C]$: molar concentration, S_c : time-averaged electronic spin

The Curie spin contribution for the outersphere mechanism is,

$$R^{OS,C} \propto \frac{\gamma_1^2 \mu_B^2 g_j^2 N_A [C]}{aD} S_C^2 J^A(\omega_1, \tau_D) \quad (4.17)$$

4.4.2. Factors Influencing the Relaxivity of Paramagnetic Metal-Containing Molecules

Important properties of molecules which contribute to paramagnetic relaxation enhancement (PRE) of a nucleus are discussed here.

Number of water molecules in the first coordination sphere

The relaxation rate, referred to as the inner sphere mechanism, is directly proportional to the number of water molecules present in the first coordination sphere, which is also known as the hydration number. This hydration number depends on the number of vacant binding sites available for solvent exchange.[181–183] More water molecules reduce thermodynamic stability; however, PM-POMs can host multiple water-binding sites without compromising their structural stability.[184]

Hyperfine interactions between spins shorten the distance between them and increase the relaxation rate of the solvent. Hydrogen bonding can orient water protons toward the paramagnetic centre, further reducing this distance. Other factors, such as the size of the paramagnetic molecules, the number of exposed water coordination sites, solvent viscosity, and the exchange-correlation time (τ_M), also influence the intermolecular distance (r).[185]

Magnetic properties of paramagnetic ions

The magnetic properties of paramagnetic ions greatly affect relaxation. For example, Gd^{3+} has seven unpaired electrons, giving it a large magnetic moment of 7.94 μB, making it an excellent T_1 contrast agent. It also has an isotropic electronic ground state called $^8S_{7/2}$, meaning its electron spin is the same in all directions (isotropic), with a total spin quantum number of 7/2. This uniformity helps produce strong and consistent magnetic effects. Other lanthanide ions typically have lower magnetic moments and anisotropic ground states, indicating that their magnetic behaviour varies with direction. These ions often show longer T_2 relaxation times, especially at high magnetic fields, where the Curie spin effect becomes important. When several paramagnetic ions are present in one molecule, their combined magnetic moments increase the relaxation rate. The magnetic properties of isolated lanthanide ions in aqueous solutions are listed in Table **4.1**.

Molecular dynamics and correlation Time (τ_C)

The random movements at the molecular level, such as molecular rotations, vibrations, and interactions in solutions like collisions, all influence the relaxation process. The correlation time (τ_C) describes how time-dependent dynamic properties of the system affect the relaxation process. The key movements that contribute to the relaxation of nuclear spins are explained as follows.

Table 4.1 Magnetic properties of isolated lanthanide ions in aqueous solutions.

Ln^{3+}	$4f^n$ electron configuration	Free-ion ground state term $^{2S+1}L_J$	Free-ion g value	$\mu eff = gJ\mu B\sqrt{J(J+1)}$	8-coordinate radius	4f electron density distribution's geometry	Free ion $\chi_m T_{calc}$ value at RT (cm^3 K mol^{-1})	τ_e (s)
La	$4f^0$	$^1S_0$	----	----	1.16	----	0	----
Ce	$4f^1$	$^2F_{5/2}$	6/7	2.54	1.14	Oblate	0.80	10^{-13}
Pr	$4f^2$	$^3H_4$	4/5	3.58	1.13	Oblate	1.60	10^{-13}
Nd	$4f^3$	$^4I_{9/2}$	8/11	3.68	1.11	Oblate	1.64	10^{-13}
Pm	$4f^4$	$^5I_4$	3/5	2.68	1.09	Prolate	0.90	10^{-13}
Sm	$4f^5$	$^6H_{5/2}$	2/7	0.85	1.08	Prolate	0.09	10^{-13}
Eu	$4f^6$	$^7F_0$	----	----	1.07	Isotropic	0	----
Gd	$4f^7$	$^8S_{7/2}$	2	7.94	1.05	Isotropic	7.88	10^{-7}
Tb	$4f^8$	$^7F_6$	3/2	9.7	1.04	Oblate	11.82	10^{-13}
Dy	$4f^9$	$^6H_{15/2}$	4/3	10.6	1.03	Oblate	14.17	10^{-13}
Ho	$4f^{10}$	$^5H_8$	5/4	10.6	1.02	Oblate	14.07	10^{-13}
Er	$4f^{11}$	$^4I_{15/2}$	6/5	9.6	1.00	Prolate	11.48	10^{-13}
Tm	$4f^{12}$	$^3H_6$	7/6	7.6	0.99	Prolate	7.15	10^{-13}
Yb	$4f^{13}$	$^2F_{7/2}$	8/7	4.5	0.99	Prolate	2.57	10^{-13}
Lu	$4f^{14}$	$^1S_0$	----	----	0.98	Isotropic	0	----

Footnote:
Ln^{3+}: Lanthanide ion (3+)
$4f^n$: Number of 4f electrons
$^{2S+1}L_J$: (2S+1)= Spin multiplicity (number of possible spin states), L = Total orbital angular momentum (represented by a letter, e.g., S, P, D, F), J = Total angular momentum (combines spin and orbital angular momentum)
$\mu eff = gJ\mu B\sqrt{J(J+1)}$ defines the effective magnetic moment of an atom, which is a measure of its magnetic properties. It combines the **8-coordinate radius:**
The ionic radius of the lanthanide ion when it is bonded to eight other atoms (coordination number 8). It reflects the size of the ion in such an environment.
4f electron density distribution's geometry:
This describes the shape of the 4f electron cloud around the lanthanide ion. It can be oblate (flattened like a disk) or prolate (elongated like a rugby ball). This shape influences the ion's magnetic behaviour.
$\chi_m T_{calc}$: This is the calculated magnetic susceptibility times temperature for the free ion at room temperature (RT). It shows how strongly the ion responds to a magnetic field.
τ_e (s): This is the electronic relaxation time, which measures how quickly the electron spins return to equilibrium after being disturbed. It is given in seconds (s).

Water exchange correlation time/residence Time (τ_M)

τ_M is the time at which a water molecule reside at the paramagnetic metal centres before it gets exchanged with the other water molecules from the bulk. The electrostatic force between the paramagnetic ions and the water molecules affects the exchange-correlation time. This effect can significantly improve the efficiency of both the inner-sphere and outer-

sphere contributions of molecules containing paramagnetic metal ions by decreasing the distance between them. However, the steric effect of bulky ligands contributes to a dominant repulsive force that increases the intermolecular distance, thereby reducing the residence time of the water molecules.[186]

Rotational / tumbling correlation time (τ_R)

Another critical factor in relaxation enhancement is the rotational, or tumbling, correlation time (τ_R). It represents how fast a paramagnetic ion with a bound water molecule rotates in solution. The rate of this rotation affects how effectively the paramagnetic ion can enhance relaxation. This is represented by the equation:

$$\tau_R = \frac{4\pi\eta a^3}{3K_B T} = \frac{\eta M}{dTK_B N_A} \quad (4.18)$$

Where η : viscosity of the solvent used, M : molar mass of the solute, a : radius of the molecule, d : density, N_A : Avogadro's constant, K_B : Boltzmann constant, T : temperature.

The rotational correlation time of a molecule is influenced by the viscosity of the solvent and the molecular size of the solute. Molecules that rotate slowly can lead to greater relaxation enhancement compared to those that rotate quickly. Molecules with high molecular weights often exhibit longer rotational correlation times. The incorporation of bulky ligands can increase the molecular weight of a molecule. A longer rotational correlation time enhances relaxivity because it improves the nuclear spin hyperfine interaction with the electron spin in the presence of an external magnetic field. For this reason, paramagnetic ions bonded to rigid, bulky ligands, such as polyoxometalates, can enhance the rotational correlation time, resulting in improved relaxation. However, the steric effects of bulky ligands may obstruct the water exchange pathway or may conceal the water binding site of the paramagnetic ion. This obstruction can lead to variations in the water exchange time or residence time of water molecules interacting with the paramagnetic ion. Therefore, optimising the rotational correlation time is crucial for improving overall relaxivity.[187]

Electronic spin correlation time (τ_e)

The electronic spin correlation time is significant in understanding the interaction between the paramagnetic centre and the nucleus. The paramagnetic metal ions, like $Gd^{3+,}$ show a higher electronic relaxation time due to their higher number of unpaired electrons in the f orbital, resulting in their high magnetic moment. This ensures a favourable interaction with the protons. Therefore, the (τ_e) value determines the distance between the metal ion and the nucleus, resulting in an enhanced relaxation rate.[185]

Diffusion correlation time (τ_D)

The hyperfine interaction between paramagnetic ions and solvent molecules depends on the distance between them as well as the relative dynamics of the molecules. Therefore, it is crucial to consider the relative diffusion coefficient (D) along with other correlation times, particularly in more complex paramagnetic systems. The diffusion correlation time is given by:

$$\tau_D = \frac{a^3}{D} \tag{4.19}$$

Where D is the relative diffusion constant, which is inversely proportional to the size of the molecule and the viscosity of the solvent, and a is the closest distance between the paramagnetic ion and the solvent.[188]

4.4.3. Electronic relaxation of a paramagnetic ion in solution

The electronic spin relaxation of various paramagnetic ions significantly affects the relaxation enhancement of different nuclear spins in both the inner and outer spheres in solution. High-resolution NMR spectra can be achieved for those paramagnetic metal ions with short electron spin relaxation times. The electronic relaxation time of paramagnetic metal ions in solution at high magnetic fields is shown in Tables **4.1** and **4.2**.

The electron relaxation mechanism is influenced by spin-orbit coupling. This coupling occurs due to the interaction between the magnetic moment of the electron's spin and the orbital motion of the charged nucleus. Additionally, molecular motion modifies the orbital magnetic moment, which in turn affects the electron's spin.

The electron relaxation time of metal ions primarily depends on the availability of low-lying excited states, which enhance the efficiency of spin-orbit coupling. Generally, metal ions with an electronic relaxation time longer than 10^{-11} s tend to have excited states that significantly exceed the energy of their ground state. Conversely, if the electronic relaxation time is shorter than 10^{-11} s, the energy states are less distinct.[189–192]

Table 4.2 The electronic relaxation time of some common paramagnetic 3d metal ions.

Metal ion	Electronic configuration	S	τ_e (s)
Ti^{3+}	d^1	1/2	10^{-10}
V^{2+}	d^3	3/2	10^{-9}
Cr^{2+}	d^4	2	10^{-11}
Mn^{3+}	d^4	2	10^{-10}

Mn^{2+}	d^5	5/2	10^{-8}
Fe^{3+}(HS)	d^5	5/2	10^{-9}
Fe^{3+}(LS)	d^5	1/2	10^{-11}
Fe^{2+}(HS)	d^6	2	10^{-12}
Co^{2+}(HS)	d^7	3/2	10^{-12}
Co^{2+}(LS)	d^7	1/2	10^{-9}
Ni^{2+}	d^8	1	10^{-10}
Cu^{2+}	d^9	1/2	10^{-9}

4.5. Application of PRE

The NMR behaviour in the presence of paramagnetic systems is used to develop and study contrast agents for Magnetic Resonance Imaging (MRI). MRI spectroscopy is an imaging technique that utilises the principles of NMR spectroscopy. Contrast agents are chemical substances used to enhance the quality of images produced by this technique. This concept was later employed in the development of suitable MRI contrast agents.[193] NMR spectroscopy quantitatively determines the efficiency of paramagnetic metal-containing molecules as potential MRI contrast agents. The fundamental theory of MRI relies on monitoring different properties and distributions of NMR-active nuclei.[194–196] An MRI scanner can generate images based on the special variation (Longitudinal (T_1) and Transverse (T_2)) of the NMR active nuclei. Magnetic Resonance Imaging (MRI) is a crucial tool in medicine and clinical research, facilitating the early diagnosis of physiological dysfunctions in the human body. One of the key advantages of MRI is that it is a non-invasive imaging technique that does not use harmful ionising radiation, making it safer than other imaging methods.[197,198]

4.6. PM-POM Clusters as MRI Contrast Agents

Paramagnetic metal ion-containing polyoxometalates (PM-POMs) have been synthesised and evaluated as MRI contrast agents. J. Feng and co-workers demonstrated the use of lanthanide-based POMs for both *in vivo* and *in vitro* tissue-specific MRI imaging. In their study, they employed two lanthanide POMs: $K_9GdW_{10}O_{36}$/**GdW_{10}** and $K_{11}[Gd(PW_{11}O_{39})_2]$/**$Gd(PW_{11})_2$**.[199] Subsequently, several research groups have reported similar studies using other POM-based materials. These PM-POMs generally exhibit higher relaxivity than GdDTPA, a commercially available MRI contrast agent. In the body, specific proteins are responsible for the distribution, transport, and elimination of contrast agents. To better understand the behaviour of POM metal clusters in a physiological environment,

their relaxivity has also been measured in the presence of BSA (bovine serum albumin) and hTF (human serum transferrin). The results are summarised in Table **4.3**.

These studies show that all POM metal clusters are more effective MRI contrast agents than GdDTPA, which is a clinically approved agent. The POM metal clusters caused various pathological changes in living cells, indicating low bioavailability as an MRI contrast agent. The MRI imaging and toxicity studies of different POM clusters are listed in Table **4.4.**

Table 4.3 The T_1 relaxivities of GdDTPA and Metal-POMs.

POM-metal clusters		**T_1 relaxivities ($mM^{-1}. S^{-1}$)**			**Ref.**
PM-POM		**In D_2O**	**in BSA**	**in hTF**	
GdDTPA	-	5:25	5.40	5.83	[200]
$[GdW_{10}O_{36}]^{9-}$	**GdW_{10}**	6.89	7.47	7.30	[199]
$[Gd(PW_{11}O_{39})_2]^{11-}$	**Gd-PW_{11}**	5.27	5.60	6.13	[199]
$Gd_2P_2W_{18}O_{62}$	**Gd_2-P_2W_{18}**	28.4	3.62	blue ppt	[199]
$[(GdO)_3(PW_9O_{34})_2]^{15-}$	**Gd_3-PW_9**	11.2	17.0	18.1	[201]
$[Gd(SiW_{11}O_{39})_2]^{13-}$	**Gd-SiW_{11}**	6.59	6.85	-	[202]
$[Gd_3O_3(SiW_9O_{34})_2]^{11-}$	**Gd_3-SiW_9**	12.6	19.3	-	[202]
$[Gd(P_2W_{17}O_{61})_2]^{17-}$	**Gd-$P2W_{17}$**	7.59	7.97	-	[203]
$[Gd(BW_{11}O_{39})_2]^{15-}$	**Gd-BW_{11}**	19.95	21.09	20.22	[204]
$[Gd(CuW_{11}O_{39})_2]^{17-}$	**Gd-CuW_{11}**	17.12	17.68	17.93	[204]
$[MnSiW_{11}O_{39}]^{6-}$	**Mn-SiW_{11}**	12.1	4.6	5.2	[205]
$[MnP_2W_{17}O_{61}]^{8-}$	**Mn-P_2W_{17}**	4.7	5.3	7.0	[206]
$[Gd(\alpha\ SiW_{11}O_{39})]^{5-}$	**Gd-SiW_{11}**	7.95	-	9.41	[206]
$[Gd(\beta_2\text{- } SiW_{11}O_{39})_2]^{13-}$	**Gd-Si_2W_{22}**	9.18	-	11.15	[206]

Even though many reports support antiviral[207] anticancer[208] and antibacterial[209] properties of POMs, the application of POM-based materials to biological systems is limited by their toxic properties. The major limitation to the use of POMs in biological applications is their instability at physiological pH. Most polyoxometalates are stable only within a specific pH range, with their hydrolytic stability restricted to that range. Consequently, at physiological pH, most polyoxometalates undergo partial or complete decomposition. Additionally, the presence of specific macromolecules in biological systems can also facilitate the decomposition of these metal oxides.[210],[211] This is why this pure inorganic POM is not in the picture of the drug development stage. The use of polyoxometalates in biological systems requires an interdisciplinary approach to reduce their toxic effects.[212],[213]

Table 4.4 List of paramagnetic metals containing POM as MRI CAs.

PM-POM cluster		Organ	Toxicity	Ref.
$[GdW_{10}O_{36}]^{9-}$	**GdW_{10}**	Kidney Liver	Toxic than Gd-DTPA	[199]
$[Gd(PW_{11}O_{39})_2]^{11-}$	**Gd-PW_{11}**	Kidney Liver	Toxic than Gd-DTPA	[199]
$Gd_2P_2W_{18}O_{62}$	**Gd_2-P_2W_{18}**	Liver	No Test	[201]
$[(GdO)_3(PW_9O_{34})_2]^{15-}$	**Gd_3-PW_9**	Liver Kidney	No Test	[201]
$[Gd(SiW_{11}O_{39})_2]^{13-}$	**Gd-SiW_{11}**	Liver Kidney	Toxic than Gd-DTPA	[202]
$[Gd_3O_3(SiW_9O_{34})_2]^{11-}$	**Gd_3-SiW_9**	Liver Kidney	Toxic than Gd-DTPA	[202]
$[Gd(P_2W_{17}O_{61})_2]^{17-}$	**Gd-P_2W_{17}**	Liver Kidney	No Test	[203]
$[Gd(BW_{11}O_{39})_2]^{15-}$	**Gd-BW_{11}**	Liver Kidney	No Test	[204]
$[Gd(CuW_{11}O_{39})_2]^{17-}$	**Gd-CuW_{11}**	Liver Kidney	No Test	[204]
$[MnSiW_{11}O_{39}]^{6-}$	**Mn-SiW_{11}**	Kidney Liver	No Test	[205]
$[MnP_2W_{17}O_{61}]^{8-}$	**Mn-P_2W_{17}**	Liver Kidney	No Test	[206]
$[Gd(\alpha\text{-}SiW_{11}O_{39})]^{5-}$	**Gd-SiW_{11}**	-	Noncytotoxic	[206]
$[Gd(\beta_2\text{-}SiW_{11}O_{39})_2]^{13-}$	**Gd-Si_2W_{22}**	-	Cytotoxic	[206]

The biocompatibility of these inorganic polyanions can be considerably reduced and improved by assembling these molecules with another substrate, such as polymers or nanomaterials[214–216] one such example is shown in Figure 4.7. However, these methods add additional synthetic steps and bring stability challenges.

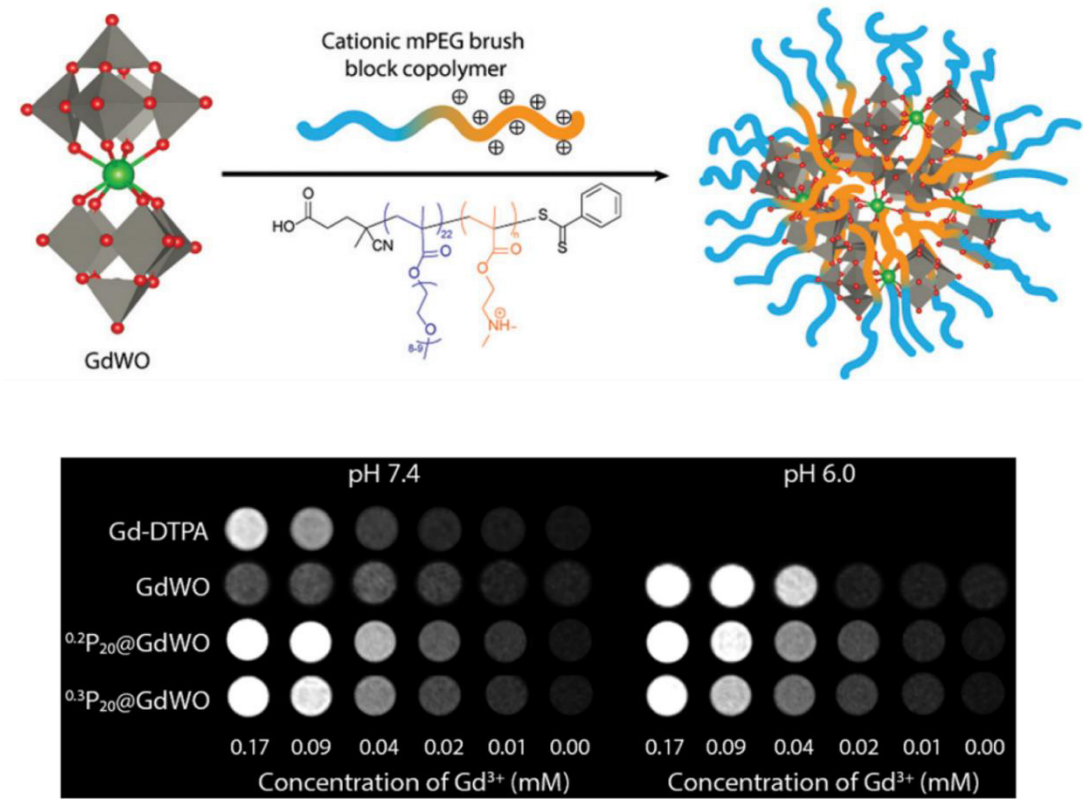


Figure 4.7 GdWO (PM POM) interacts with cationic mPEG brush block copolymer to form the nano-assemblies (above). T_1-weighted MRI phantom images of Gd-DTPA, GdWO and the nano-assemblies (below).[215]

Similar to organic ligands,[217] lacunary species of POMs or POM ligands can incorporate various types and numbers of spin-coupled paramagnetic metal ions, including 3d, 4f, and 3d-4f metals, to form stable metal clusters. These lacunary species can be considered inorganic analogues of porphyrins (Figure **4.8**). An important advantage of POM-based paramagnetic materials is that they are easy to prepare, soluble in water, and stable over a wide temperature range. Through careful tuning of the synthetic procedures, it is possible to create metal clusters with high nuclearity.[218] For these reasons, POM-based paramagnetic metal clusters are excellent candidates for developing MRI contrast agents.

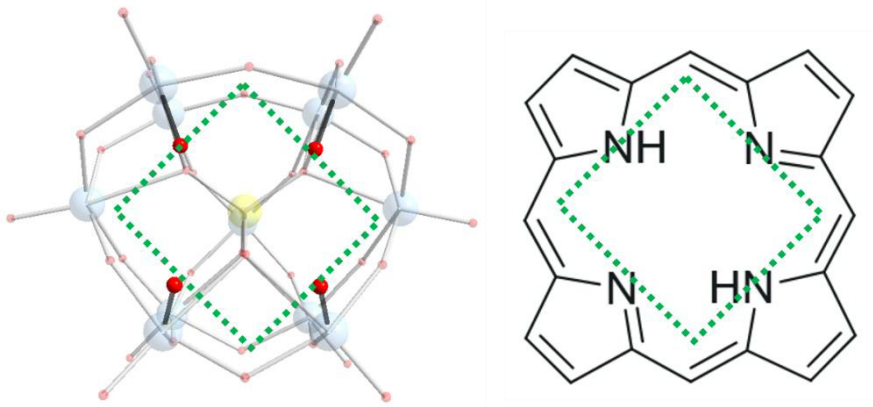


Figure 4.8 Analogy of monolacunary POM ligand $[GeW_{11}O_{39}]^{8-}$ with porphyrin.

The scope of MRI techniques is now beyond medical applications,[219–221] such as monitoring and characterising dynamic processes, especially diffusion and flow of fluids. In chemistry, MRI applications include monitoring chemical waves, temperature, and electrochemical reactions.[222] An MRI image during galvanic corrosion of zinc in saturated lithium chloride is shown in Figure **4.9**.

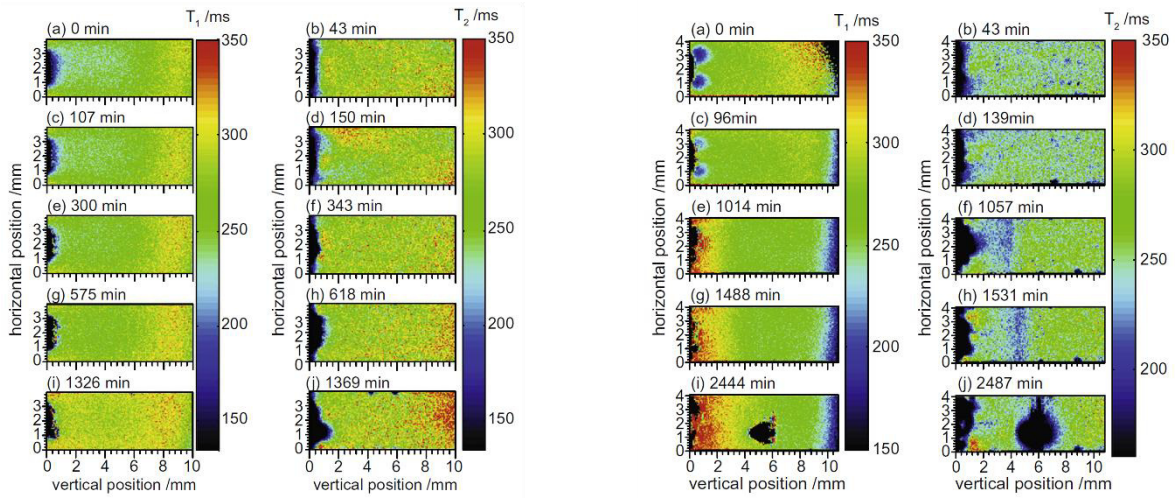


Figure 4.9 MR T_1 and T_2 images before Zn corrosion (left), MR T_1 and T_2 images of Zn during corrosion (right).[223]

In both medical and non-medical applications, the main drawback of MRI is its low sensitivity. A commonly suggested strategy to enhance MRI's imaging capability is to increase the magnetic field strength, thereby improving the signal-to-noise ratio (SNR). In medical MRI, the trend is to move from 1.5 T to as high as 11 T. However, further research is needed to ensure stability and homogeneity of the magnetic field for clinical use.[224] For instance, the currently available analytical NMR system is operated with 23.5 T and preclinical instruments are operated at a maximum of 21 T magnetic fields. For material science applications, superconducting and resistive magnets of 45 T to 100 T are available.[225] The non-destructive and high-performing nature of this versatile technique has proven beneficial across various fields, including food industries, polymer technologies,

agriculture, and artificial medical implants. It is an efficient technique for imaging an opaque system used in industries such as chemical process engineering.[226],[227] PM-POM clusters are a promising option for various non-medical applications, particularly for magnets used in high fields.

4.7. NMR Relaxivity Measurements of POM Clusters at Ultra-High Fields

High magnetic field MRI systems have specific requirements, including the advanced composition of magnets, radiofrequency coils, and innovative designs for contrast agents. Consequently, it is essential to discuss the design and synthesis of a more versatile MRI contrast agent that remains stable across a wide range of magnetic fields. Additionally, the diverse applications of MRI in various fields further drive the development of new contrast agent structures.[228] Gd^{3+} based T_1 contrast agents are more common for medical imaging applications due to their isoelectronic ground state ($^8S_{7/2}$) and the long electronic relaxation time of the Gd^{3+} ion. The disadvantage of these Gd^{3+} based contrast agents is their inability to perform at increased magnetic fields.[229]

A new class of giant heterometallic polyoxometalate (POM) clusters, $[Ln_{30}Co_8Ge_{12}W_{108}O_{408}(OH)_{42}(H_2O)_{30}]^{56-}$ (**$Ln_{30}Co_8$**, Ln = Dy, Gd, Eu, Y), has been reported. These clusters comprise two distinct coordination motifs, $\{Ln^{3+}{}_3\}$ and $\{M^{2+}{}_2Ln^{3+}{}_3\}$, based on 4f and mixed 3d-4f metal ions, respectively, and are stabilised by trilacunary Keggin POM ligands. Among them, **$Dy_{30}Co_8$** behaves as a single-molecule magnet, while **$Dy_{30}Co_8$** and **$Gd_{30}Co_8$** demonstrate high potential as MRI contrast agents in non-clinical applications.

Longitudinal (T_1) and transverse (T_2) relaxivity measurements at ultra-high magnetic fields indicated exceptional contrasting capabilities, surpassing those of commercially available Gd-based agents. The large size and highly negative charge of these high-spin clusters were shown to enhance penetration and adsorption, as observed in axial MR imaging during in situ dead-end membrane filtration of skimmed milk (Figure **4.10**).[230]

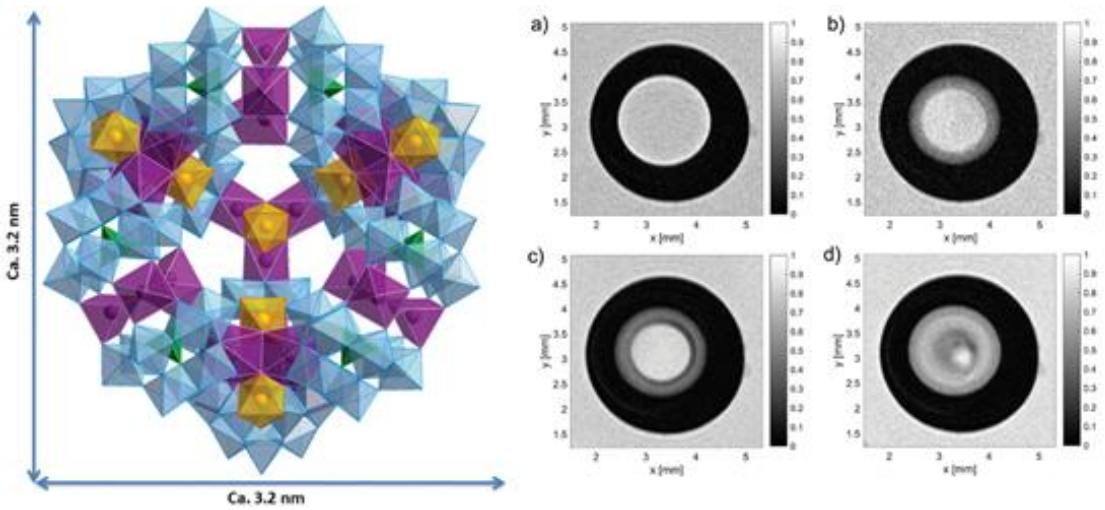


Figure 4.10 Structure of $[Gd_{30}Co_8Ge_{12}W_{108}O_{408}(OH)_{42}(OH_2)_{30}]^{56-}$ (left). Axial MR images during an in situ dead-end membrane filtration of skimmed milk: a) Reference image of ceramic hollow fibre before starting the filtration. b) After 3 hours and 10 minutes, a thick deposit layer formed inside the hollow fibre. c) After applying contrast agent **$Gd_{30}Co_8$,** the image contrast is enhanced, but it does not penetrate the deposited layer. d) Back diffusion, the moieties in the second filtration layer containing CA diffuse back into the inner membrane (right).[230]

The pronounced, field-dependent relaxivities were attributed to the large total electron spin, while sensitivity to motional correlation times provided further insight into their MRI behaviour. These results highlight the potential of paramagnetic metal-containing POMs as efficient contrast agents, with both magnetic and size-dependent effects influencing imaging performance.

In addition to the {**$Ln_{30}Co_8$**} clusters described above, comparative NMR relaxivity studies have been reported on two paramagnetic POMs: $[Mn_4(H_2O)_2(P_2W_{15}O_{56})_2]^{16-}$ (**Mn_4-P_2W_{15}**) and $[\{Dy(H_2O)_6\}_2Mn_4(H_2O)_2(P_2W_{15}O_{56})_2]^{10-}$ (**Dy_2Mn_4-P_2W_{15}**). These studies illustrate how variations in the electronic and chemical characteristics of the clusters influence their paramagnetic relaxation enhancement (PRE) behaviour. Both compounds exhibit substantially higher longitudinal (T_1) and transverse (T_2) relaxivities than commercially available MRI contrast agents. Among them, **Dy_2Mn_4-P_2W_{15}** demonstrates superior relaxivity values compared to **Mn_4-P_2W_{15}**, attributable to the larger total electron spin associated with the Dy^{3+} centres. The molecular structure also plays a key role, with the pronounced PRE effect arising primarily from inner-sphere contributions, namely, the exchange interactions between coordinated water molecules and the paramagnetic centres.[231]

4.8. NMR Relaxivities of Paramagnetic POMs Investigated during this PhD Work

Experimental determination of PRE

A longitudinal and transverse relaxivity study gives the experimental validation of the PRE process. The Nuclear Magnetic Resonance dispersion (NMRD) technique allows for measuring the relaxivity as a function of the magnetic field. Since the PRE is a field-dependent phenomenon, the current study is focused on the relaxivity of the PM POM with a range of magnetic fields (20 MHz to 1.4 GHz). The NMRD measurements provide insight into the molecular dynamics and transport properties of this pure inorganic PM POM in solution; hence, NMRD offers an additional advantage in figuring out the solution behaviour of the molecules. The information from each NMRD in a particular magnetic field can estimate the essential parameters (q, τ_M, τ_R, $\tau_{s,}$ etc.) that directly influence the relaxation rate, which leads to quantifying the efficiency of PM POM as a potential contrast agent. Additional experimental techniques such as Electron Paramagnetic Resonance (EPR and ^{17}O are also used to analyse parameters like ($\tau_{s,}$ $\tau_{M,}$ q).

4.8.1. NMR Relaxivities of 3d Metal-Containing POMs

Three high-nuclearity 3d transition-metal-containing POMs, $[M_{16}\{(OH)_3PO_4\}_4(XW_9O_{34})_4]^{28-}$ (M = Co^{2+}, Ni^{2+}, $Mn^{2+/3+}$, X = Si, P), were selected for NMR relaxivity studies. Among these, only the Mn-containing POM exhibits mixed-valence oxidation states, represented by the formula $[Mn^{2+}{}_{12}Mn^{3+}{}_4\{(OH)_{12}PO_4\}_4(SiW_9O_{34})_4]^{28-}$(**$Mn_{16}$-$SiW_9$**). The **$Co_{16}$-$PW_9$** and **$Ni_{16}$-$PW_9$** clusters possess uniform oxidation states but adopt structural topologies identical to **Mn_{16}-SiW_9.**

For clarity in the structural description, only the **Mn_{16}-SiW_9** cluster is shown in Figure **4.11** to highlight the positions of the Mn^{2+} and Mn^{3+} centres. The structures of **Co_{16}-SiW_9** and **Ni_{16}-SiW_9** are identical and therefore not depicted. These POMs were synthesised and reported by PD. Dr. Masooma Ibrahim.

The molecular structure of $[Mn^{2+}{}_{12}Mn^{3+}{}_4\{(OH)_{12}PO_4\}_4(SiW_9O_{34})_4]^{28-}$ (**Mn_{16}-SiW_9**). (Figure **4.11**) contains 16 manganese centres forming a paramagnetic spin core. Two oxidation states of manganese ions are present: four Mn^{3+} ions and twelve Mn^{2+} ions. The four Mn^{3+} ions (Figure 4.**11(b)**) were arranged in the centre as a $\{Mn_4O_4\}$ cubane unit, which is capped by four tri-manganese-substituted $\{Mn_3(SiW_9)\}$ Keggin ion units. The overall assembly is interconnected by four phosphate $\{PO_4\}$ linkers.[232]

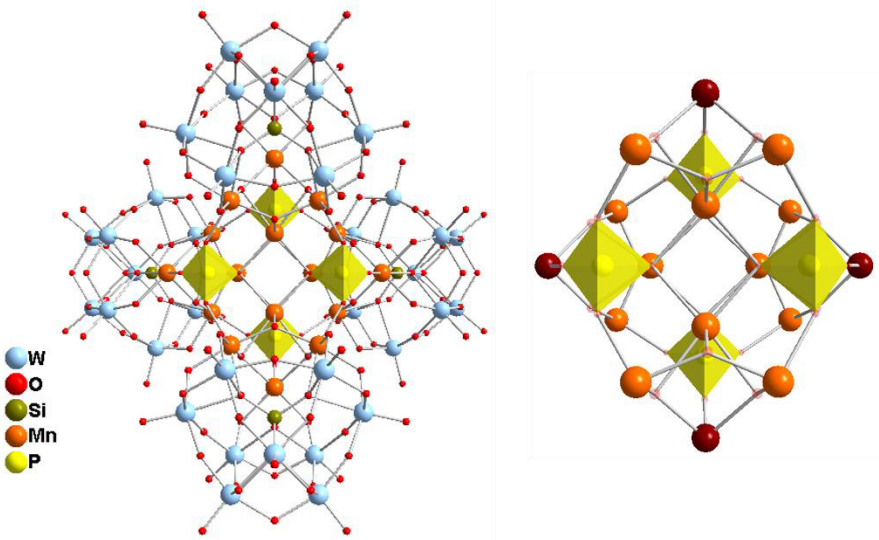


Figure 4.11 Combined ball and stick and polyhedral representation of $[Mn^{2+}_{12}Mn^{3+}_{4}\{(OH)_{12}PO_4\}_4(PW_9O_{34})_4]^{28-}$ (left) and mixed valent $[Mn^{2+}_{12}Mn^{3+}_{4}\{(OH)_{12}PO_4\}_4]^{12-}$. Colour code: Mn^{2+} orange, Mn^{3+} dark red (right).[232]

Co_{16}-PW_9 and **Ni_{16}-PW_9** are isostructural with **Mn_{16}-SiW_9**, containing 16 Co^{2+} and Ni^{2+} ions, respectively, all in the 2+ oxidation state. In both cases, the central $\{M_4O_4\}$ cubane is capped by tri-metal-substituted Keggin ion fragments $[\{M(OH)\}_3(PW_9O_{34})]^{6-}$, which are further connected via four phosphate $\{PO_4\}$ linkers, analogous to the arrangement in **Mn_{16}-SW_9**.[91]

Water ^{1}H relaxation measurements

To determine the water relaxivities of 3d POM metal clusters, pure crystals of **Mn_{16}-SiW_9**, **Co_{16}-PW_9**, and **Ni_{16}-PW_9** were dissolved in a 9:1 D_2O/H_2O mixture at a concentration of 1 mM. The resulting solution was further diluted using the same solvent, and five sets of dilutions were made: 0, 0.2, 0.4, 0.6, 0.8, and 1 mM. The stock solution appeared yellow-brown, pale purple and pale green, respectively. The solution remained clear and retained its colour throughout the NMR relaxivity experiments. The dependence of the longitudinal relaxation rate on the concentration of **Mn_{16}-SiW_9** was measured from 20 MHz to 1.4 GHz. Due to time constraints and limited availability of high-power (24 MW) resistive magnets (≥ 800 MHz), only the 1 mM and 0 mM dilutions of **Mn_{16}-SiW_9** were measured with the resistive magnets operating at frequencies of 800 MHz and above. For **Co_{16}-PW_9** and **Ni_{16}-PW_9**, the longitudinal relaxation rate as a function of concentration was measured only at 20, 80, 300, and 400 MHz. The transverse relaxation measurements of all metal clusters (**Mn_{16}-SiW_9**, **Co_{16}-PW_9**, and **Ni_{16}-PW_9**) were measured at 20, 80, 300 and 400 MHz.

Parameters affecting the ^{1}H relaxivity behaviour of transition metal ions

PRE in high-nuclearity 3d-metal-containing POM clusters was determined by a combination of structural, dynamic, and electronic factors. The **Mn_{16}-SiW_9**, **Co_{16}-PW_9**, and **Ni_{16}-PW_9** clusters exhibit an identical polyanionic framework, ensuring that structural parameters

relevant to PRE, such as the metal-proton distances and the closest approach of diffusing water molecules, were effectively constant across the series. Under these conditions, the observed differences in relaxivity can be attributed predominantly to the intrinsic electronic properties of the 3d metal ions, including their magnetic moments, electronic relaxation times, and zero-field splitting effects.

The ^{1}H relaxivity of these isostructural clusters arises from outer/inner sphere contributions. In the structural framework, the 16 paramagnetic metal ions were surrounded by a diamagnetic POM framework. Dynamic parameters such as τ_r, τ_M, J_{Diff} are the main contributions to the paramagnetic relaxation enhancement of these metal clusters, which are also assumed to be similar because of the isostructural frameworks of the molecules.

The outer sphere relaxivity is influenced by the electronic properties of the paramagnetic molecule, the intermolecular distance between solvent molecules and the paramagnetic ion centre, and the diffusion coefficient.[233]

The main determining factor contributing to the difference in the relaxivity data is the variation of the electronic relaxation times (T_{ele}) for each metal ion. Table **4.5** gives details of the electronic spin behaviour of the paramagnetic metal ions, which can affect the PRE properties.

Table 4.5 NMRD parameters and magnetic behaviour of paramagnetic metal ions in aqueous media.[234]

Metal ion	**Electronic configuration**	**S**	**L**	**Free ion configuration**	**Ligand field O_h**	**T_{1e}[(a)] (s)**	**Magnetic moments**		**Main electron relaxation mechanism**
							$\mu_{expected}$ (BM)	**$\mu_{calculated}$ [(b)] (BM)**	
Mn^{2+}	$3d^5$	5/2	0	^6S	^6A	10-8a	5.65-6.10	5.92	ZFS* modulated
Mn^{3+}	$3d^4$	2	2	^2D	^5E	10-11	4.90-5.00	4.90	ZFS modulated
Co^{2+} (HS)	$3d^7$	3/2	3	^4F	^4T	10-12	4.30-5.20	3.88	Orbach and ZFS modulation
Ni^{2+}	$3d^8$	1	1	^3F	^3A	10-10	2.80-3.5	3.88	ZFS modulated

*[(a)] The electronic relaxation time of the paramagnetic metal ions and nuclear relaxation rates for the proton at 5 Angstroms of the metal at 800MHz. [(b)] spin-only value. * Zero field splitting.*

The electronic relaxation time depends on the low-lying excited states, which makes the spin-orbit coupling efficient. Manganese-based NMR contrast agents are widely studied and

accepted as lanthanide-free contrast agents. Mn (Mn^{2+} and Mn^{3+}) also have a T_2 effect, which reduces the signal intensity.[235,236]

In the case of Mn^{2+} ($3d^5$), each of the five d orbitals contains one unpaired electron, contributing to the overall spin density. The octahedral field gives a nondegenerate ground state (^6A); in this case, electron relaxation is inefficient. However, in this case, the spin-orbit coupling is caused by zero-field splitting (ZFS). This most efficient PRE relaxation mechanism arises from the rotation of the molecule or from distortions of the coordination sphere due to collisions with solvent molecules. On the other hand, for Mn^{3+}, with an integer spin S=2, due to the lower symmetry of this Jahn-Teller ion and the doubly degenerate ground state (^5E), the electronic relaxation is modulated due to the ZFS.

The octahedral symmetry of Co^{2+} corresponds to a triply degenerate ground state (^4T). The PRE relaxation process is explained in the literature in terms of the Orbach mechanism, and the relaxation is further modulated by ZFS. The electron relaxation time is 10^{-12} s in this case. On the other hand, Ni^{2+} (d^8) has a nondegenerate ground state (^3T) and in this case, the electronic relaxation time amounts to 10^{-10} s.[234]
Here, the Orbach mechanism is expected to be inefficient, and the PRE relaxation is modulated by ZFS, which arises from the reorientation or collision with the solvent molecules.

Relaxation rate of Mn_{16}-SiW_9

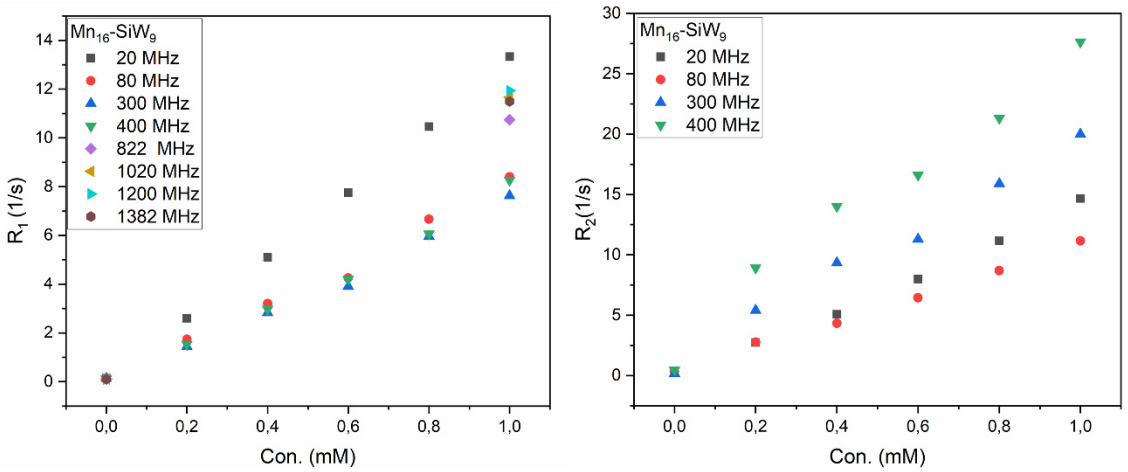


Figure 4.12 Relaxation rates of R_1 and R_2 as a function of the concentration of **Mn_{16}-SiW_9** clusters. R_1 shows a linear dependence on the concentration in all magnetic fields. The value of the slope is dependent on the magnetic field (left) R_2 shows linear dependence with the magnetic field, and the slope increases with increasing magnetic field up to 400 MHz (right).

The longitudinal and transverse relaxation rates of various concentrations of **Mn_{16}-SiW_9**, **Co_{16}-PW_9** and **Ni_{16}-PW_9** at different magnetic fields were measured. All the relaxation data for **Mn_{16}-SiW_9** are shown in Figure **4.12**. It is evident that, at all field strengths, both

relaxation rates increase linearly with an increase in concentration. The observed errors result from deviations in the exact concentration used as well as in the relaxation measurements (instrumental and modelling errors). The slopes of the corresponding linear fits give the longitudinal and transverse relaxivities. The same observations were obtained for other transition metal clusters (**A.4.1 and A.4.2**)

According to the data of **Mn_{16}-SiW_9**, the longitudinal relaxation rates increase with concentration. This dependence can be modelled linearly. The slopes, the relaxivities, however, do not show a consistent increase with rising magnetic field strength. For longitudinal relaxation, the highest relaxivity was observed at 20 MHz, gradually decreasing to 300 MHz. With larger fields, it begins to rise again, reaching a plateau around 1200 MHz.

In contrast, the transverse relaxation rate of the **Mn_{16}-SiW_9** molecules, as a function of concentration, is significantly larger than that of the longitudinal relaxation rate. In all cases, the relaxation rate increases linearly with increasing concentration.

Longitudinal and transverse relaxation rates vs concentration of **Co_{16}-PW_9** and **Ni_{16}-PW_9** also show a linear dependence on the field at different concentrations. This linear dependence is also expected in PRE theory.

Longitudinal and transverse relaxivity of M_{16}-SiW_9 POM

Longitudinal relaxivity (r_1) and transverse relaxivity (r_2) (Figure **4.13)** were deduced as slopes from the relaxation rate vs concentration data.

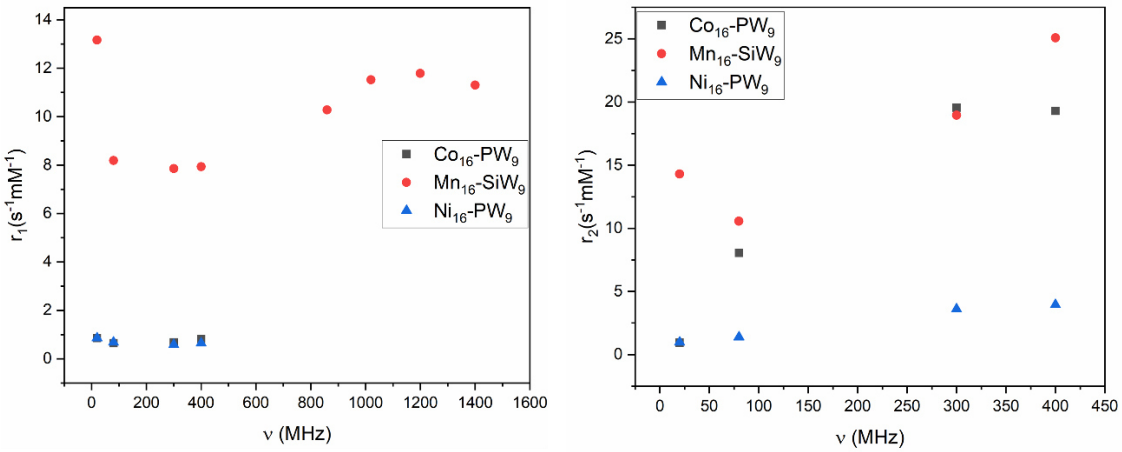


Figure 4.13 PRE measured in form of D_2O: H_2O (90:10) relaxivities for **Mn_{16}-SiW_9**, **Co_{16}-PW_9** and **Ni_{16}-PW_9** dissolved crystals with Larmor frequencies: r_1 relaxivities of **Mn_{16}-SiW_9** up to 1400 MHz and for **Co_{16}-PW_9** and **Ni_{16}-PW_9** up to 400 MHz (left), r_2 relaxivities with increasing Larmor frequencies up to 400 MHz (right).

Longitudinal relaxivity r_1

The longitudinal relaxivity of **Mn_{16}-SiW_9**, **Co_{16}-PW_9** and **Ni_{16}-PW_9** clusters is shown in Figure **4.13.** The largest relaxivities were observed at low magnetic fields. For **Mn_{16}-SiW_9** is at 20 MHz (r_1=13.16 $s^{-1}mM^{-1}$), **Co_{16}-PW_9** is at 80 MHz (r_1=0.85318 $s^{-1}mM^{-1}$), and **Ni_{16}-PW_9** is at 20 MHz (r_1=0.85918 $s^{-1}mM^{-1}$). **Mn_{16}-SiW_9**, after the initial decrease at 20 MHz, becomes field-independent.[237]

The longitudinal relaxivity of **Co_{16}-PW_9** is larger than that of **Ni_{16}-PW_9**; both molecules show a large r_1 value at a lower Larmor frequency. Further increasing the magnetic field results in a slight increase in longitudinal relaxivity. This is due to the rise in population at the electronic d orbitals resulting from crystal field distortions. Among these three molecules, the difference in longitudinal relaxivity might be because of different electronic relaxation times, which were observed for the pure ions, and the total spin contributions of the paramagnetic 3d metal ions.[238]

In these molecules, the major contribution to the longitudinal relaxivity is from the outer-sphere contribution, since there are no exchangeable water molecules within the molecular framework. In the lower magnetic field, the dipole-dipole contribution and Curie spin contribution result in very large relaxivity. Both contributions were modulated by different correlation times, such as rotational, diffusional and electronic correlation times of the molecules. This effect was observed in the longitudinal relaxivity data. The spin-spin coupling of the metal ions within the core also contributes to the hyperfine interaction between the water ^1H and the paramagnetic metal core.[239] The diffusional correlation time of water molecules plays an important role in bringing the water molecules to their closest distance to the paramagnetic centre.[240] The large molecular weight of **M_{16}-XW_9** POM species and the rigid framework of the POM ligand increase its rotational correlation time, which might result in high relaxivity at low magnetic fields. Further studies and modelling of the data are required to gain insight into the PRE parameters that contribute to the relaxivities. In addition, the electronic relaxation times of these molecules could be measured by EPR.

Transverse relaxivity r_2

The study of transverse relaxation in **M_{16}-XW_9** clusters reveals larger values compared to longitudinal relaxivity. All the clusters exhibit an increase in transverse relaxivity with the magnetic field, as shown in Figure **4.13.** Similar to r_1, the major contributions of r_2 were also due to the outer sphere mechanism. The increase in relaxivity results from dipole-dipole interactions due to strong hyperfine interactions between the paramagnetic centres

and the water ^{1}H. The intermediate correlation time also provides larger transverse relaxivity at larger fields.

4.8.2. NMR Relaxivities of 4f-metal Containing POMs

In this section, the structures of lanthanide-containing POMs were first described, followed by the presentation of the PRE studies.

Monolanthanide-substituted mono-Keggin-type POM

The structures of $[Dy^{3+}(H_2O)_4GeW_{11}O_{39}]^{5+}$ (**Dy-W$_{11}$**) and $[Er^{3+}(H_2O)_3GeW_{11}O_{39}]^{5+}$ (**Er-W$_{11}$**), each containing a Dy^{3+} or Er^{3+} ion coordinated to a mono-lacunary Keggin $[GeW_{11}O_{39}]^{8+}$, are shown in Figure **4.14**. In both structures, the lanthanide ion occupies the vacant site created by the removal of one terminal W–O_t unit from the plenary $[GeW_{12}O_{40}]^{4+}$ anion. The only structural difference between these two lanthanide-containing species lies in the number of coordinated water molecules: Dy^{3+} binds four terminal aqua ligands, whereas Er^{3+} binds three, due to the smaller ionic radius of Er^{3+}.[241]

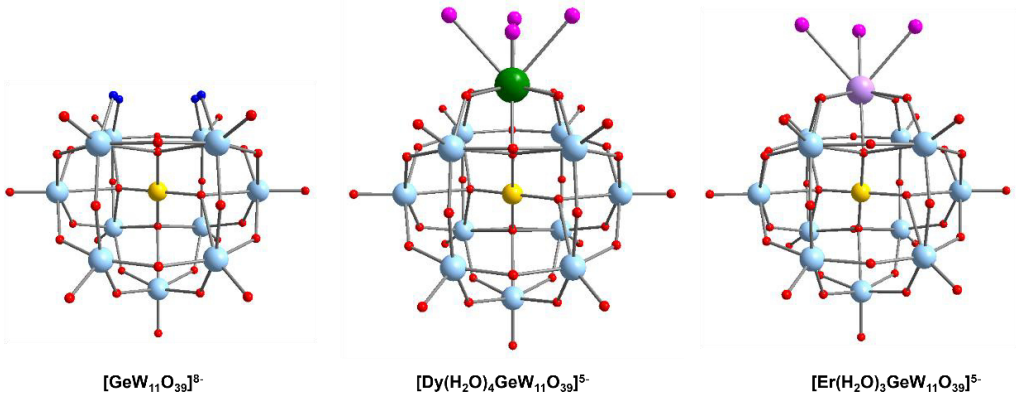


Figure 4.14 Ball-and-stick representation of monolacunary Keggin POM ligand $[GeW_{11}O_{39}]^{8-}$; four oxo ligands that coordinate to paramagnetic metal ions marked as dark blue (left). $[Dy(H_2O)_4GeW_{11}O_{39}]^{5-}$(middle), and $[Er(H_2O)_3GeW_{11}O_{39}]^{5-}$(right). Colour code: Dy^{3+} (green) and Er^{3+} (lavender).

Solution stability studies

ESI-MS analyses of the lanthanide-containing metal clusters (**Dy-W$_{11}$**) and **(Er-W$_{11}$)** demonstrate that both clusters remain stable, with the lanthanide metal ions securely attached to the POM moieties. However, the closed three-dimensional framework of one POM cluster with another via K^+ ion linkers collapse in solution.[241]

Di Er^{3+}- substituted Wells-Dawson type POM

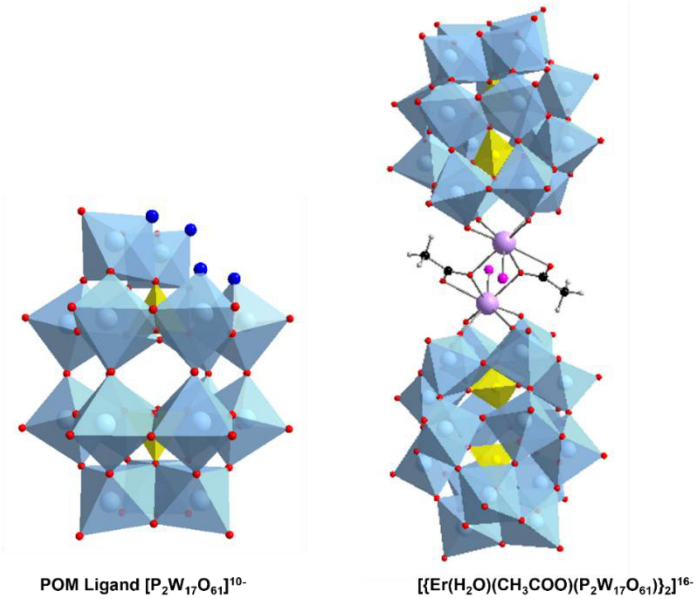


Figure 4.15 Combined polyhedral/ball-and-stick representation of Wells-Dawson POM ligand $[P_2W_{17}O_{61}]^{10-}$ (left) and $[\{Er(H_2O)(CH_3COO)(P_2W_{17}O_{61})\}_2]^{16-}$(right). Colour code: Four oxo ligands that coordinate to paramagnetic metal ions are marked as dark blue and Er^{3+} (lavender).

The anionic $[\{Er^{3+}(H_2O(CH_3COO)(P_2W_{17}O_{61})\}_2]^{16-}$(**$Er_2$-$W_{34}$**) consists of two Er^{3+} containing central cores; $[\{Er(H_2O)(CH_3COO)\}_2]^{4+,}$ which are coordinated with four oxygen atoms between two mono lacunary Wells-Dawson $[P_2W_{17}O_{61}]^{10-}$ anions (Figure **4.15**)**.** These two central Er^{3+} ions are bridged by acetate groups in η^1: η^2: μ^2 fashion. Each Er^{3+} ion forms an eight-coordinated antiprismatic geometry by accepting three oxo ligands from two acetate groups, four oxo ligands from the four coordination sites of the $[P_2W_{17}O_{61}]^{10-}$ monolacunary anion and one from the coordinated water molecule.[242]

Solution stability studies

ESI-MS studies of the Er_2-W_{34} polyanion indicate that it fragments into monomeric species, as reported previously.[242]

To confirm the solution-phase behaviour of the POM under PRE conditions, ESI-MS experiments were conducted on further diluted samples (0.2 mM) directly taken from the NMR tubes used in the relaxivity studies. This allowed evaluation of the stability and speciation of the polyanion under the exact conditions employed for PRE measurements (Figure **4.16**).

The experiment was performed with 1:1 ACN/H_2O. Similar spectra were obtained as reported previously. To minimise excessive fragmentation of the **Er_2-W_{34}** polyanion caused by the conditions used in mass spectrometry, comparatively gentler solution stability analyses were conducted.

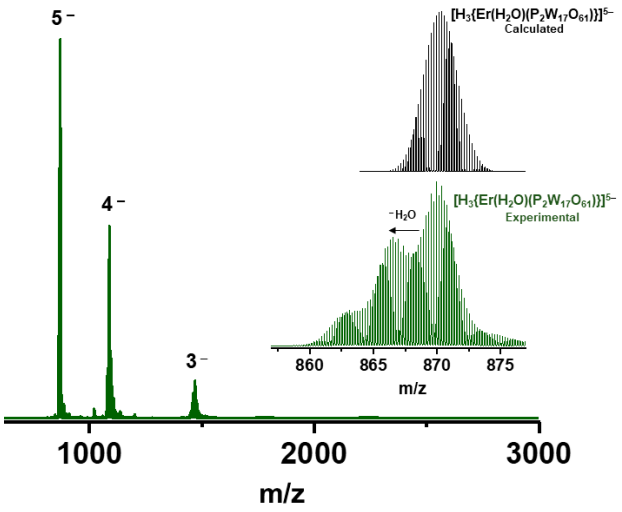


Figure 4.16 Negative ion ESI-MS was performed on the **Er_2-W_{34}** sample at a concentration of 0.2 mM, obtained from the NMR tube and further diluted in a 1:1 ACN/H_2O mixture. The inset highlights the expanded 5^- region, where the observed peaks are compared with their calculated isotope pattern.

Dynamic Light Scattering (DLS) and Zeta Potential (Z-pot) measurements

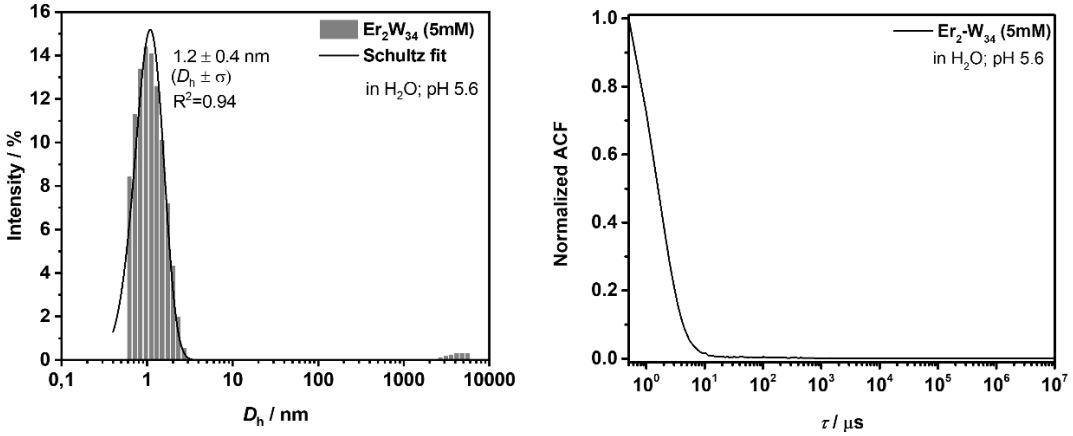


Figure 4.17 DLS Analysis of **Er_2-W_{34}** (5 mM) at pH 5.6 in water; Hydrodynamic diameter (Dh) of **Er_2-W_{34}**, indicating particle size distribution (left). Corresponding normalised autocorrelation function, demonstrating the temporal stability and correlation of particle movement in the dispersion (right).

DLS and Z-pot analysis were employed to examine the colloidal dispersions of **Er_2-W_{34}** (5 mM in distilled water). The hydrodynamic diameter (D_h) of **Er_2-W_{34}** was measured at pH 5.6, the pH used for NMR relaxivity studies, and at pH 7.0 to assess the stability at physiologically relevant pH values. As shown in Figure **4.17** at pH 5.6, **Er_2-W_{34}** exhibited an average D_h of 1.2 ± 0.4 nm with a polydispersity index (PDI) of 0.147, indicating good colloidal stability in water. Comparable stability was observed at pH 7.0 (Figure **4.18**), where the hydrodynamic size remained similar (D_h = 1.3 ± 0.4 nm; PDI = 0.193). However, a second population of particles with a significantly larger mean D_h of 176.6 ± 71.1 nm was also detected. This secondary population is likely due to the aggregation caused by using

the sodium hydroxide solution to adjust the pH, as the presence of positively charged Na^+ ions may promote aggregation through electrostatic interactions.

Zeta potential measurements confirmed the net negative charge of **Er_2-W_{34}** in water. At pH 5.6, the POM exhibited a Z-pot value of -9.0 ± 0.8 mV. At neutral pH, the Z-pot became more negative (-20.4 ± 0.1 mV), which can be attributed to the increased deprotonation of oxygen groups at higher pH levels, contributing to a greater number of negative charges.

Since acetate groups connected the anionic units of **Er_2-W_{34}**, the potential for a change in the aggregation state of POM upon the addition of acid was further investigated using DLS analysis. The acetate linker (pKa of acetic acid = 4.7) was expected to become fully protonated in strongly acidic media (pH 2), losing its coordination ability and potentially inducing significant charges in the aggregation state of POM.

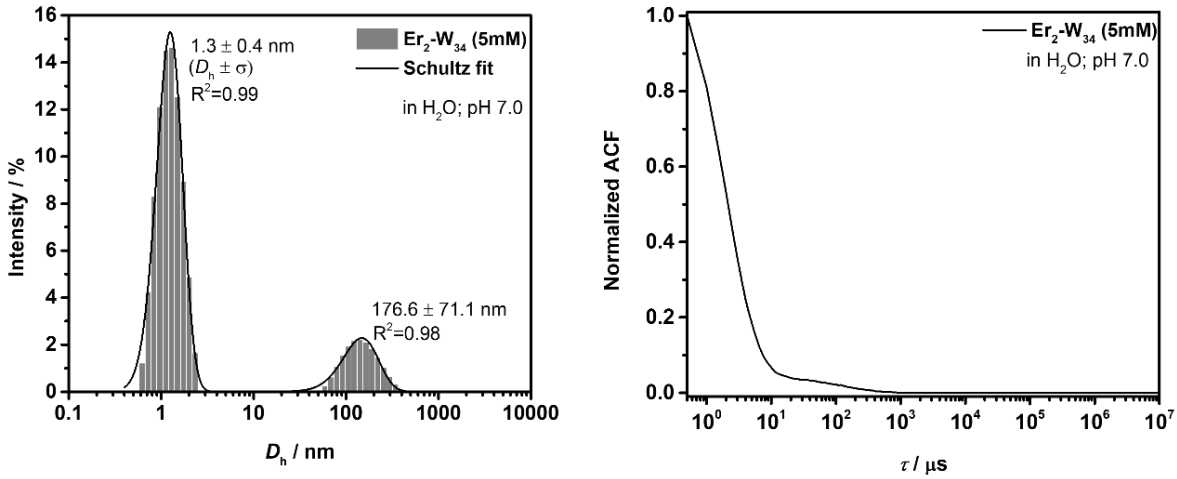


Figure 4.18 DLS Analysis of **Er_2-W_{34}** (5 mM) at pH 7.0 in water; Hydrodynamic diameter (Dh) of **Er_2-W_{34}**, showing the particle size distribution (left). Corresponding normalised autocorrelation function, highlighting the temporal stability and correlation of particle movement in the dispersion (right).

To test this hypothesis, the hydrodynamic diameter (Dh) was measured at pH 5.6 and again 40 minutes after acidification with aqueous HCl (pH 2). As shown in Figure **4.19**, the scattering intensity of the initial population of small particles (Dh ~ 1.2 nm) decreases significantly at pH 2, accompanied by the emergence of a second population of large particles with a Dh of approximately 187 nm. This larger population likely formed due to the degradation of smaller particles, resulting in the generation of large aggregates.

These observations suggest that the dimeric structure of **Er_2-W_{34}** remains stable in water unless the dispersion is acidified to a pH level below 4.7.

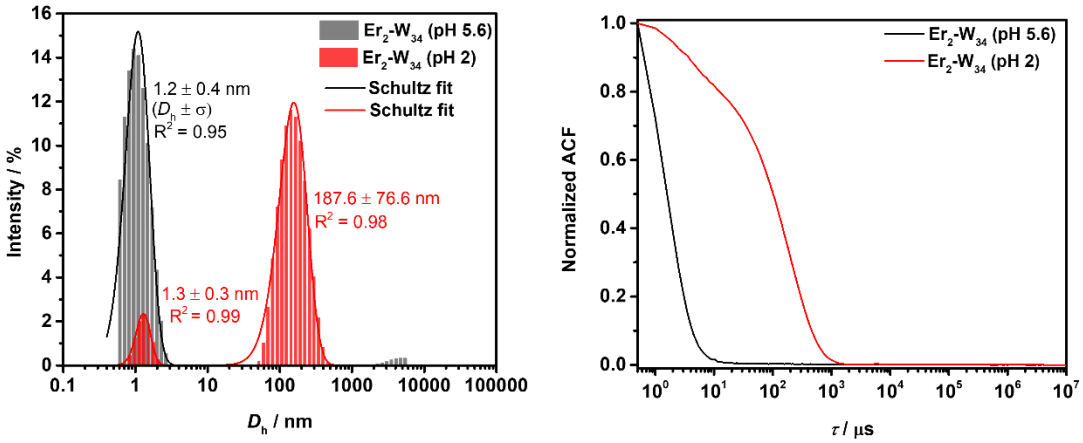


Figure 4.19 DLS Analysis of **Er_2-W_{34}** (5 mM) at Different pH Values: Hydrodynamic diameter (Dh) of **Er_2-W_{34}** at pH 5.6 (grey) and 40 minutes after the addition of aqueous HCl (37%, 3 µL to 500 µL of sample) at pH 2 (left). Corresponding normalised autocorrelation function, illustrating changes in particle behaviour and stability under different pH conditions (left).

ATR-FTIR spectroscopy

ATR-FTIR spectroscopy was performed on a dried **Er_2-W_{34}** sample obtained by evaporating the aqueous solvents. The ATR-FTIR spectra (Figure **A.4.3**) of the recovered **Er_2-W_{34}** exhibited the expected absorption bands characteristic of the pristine POM. The two spectra showed perfect alignment, with no observed wavenumber shift, confirming the stability of **Er_2-W_{34}** in solution.

Xylenol orange Test

In addition to the instrumental analysis to assess the integrity of **Er_2-W_{34}** in solution, a quick visual Xylenol orange test was performed to detect the presence of free Er^{3+} ions (Figure **A.4.4**). The Xylenol orange test provides a method for evaluating the amount of free metal ions and ligands in the solution that undergoes a colour change from orange to violet, which can be visually detected.

No Colour change was observed upon the addition of Xylenol orange (30 µL) to the **Er_2-W_{34}** solution (pH 5.6) used for NMR relaxivity studies, indicating that Er^{3+} ions do not leach into the solution. In contrast, a violet colour appeared when Xylenol orange was added to an **Er_2-W_{34}** solution containing approximately 2 mg of $Er(NO_3)_3{\cdot}6H_2O$, which serves as a source of free Er^{3+} ions.[243]

Dilanthanide-substituted di-Keggin type POM

The anionic structure $[\{Ln(CH_3COO)(GeW_{11}O_{39})(H_2O)\}_2]^{12-}$ (**Ln-W_{11}**), Ln = Gd^{3+}, Dy^{3+}, Er^{3+}; consists of two Ln^{3+} ions in the central core, as $[\{Ln(H_2O)(CH_3COO)\}_2]^{4+}$. The central metal

core was coordinated with four oxygen atoms between two mono-lacunary Keggin $[GeW_{11}O_{39}]^{8-}$ anions (Figure **4.20**). These two central Ln^{3+} ions are bridged by acetate groups in η^1: η^2: μ^2 fashion. Each Ln^{3+} ion forms an eight-coordinated antiprismatic geometry by accepting three oxo ligands from two acetate groups, four oxo ligands from the four coordination sites of the $[GeW_{11}O_{39}]^{8-}$ monolacunary anion, and one from the coordinated water molecule.[244]

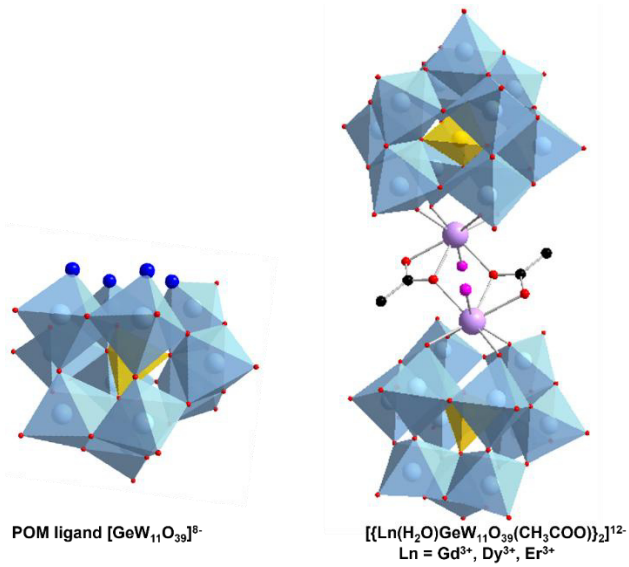


Figure 4.20 Combined polyhedral/ball-and-stick representation of Keggin POM ligand $[GeW_{11}O_{39}]^{8-}$ (left). $[\{Ln(CH_3COO)(GeW_{11}O_{39})(H_2O)\}_2]^{12-}$, Ln = Gd^{3+}, Dy^{3+}, Er^{3+}(right).

NMR relaxivity of lanthanide-containing POMs

The paramagnetic relaxation enhancement of the molecules **Dy-W$_{11}$**, **Er-W$_{11}$**, **Er$_2$-W$_{34}$**, **Er$_2$-W$_{22}$**, **Gd$_2$-W$_{22}$**, and **Dy$_2$-W$_{22}$** was investigated. Longitudinal (T_1) and transverse (T_2) relaxation measurements were performed at ^{1}H Larmor frequencies ranging from 20 MHz to 1.4 GHz, as detailed in the experimental section of this chapter.

For these studies, pure POM crystals were dissolved in a 9:1 D_2O/H_2O mixture, and dilutions of 0, 0.2, 0.4, 0.6, 0.8, and 1 mM were prepared. The clusters were fully soluble, forming clear aqueous solutions that remained stable throughout the NMR measurements. Due to the limited availability of a high-power (24 MW) resistive magnet (≥ 800 MHz), only the 1, 0.6, 0.2, and 0 mM samples were measured.

Inversion recovery, progressive saturation recovery, and CPMG multi-echo pulse sequences were used to determine T_1 and T_2 values, respectively. All compounds exhibited monoexponential relaxation, which remained unchanged over several weeks, indicating that the cluster solutions were stable and no phase separation occurred.

Relaxation rates (R_1 and R_2) were determined as a function of cluster concentration. At each magnetic field, a linear relationship was observed, consistent with homogeneous solutions. Longitudinal relaxivity (r_1) and transverse relaxivity (r_2) were calculated from the slopes of these linear fits. For these studies, concentrations were based on the entire cluster rather than individual paramagnetic ions, treating the 4f-POM molecule as a single magnetic entity that interacts with surrounding ^{1}H nuclei, similar to a conventional contrast agent.

The relaxivity behaviour of 4f-POM clusters reflects the influence of paramagnetic lanthanide centres embedded in a diamagnetic POM ligand. Hyperfine interactions between the paramagnetic ions and neighbouring protons, along with other molecular dynamics, modulate the relaxation properties. The following section presents a detailed comparison of different POM clusters containing various 4f ions and the factors affecting their paramagnetic relaxation enhancement at the molecular level.

Longitudinal relaxivity r_1

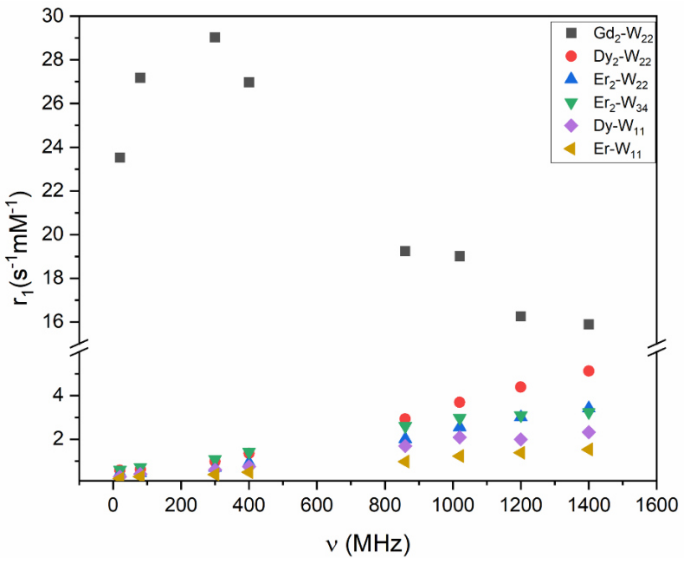


Figure 4.21 PRE as measured by longitudinal relaxivities r_1 of ^{1}H water with POM metal clusters (**Dy-W$_{11}$**, **Er-W$_{11}$**, **Er$_2$-W$_{34}$**, **Er$_2$-W$_{22}$**, **Gd$_2$-W$_{22}$** and **Dy$_2$-W$_{22}$**) as a function of the Larmor frequency.

The longitudinal relaxivity r_1 of **Dy-W$_{11}$**, **Er-W$_{11}$**, **Er$_2$-W$_{34}$**, **Er$_2$-W$_{22}$**, **Gd$_2$-W$_{22}$**, and **Dy$_2$-W$_{22}$** were measured across a wide range of ^{1}H Larmor frequencies (20 MHz–1.4 GHz), as shown in Figure **4.21**. For all clusters except **Gd$_2$-W$_{22}$**, r_1 increases monotonically with field, with **Dy$_2$-W$_{22}$** exhibiting the highest values among the non-Gd systems at high field. In contrast, **Gd$_2$-W$_{22}$** displays exceptionally high r_1 values at low field (≈26–29 s^{-1} mM^{-1}) with only weak field dependence up to ~400 MHz, followed by a gradual decrease in relaxivity at ultra-high fields (>800 MHz). Despite this decline, **Gd$_2$-W$_{22}$** consistently shows the highest r_1 across the entire frequency range, greatly surpassing the other 4f–POM clusters. These trends reflect the strong influence of the lanthanide ion's magnetic properties, particularly the large,

isotropic magnetic moment of Gd^{3+} compared to the more anisotropic Dy^{3+} and Er^{3+}, as well as the number of paramagnetic centres within each POM framework.

Factors governing longitudinal relaxivity behaviour of 4f–POM clusters

The longitudinal relaxivity (r_1) of 4f–POM clusters was determined by a combination of structural, dynamic, and electronic parameters. These influence the paramagnetic relaxation enhancement (PRE) through mechanisms involving water exchange, molecular tumbling, and the intrinsic magnetic properties of the lanthanide ions.

Nature of the paramagnetic ion

Table 4.6 Magnetic properties of non-interacting lanthanide ions.

Ln^{3+}	Gd^{3+}	Dy^{3+}	Er^{3+}
Free ion ground state term $^{2S+1}L_j$	$^8S_{7/2}$	$^6H_{15/2}$	$^4I1_{5/2}$
S	7/2	5/2	3/2
L	0	5	6
J	7/2	15/2	15/2
g - factor	7/2	4/3	6/5
$\mu_{eff=gJ\mu B\sqrt{J(J+1)}}$	13.9	10.6	9.6
χ_T expected value for non-interacting ions per complex (cm^3Kmol^{-1})	7.87	14.7	11.5

The intrinsic magnetic properties of lanthanide ions (Gd^{3+}, Dy^{3+}, Er^{3+}) play a critical role in r_1 relaxivity. Gd^{3+}, with its isotropic electronic ground state and long electronic relaxation times, generally provides higher relaxivity, particularly at low and intermediate magnetic fields. Dy^{3+} and Er^{3+}, with strong magnetic anisotropy, can enhance relaxivity at higher fields but may reduce it at lower fields due to faster electronic relaxation. [245] The magnetic moments of these ions (Gd^{3+}: 13.9 μB; Dy^{3+}: 10.6 μB; Er^{3+}: 9.6 μB) further influence the observed relaxivities, with dimerised species (**Er_2-W_{22}**, **Er_2-W_{34}**, **Dy_2-W_{22}**, **Gd_2-W_{22}**) showing roughly double the magnetic moment and correspondingly higher r_1 values compared to monomeric species (**Er-W_{11}**, **Dy-W_{11}**) (Table **4.6**).

Cluster nuclearity, geometry, and size

The number of paramagnetic centres per cluster and their spatial arrangement determine the total paramagnetic moment and the efficiency of dipolar interactions with water protons. Dinuclear clusters (e.g., **Er_2-W_{22}**, **Dy_2-W_{22}**) often display higher relaxivity than mononuclear

species (e.g., **Dy-W$_{11}$**, **Er-W$_{11}$**) due to increased unpaired electron density and additive dipolar contributions. Similarly, the overall size (Figure **4.22**) of the molecule affects rotational dynamics: larger clusters, such as **Ln$_2$-W$_{34}$**, tumble more slowly, enhancing r_1 at higher fields through improved coupling of nuclear and electronic spins. However, larger frameworks may also restrict water exchange, highlighting the need to balance size and accessibility.

Water accessibility and exchange rate

The presence, number, and positioning of inner-sphere water molecules are crucial for the PRE. For example, **Dy-W$_{11}$** has four exchangeable water ligands, while **Er-W$_{11}$** has three, which correlates with higher relaxivity for **Dy-W$_{11}$**. In larger clusters such as **Ln$_2$-W$_{22}$** and **Er$_2$-W$_{34}$**, in contrast, for **Ln$_2$-W$_{22}$** and **Er$_2$-W$_{34}$**, there is only one aqua ligand coordinated to each lanthanide. This is likely to affect the observed PRE (Figure **4.22**). In these molecules, the bulky POM ligands may limit accessibility, impacting the observed r_1 values Fast exchange rates facilitate efficient transfer of relaxation enhancement to bulk water, while restricted access or slow exchange rates reduce relaxivity.

Magnetic field dependence

Relaxivity varies with Larmor frequency due to the interplay between rotational correlation times (τ_R), electronic relaxation rates (T_e (s)), and magnetic field strength. Relaxivity studies of free Gd^{3+} ions in aqueous solution reveal a plateau at high fields, starting from 20 MHz. This behaviour occurs because, for free Gd^{3+} ions in an aqueous solution, the rotational correlation time (τ_R) predominates over the dipolar contribution For Gd^{3+} aqua ions, the correlation times follow this order: $\tau_R < \tau_M < \tau_e$.[246] In the relaxivity study of **Gd$_2$-W$_{22}$**, there is a slight decrease in relaxivity at higher magnetic fields, which can be attributed to the variations in correlation time specific to the **Gd$_2$-W$_{22}$** cluster. This trend was also observed in previous studies of Gd^{3+}containing metal clusters.[247,248]

Most clusters show increasing r_1 with the field due to improved matching between the proton Larmor frequency and the electron relaxation dynamics. However, **Gd$_2$-W$_{22}$** exhibits a slight decrease in relaxivity at ultra-high fields, likely due to the slower modulation of the electron–nucleus dipolar interaction, which limits its efficiency at very high frequencies.

Dynamic and structural contributions

The combined effects of molecular size, rotational tumbling, and cluster nuclearity were evident when comparing **Er-W$_{11}$**, **Er$_2$-W$_{22}$**, and **Er$_2$-W$_{34}$** (Figure **4.22**). Despite identical

paramagnetic ions, the largest cluster, **Er_2-W_{34}**, shows the highest r_1 due to slower tumbling rates. Similarly, dimerisation in sandwich-type clusters may effectively double the magnetic moment, further enhancing relaxivity.

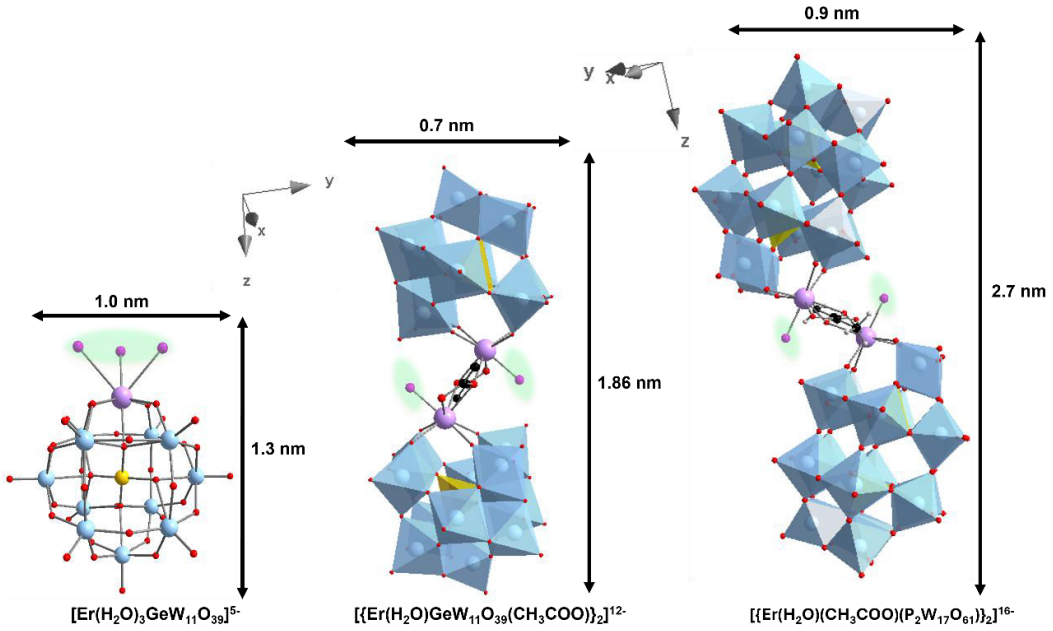


Figure 4.22 Comparing the molecular size and water molecules in the structural framework of metal clusters between **Ln-W_{11}**, **Ln_2-W_{34}**, and **Ln_2-W_{22}**. The position of the water molecules is highlighted in green.

In summary, the r_1 of 4f-POM clusters depend on the number of exchangeable water molecules, the size and rotational dynamics of the cluster, and the magnetic properties of the Ln^{3+} ions. Larger clusters or those containing paramagnetic ions with higher magnetic moments (i.e., more unpaired electrons or multiple paramagnetic centres) usually exhibit higher relaxivity; however, limited water access or steric hindrance can reduce this effect.

Transverse relaxivity r_2

Determining the transverse relaxivity (r_2) is as important as longitudinal relaxivity (r_1), especially in the context of using magnetic clusters as contrast agents. This significance stems from the effect of transverse relaxivity, which can result in negative image contrasts. As the magnetic field increases, r_2 values are typically much higher than r_1 values. In this study, measurements of r_2 at very high magnetic fields (above 800 MHz) were not performed due to the large T_2 values of the complexes, which exceeded the field fluctuations of the resistive magnet.

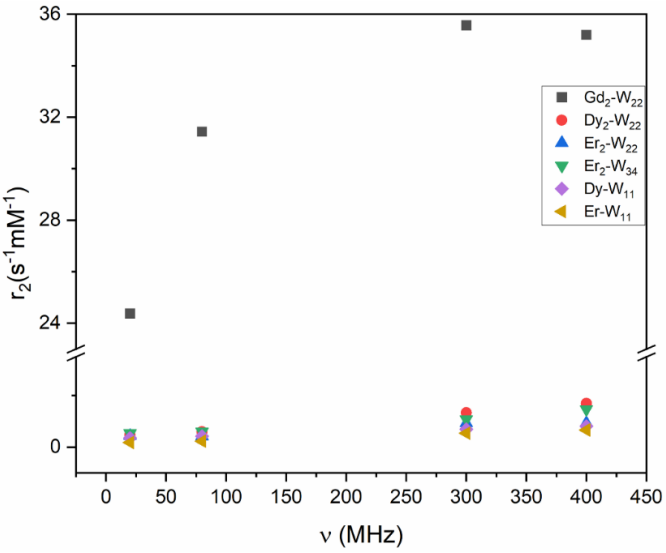


Figure 4.23 PRE as measured by transverse relaxivities r_2 of ^{1}H water with POM metal clusters (**Dy-W$_{11}$**, **Er-W$_{11}$**, **Er$_2$-W$_{34}$**, **Er$_2$-W$_{22}$**, **Gd$_2$-W$_{22}$** and **Dy$_2$-W$_{22}$**) as a function of the Larmor frequency.

Among the studied POM clusters, all paramagnetic metal-containing complexes exhibited a monotonically increasing transverse relaxivity with increasing fields, except for **Gd-W$_{22}$**. At 400 MHz, these clusters demonstrated higher r_2 values compared to their r_1 (Figure **4.23**). In the case of **Gd-W$_{22}$**, the transverse relaxivity reached its maximum at 300 MHz and then decreased at 400 MHz.

The r_2 value is proportional to the square of the magnetic moment of the lanthanide. This explains why the r_2 value of Gd^{3+} containing clusters is higher than that of Dy^{3+} and Er^{3+}. Like longitudinal relaxivity, transverse relaxivity also depends on the number of paramagnetic centres within the molecule. This is evident from the higher r_2 value of **Dy$_2$-W$_{22}$** compared to **Dy-W$_{11}$**. Furthermore, a comparison of **Er$_2$-W$_{34}$**, **Er$_2$-W$_{22}$**, and **Er-W$_{11}$** indicates that the PRE-induced transverse relaxivity (r_2) of POM metal complexes also rely on the number of paramagnetic centres in the molecule.

Additionally, the r_2 values of **Er$_2$-W$_{34}$** and **Er$_2$-W$_{22}$** show deviations from linear field dependence above 300 MHz. This behaviour was consistent with an increasing contribution from Curie spin to the relaxivity, which has a quadratic field dependence and is enhanced in larger molecules at high magnetic fields. At 400 MHz, the r_2 value of **Er$_2$-W$_{22}$** begins to decline, possibly due to the different diffusional and rotational correlation times of the POM clusters in the solution.

4.8.3. NMR Relaxivities of Heterometallic 3d-4f Containing POMs

Structure of the molecule

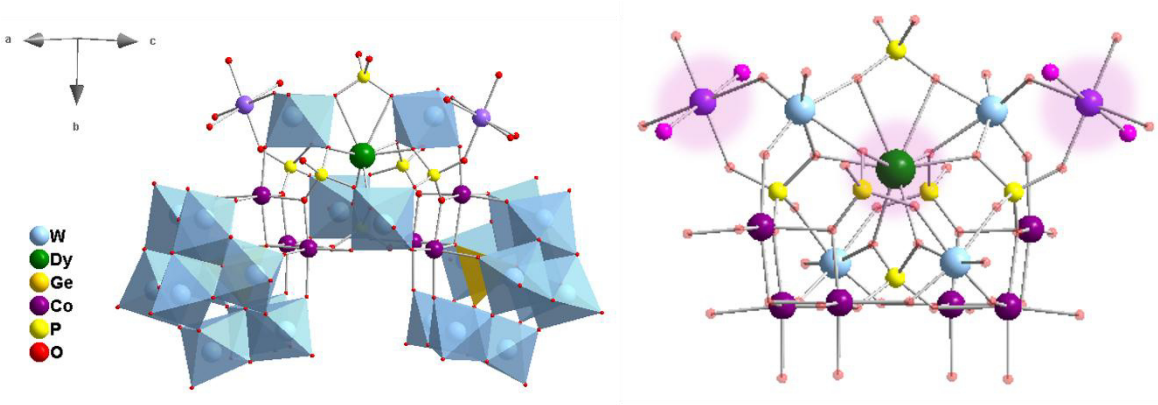


Figure 4.24 A single unit of (**$Co_7Ln_xNa_{1-x}$-GeW_9**), two trilacunary Keggin species were connected to the central lanthanide unit through three Co^{2+} ions. The Ln^{3+} ions were located at the centre and are connected to six phosphate ions (left). Central metal core, which includes all paramagnetic ions (3d and 4f) without two Keggin ion units. The two cobalt ions from a connection with another single unit are labelled in Lavender.

The heterometallic 3d-4f containing POMs $[(W_9GeO_{34})_2(WO_3)_4(PO_4)_6Co_6(Ln_x^{3+}/Na_{1-x})(Co_y^{2+}/Na_{1-y})]n-$ (where Ln^{3+} = Dy^{3+}, Gd^{3+}, Y^{3+}), which are denoted as **$Co_7Ln_xNa_{1-x}$-GeW_9**, consist of two trilacunary Keggin fragments, each stabilised by three cobalt ions to form $\{Co_3GeW_9O_{34}\}$ units. These two subunits were connected through a central cluster built around a disordered Ln^{3+}/Na^+ site. The Ln/Na centre was further coordinated by six phosphate anions and four tungsten oxide octahedra, while two additional disordered Co^{2+}/Na^+ positions serve as linkers between the fragments. Altogether, this arrangement generates a heterometallic polyoxometalate framework in which the two $\{Co_3GeW_9\}$ units were bridged by the Ln/Na-phosphate-tungstate-cobalt/Na cluster, resulting in a stable and architecturally complex assembly. Additionally, a mixed-occupancy Co/Na site (50:50) functions as a linker, connecting the individual molecular units into a one-dimensional chain. This connectivity gives rise to a linear assembly in which the molecules were bridged alternately by Co^{2+} ions and Co/Na linker sites (Figures **4.24 and 4.25**). The detailed crystallographic parameters and bonding interactions of this cluster are presented in Section **3.3.1** of this thesis.

The molecular formula for the 3d-4f-POM clusters used for the NMR relaxivity studies is as follows:

1. $Na_{21.5}Cs_{1.3}[(W_9GeO_{34})_2(WO_3)_4(PO_4)_6Co_6(Dy_{0.3}/Na_{0.7})(Co_{0.6}/Na_{0.4})]\cdot 75H_2O$

   ($Co_7Dy_{0.3}Na_{0.7}$-GeW_9)

2. $Na_{21.7}Cs_{1.7}[(W_9GeO_{34})_2(WO_3)_4(PO_4)_6Co_6(Gd_{0.1}/Na_{0.9})(Co_{0.5}/Na_{0.5})]\cdot 75H_2O$

   ($Co_7Gd_{0.1}Na_{0.9}$-GeW_9)

3. $Na_{21.65}Cs_{1.5}[(W_9GeO_{34})_2(WO_3)_4(PO_4)_6Co_6(Y_{0.3}/Na_{0.7})(Co_{0.5}/Na_{0.5})]\cdot 75H_2O$

   ($Co_7Y_{0.3}Na_{0.7}$-GeW_9)

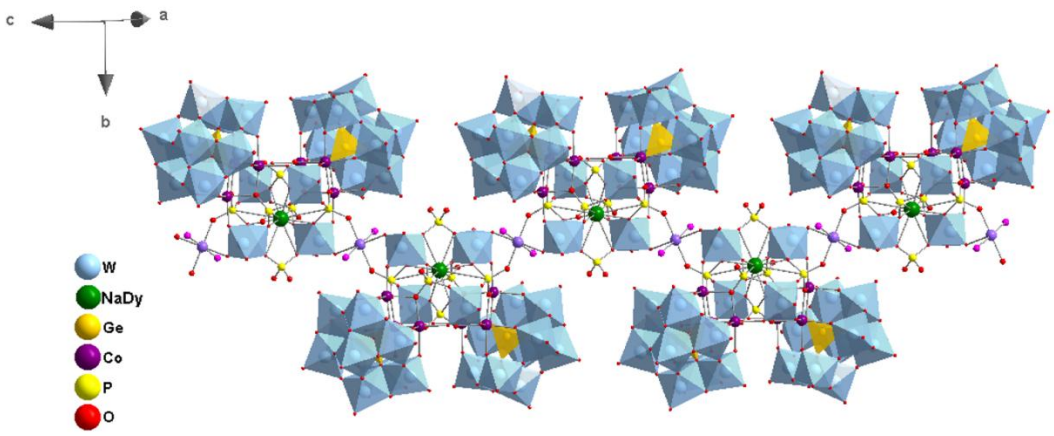


Figure 4.25 The Co^{2+} ions connect every single unit and form an ID chain. The Co^{2+}/Na^{+} linkages are shown in lavender colour.

NMR relaxivity studies

Relaxivity studies of the Co7LnxNa1-x-GeW9 cluster, which contains various lanthanides such as Gd3+, Dy^{3+} and $Y^{3+,}$ help to explain the behaviour of PRE in different magnetic fields. This provides insight into the cooperative magnetic effects of the different paramagnetic ions in the molecules and the dependence of the molecular framework and ion arrangements on PRE behaviour.

For the current studies, five sets of dilutions were prepared from **$Co_7Dy_{0.3}Na_{0.7}$-GeW_9** (0.2, 0.4, 0.6, 0.8, 1 mM) and three dilutions were prepared from **$Co_7Gd_{0.1}Na_{0.9}$-GeW_9**, and **$Co_7Y_{0.3}Na_{0.7}$-GeW_9** (0.3, 0.5, 1 mM) with 9:1 D_2O/H_2O. The NMR relaxation measurements of these dilutions with each magnetic field showed a linear dependence on the concentration.

The longitudinal and transverse relaxivity vs magnetic field of these materials were shown in Figure **4.26**.

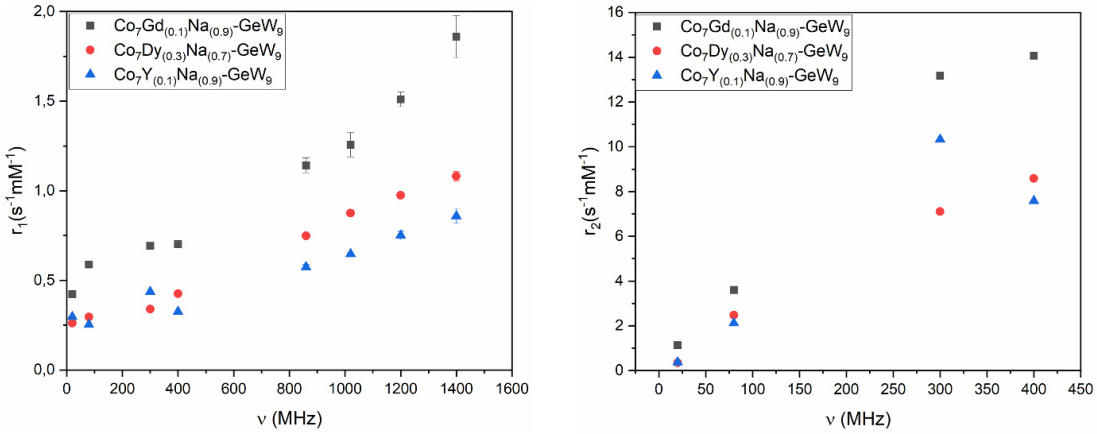


Figure 4.26 The longitudinal (left) and transverse (right) relaxivity vs magnetic field of (**$Co_7Gd_{0.1}Na_{0.9}$-GeW_9**), (**$Co_7Dy_{0.3}Na_{0.7}$-GeW_9**) and (**$Co_7Y_{0.3}Na_{0.7}$-GeW_9**).

Longitudinal relaxivity (r_1)

The longitudinal relaxivity (r_1) values increase with increasing magnetic field strength for all three clusters. Among them, **$Co_7Gd_{0.1}Na_{0.9}$-GeW_9** shows the highest r_1 values across the field range, followed by **$Co_7Dy_{0.3}Na_{0.7}$-GeW_9**, while **$Co_7Y_{0.1}Na_{0.9}$-GeW_9** exhibits the lowest. This trend highlights the stronger paramagnetic contribution of Gd^{3+} compared to Dy^{3+} and the diamagnetic nature of Y^{3+}. Interestingly, although Dy^{3+} has a higher occupancy (0.3 vs. 0.1 for Gd^{3+}), its r_1 values are lower, which can be attributed to its fast electronic relaxation that diminishes the efficiency of proton relaxation. In contrast, Y^{3+}, being diamagnetic, contributes negligibly to relaxation, so its relaxivity arises primarily from the Co^{2+} ions and structural effects.

The field-dependent behaviour of **$Co_7Ln_xNa_{1-x}$-GeW_9** clusters differs from the typical field-independent nature observed in Gd^{3+} and Co^{2+} ions in aqueous solution.[238,249] The influence of Gd^{3+}, Dy^{3+}, and Y^{3+} ions, along with the paramagnetic Co^{2+} ions, was reflected in the overall shift of the longitudinal relaxivity plot. These observations indicate that the 3d-4f clusters behave as a unified entity rather than as individual, independent ions.

Although the clusters show increased longitudinal relaxivity with applied magnetic fields, the enhancement was less pronounced than expected from paramagnetic relaxation enhancement (PRE) studies of aqueous Gd^{3+}, Dy^{3+}, and Co^{2+} ions. This behaviour can be attributed to the structural characteristics of these 3d-4f POM clusters. Metal disorder at the central positions (Gd: Na = 10:90, Dy: Na = 30:70) and partial occupancy of the linking Co^{2+} ions (Co: Na = 50:50) likely reduce the overall magnetic moments. The limited number of exchangeable water sites further diminishes the PRE effect.

In these structures, lanthanide ions were centrally located and coordinated by six phosphate groups, minimising interactions with outer-sphere water molecules. While the bridging Co^{2+} ions contribute two water ligands, their occupancy was low. The two Co_3 triangles, which were the key paramagnetic components, lack directly coordinated water ligands. Additionally, potential agglomeration of the clusters in aqueous solution may also contribute to the lower relaxivity.

These observations highlight the need for extended solution studies to evaluate structural stability and for modelling relaxivity across various magnetic fields to better understand the underlying mechanisms.

Transverse relaxivity r_2

In the present studies, **$Co_7Dy_{0.3}Na_{0.7}$-GeW$_9$** and **$Co_7Gd_{0.1}Na_{0.9}$-GeW$_9$** show a linear dependence on magnetic field strength. However, **$Co_7Y_{0.3}Na_{0.7}$-GeW$_9$** exhibits a sharp decrease after reaching 300 MHz. Notably, the highest transverse relaxivity was observed for **$Co_7Gd_{0.1}Na_{0.9}$-GeW$_9$**. Both **$Co_7Dy_{0.3}Na_{0.7}$-GeW$_9$** and **$Co_7Y_{0.3}Na_{0.7}$-GeW$_9$** demonstrate a similar trend as r_1 across all magnetic fields, while a steady increase was noted for **$Co_7Dy_{0.3}Na_{0.7}$-GeW$_9$**. The transverse relaxation data also indicate that the paramagnetic relaxation enhancement (PRE) induced transverse relaxivity (r_2) of the POM metal complexes depends on the number of paramagnetic centres present in the molecules. Similar to r_1, the overall shift in values reflects the influence of paramagnetic lanthanide ions, which was confirmed by the differentiation of diamagnetic Y^{3+} in (**$Co_7Y_{0.3}Na_{0.7}$-GeW$_9$**). Further systematic studies are required to understand the complex behaviour of these POM metal clusters, including their solution stability and the underlying microscopic mechanisms responsible for the observed PRE.

4.8.4. Ageing and Structural Changes of Lanthanide Containing-POM Affecting NMR Relaxivity

Molecular structure

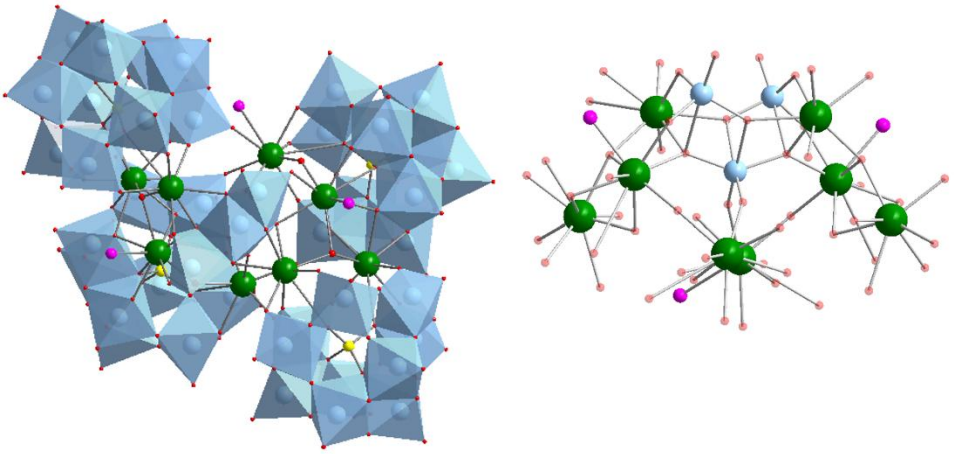


Figure 4.27 Combined polyhedral/ball and stick representation of $[Ln_8O_4(H_2O)_3(PW_{10}O_{37})_4(W_3O_{12})]^{26-}$ (**Ln_8-PW_{10}**) Ln^{3+} = Dy^{3+}, Gd^{3+}, Ho^{3+}, Er^{3+}, Y^{3+} (left), ball and stick representation of eight Ln^{3+} containing central core with exchangeable water molecules (right).

The POM cluster $[Ln_8O_4(H_2O)_3(PW_{10}O_{37})_4(W_3O_{12})]^{26-}$ (**Ln_8-PW_{10}**; Ln = Dy^{3+}, Gd^{3+}, Ho^{3+}, Er^{3+}, Y) is one of the reported high-nuclearity lanthanide POM structures.[250] It consists of eight lanthanide ions in the core, arranged into two separate Ln_4^{3+} units that are bridged by a chain of three tungsten atoms (Figure **4.27**). The lanthanide core is further stabilised and encapsulated by four dilacunary $[PW_{10}O_{37}]^{7-}$ Keggin ion units.

The very high total electronic spin of the eight Ln^{3+} ions, together with the large molecular weight and the presence of three exchangeable water molecules directly bound to the lanthanide ions, makes these clusters promising PRE agents and interesting to study and compare their NMR relaxivity behaviour.

Sample preparation for the PRE studies

To prepare the sample for PRE studies, pure crystals of **Ln_8-PW_{10}** were dissolved in a D_2O/H_2O (90/10) mixture, and a 1 mM stock solution was prepared. This solution was then diluted to lower concentrations (0.1, 0.2, 0.4, 0.6, 0.8, and 1 mM).

Relaxation rate measurements

Longitudinal (R_1) and transverse (R_2) relaxation rates of **Gd_8-PW_{10}**, **Dy_8-PW_{10}**, **Er_8-PW_{10}**, **Ho_8-PW_{10}**, and **Y_8-PW_{10}** clusters were measured at different concentrations and magnetic fields (20, 80, 300, and 400 MHz). Both R_1 and R_2 increased with increasing magnetic field strength. However, in both cases, an offset was observed between the solvent and the

lowest concentration (0.2 mM). This linear dependence with an offset is considered a deviation from the usual PRE behaviour.

To investigate this deviation, the relaxation studies of **Gd_8-PW_{10}** were analysed in more detail. The longitudinal and transverse relaxation rates of **Gd_8-PW_{10}** as a function of concentration at different magnetic fields are shown in Figure **4.28.**

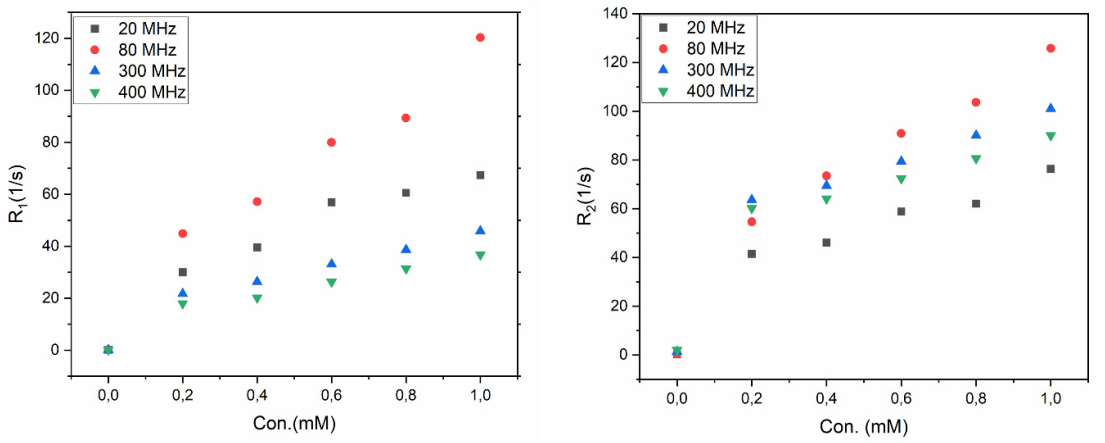


Figure 4.28 Relationship of relaxation rate with concentration with an offset, Longitudinal relaxation rate vs concentration (left), Transverse relaxation rate vs concentration (right).

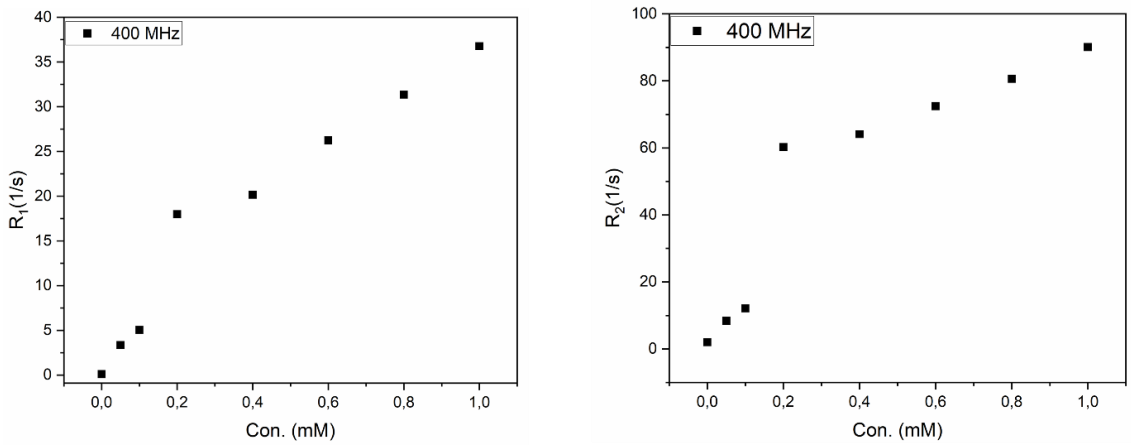


Figure 4.29 The longitudinal and transverse relaxation rate of **Gd_8-PW_{10}** vs concentration (with additional 0.05 and 0.1 mM).

To rule out the offset, lower concentrations (0.05 and 0.1 mM) of the **Gd_8-PW_{10}** clusters were prepared. Relaxation studies with these concentrations were performed at 400 MHz (Figure **4.29**). A substantial deviation from linearity was visible even at low concentrations, where the relaxation rates approached the solvent. Several longitudinal and transverse experiments were conducted with the same **Gd_8-PW_{10}** samples, as well as with freshly prepared samples. The data obtained from these repeated experiments indicate that the relaxation rate value was inconsistent over time.

Exploring potential structural changes of Ln_8-PW_{10} in solution

The POMs are known to be soluble and stable in aqueous and polar solvents.[251] Most structural characterisation of these materials is performed before dissolution. Due to the rapidly growing application of POM materials in solution, it is relevant to determine the solution behaviour and speciation profile of these materials.[252] Numerous techniques are used for the solution characterisation of POM, such as NMR spectroscopy, ESI-MS, and small-angle X-ray Scattering (SAXS).[252]

To investigate the reason behind the observed offset in PRE measurements, the solution stability of the **Ln_8-PW_{10}** cluster was studied. For these studies, the diamagnetic **Y_8-PW_{10}** analogue was selected to perform solution NMR experiments, providing a model system comparable to **Gd_8-PW_{10}**

^{31}P NMR spectroscopy

^{31}P NMR spectroscopy was carried out with $[Y_8O_4(H_2O)_3(PW_{10}O_{37})_4(W_3O_{12})]^{26-}$ (**Y_8-PW_{10}**) cluster. Since this molecule contains phosphorus as the heteroatom, ^{31}P NMR was the reliable technique to identify the species in solution. Figure **4.30** shows that the two types of phosphorus are present in the crystal structure. So, it is expected to have two peaks in the ^{31}P NMR spectra. According to the literature, the chemical shift range is between -15 to -2 ppm for Keggin ion POM species with phosphorus as the heteroatom.[253]

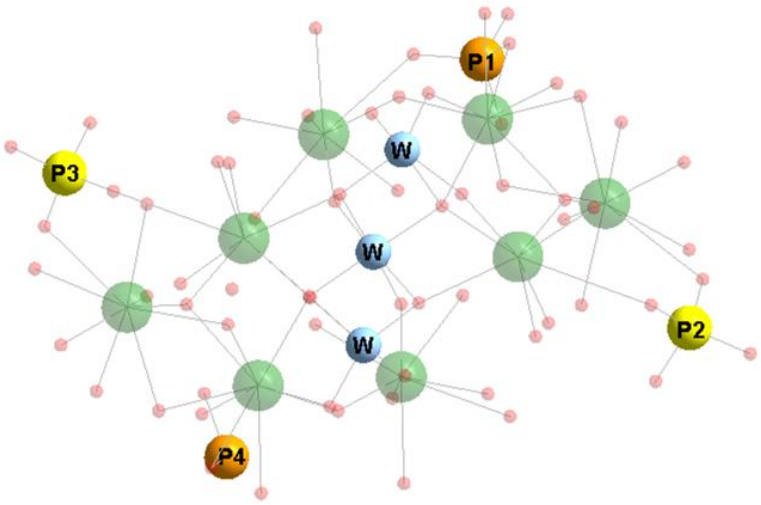


Figure 4.30 The structure includes two types of phosphorus. P1 and P4 are one type and are labelled in orange, while P2 and P3 are another type and are labelled in yellow.

A comparative ^{31}P NMR study was conducted to evaluate differences between fresh and aged **Y_8-PW_{10}** samples. Fresh solutions of **Y_8-PW_{10}** were prepared in concentrations of 0.1, 0.2, 0.4, 0.6, 0.8, and 1 mM, using a mixture of D_2O and H_2O (90/10). ^{31}P NMR spectroscopy

was performed immediately after preparation. Figure **4.31** displays the ^{31}P NMR spectra for both the fresh and aged samples across all concentrations. In both sets of samples, two prominent peaks were observed. Additionally, an extra peak appeared at lower chemical shifts in the spectra of the aged samples. The integral signals were higher for the fresh samples compared to the aged ones.

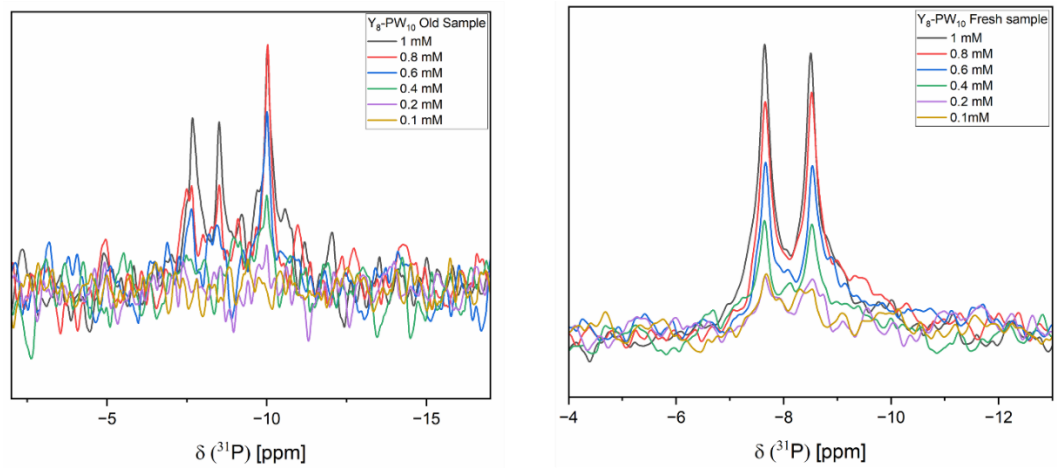


Figure 4.31 ^{31}P spectra of various concentrations of **Y_8-PW_{10}**, aged sample (left), fresh sample (right).

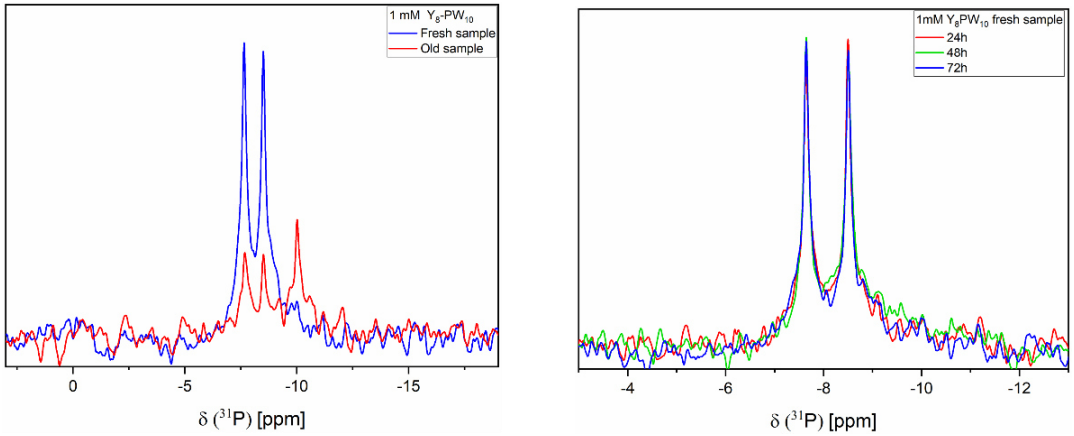


Figure 4.32 ^{31}P spectra of 1mM **Y_8-PW_9**, comparison of fresh and aged samples. The spectra of the aged sample show an additional peak in the lower chemical shift region (left). Periodic ^{31}P spectra of freshly prepared 1 mM **Y_8-PW_9**. The spectra remained static for up to 72 hours (right).

The differences in peak intensities between fresh and aged samples, as well as the emergence of additional peaks in the aged samples, become evident when comparing the spectra of 1 mM aged and fresh samples (Figure **4.32**). To monitor the appearance of these additional peaks, a periodic experiment was conducted using a 1 mM fresh **Y_8-PW_{10}** sample (Figure **4.32**). The results showed that the sample remained clear for up to 74 hours, or 3 days.

ATR-FTIR spectroscopy

The objective of this investigation was to assess the stability of the solute **Y_8-PW_{10}** in solution. The solute was recovered from the solution by evaporating the solvent from both old and fresh samples. ATR-FTIR spectroscopy was conducted on the dried solute (Figure **4.33**). The ATR-FTIR spectrum of the fresh sample closely matches the reference spectrum. In contrast, the spectrum of the solute obtained from the evaporation of the old sample displayed significant distortion in the absorption bands compared to the reference. This observation suggests that material changes occur as the sample ages.

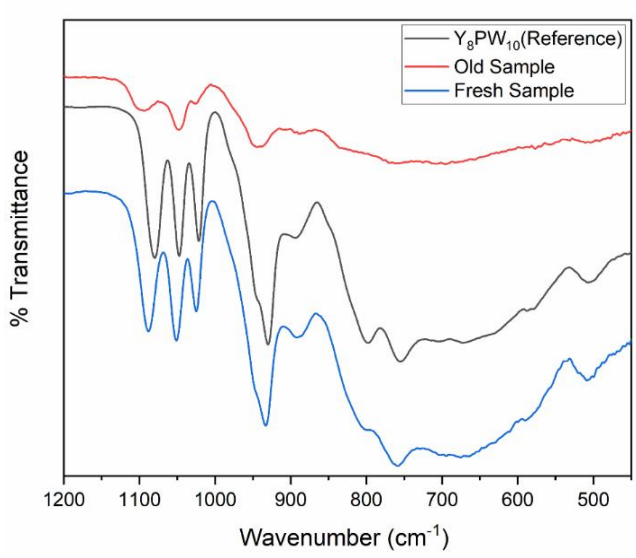


Figure 4.33 Comparison study of the ATR-FTIR spectra of the old and fresh **Y_8-PW_{10}** with the reference.

The combined ATR-FTIR and ^{31}P NMR analyses indicate that **Y_8-PW_{10}** undergoes time-dependent changes in aqueous solution. ATR-FTIR spectra of solutes recovered from aged NMR samples show distortions compared to fresh samples, while ^{31}P NMR reveals additional peaks and decreased signal intensity in aged solutions. Together, these results suggest that the clusters experience partial structural transformations or chemical modifications over time, highlighting the importance of considering solution stability when interpreting PRE measurements. This process needs more systematic studies to understand the complex behaviour of these POM metal clusters in solution and their effect on the PRE mechanism.

4.9. Conclusion and Outlook

This chapter describes the use of the measured ^{1}H relaxivities as a determining factor for assessing the efficiencies of MRI contrast agents. Paramagnetic metal ions with higher relaxivities can significantly improve image quality, thereby enhancing the overall quality of

MRI images. The studies conducted focus on three types of paramagnetic ion-incorporated polyoxometalates: 3d-POM, 4f-POM, and 3d-4f-POM, measured over a range of magnetic fields from 20 MHz to 1.4 GHz. The values of relaxivity r_1 and r_2 represent the linear slopes of relaxation rates R_1 and R_2 as functions of PM-POM concentration, respectively.

Three isostructural 3d polyoxometalates (3d-POMs)-**Co_{16}-PW_9**, **Ni_{16}-PW_9**, and **Mn_{16}-SiW_9** were evaluated for their comparative relaxivities. The results reveal that paramagnetic 3d ions in these POMs significantly enhance relaxivity. Since these 3d-POMs are isostructural, the primary factor influencing the differences in their relaxivity (r_1 and r_2) is their electronic spin relaxation time. In this study, the electronic spin relaxation time of the pure 3d metal ions in aqueous solution was used as the reference. All three 3d-POMs exhibit higher relaxivity at lower magnetic fields. However, this relaxivity varies with increasing magnetic field strength. Among the three, **Mn_{16}-SiW_9** shows the highest r_1 due to the longer electronic relaxation time of $Mn^{2+/3+}$ ions; however, the relaxivity becomes field-independent as r_1 increases with rising magnetic fields. For **Co_{16}-PW_9** and **Ni_{16}-PW_9**, the relaxivity shows a slight increase as the magnetic field strength increases. Conversely, r_2 for all studied 3d-POMs, relaxivity increases with magnetic field strength. The higher relaxivity observed at lower magnetic fields can be attributed to contributions from the dipole-dipole interactions and the total Curie spin contributions.

In the relaxivity studies of 4f paramagnetic metal ion-containing polyoxometalates (4f-POMs), six clusters containing Dy^{3+}, Er^{3+}, and Gd^{3+} ions were evaluated: **Dy-W_{11}**, **Er-W_{11}**, **Er_2-W_{34}**, **Er_2-W_{22}**, **Gd_2-W_{22}**, and **Dy_2-W_{22}**. Among these, the Gd^{3+} containing POM, **Gd_2-W_{22}**, exhibited the highest relaxivity. However, its relaxivity was observed to be field-independent. This behaviour can possibly be attributed to the longer relaxation times of Gd^{3+} ions compared to the other 4f metal ions. In contrast, the other 4f-POM clusters showed an increase in relaxivity with rising magnetic field strengths. To interpret the behaviour of the r_1 and r_2 of the other 4f-POMs, several factors affecting the PRE properties were considered. These factors include the number of paramagnetic ion centres, the total electronic spin of the metal cluster, magnetic moments of the Ln^{3+} ions, the number of exchangeable water molecules, and correlation times.

In terms of 3d-4f POMs, **$Co_7Ln_xNa_{1-x}$-GeW_9** (Ln = Gd^{3+}, Dy^{3+}, and Y^{3+}), the relaxivity behaviour of these paramagnetic 3d-4f-POM clusters was assessed based on their structural characteristics, apart from the usual parameters that contribute to the PRE behaviour of the PM-POM clusters. The crystal structure of **$Co_7Ln_xNa_{1-x}$-GeW_9** reveals a 1D chain in the solid state, along with Na/Ln positional disorder at the centre and Co^{2+}/Na^+ disorder at the linker position. Notably, the observed increase in relaxivity for compounds

containing Gd^{3+} and Dy^{3+} suggests that the relaxivity primarily originates from the 3d metal ions (Co^{2+}). However, the presence of lanthanide ions (Gd, Dy, and Y) significantly influences the overall relaxivity, resulting in a pronounced increase for the Gd-containing compounds compared with those with paramagnetic Dy^{3+} or diamagnetic Y^{3+}. Moreover, the somewhat low values of relaxivity observed for these 3d-4f-POMs indicate the effect of their inherent one-dimensional chain structure in solution. However, this interpretation is contradicted by the ESI-MS studies, which can accurately identify the fundamental POM building blocks.

In addition, one example of deviation from the standard relaxivity behaviour of high-nuclearity lanthanide-containing POMs, **Gd_8-PW_{10}**, was discussed. This measurement lacks a linear relationship when plotting R_1against concentration. This issue arises from the transition of metal clusters after the solution was prepared. This section contains detailed troubleshooting experiments that include both solution-based and solid-state characterisation of diamagnetic (**Y_8-PW_{10}**) as a benchmark.

The experimental section of this chapter provides details of the NMR instruments and parameters used for the PRE relaxivity measurements of PM-POMs. Furthermore, pictorial representations relevant to the high magnetic field experiments conducted at LNCMI, Grenoble.

Overall, the relaxivity study involving 3d, 4f, and 3d-4f POMs across a range of magnetic fields (20 MHz-1.4GHz) indicates that paramagnetic POMs (PM-POMs) can enhance relaxivity properties as the magnetic field strength increases. Consequently, PM-POMs can act as potential MRI contrast agents at high magnetic fields, depending on the nature of the paramagnetic ions used. The POM framework offers unique structural stability and rigidity to the PM-POM clusters in solution, which significantly affects the relaxivity behaviour of the metal clusters. Also, lacunary POM ligands allow for the incorporation of a greater number of paramagnetic centres within a single molecule. Despite their positive impact on relaxivity, further studies are needed to understand the underlying mechanisms of these clusters in solution and to elucidate the relaxivity process in greater detail. For instance, data modelling and measurements of electronic relaxation times using EPR spectroscopy could provide valuable insights into these mechanisms.

4.10. Experimental Section

Sample preparations for the NMR Relaxivity measurements

Different methods, instruments, and sample preparation procedures were employed to assess the NMR relaxivity of the paramagnetic metal-containing POMs in various Larmor frequencies from 20 MHz to 1.4 GHz. The solvent used for the sample preparation was a D_2O/H_2O (90/10) mixture. The 1 mM stock solution was prepared using high-purity material crystals, which were further diluted using the D_2O/H_2O solvent to various dilutions (0.8, 0.6, 0.4 and 0.2 mM) for the systematic relaxivity studies. Depending on the availability and nature of the materials, the number of dilutions made for each PRE study varies as specified in the results and discussion section.

To perform the NMR relaxivity studies from 20-400 MHz Larmor frequencies, Wilmad NMR sample tubes of 5.00 mm outer diameter (OD) were used. NMR spectrometers 20 MHz and 80 MHz are equipped with permanent magnets, and 300 MHz and 400 MHz are equipped with superconducting magnets. Capillary tubes of 1.2 mm OD and 1.0 mm inner diameter (ID) and a length of 10 mm were used for the PRE studies of the PM-POM in resistive magnets. 1 µL of the same sample solution from a 5.00 mm NMR tube was manually transferred into the 10 mm long capillary tube using a 10 µL micropipette. To prevent evaporation, the capillary tubes were sealed with proton-free fluorinated polymer grease (DAIFLOIL from Daikin Company). The proton-free grease was sealed on both sides of the capillary tube using a tool (Figure **4.34.a**) which works based on the internal pressure variation of the sample column and the grease seals on both sides. This helps to position the sample column at the centre of the tube, as shown in the sample tube picture in Figure **4.34.b**.

In addition, when preparing the samples, it is important to check the semisolid nature of the gel. For instance, in hot weather, the gel may become too runny to handle. In this situation, keep the gel in a cool room until it regains its original state, which helps to keep the gel in place without falling out. After sample preparation, it is essential to store them in a temperature-regulated location to keep the gel plug in place, prevent sample evaporation and maintain the specific concentration.

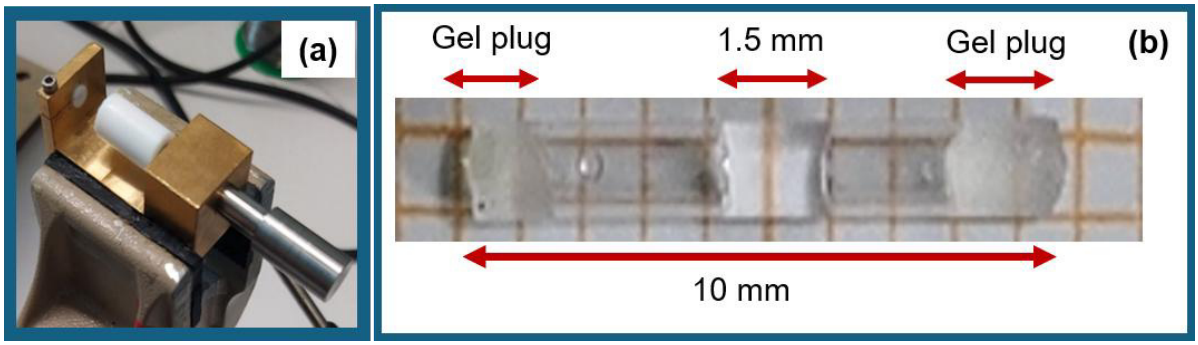


Figure 4.34 a. The tool is used to fill the gel on both sides of the capillary to maintain the sample column at the centre. **b.** The 10 mm capillary tube with gel seal and the 1.5 mm sample column at the centre.

NMR instruments

The NMR relaxivity measurements were performed on samples with different Larmor frequencies, ranging from 20 MHz to 1.4 GHz, using various instruments. Commercial Bruker NMR instruments at the Institute of Mechanical Process Engineering and Mechanics (MVM), Karlsruhe Institute of Technology (KIT), Karlsruhe, Germany, were used to measure Larmor frequencies of 20, 80, 300, and 400 MHz. For the ultra-high field NMR relaxivity studies at 870 MHz, 1050 MHz, 1200 MHz, and 1400 MHz, experiments were carried out at the Laboratoire National des Champs Magnétiques Intenses (LNCMI) in Grenoble. The 24 MW resistive magnet provides variable fields up to 35 T at room temperature.

NMR instruments and radio frequency signals were used for the experiments

Time Domain NMR (TD-NMR) instrument

The Time Domain NMR (TD-NMR) instrument of the Bruker minispec series was used for the investigation of T_1 and T_2 relaxation times at 20 MHz. The T_1 was measured with a progressive saturation recovery (PSR) pulse sequence. T_2 was recorded using the CPMG pulse sequence, which improves the low magnetic field homogeneity of the TD-NMR instruments.

Frequency Domain NMR instrument

The 80, 300 and 400 MHz NMR instruments are frequency-domain NMR instruments. The 80 MHz NMR spectrometer is a Benchtop NMR spectrometer of the Bruker Fourier series, and 300 and 400 MHz are Bruker ASCEND^{TM} series. These NMR instruments are autotuned and have active z-gradient shimming. Data obtained with Bruker TopSpin VERSION 3+4 software, and data processing and phase-corrected spectra were stored in the 2D data file. For analysis of T_1 and T_2, spin dynamic software enables the user to choose the size of the

integration window for the moment equations to determine the magnetisation values. In these NMR spectrometers, T_1 was measured using an inversion recovery (IR) pulse series and T_2 was measured with a CPMG echo sequence.

4.10.1. Resistive Magnet

The ultra-high field NMR relaxivity experiment of Larmor frequencies above 800 MHz was evaluated using a 24 MW resistive magnet with variable field up to 37 T in a 34 mm room temperature bore. After sample preparation, it is vital to store them in a temperature-regulated location. To overcome the low field homogeneity of 50 ppm/mm at a 1 mm off-centre position at the centre of these resistive magnets, small sample volumes were prepared in a 10 mm length capillary tube. The pulse sequences used to measure the T_1 and T_2 relaxivity are progressive saturation recovery (PSR) and CPMG echo pulse sequences, respectively. The FID signals collected after the measurement are initially collected by LabVIEW software. The FID signals are processed by the MATLAB computer program, and the final fitting to determine the magnetic moment was performed with the OriginPro 2023 software.

M9 magnet site at LNCMI, Grenoble

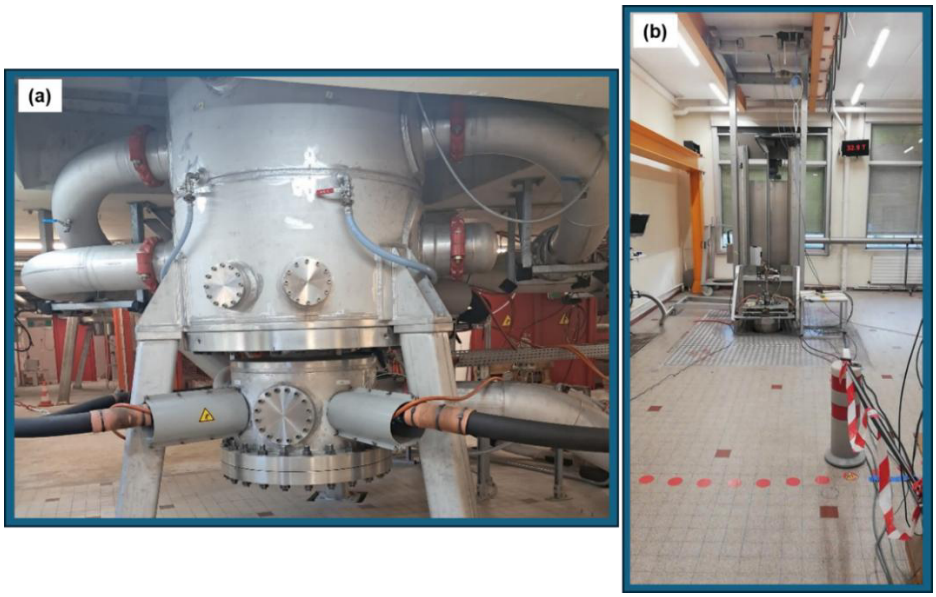


Figure 4.35 a. The outer view of the resistive magnet placed in the basement of the M9 magnet site, LNCMI, Grenoble. The total height of the magnet is 2 meters. The big metallic tubes on the upper part are the cooling system, which carries 300 litres of water per second. The two tubes at the bottom of the magnet provide the electric current. It consumes 6000 A at 400V, which means 24 MW of power. **b.**The elevator system is located on the top of the resistive magnet, located on one floor up to the basement. The 5-guess line separates the perimeter of the magnet from the workstation. When the magnet is operating, the field is displayed on the site.

The large resistive magnet is located in the basement of the M9 site. The exterior view of the magnet is shown in Figure **4.35.a**. Access to the centre of the magnet is via a 34 mm bore from the upper floor.

The cryostat containing liquid nitrogen surrounds the bore, maintaining the room temperature of the sample throughout the experiment. The temperature of the sample was continuously monitored throughout the experiment with the electronic thermometer attached near the sample holder. The position of the cryostat on top of the magnet can be controlled by an elevator unit (Figure **4.35.b**).

The NMR spectrometer part is installed at the site, which includes the RF signal synthesiser, pulse generator, amplifier, oscilloscope, etc, which controls the RF signal and collects the signal back after the measurement. Several computers control the entire experiment and are used for T_1 and T_2 analysis (Figure **4.36**).

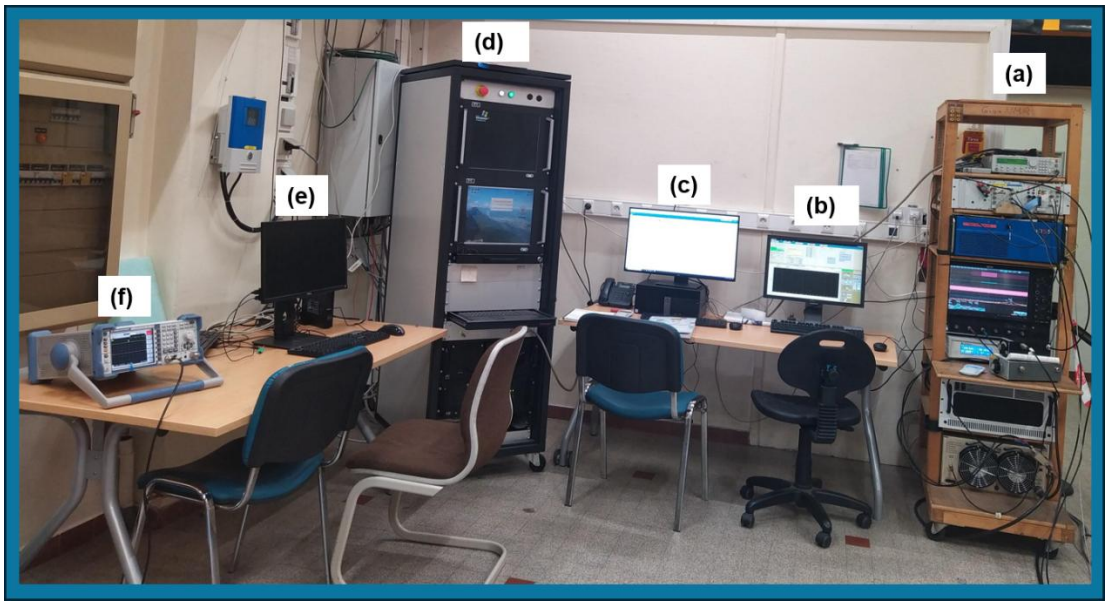


Figure 4.36 The workstation is in the same room, which is separated from the elevator unit with a 5 Gauss line. It includes several functional units to control and coordinate the experiment. **a.** The spectrometer includes an RF signal synthesiser, amplifier, oscilloscope, pulse generator, etc. **b.** The computer controls the experiment, and the raw data generated from the spectrometer is collected by this computer using LabVIEW software. **c.** The first data processing unit is performed by this computer with MATLAB software. **d.** Magnet controller, where the information about the magnet will be displayed on this screen. **e.** The second data processing unit, which is working with Origin software, is where the data processing is completed. **f.** Wobbler, which is used to tune the probe.

Sample holder/probe used for resistive Magnet

For the resistive magnet, to reach the magnetic centre, a very long probe of length approximately 1700 mm was used (Figure **4.37.a**). This probe head is occupied with a radio frequency coil where the 10 mm long sample capillary tubes are placed. The coil and the

sample tubes are supported by a Teflon disc. The picture of the probe and the probe head is shown in Figure **4.37.b**. The height of the probe head is adjusted manually to achieve the symmetric wobble curve.

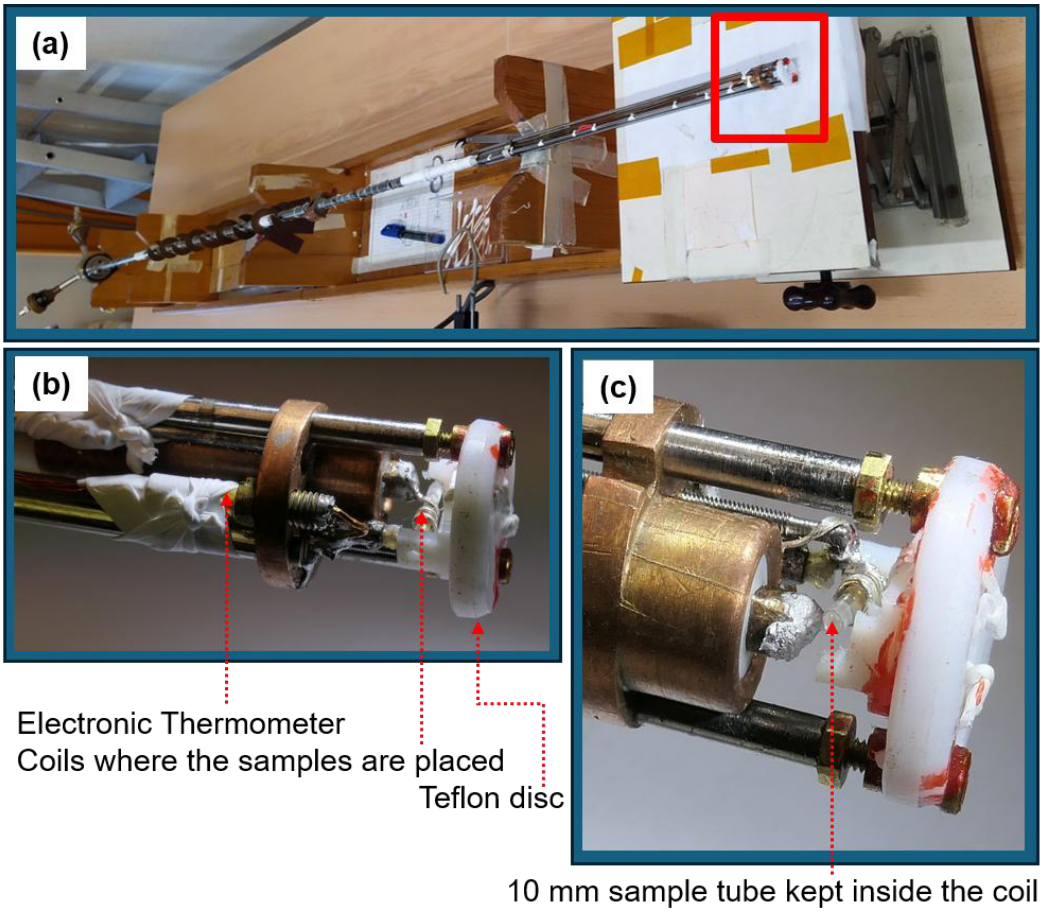


Figure 4.37 a. Full view of the 1700 mm probe, the probe head is marked in the red box, which is further enlarged in the pictures **b.** and **c.,** showing a close view of the sample placed inside the coil.

Steps involved in the relaxivity measurements of samples in Bruker's superconducting NMR Instruments (80 MHz, 300 MHz and 400 MHz)

1. Sample insertion: The length of the 5 mm NMR sample tubes was adjusted using the depth gauge, and the outer walls of the NMR tubes were cleaned before inserting them into the magnet to make sure the sample solution was clear without any solid sediments or bubbles. the sample tube was then inserted along with the spinner into the tube after turning on the lift air.
2. Tuning the probe head: To obtain a nice signal-to-noise ratio and a meaningful result, the tuning of the probe head should correctly match the RF circuit to the desired resonance frequency. For this experiment, an Automatic Tuning Module (ATM) by Bruker was used. Tuning and matching were performed automatically.

3. Lock the field: The magnetic field was locked using a 2D signal of the deuterated solvent (90/10; D_2O/H_2O) as a reference to ensure the full field strength of the respective magnet, it helps to prevent the field drift.
4. Shimming: To optimize the homogenous magnetic field, throughout the experiment, shimming can be done before the experiment. For the current studies, the shimming of the magnet was done with the Bruker procedure.
5. The auto calibration process was used to calibrate the pulses.
6. T_1 and T_2 experiments were performed. The details of the signals and the parameters set for the relaxivity experiments are given in Table **4.7**
7. The data T_1 and T_2: Raw data obtained from the TopSpin Bruker software is analysed with TopSpin software and TopSpin's new feature, Dynamic Centre, which includes automated optimisation of acquisition parameters of T_1 and T_2 experiments.

Steps involved in the relaxivity measurements of samples (Resistive magnetic above 860 MHz)

1. Sample preparation: The details of the sample preparation for the resistive magnet are discussed in the previous section.
2. Sample positioning: The vertical height there by the sample position was calculated based on the magnetic centre position displayed in the resistive magnet control unit. A highly concentrated solution of the short relaxing sample (50 mM of $GdCl_3$) was used to tune the probe with the set magnetic field (860 MHz). The sample position was fixed by manually adjusting the vertical position of the probe at the point where the narrowest NMR signal was found.
3. Pulse calibration: The pulse calibration was performed using the same highly concentrated $GdCl_3$ (50 mM) solution. The pulse length of 90^0 and 180^0 signals was calibrated for each magnetic field.
4. The sample capillary was placed inside the coil in the probe head. The sample column in the middle of the radio frequency coil was carefully adjusted, and the probe was carefully inserted into the bore.
5. Relaxivity measurements were performed using the appropriate radio frequency signals. The raw data generated in the LabVIEW software is collected and treated.

Table 4.7 NMR pulse sequences and measurement parameters as used in the experiments at ^{1}H Larmor frequencies used for the relaxivity measurements.

Larmor frequency [MHz]	**20**	**80**	**300**	**400**	**870**	**1050**	**1200**	**1400**
Parameters for T_1								
Pulse sequence	Saturation recovery		Inversion recovery					
Number of scans	4	4	4	4	1	1	1	1
No of recovery delays	16	16	16	16	20-30	20-30	20-30	20-30
Parameters for T_2								
Pulse sequence	CPMG	CPMG	CPMG	CPMG	-	-	-	-
Number of scans	4	4	4	4	-	-	-	-
Number of echos	$2i_{max}$ =100	List of 16 elements $2i_{max}$= 500	List of 16 elements $2i_{max}$= 500	List of 16 elements $2i_{max}$=500	-	-	-	-

The data processing procedure involved in the relaxivity experiments

Several methods were used to process the time domain raw data obtained after the relaxometry experiment. Depending on the type of instrument, magnets, etc. However, the methods followed for processing the raw data are similar in all kinds of spectrometers.

The spectrometer records a time domain signal FID, and converts this to a frequency domain spectrum by the application of the Fourier transform (FT). Baseline corrections of the FT converted spectrum were done by selecting a window for integration. Followed by automatic moment calculation.

In the case of superconducting-equipped NMR instruments, the TopSpin software by Bruker offers automatic options to convert the raw data to a spectrum. Further data processing was done by another feature of TopSpin called Dynamic Centre. The peak area integrals were selected. Depending on the experiment requirement, a function of fit was defined. The final report function summarises all fitting results and the decay curve. The relaxivity was obtained from the T_1 and T_2 values.

In the case of resistive magnets, for each sample, raw data collected from the LabVIEW software is initially processed and Fourier transformed by MATLAB with a specific script exclusively compatible with the relaxivity measurements. Relaxation time was calculated by fitting the graphs. T_1 and T_2 were determined by fitting the mono-exponential to the experimental data by OriginPro 2023 software.

Relaxation rate (R_1 and R_2) was obtained by inverting the relaxation time (T_1 and T_2) obtained from the experiment.

$$R_{1,2(c)} = r_{1,2}.C \tag{4.20}$$

A graph was plotted with relaxation rate vs concentration. The slope of this linear plot determines the relaxivity. To compare the relaxivity behaviour of one specific sample in various magnetic fields ranging from 20 MHz to 1.4 GHz, another graph was plotted with relaxivity vs magnetic field. This data is crucial to studying the PRE effect of the paramagnetic molecule.

5. Electrochemistry and Electrocatalytic Behaviour of POMs

5.1. Introduction

A key electrochemical feature of POMs is governed by their electronic structure and delocalised redox-active centres. The redox activity of POM species arises from their metal centres containing empty and non-bonding d orbitals. During reduction, addenda atoms accept electrons. If POM species, such as Keggin ion, Wells-Dawson ion, and Lindqvist ion types, possess the same addenda atoms, the accepted electrons are distributed evenly among these atoms. In contrast, Anderson-type anions lose reversibility due to structural changes caused by added electrons occupying antibonding orbitals during the reduction process. Therefore, the POMs can transfer electrons and protons or accept or donate electrons without altering the structure. However, the reduced POM often exhibits a characteristic deep blue colour due to electron delocalisation among metal centres in different oxidation states, a phenomenon known as heteropoly blue or poly blue. This phenomenon was observed in tungsten and molybdenum-based POM materials. The reduction increases the density of negative charges, which enhances its basicity. Subsequently, protonation occurs.[254]

The Keggin ion and Wells-Dawson ion POM show distinct redox behaviours in solution; however, the electrochemical properties of these materials can be altered by the substitution of other materials, such as transition metal ions[255,256] and organic ligands on the lacunary derivatives of the parent POM species[257] and POM-based metal organic frameworks (POMOFs).[258,259] POM-based functional materials are widely investigated for electrocatalysis because of their reversible redox activity, structural versatility, and capacity for precise modification. Their tunable size, shape, solubility, and remarkable redox stability make them attractive candidates for catalytic applications. A key advantage lies in their ability to incorporate different addenda ions without disrupting structural integrity, enabling fine control over electronic and catalytic behaviour.

By adjusting their composition through metal substitution or organic ligand incorporation, the electronic structure, surface interactions, and stability of POMs can be optimised, leading to enhanced catalytic performance. Such tailored modifications allow the

development of highly efficient POM-based catalysts for diverse electrochemical applications.

Theoretical background of electrocatalysis

Electrocatalysis refers to the process of accelerating the rate of an electrochemical reaction using a substance known as an electrocatalyst. Unlike reactants, the electrocatalyst is not consumed during the reaction, allowing it to facilitate the reaction multiple times. This enhancement is crucial for improving the efficiency of various electrochemical applications, including fuel cells and batteries.[260] The reactions associated with renewable energy technologies include the oxygen evolution reaction (OER), the oxygen reduction reaction (ORR), the hydrogen evolution reaction (HER), and the carbon dioxide reduction reaction (CO_2RR). These processes occur in the presence of a catalyst. In addition to converting carbon dioxide into hydrocarbons or carbon monoxide, electrocatalysis enables key processes such as oxygen transfer from biomass and the reduction of nitrates to nitrogen and ammonia. Electrocatalysts play a vital role in these reactions by lowering the activation energy, thereby improving reaction efficiency and feasibility.

In electrochemical systems, activation energy is directly related to the voltage or potential required for redox reactions. As depicted in Figure **5.1**, activation energy is typically represented as a function of the energy levels of reactants and products, highlighting the impact of electrocatalysts in facilitating reaction pathways and reducing energy barriers.[261]

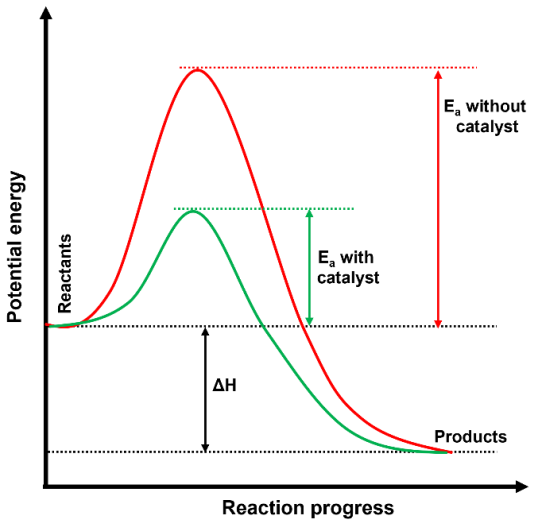


Figure 5.1 Illustration of the potential energy of a chemical reaction with and without a catalyst. Catalysts speed up chemical reactions by lowering activation energy ($\mathbf{E_a}$) while remaining unchanged. Similarly, an electrocatalyst reduces electrochemical activation energy by decreasing the required electric voltage for the reaction to occur.

When voltage is applied, the appropriate electrode surface facilitates electron transfer between chemical species, enabling electrochemical transformations. The electrocatalyst

reduces the voltage required to carry out the electrochemical process.[262] The three key factors assessed in developing new electrocatalysts are activity, selectivity, and stability. Activity can be calculated by the current density and thereby the reaction rate. Stability is the measure of how compact the catalyst is in terms of its conversion potential. Selectivity is the formation of specific products from reactants. For practical applications, the electroactivity of a catalyst for a particular reaction may not lead to the desired product selectivity. In developing a new catalyst, the goal is to identify materials with the highest current density under specific conditions.[263] The performance of electrochemical devices is affected by factors such as reaction kinetics, product transport, reactant and ion transport, and electron conduction.[264,265]

5.2. Fundamentals of Electrochemical Analysis

The standard technique used to measure electrochemical data is Cyclic Voltammetry (CV). Electrochemical reactions involve the movement of electrons, resulting in a chemical change.

$$\mathbf{A} + \mathbf{e}^{-} \rightleftarrows \mathbf{B} \qquad (5.1)$$

Equation 5.1 represents the basic electrochemical redox reaction. In this process, electrons are transferred between the conductive electrode surface and the oxidative (A) - reductive (B) pair. A potentiostat supplies the external energy required for this heterogeneous electron transfer. CV is used to investigate these reductive and oxidative processes and study the reactions initiated by the electrons, including electrocatalysis.

The CV experiment is conducted in a one-compartment electrolytic cell. The two main components of electrolytic cells are electrolytes and electrodes. Buffer solutions of various pH ranges are used for electrochemical analysis. The buffer solution resists changes in pH at the electrode-electrolyte interface during the redox process. A methodical strategy is essential when choosing an appropriate buffer for the analysis. This involves carefully considering factors such as the buffer's pKa value, analyte concentration, and stability. By systematically evaluating these aspects, one can ensure optimal conditions for accurate and reliable analytical results.

As a consequence of the proton-coupled electron transfer, the proton concentration at the electrode-electrolyte interface differs from the bulk solution. The movement of substances within the electrolyte is regulated by three methods of mass transport: convection, migration, and diffusion. Mechanical forces such as vibration and mechanical stirring facilitate convection mass transport; the movement of solute is influenced by an electric field, generating migration mass transport; and differences in concentration between two

parts regulate diffusion mass transport. The faster production and consumption of H^+/OH^- compared to mass transfer is still challenging to predict. This is due to the lack of efficient techniques available for precisely and instantaneously analysing the local proton concentration at the electrode-electrolyte interface.[266]

The electrochemical cell is equipped with three electrodes (Figure **5.2**): a working electrode, a reference electrode and a counter electrode.

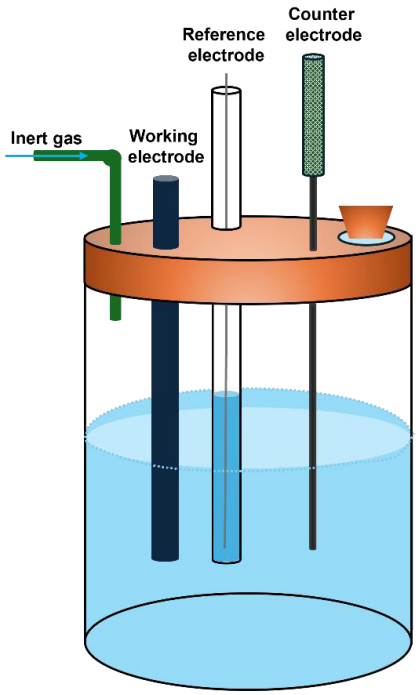


Figure 5.2 A standard three-electrode setup consists of a working electrode, a counter electrode, and a reference electrode, all immersed in a solution containing electrolyte and analyte. An inert gas inlet allows for sparging the system with dinitrogen or argon.

Working electrode: The working electrode is made up of chemically inert materials such as carbon or platinum. A potentiostat applies a specific voltage to the working electrode relative to the reference electrode's potential. This externally applied potential facilitates the electrochemical reaction of interest on the surface of the working electrode. Preparing the working electrode surface before the process is crucial for ensuring the electrochemical reaction occurs effectively, which is essential for accurate analysis.

Reference electrode: The reference electrode has a stable and reproducible electrode potential. The accurate electrode potentials of the other electrodes are measured relative to the stable potential of the reference electrode. Commonly used reference electrodes include the standard hydrogen electrode (SHE), saturated calomel electrode (SCE), and AgCl/Ag electrode. Usually, the reference electrodes are separated from the electrolytes in

the cell by a porous frit. It is crucial to minimise junction potentials by matching the solvent and electrolyte in the reference compartment to those used in the experiment.

Counter electrode: The counter electrode is used to complete the electrical circuit within the electrochemical cell. When a potential is applied to the working electrode, a redox reaction occurs at the analyte. As a result, current flows between the working electrode and the counter electrode. This means that a simultaneous oxidative or reductive reaction occurs on the surface of the counter electrode, depending on the reaction at the working electrode. For this reason, inert materials with a much higher surface area are chosen to act as the counter electrode.

5.3. Electrocatalysis of POM Systems

POM substituted with a transition metal possesses electrochemical properties different from those of its pristine species and depends on the metal ion incorporated into it. [267]

In the case of organic POM hybrid materials, the organic part provides additional structural functionality as well as structure-directing properties to these organic-inorganic hybrid materials.[268,269]

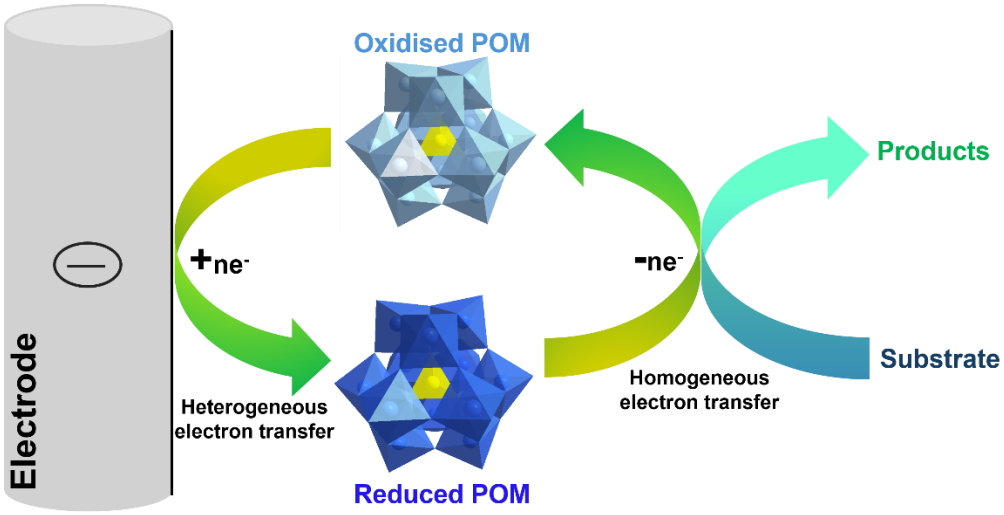


Figure 5.3 Electrochemical reaction catalysed by heterogeneous redox activation and homogeneous oxidation of POM species.

The unique electrochemical properties of POM and POM-based molecules make them attractive as homogeneous and heterogeneous redox catalysts (Figure **5.3**). During the catalysis process, the electrocatalyst, which is uniformly dispersed throughout the solution, undergoes activation upon interaction with the electrode surface via a heterogeneous redox reaction. This crucial step initiates the transformation of the electrocatalyst, allowing it to facilitate subsequent reactions. Following this activation, the POM species engages in homogeneous reactions with the substrate present in the bulk solution. This interaction

enables the POM to catalyse the conversion of the substrate. Notably, throughout this process, the POM species are regenerated, maintaining the catalytic cycle and enabling continuous reactivity within the system. This intricate interplay between heterogeneous activation and homogeneous reaction underscores the efficiency of the electrocatalytic mechanism [270]

The rapid transfer of electrons and protons allows the POM system to function as a potential redox catalyst in electrocatalytic processes that involve multiple electron and proton exchanges.[271,272] POM and POM-based systems can be utilised to produce high-value chemicals, such as hydrogen (H_2), hydrocarbons, and ammonia.[273–275] These systems facilitate various electrocatalytic processes, including the hydrogen evolution reaction (HER), the oxygen evolution reaction (OER)[276], hydrogen/oxygen reduction reactions (HOR/ORR), carbon dioxide reduction reactions (CO_2RR),[277–280] and nitrogen reduction reactions (NRR)[281] (Figure **5.4**).

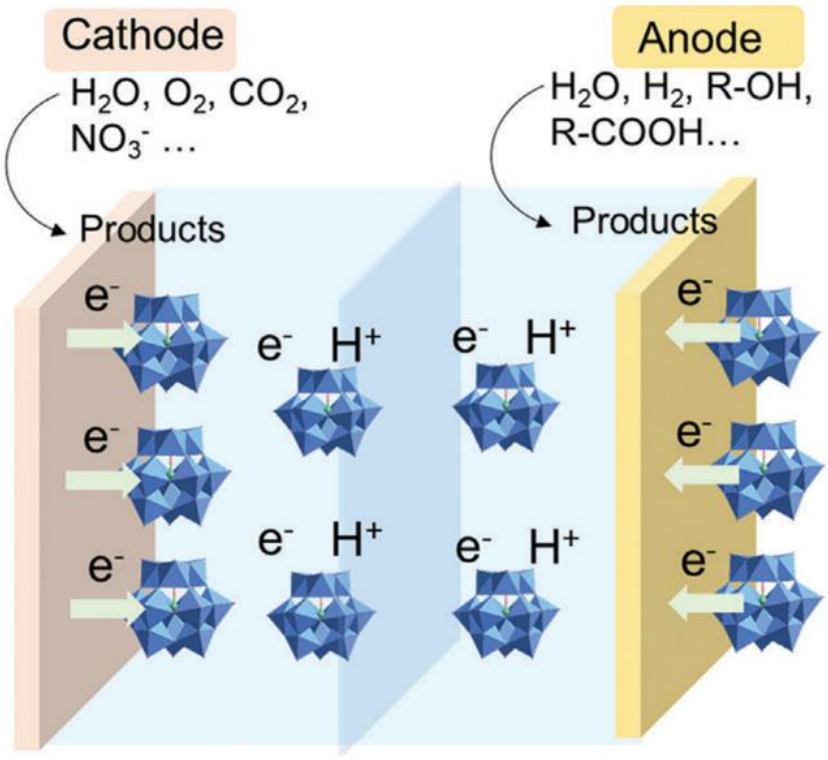


Figure 5.4 Representation of POM in electrocatalysis.[282]

This thesis focuses on the water oxidation reaction and the reduction reactions of nitrite, hydrogen peroxide, and dioxygen using metal-substituted POMs. The next section will emphasise the importance of electrocatalytic reactions enabled by transition metal-substituted POMs.

5.3.1. Electrocatalytic Water Oxidation by Transition Metal-Substituted POMs

Transition metal ions-substituted POM (TM-POMs) species can be a potential electrocatalyst for the water oxidation reaction. An effective water oxidation catalyst can keep the potential minimum for the water splitting step below.[283]

$$(2H_2O \rightarrow O_2 + 4H^+ + 4e^-;\ E_0 = 1.23\ V\ vs.\ NHE\ at\ 25°C) \qquad (5.2)$$

The increasing demand for renewable green energy and the need to address environmental issues have highlighted the importance of developing efficient water oxidation catalysts (WOCs). Significant efforts have been made to develop both heterogeneous and homogeneous WOCs.[284] Transition metal substituted POM stands out as an important subclass of water splitting catalyst due to its Lewis acidic nature, electron-rich properties, structural diversity, and ability to act as a homogeneous as well as heterogeneous condition without structural degradation.[285,286] Metal-substituted POM species serve as carbon-free and oxidatively stable homogeneous WOCs.[287,288] Notably, the tetra-ruthenium-incorporated metal complex, $[\{Ru^{IV}_4O_4(OH)_2(H_2O)_4\}(\gamma\text{-}SiW_{10}O_{36})_2]^{10-}$, is the first carbon-free, all-inorganic POM molecule reported to exhibit water oxidation catalytic properties, with its findings published in 2008 by C. Hill and coworkers (Figure **5.5**).[289]

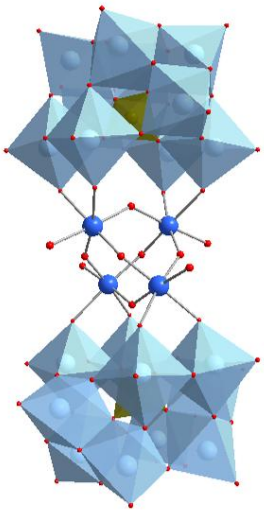


Figure 5.5 Combined ball-and-stick and polyhedral representation of $[Ru^{IV}_4O_4(OH)_2(H_2O)_4\}(\gamma\text{-}SiW_{10}O_{36})_2]^{10-}$.[289]

In 2010, the same group reported Cobalt containing POM $[Co_4(\mu\text{-}OH)(H_2O)_3\}(Si_2W_{19}O_{70})]^{11-}$(Figure **5.6**), which is an economically feasible, highly active, oxidatively stable and homogenous molecular electrocatalyst for WOC.[283]

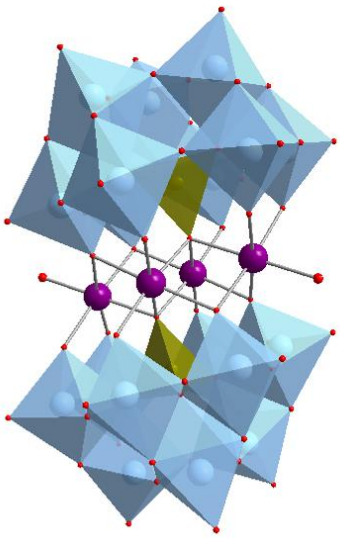


Figure 5.6 Combined ball-and-stick and polyhedral representation of [{Co_4(μ-OH)$(H_2O)_3$}$(Si_2W_{19}O_{70})$]$^{11-}$.[283]

Table 5.1 Transition Metal substituted POMs (TM-POMs) as a WOCs.

TM-POMs		TM Nuclearity	Fig.	Ref.
$[(Mn(H_2O)_3)_2(H_2W_{12}O_{42})]^{6n-}$	**Mn_2-W_{12}**	Mn_2		[290]
$[Mn_3(H_2O)_3(SbW_9O_{33})_2]^{12-}$	**Mn_3-SbW_9**	Mn_3		[291]
$[Mn^{III}_3\ Mn^{IV}O_3\ (CH_3COO)_3$(A-α-$SiW_9O_{34})]^{6-}$	**Mn_4-SiW_9**	Mn_4		[292]
$[Mn_6Ge_3W_{24}O_{94}(H_2O)_2]^{18-}$	**Mn_6-GeW_9**	Mn_6		[293]
$[Fe_{11}(H_2O)_{14}(OH)_2(W_3O_{10})_2$(α-$SbW_9O_{33})_6]^{27-}$	**Fe_{11}-SbW_9**	Fe_{11}	(a)	[294]
$[NaFe_{15}(OH)_{12}(PO_4)_4$(A-α-$SiW_9O_{34})_4]^{21-}$	**Fe_{15}-SiW_9**	Fe_{15}		[295]
[{Co_4(μ-OH)$(H_2O)_3$}$(Si_2W_{19}O_{70})$]$^{11-}$	**Co_4-SiW_9**	Co_4	(b)	[283]
[{$Co^{II}_7As^{III}_6O_9(OH)_6$}(A-α-$SiW_9O_{34})_2]^{12-}$	**Co_7-SiW_9**	Co_7	(c)	[296]
$[Co_9(H_2O)_6(OH)_3(HPO_4)_2(PW_9O_{34})_3]^{16-}$	**Co_9-PW_9**	Co_9	(d)	[297]
[{$Co_4(OH)_3(PO_4)$}$_4(MW_9O_{34})_4]^{32-}$, M= Si, Ge, P	**Co_4-MW_9**	Co_{16}	(e)	[298]
[{β-$SiNi_2W_{10}O_{36}(OH)_2(H_2O)$}$_2]^{24-}$	**Ni_4-SiW_{10}**	Ni_4	(f)	[299]
$[Ni_5(OH)_6(OH_2)_3(Si_2W_{18}O_{66})]^{12-}$	**Ni_5-SiW_9**	Ni_5	(g)	[300]
$[Ni_{12}(OH)_9(CO_3)_3(PO_4)(SiW_9O_{34})_3]^{24-}$,	**Ni_{12}-SiW_9**	Ni_{12}	(h)	[301]
$[Ni_{13}(H_2O)_3(OH)_9(PO_4)_4(SiW_9O_{34})_3]^{25-}$	**Ni_{13}-SiW_9**	Ni_{13}		[301]
$[Ni_{25}(H_2O)_2OH)_{18}(CO_3)_2(PO_4)_6(SiW_9O_{34})_6]^{50-}$	**Ni_{25}-SiW_9**	Ni_{25}	(i)	[301]
$[Cu_5(OH)_4(H_2O)_2$(A-α-$SiW_9O_{33})_2]^{10-}$	**Cu_5-SiW_9**	Cu_5	(j)	[302]
$[(Co_{2.5}Fe_{0.5}(H_2O)(PW_9O_{34})_2(PW_6O_{26})]^{16-}$	**$Co_{2.5}Fe_{2.5}$-PW_9**	$Co_{2.5}Fe_{0.5}$	(k)	[303]

Due to their versatile nature, high efficiency, and cost-effective synthetic procedures, many studies have explored the catalytic properties of first-row transition metals substituted POMs

as WOC. All the reported inorganic POM-based WOCs are listed in Table **5.1**, and some molecular structures of POM-based WOCs are shown in Figure **5.7**

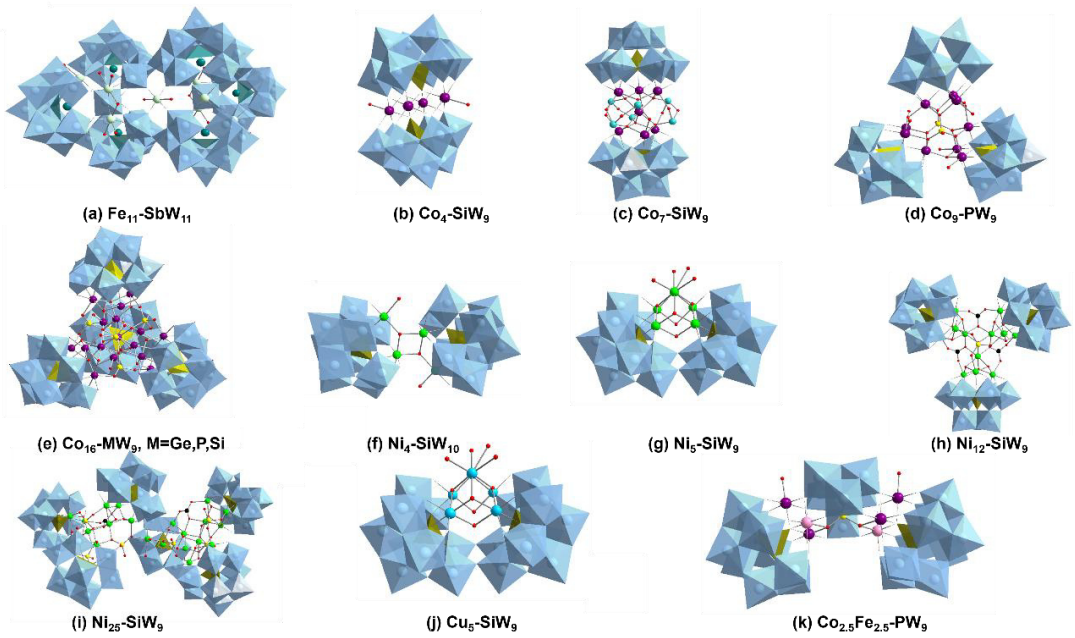


Figure 5.7 Molecular structures of various TM-POMs exhibiting WOC properties.

5.3.2. Electrocatalytic Reduction of NOx by Transition Metal-Substituted POMs

Table 5.2 Transition Metal-substituted POMs (TM-POMs) as NO_x reduction catalysts.

TM-POMs		**TM Nuclearity**	**Ref.**
$[NaMn_3(H_2O)_2(P_2W_{15}O_{56})_2]^{17-}$	**Mn_3-P_2W_{15}**	Mn_3	[304]
$[(H_2O)Fe^{III}MW_{11}O_{39}]^{n-}$ (M = Si, Ge, As, P)	**Fe-MW_{11}**	Fe	[305]
$[(Ni^{II}OH_2)_2(Fe^{III})_2(M_2W_{15}O_{56})_2]^{14-}$M = P, As	**Ni_2Fe_2-MW_{15}**	Ni_2Fe_2	[306]
$[Cu_4(H_2O)_2(H_4AsW_{15}O_{56})_2]^{18-}$	**Cu_4-AsW_{15}**	Cu_4	[307]
$[Cu_5(OH)_4(H_2O)_2(A\text{-}r\text{-}SiW_9O_{33})_2]^{10-}$	**Cu_5-SiW_9**	Cu_5	[308]
$[Cu_{20}Cl(OH)_{24}(H_2O)_{12}(P_8W_{48}O_{184})]^{25-}$	**Cu_{20}-P_8W_{48}**	Cu_{20}	[309]
$[(Zn^{II}OH_2)_2(Fe^{III})_2(P_2W_{15}O_{56})_2]^{14-}$	**Zn_2Fe_2-P_2W_{15}**	Zn_2Fe_2	[310]
$[Zn_4(H_2O)_2(H_4AsW_{15}O_{56})_2]^{18-}$	**Zn_4-As_2W_{15}**	Zn_4	[307]
$[Er(H_2O)_3GeW_{11}O_{39}]^{5-}$	**Er-GeW_{11}**	Er	[311]

The electro-catalytic conversion of NO_x species, including nitrate and nitrite/nitrous acid, is a crucial process due to the increasing presence of these pollutants in gaseous and ionic forms.[312] Their accumulation poses significant threats to the environment and public health.

Catalytic reduction transforms these pollutants into valuable products such as ammonia.[313] and hydroxylamine, as well as environmentally friendly byproducts like nitrogen gas (N_2) and nitrous oxide (which is used in medicine and as an oxidant).[314] This process not only supports environmental remediation and the sustainable management of the nitrogen cycle but also produces nitrogen-based value-added materials. Its primary application is in wastewater treatment.[315]

The electrocatalytic reduction of nitrite involves multiple steps characterised by electron and proton transfer.[316] Therefore, it is crucial to design stable and efficient catalysts that can endure the conditions associated with electron transfer to facilitate this catalytic process.[317].[308] Transition metal substitution on the POM structural framework will provide enhanced reduction ability and stability towards the redox reaction. There are many metal-substituted POM species reported for the nitrate reduction, some of which are listed in the table (Table **5.2**).

5.3.3. Electrocatalytic Reduction of Dioxygen and Hydrogen Peroxide

The electrocatalytic reduction of dioxygen (ORR) to water or hydrogen peroxide is an important cathodic reaction. This has significant applications in the energy converting system, such as fuel cells, biological systems and oxidative functionalisation reactions. Platinum electrodes are the heterogeneous catalyst used for ORR, which involves the transfer of four electrons. Transition metal-substituted POMs are inexpensive alternatives to the expensive Pt materials.[318,319]

The electrochemical reduction of hydrogen peroxide (H_2O_2) is important for various applications, including fuel cells, biosensors, and wastewater treatment. This reduction process involves the transfer of two electrons, resulting in the formation of either water (H_2O) or hydroxide ions (OH^-). The most used efficient catalysts for this reduction are platinum (Pt) or palladium (Pd) electrodes. However, metal-substituted POM species also provide an effective alternative, facilitating the reaction with minimal overpotential and serving as a more cost-effective option compared to precious metals.[320–323]

While transition metal-substituted POMs are already established catalysts, their electrocatalytic performance in reducing dioxygen and hydrogen peroxide can be further improved by combining all inorganic POM materials with other materials, such as carbonaceous support or with organic moieties.[324,325]

The following section provides a detailed analysis of the electrocatalytic behaviour and properties of the newly synthesised 3d and 3d-4f POMs. These POM-based molecules are

synthesised and structurally characterised during the research work of this thesis (Chapter **3**).

5.4. Results and Discussion

5.4.1. Electrochemical Characterisation of Co_{12}-GeW_{10}

Redox behaviour at pH 2.0 and 3.

The LiH_2PO_4 medium proved to be one in which the compound exhibited enough solubility and adequate stability to be characterised by cyclic voltammetry. The study was therefore carried out in this medium at five different pH levels: 2.0, 3.0, 4.0, 5.0 and 5.9.

At pH 2.0, **Co_{12}-GeW_{10}** was unstable but could still be characterised by CV. Scanning to negative potentials reveals two reduction steps at -0.50 V and -0.58 V vs. SCE, followed by reoxidation at -0.46 V and -0.54 V vs. SCE (Figure **5.8.a**). These processes are associated with the W^{6+} centres of **Co_{12}-GeW_{10}**.

Upon scanning towards positive potentials, from +0.50 V to +1.65 V vs. SCE, an irreversible oxidation wave was observed, which can be reasonably attributed to the electrocatalytic oxidation of H_2O after the oxidation of the Co^{2+} centres (Figure **5.8.b**). The following electrochemical reaction equations can summarise this process:

$$[GeW_{10}Co^{2+}{}_2O_{38})_6]^{48-} \xrightarrow{1} [GeW_{10}Co^{3+}{}_2O_{38})_6]^{36-} + 12e^- \quad (5.3)$$

$$[GeW_{10}Co^{3+}{}_2O_{38})_6]^{36-} + 12\,e^- \xrightarrow{2} [GeW_{10}Co^{2+}{}_2O_{38})_6]^{48-} \quad (5.4)$$

$$6\,H_2O \xrightarrow{1} + 3\,O_2 + 12\,H^+ + 12\,e^- \quad (5.5)$$

(5.3): electron transfer to the electrode, leading to the formation of a highly reactive oxidised form. (5.4) and (5.5): electron transfer between two chemical species in solution to regenerate the starting form and oxidise water, producing dioxygen.

The reaction modifies the working electrode surface, as observed when scanning from positive to negative potentials (shape and size of the reduction W wave observed in Figure **5.8.c**. The first reduction step shifts 50 mV towards less negative potentials to -0.45 V vs. SCE, while the second step moves to -0.60 V vs. SCE.

A comparison with the CV of the GeW_{10} ligand couldn't be done under the same conditions due to the instability of lacunary POM fragments at low pH. values.

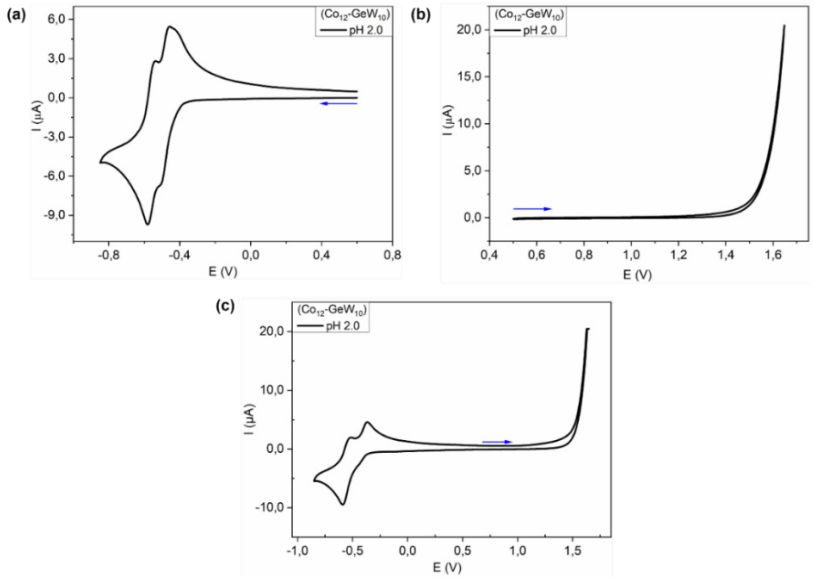


Figure 5.8 CVs recorded on an EPG electrode at a scan rate of 20 mV.s^{-1} in LiH_2PO_4 + LiOH / pH 2.0. POM concentration, 0.2 mM. Auxiliary electrode, Pt. Reference electrode, SCE. **a.** Potential scan towards negative potentials, from 0.60 V to -0.85 V. **b.** Potential scan towards positive potentials, from 0.5 V to 1.65 V. **c.** Potential scan first towards positive potentials and then towards negative potentials in the same potential range.

a) Shift of the CV waves of Co_{12}-GeW_{10} at pH 3.0

At pH 3.0, a negative shift in the CV waves of **Co_{12}-GeW_{10}** indicates that electron transfer to POMs in aqueous medium is pH-dependent and involves proton transfer (Figure **5.9.a**). The W^{6+} reduction steps show a shift of 120 mV, while the catalytic wave for water oxidation linked to Co^{2+} oxidation shifts by 80 mV (Figure **5.9.b** and Table **A.5.1**).

b) Modification of the electrode surface

A preliminary scan to +1.55 V vs. SCE, followed by a reverse scan to negative potentials, modifies the electrode's surface, impacting the wave shapes as seen at pH 2.0. The first reduction step merges with the second, appearing as a shoulder, shifting from -0.62 V to -0.52 V. In comparison, the second step changes minimally from -0.70 V to -0.71 V. This change results from cobalt oxide formation during Co^{2+} oxidation on the working electrode surface. However, when the potential scan is limited between 0.6 V and -1.0 V vs. SCE, two consecutive CVs show no changes in wave shapes, remaining superimposable (Figure **5.9.c**).

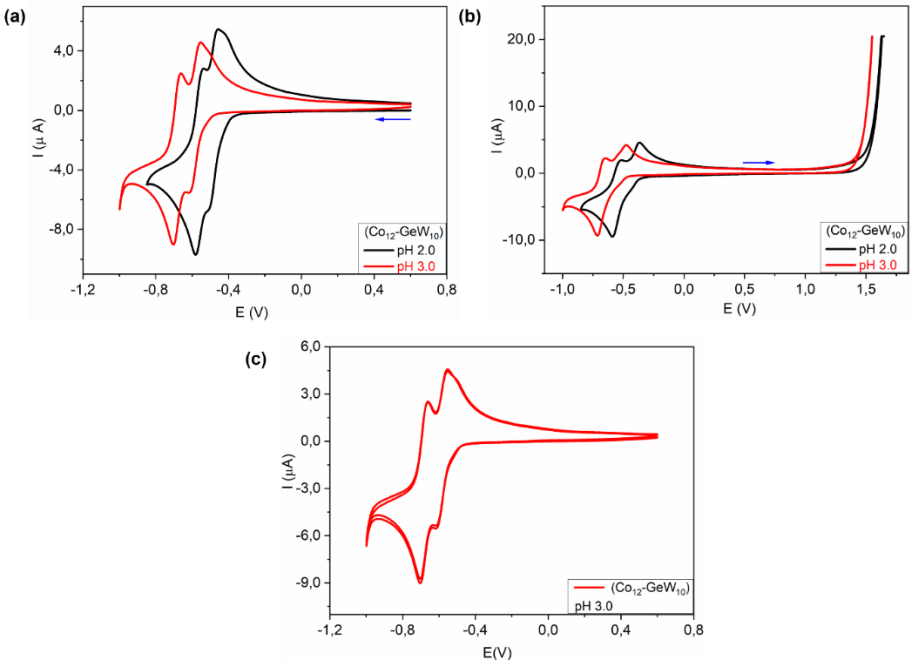


Figure 5.9 CVs recorded on an EPG electrode at a scan rate of 20 $mV.s^{-1}$ in 0.4 M LiH_2PO_4 + LiOH / pH 2.0 (black) and pH 3.0 (red). POM concentration, 0.2 mM. **a.** Potential scan towards negative potentials. **b.** Second cycle, potential scan first towards positive potentials, +1.55V, then towards negative potentials, -1.0 V. **c.** Two consecutive CVs recorded between 0.6 V and -1.0 V.

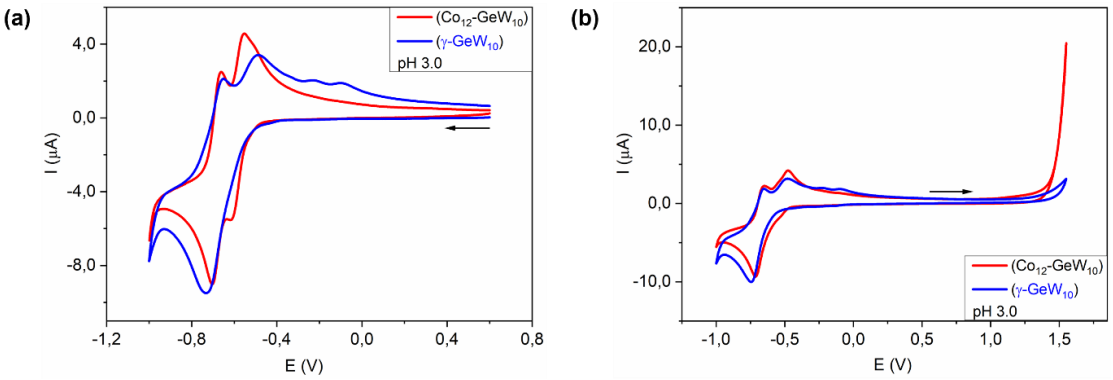


Figure 5.10 CVs of **Co_{12}-GeW$_{10}$** (red) and **γ-GeW$_{10}$** (blue) recorded on an EPG electrode at a scan rate of 20 $mV.s^{-1}$ in 0.4 M LiH_2PO_4 + LiOH / pH 3.0. The concentrations of both compounds are adjusted to facilitate comparison: 0.2 mM for **Co_{12}-GeW$_{10}$** and 1.2 mM for **γ-GeW$_{10}$**. **a.** Potential scan towards negative potentials, down to -1.0 V vs. SCE. **b.** Potential scan first towards positive potentials, up to +1.55 V, then towards negative potentials, down to -1.0 V vs. SCE.

Figure **5.10** compares the CVs of **Co_{12}-GeW$_{10}$** (red) and the **γ-GeW$_{10}$** ligand (blue) under the same conditions and with adjusted concentrations to facilitate comparison. The ligand shows a single-step reduction at -0.75 V vs. SCE, with two re-oxidation steps at -0.47 V and -0.65 V vs. SCE. Notably, the absence of a catalytic oxidation wave for the **γ-GeW$_{10}$** ligand indicates the active presence of Co^{2+} centres in **Co_{12}-GeW$_{10}$** (Figure **5.10.b**). Additionally, no modification of the electrode surface occurs during positive potential scans.

The stability of **Co_{12}-GeW_{10}** and its precursor ligand **γ-**GeW_{10} was tested at pH 3.0, where **γ-GeW_{10}** degrades rapidly, showing two small reduction waves before the large reduction wave **(A.5.1.a)**. These waves suggest the presence of $[GeW_{12}O_{40}]^{4-}$.[326] In contrast, the degradation of **Co_{12}-GeW_{10}** is slower. It leads to a different compound, evidenced by changes in its CV after 45 minutes, with the first reduction step splitting into a peak at -0.53 V and a reoxidation peak at -0.49 V vs. SCE (**A.5.1.b**).

Redox behaviour at pH 4.0, 5.0, and 5.9

Co_{12}-GeW_{10} is expected to show greater stability in solution at pH 4.0 and above than at pH 2.0 and 3.0.

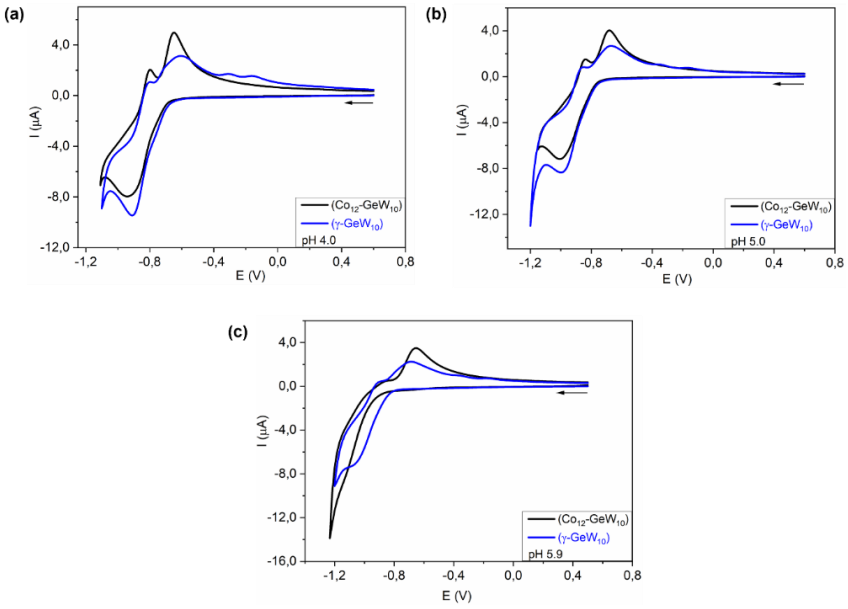


Figure 5.11 CVs of **Co_{12}-GeW_{10}** (black) and **γ-GeW_{10}** (blue) recorded on an EPG electrode at a scan rate of 20 $mV.s^{-1}$ in 0.4 M LiH_2PO_4 + LiOH. Negative scan down to -1.0 V vs SCE. The concentrations of both compounds are adjusted to facilitate comparison: 0.2 mM for **Co_{12}-GeW_{10}** and 1.2 mM for **γ-GeW_{10}**. **a.** pH 4.0, **b.** pH 5.0 and **c.** pH 5.9.

When comparing the CVs of **Co_{12}-GeW_{10}** and **γ-GeW_{10}** at pH 4.0 immediately after dissolution, both show similar redox behaviours (**Figure 5.11**.**a**). Scanning from 0.6 V vs. SCE towards negative potential reveals a single reduction step for each compound, with reduction peak potentials at -0.94 V for **Co_{12}-GeW_{10}** and -0.91 V for **γ-GeW_{10}**. During the reverse scan towards positive potential, **Co_{12}-GeW_{10}** exhibits two re-oxidation steps (E_{a1} = -0.65 V and E_{a2} = -0.80 V vs. SCE), while **γ-GeW_{10}** shows a first step at E_{a1} = -0.60 V and a composite wave with a shoulder at E_{a2} = -0.70 V and a main peak at E_{a3} = -0.80 V. Two small waves in **γ-GeW_{10}** CV indicate the beginning of degradation.

Approximately the same behaviour was observed at pH 5.0 for **Co_{12}-GeW_{10}** and **γ-GeW_{10}**, but at pH 5.9, the reduction wave was "ill-defined" with a peak that can be located around -1.12 V vs. SCE (**Figure 5.11.b and c**), and the process was irreversible and slow, with an oxidation peak, after this reduction, located at -0.65 V vs. SCE. The redox peak potential values are summarised in Table **A.5.2**.

a) Further Insights into the Stability of Co_{12}-GeW_{10}

As mentioned earlier, the **Co_{12}-GeW_{10}** complex was expected to exhibit enhanced stability at pH 4.0 and above. However, observations revealed a novel phenomenon that does not appear to be the degradation of the starting compound, but rather an evolution towards a highly stable form in solution starting from pH 4.0.

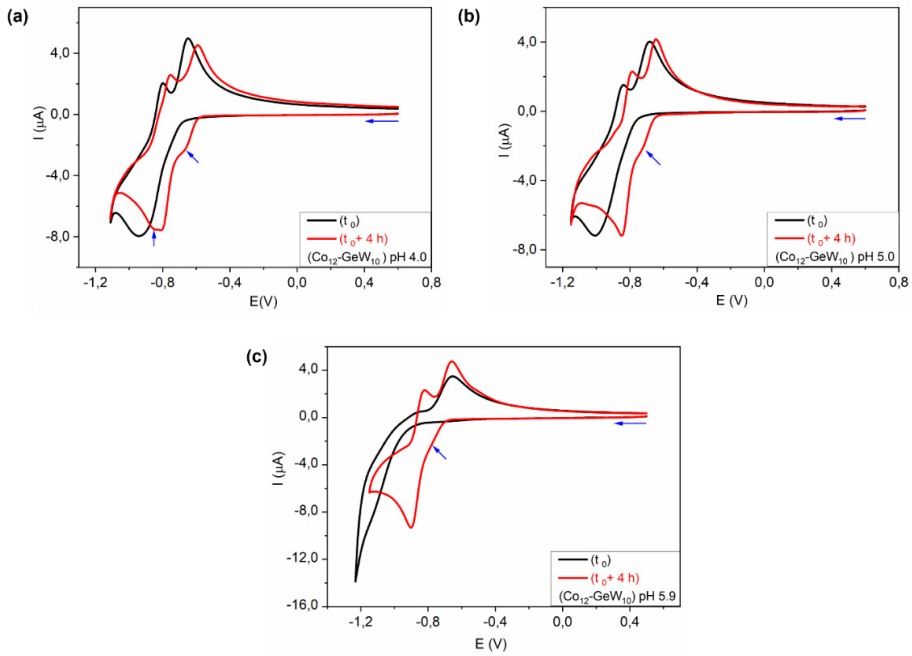


Figure 5.12 CVs of **Co_{12}-GeW_{10}** recorded at t_0 (black) and t_0 + 4 h (red), on an EPG electrode at a scan rate of 20 mV.s^{-1} in 0.4 M LiH_2PO_4 + LiOH. Negative scan down to -1.0 V vs SCE. POM concentration, 0.2 mM. **a.** pH 4.0 **b.** pH 5.0 and **c.** pH 5.9.

CV of **Co_{12}-GeW_{10}** in Figure **5.12.a**, taken immediately after dissolution in 0.4 M LiH2PO4 + LiOH at pH 4.0, shows a shift towards less negative potentials by about 100 mV over 4 hours. New reduction steps appear, one before the prominent peak at -0.67 V vs. SCE and another splitting the primary peak at -0.84 V vs. SCE.

Similarly, at pH 5.0, there is a more significant shift in peak potentials (△E = 140 mV) and a more pronounced first reduction step at -0.73 V vs. SCE (Figure **5.12.b** and Table **5.3**).

At pH 5.9, the differentiation between the new reduction step and the main peak is less distinct, seen as a slight shoulder at -0.81 V vs. SCE (Figure **5.12.c**). The shift in potentials towards less negative values is even greater than at pH 5.0, △E = 170 mV.

Table 5.3 Peak potential values in the media 0.4 M LiH_2PO_4 + LiOH at pH 4.0, 5.0 and 5.9 for **Co_{12}-GeW_{10},** taken from the CVs for the first scan and after stabilisation. Reference electrode: SCE. Auxiliary electrode: Pt. Working electrode: EPG. Scan rate 20 $mV.s^{-1}$.

	1st scan		After stabilisation	
	E_{Pc}	E_{Pa}	E_{Pc}	E_{Pa}
pH 4.0	-0.91	-0.60	-0.67*	-0.59
		-0.70	-0.81	-0.75
		-0.80	-0.84	-0.82
pH 5.0	-0.99	-0.67	-0.73*	-0.64
		-0.86	-0.85	-0.78
pH 5.9	-1.07	-0.69	-0.81*	-0.66
		-0.90	-0.90	-0.82

* ***Shoulder on the main wave.***

Interpretation

These observations indicate that **Co_{12}-GeW_{10}** undergoes a gradual structural rearrangement or change in its electronic configuration when dissolved in solutions with a pH of 4.0 and above. This process leads to the formation of a highly stable form, which exhibits distinct redox behaviour compared to the original **Co_{12}-GeW_{10}**. The stability of this new form increases with rising pH, as demonstrated by the CV results, which remain reproducible for more than 48 hours.

Reinvestigating the redox behaviour of Co_{12}-GeW_{10}

Once the stable form of **Co_{12}-GeW_{10}** was obtained, the redox behaviour of the Co^{2+} centres can be examined by extending the positive potential scan (reverse scan) to higher values. Initially, this stepwise approach identified the CV wave related to Co^{2+} oxidation, and the potential range was then expanded to assess its catalytic efficiency for water oxidation.

Figure **5.13.a** shows the CV with a reverse scan to +1.20 V vs SCE, highlighting the oxidation wave of Co^{2+} to Co^{3+} with a peak at 1.08 V and a reduction peak at +0.93 V. Extending the scan to +1.25 V (Figure **5.13.b**) not only increases the oxidation current but also reveals a cross-over of the current curve during the reverse scan at 1.15 V. This cross-over, caused by the increase in current due to electrode surface modification, clearly

indicates that the oxidation of Co^{2+} centres in the **Co_{12}-GeW_{10}** complex leads to the formation of cobalt oxides. These oxides, deposited on the working electrode surface, facilitate the electrocatalytic water oxidation reaction. As the applied potential is increased further (Figures **5.13.c** and **d**), the catalytic current continues to rise.

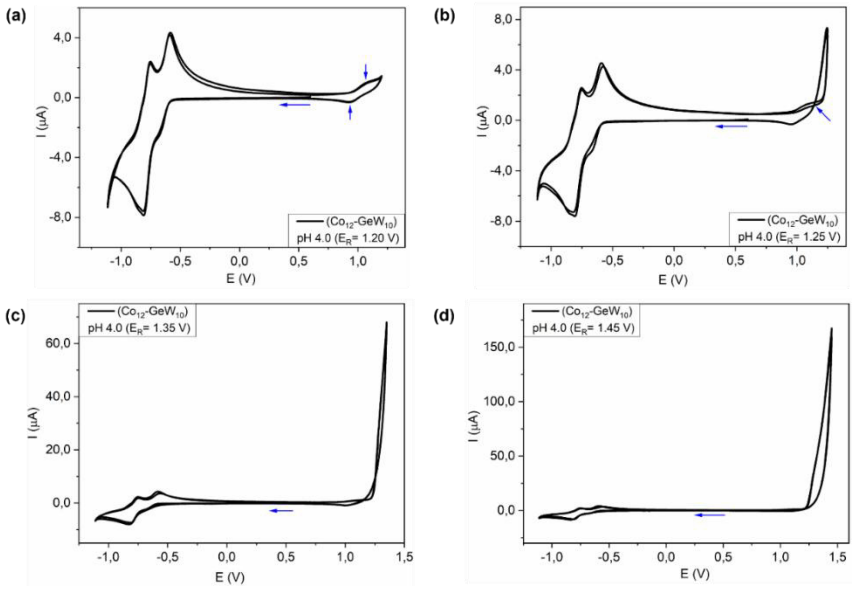


Figure 5.13 CVs of **Co_{12}-GeW_{10}** recorded on an EPG electrode at a scan rate of 20 $mV.s^{-1}$ in 0.4 M LiH_2PO4 + LiOH / pH 4.0. Potential scan towards the negative direction, down to -1.0 V vs SCE, and then towards the positive direction up to the indicated E_R value. **a.** E_R = 1.20 V vs SCE. **b.** E_R = 1.25 V vs SCE. **c.** E_R = 1.35 V vs SCE. **d.** E_R = 1.45 V vs SCE.

Interpretation

These results demonstrate that the stable form of **Co_{12}-GeW_{10}** exhibits electrocatalytic activity towards water oxidation. The formation of cobalt oxides on the electrode surface plays a crucial role in enhancing this catalytic activity.[327]

Investigation of Co^{2+} oxidation at pH 5.0 with increasing E_R values.

At pH 5.0 and 5.9, CVs shift towards negative potentials, aiding Co^{2+} oxidation. CVs were recorded with two cycles: a negative scan to reduce tungsten centres (-1.15 V vs SCE), followed by a positive scan with increasing reverse potential (E_R) in each set of two cycles.

Figures **5.14.a** and **b** show the CVs at pH 5.0 for E_R = 0.60 V and 1.00 V. At these potentials, the oxidation of Co^{2+} centres was not observed, and the CVs were superimposable. This indicates that higher reversal potentials than +1.0 V vs. SCE are needed for the oxidation of Co^{2+} in **Co_{12}-GeW_{10}** at pH 5.0. As the reversal potential (E_R) increased from 1.10 V to 1.20 V vs SCE, the CVs reveal fascinating insights into the redox behaviour of **Co_{12}-GeW_{10}** at pH 5.0.

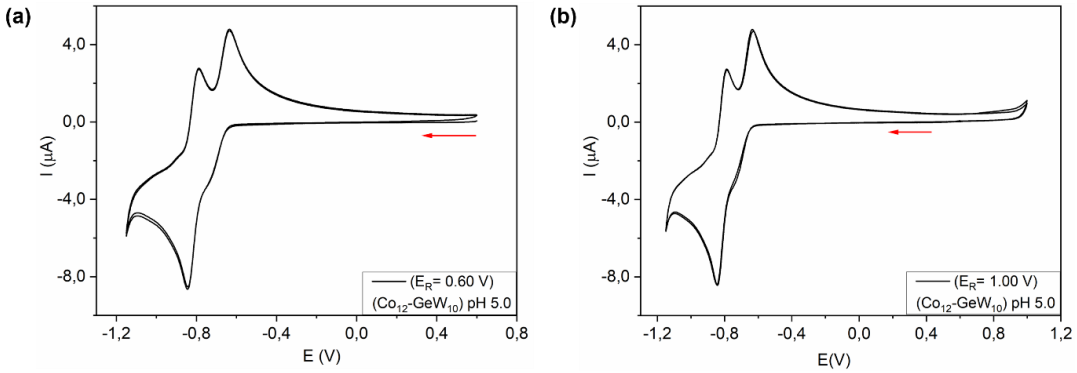


Figure 5.14 CVs of **Co_{12}-GeW_{10}** recorded on an EPG electrode at a scan rate of 20 mV.s^{-1} in 0.4 M LiH_2PO_4 + LiOH / pH 5.0. Potential scan towards the negative direction, down to -1.0 V vs SCE, and then towards the positive direction up to the indicated E_R value. **a.** E_R = 0.60 V vs SCE. **b.** E_R = 1.00 V vs SCE.

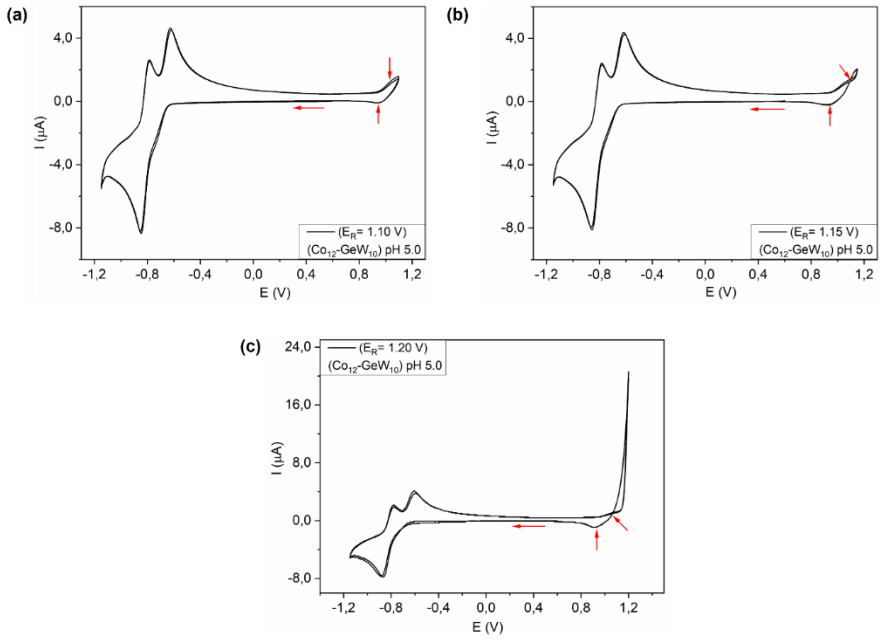


Figure 5.15 CVs of **Co_{12}-GeW_{10}** recorded on an EPG electrode at a scan rate of 20 mV.s^{-1} in 0.4 M LiH_2PO_4 + LiOH / pH 5.0. Potential scan towards the negative direction, down to -1.0 V vs SCE, and then towards the positive direction up to the indicated E_R value. **a.** E_R = 1.10 V vs SCE. **b.** E_R = 1.15 V vs SCE. **c.** E_R = 1.20 V vs SCE.

Figure **5.15.a** displays the CV recorded at an electrode potential (E_R) of 1.10 V. In this scan, an oxidation wave corresponding to Co^{2+} centres appears, peak at 1.05 V vs. SCE. During the reverse scan, a distinct reduction wave is observed, peak at 0.95 V vs. SCE. In Figure **5.15.b**, the CV recorded at E_R = 1.15 V shows that the currents for oxidation and reduction intersect at a potential of +1.10 V. This value appears to be the threshold at pH 5.0, above which cobalt oxides begin to deposit on the surface of the working electrode. Below this threshold, the oxidation of Co^{2+} centres can be considered reversible and occurs without altering the working electrode surface, as indicated by the superimposition of two consecutive CVs. Figure **5.15.c** presents the CV recorded at E_R = 1.20 V. As anticipated,

the catalytic current increases, and the same intersection of oxidation and reduction currents was observed. Additionally, during the second cycle of potential scanning in the negative direction, a slight shift of the W^{6+} centres reduction wave towards more negative potentials was noted. This suggests that the modification of the electrode surface makes the reduction process more challenging.

These results suggest that the oxidation of Co^{2+} centres in **Co_{12}-GeW_{10}** at pH 5.0 becomes irreversible above a threshold potential of +1.10 V, leading to the deposition of cobalt oxides on the working electrode surface. This surface modification enhances the catalytic activity towards water oxidation but also hinders the reduction of W^{6+} centres. To further investigate this hypothesis, the E_R value is increased further.

Investigation of catalytic activity and surface changes at high E_R values

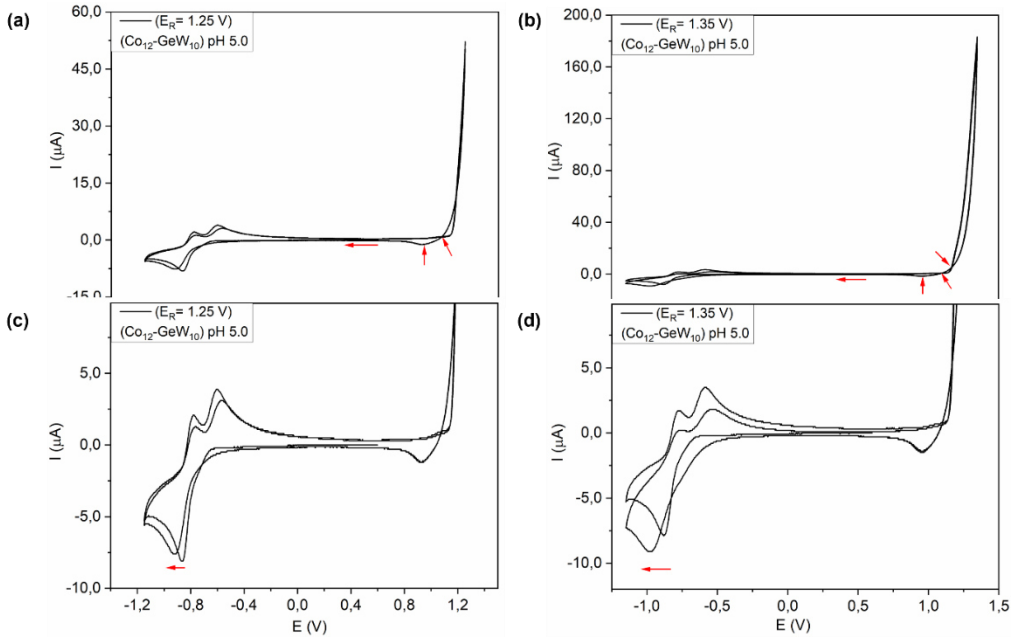


Figure 5.16 CVs of **Co_{12}-GeW_{10}** recorded on an EPG electrode at a scan rate of 20 $mV.s^{-1}$ in 0.4 M LiH_2PO_4 + LiOH / pH 5.0. Potential scan towards the negative direction, down to -1.0 V vs SCE, and then towards the positive direction up to the indicated E_R value. **a.** E_R = 1.25 V vs SCE. **b.** E_R = 1.35 V vs SCE. **c.** Zoom of Figure **a**. **d.** Zoom of Figure **b**.

At high E_R values suitable for evaluating the catalytic activity of **Co_{12}-GeW_{10}** for water oxidation, namely E_R = 1.25 V (Figure **5.16.a**) and E_R = 1.35 V (Figure **5.16.b**), an exponential increase in the oxidation current was observed, along with a shift of the W^{6+} centres reduction wave towards negative potentials during the second cycles (Figure **5.16.c** and **d**). While the deposition of cobalt oxides appears to favour water oxidation, it also hinders the electrode's reduction capabilities.

Figure **5.16.a** shows the CV recorded at E_R = 1.25 V. The oxidation current increases significantly, indicating enhanced catalytic activity for water oxidation. However, the W^{6+} centre reduction wave shifts towards negative potentials, suggesting that the deposited cobalt oxides hinder the reduction process (Figure **5.16.c**).

Figure **5.16.b** shows the CV recorded at E_R = 1.35 V. The oxidation current further increases, demonstrating even greater catalytic activity. However, the shift of the W^{6+} centres reduction wave towards negative potentials becomes more pronounced, further emphasising the inhibitory effect of cobalt oxide deposition on reduction (Figure **5.16.d**).

Electrocatalytic Aativity at pH 5.9

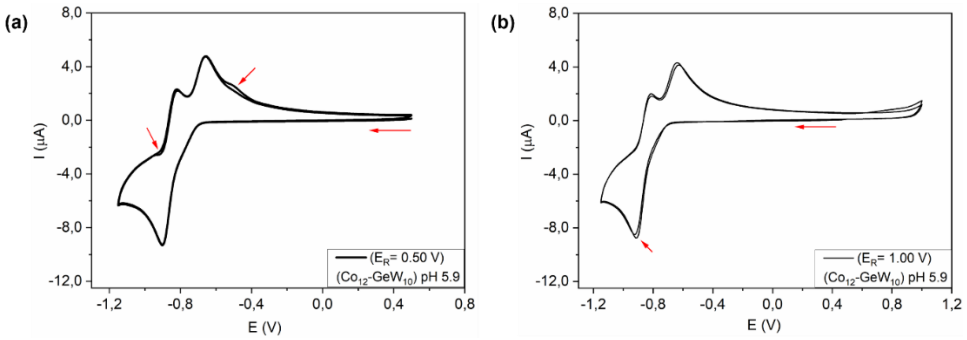


Figure 5.17 CVs of **Co_{12}-GeW_{10}** recorded on an EPG electrode at a scan rate of 20 $mV.s^{-1}$ in 0.4 M LiH_2PO_4 + LiOH / pH 5.9. Potential scan towards the negative direction, from 0.50 V to -1.15 V vs SCE, and then towards the positive direction up to the indicated E_R value. **a.** E_R = 0.50 V vs SCE. **b.** E_R = 1.00 V vs SCE.

A similar study at pH 5.9 showed few notable differences. Unlike pH 5.0, the two consecutive CVs at a scan rate of 20 mV.s-1 were not superimposable. The CVs at E_R = +0.50 V vs SCE, where the second CV has an inflexion point at -0.91 V and a bulge at -0.48 V, indicating slower scan rates may be needed for a complete characterisation (Figure **5.17.a**). CVs at E_R = +1.00 V vs SCE, revealing an early shift in the reduction peak potential of W^{6+} centres, suggesting easier surface modification of the working electrode at pH 5.9 (Figure **5.17.b**).

Figure **5.17.b** shows the CVs recorded at E_R = +1.00 V vs SCE. A slight shift in the reduction peak potential of W^{6+} centres is already apparent, a phenomenon that was only observed at E_R = +1.20 V vs SCE at pH 5.0. This suggests that the surface modification of the working electrode occurs more readily at pH 5.9.

One key difference observed at pH 5.9 compared to pH 5.0 is the onset potential for the water oxidation catalytic reaction. At pH 5.9, the reaction initiates very early, at +1.02 V vs SCE, and is concomitant with the oxidation of the Co^{2+} centres. Unlike at pH 5.0, the oxidation of Co^{2+} centres is not observed as a distinct peak. However, their reduction during

the reverse scan is visible, with a reduction peak potential of +0.83 V vs SCE (Figure **5.18. a**). The oxidation and reduction currents intersect at +0.97 V vs SCE, indicating an earlier onset of deposition. Additionally, the catalytic current increases more rapidly at pH 5.9 compared to pH 5.0.

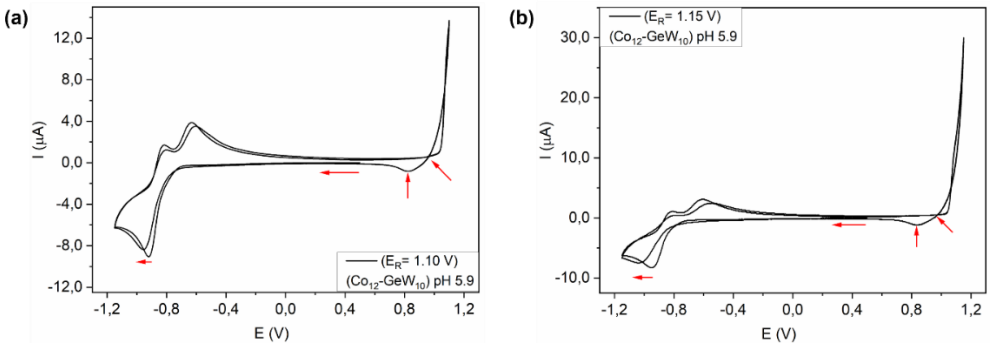


Figure 5.18 CVs of **Co_{12}-GeW_{10}** recorded on an EPG electrode at a scan rate of 20 mV.s^{-1} in 0.4 M LiH_2PO_4 + LiOH / pH 5.9. Potential scan towards the negative direction, from 0.50 V to -1.15 V vs SCE, and then towards the positive direction up to the indicated E_R value. **a.** E_R = 1.10 V vs SCE. **b.** E_R = 1.15 V vs SCE.

Due to the observed deposition of cobalt oxides, which enhances water oxidation but hinders reduction, the study was limited to an E_R value of 1.15 V vs SCE (Figure **5.18.b**).

The results suggest that at pH 5.9, the surface modification of the working electrode occurs more readily, leading to an earlier onset of water oxidation. However, this surface modification also inhibits the reduction of the W^{6+} centres.

Comparison of water oxidation behaviours at pH 5.0 and pH 5.9

A comparison of the results at pH 5.0 and pH 5.9 reveals that the electrochemical oxidation of water by Co^{2+} centres, as summarised by electrochemical equations (5.3), (5.4), and (5.5), is more efficient at pH 5.9 (Figure **5.19.a**).

To confirm that cobalt oxide deposits on the electrode do not inhibit water oxidation, the study at pH 5.0 included cycles from 0.50 V to 1.35 V. The first five CVs showed a continuous increase in oxidation current, indicating the electrode surface remained active despite the deposits. No decrease in current was noted between the two series of cycles (Figure **5.19.b**).

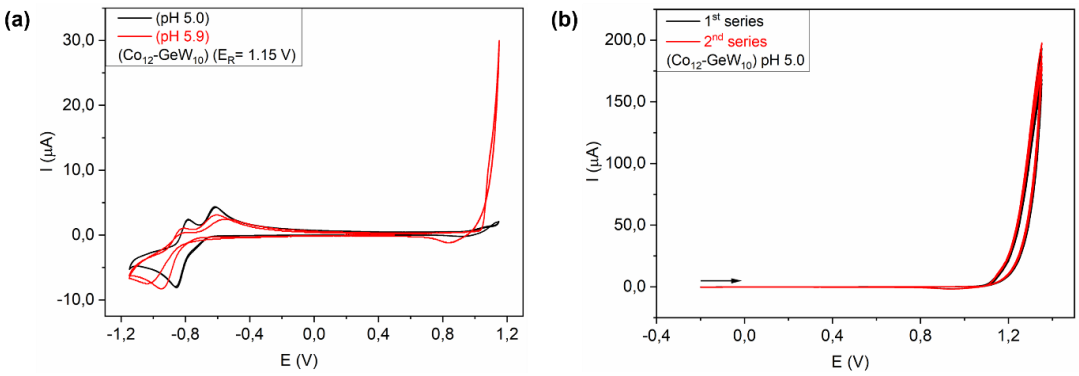


Figure 5.19 CVs of **Co_{12}-GeW_{10}** recorded on an EPG electrode at a scan rate of 20 mV.s^{-1} in 0.4M LiH_2PO_4 + LiOH. **a.** Potential scan towards the negative direction, from 0.50 V to -1.15 V vs SCE, followed by a scan towards the positive direction up to an E_R value of 1.15 V vs SCE. pH 5.0 (black) and pH 5.9 (red). **b.** Potential scan from positive to negative directions, between 0.5 V and 1.35 V vs SCE. 2 series of 5 cycles each / pH 5.0.

Evaluation of the catalytic efficiency for water oxidation

To assess the catalytic efficiency of **Co_{12}-GeW_{10}** for water oxidation, compare its CV to that of the **γ-GeW_{10}** ligand under identical conditions (Figure **5.20**). The normalised current (I_N) can be calculated for various potential values using equation (5.6):

$$I_N = \left[\frac{I_X - I_0}{I_0}\right] \times 100 \qquad (5.6)$$

where I_0 is the current measured at a given potential on the CV of **γ-GeW_{10}** and I_X , is the current measured at the same potential on the CV of **Co_{12}-GeW_{10}**.

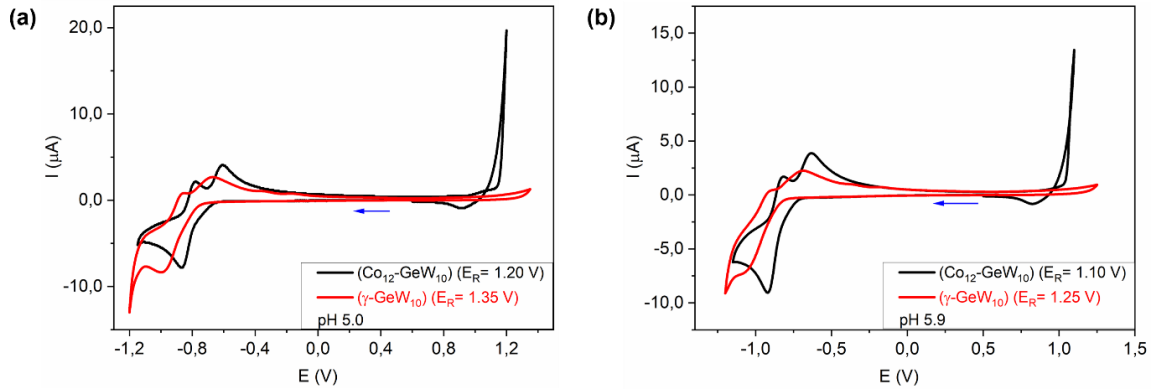


Figure 5.20 CVs of **Co_{12}-GeW_{10}** (black) and **γ-GeW_{10}** (red) recorded on an EPG electrode at a scan rate of 20 mV.s^{-1} in 0.4M LiH_2PO_4 + LiOH. There is a potential scan towards the negative direction, followed by a scan towards the positive direction. **a.** pH 5.0. **b.** pH 5.9.

Table **5.4** summarises the values of I_0, I_X, and I_N obtained at pH 5.0 and pH 5.9. Figure **5.21** illustrates the trend in catalytic efficiency for water oxidation in both media.

The comparison of CVs and the calculation of normalised currents reveal that **Co_{12}-GeW_{10}** exhibits significantly enhanced catalytic activity for water oxidation compared to the **γ-GeW_{10}** ligand alone. This enhanced efficiency was particularly evident at pH 5.9, supporting the proposed mechanism for water oxidation by Co^{2+} centres.

Table 5.4 Oxidation currents (I_0) measured on the CVs of **γ-GeW_{10}**, oxidation currents (I_x) measured on the CVs of **(Co_{12}-GeW_{10})**, and normalised current values (I_N) calculated at pH 5.0 and pH 5.9.

E / V vs. SCE	I_0 (μA)	I_x (μA)	I_N (%)	I_0 (μA)	I_x (μA)	I_N (%)
	pH 5.0			pH 5.9		
1.00	0.38	1.12	195	0.49	1.48	202
1.10	0.49	1.59	224	0.60	13.45	2142
1.15	0.56	2.08	271	0.69	29.50	4175
1.20	0.68	20.8	2959	---	---	---
1.25	0.82	50.30	6034	---	---	---
1.35	1.29	174.30	13411	---	---	---

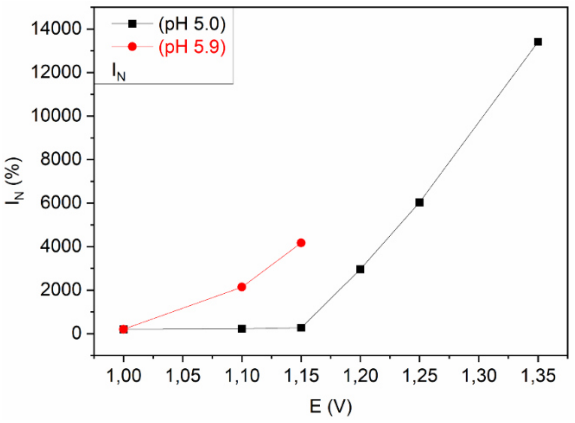


Figure 5.21 Plot of the normalised current (I_N) vs. potential at pH 5.0 (black) and pH 5.9 (red).

Electrocatalytic behaviour toward reduction

The electrocatalytic reduction properties of **Co_{12}-GeW_{10}** were studied in the homogeneous phase. The electron transfer process was found to be diffusion-controlled, indicating that the compound does not adsorb onto the electrode surface, and the reaction occurs exclusively in solution. The impact of scan rate on the reduction peak current in pH 5.0 and 5.9 was analysed (**Figure A.5.2.a** and **b**). An increase in reduction current with the square root of the scan rate supports the diffusion-controlled behaviour, consistent with the Randles-Sevcik equation. The linear correlation coefficient R^2 averaged 0.9964, showing

slight deviation at low scan rates (v ≤ 10 mV/s). Thus, the electrocatalytic reduction processes are believed to occur in solution within the homogeneous phase.

Electrocatalytic reduction of dioxygen

The electrocatalytic O_2 reduction reaction was studied at pH 5.0 and 5.9, with O_2 saturation achieved through bubbling and maintaining a positive pressure of this gas. CV assessed the catalytic activity of **Co_{12}-GeW_{10}** at scan rates of 10 to 200 mV.s^{-1}. Figure **5.22** shows CVs under inert (black) and oxygen (red) conditions at 20 mV.s^{-1}, revealing a notable positive shift in the onset potential for O_2 reduction due to the catalytic properties of **Co_{12}-GeW_{10}**. At pH 5.0, the reduction begins at -0.67 V vs. SCE, shifting to -0.49 V vs. SCE in the presence of O_2, equating to a 180 mV shift ((**Figure 5.22.a**) The normalised current, I_N, calculated using equation 5 (6), indicated a catalytic efficiency of about 190%, which is relatively low compared to typical values for POMs.[328] This efficiency remained constant across varying scan rates, raising questions about the actual catalytic activity of **Co_{12}-GeW_{10}** Table **5.5** and Figure **5.23.b**).

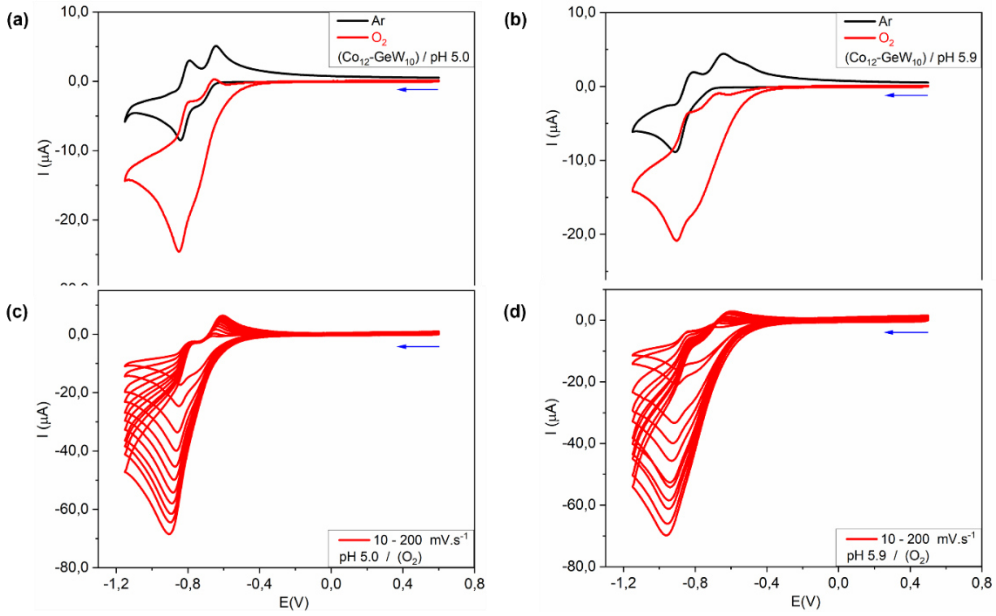


Figure 5.22 CVs of **Co_{12}-GeW_{10}** recorded on an EPG electrode in 0.4M LiH_2PO_4 + LiOH, under Ar atmosphere (black) and in an O_2-saturated solution under a positive pressure of O_2 (red). **a.** pH 5.0 at scan rate 20 mV.s^{-1}. **b.** pH 5.9 at scan rate 20 mV.s^{-1}. **c.** pH 5.0 at varying scan rates from 10 to 200 mV.s^{-1}. **d.** pH 5.9 at varying scan rates from 10 to 200 mV.s^{-1}. Potential scan from positive to negative directions.

At pH 5.9(Figure **5.21.b**), the onset potential for O_2 reduction shifts positively to -0.45 V vs. SCE, compared to -0.75 V vs. SCE for **Co_{12}-GeW_{10}** alone (ΔE = 300 mV). The catalytic reaction starts at higher potentials than at pH 5.0 (Figure **5.23.a**), but the efficiency at 20

mV.s^{-1} is lower (< 140%). However, at scan rates above 60 mV.s^{-1}, the efficiency surpasses that at pH 5.0, contrary to the usual trend of increased catalytic current at lower scan rates.

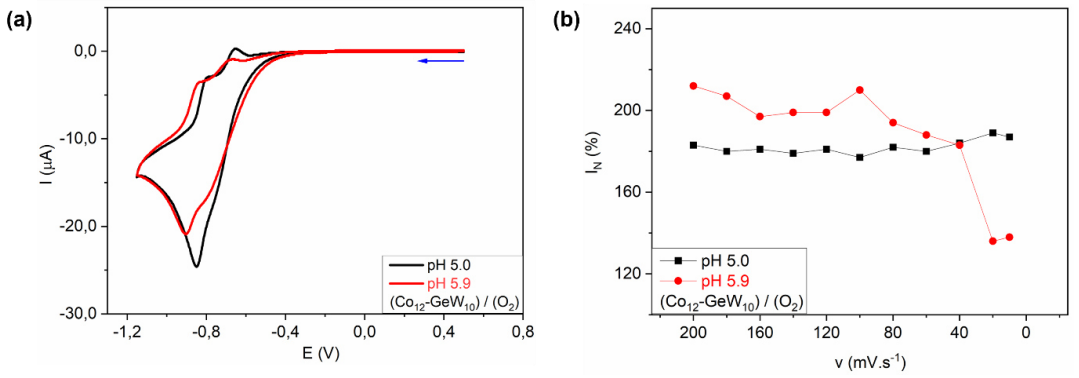


Figure 5.23 a. CVs at a scan rate of 20 mV.s^{-1} of **Co_{12}-GeW_{10}** recorded on an EPG electrode in 0.4 M LiH_2PO_4 + LiOH solution saturated by O_2 and under a positive pressure of O_2, pH 5.0 (black) and pH 5.9 (red). **b.** Evolution of the normalised current, **I_N**, as a function of the scan rate at pH 5.0 (black) and pH 5.9 (red).

The observations on the electrocatalytic reduction of O_2 by **Co_{12}-GeW_{10}** at pH 5.0 and pH 5.9 prompted a study of dioxygen reduction on a bare EPG electrode. Comparing these results with those in the presence of **Co_{12}-GeW_{10}** (Figure **5.24**), we conclude that the O_2 reduction observed with **Co_{12}-GeW_{10}** is not catalysed by reduced **Co_{12}-GeW_{10}** but occurs directly at the working electrode's surface.

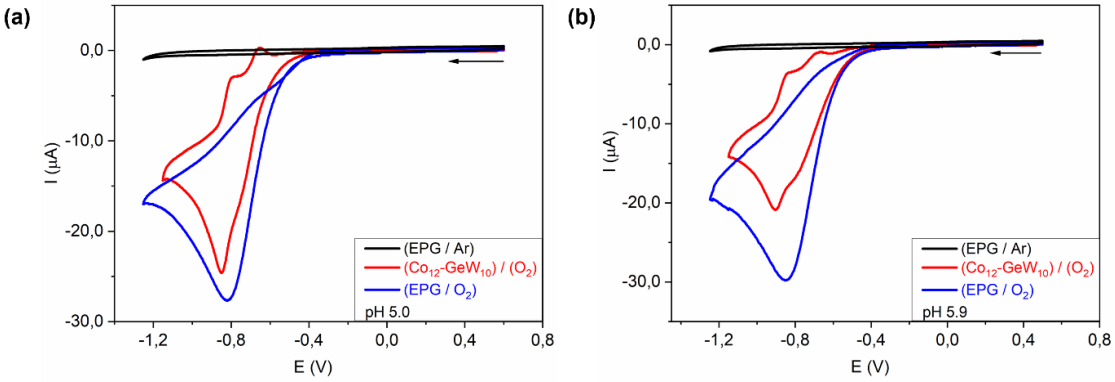


Figure 5.24 CVs recorded on an EPG electrode at a scan rate 20 mV.s^{-1}. Electrolyte alone under argon atmosphere (black). O_2 saturated solution under a positive pressure of O_2 in the presence of **Co_{12}-GeW_{10}** (red), and in the absence of **Co_{12}-GeW_{10}** (blue). **a.** In 0.4M LiH_2PO_4 + LiOH, pH 5.0. **b.** In 0.4M LiH_2PO_4 + LiOH, pH 5.9.

The normalised reduction current of O_2 on the bare EPG electrode was analysed as a function of scan rate (see Figure **A.5.3)**. The current (I_0) recorded in an argon atmosphere (Figure **A.5.4**) reveals that the catalytic efficiency of **Co_{12}-GeW_{10}** for the electrochemical reduction of O_2 is negligible when compared to the normalised current from the CVs.

Table 5.5 Values of the normalised currents, I_N, calculated for the different electrocatalytic reduction processes of O_2 in both pH 5.0 and pH 5.9 media at different scan rates ranging from 200 to 10 $mV.s^{-1}$.

v ($mV.s^{-1}$)	200	180	160	140	120	100	80	60	40	20	10
Co_{12}-GeW_{10} / O_2											
pH 5.0 / %	183	180	181	179	181	177	182	180	184	189	187
pH 5.9 / %	212	207	197	199	199	210	194	188	183	136	138
Electrolyte alone / O_2											
pH 5.0 / %	2340	2678	2849	2978	3109	3328	3576	3909	4406	5227	4875
pH 5.9 / %	2641	2997	3293	3255	3436	3593	3843	4275	4743	5860	6338

Electrocatalytic reduction of nitrite ion and hydrogen peroxide

Nitrite reduction

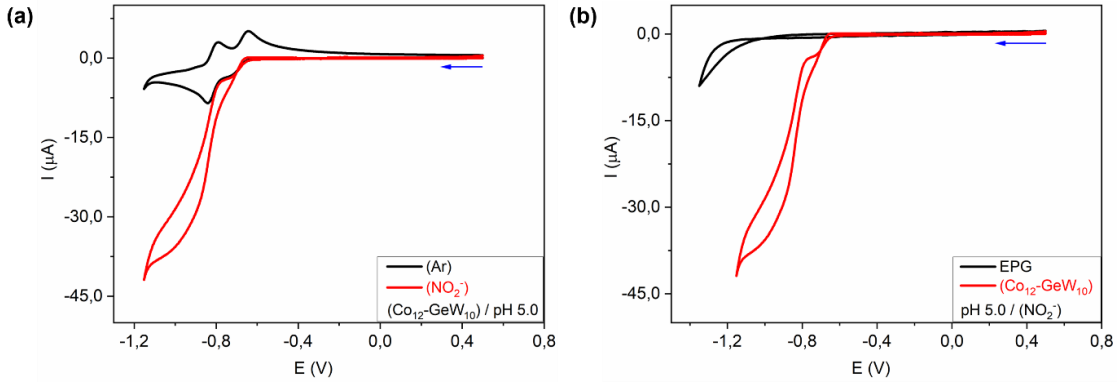


Figure 5.25 CVs recorded on an EPG electrode at scan rate 20 $mV.s^{-1}$ in 0.4 M LiH_2PO_4 + LiOH / pH 5.0. **a.** **Co_{12}-GeW_{10}** alone (black) and **Co_{12}-GeW_{10}** + NO_2^- (red). **b.** NO_2^- alone (black) and **Co_{12}-GeW_{10}** + NO_2^- (red).

The electrocatalytic reduction of nitrite ions was studied at pH 5.0, where NO_2^- is predominant. CV in **Figure 5.25.a** shows that the reduction of NO_2^- starts with the reduction of W^{6+} centres in **Co_{12}-GeW_{10}**. The normalised current increased with decreasing scan rates, indicating an electrocatalytic process. Figure **5.25.b** compares the electrochemical reduction of NO_2^- on a bare EPG electrode versus **Co_{12}-GeW_{10}**, showing that the onset potential for the bare EPG electrode is -1.14 V vs. SCE, while it's -0.66 V vs. SCE in the presence of **Co_{12}-GeW_{10}**, along with a notable exponential rise in reduction current.

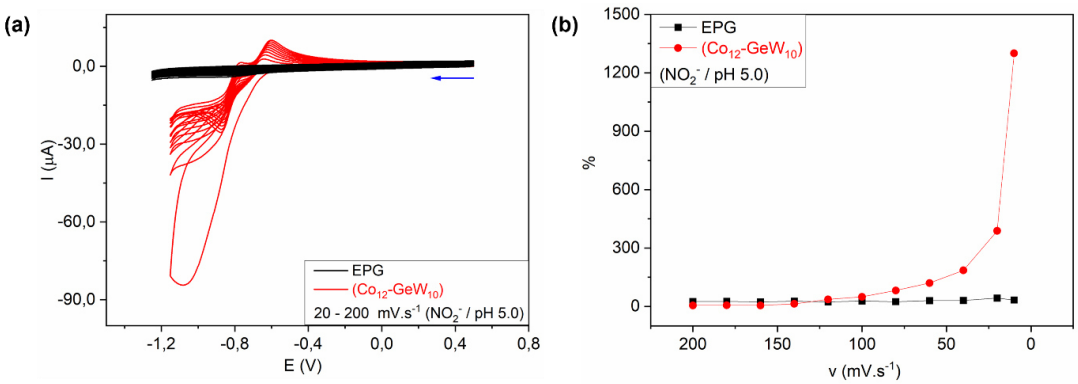


Figure 5.26 a. CVs of nitrite ion reduction in 0.4 M LiH_2PO_4 + LiOH / pH 5.0, recorded on an EPG electrode at potential scan rates ranging from 200 to 10 $mV.s^{-1}$. Black CVs: in the absence of **Co_{12}-GeW_{10}**. Red CVs: in the presence of **Co_{12}-GeW_{10}** with γ = 100. **b.** Evolution of the normalised current, I_N, as a function of the scan rate (values calculated from data obtained from the CVs in Figure **5.26 (a)**.

The variation of the reduction current of NO_2^- with potential scan rate, both with and without POM, highlights the catalytic role of **Co_{12}-GeW_{10}** (Figure **5.26**). Without **Co_{12}-GeW_{10}**, the reduction current of nitrite was weak, with only a slight increase above 100% even at low scan rates. In contrast, the presence of **Co_{12}-GeW_{10}** led to a significant enhancement as the scan rate decreased from 200 $mV.s^{-1}$. However, the normalised current remained modest between 200 and 100 $mV.s^{-1}$, with I_N values below 150%. A substantial increase in normalised current was observed at scan rates of 60 $mV.s^{-1}$ and below, peaking at 1300% at 10 $mV.s^{-1}$ (see Table **A.5.3**).

Hydrogen peroxide reduction

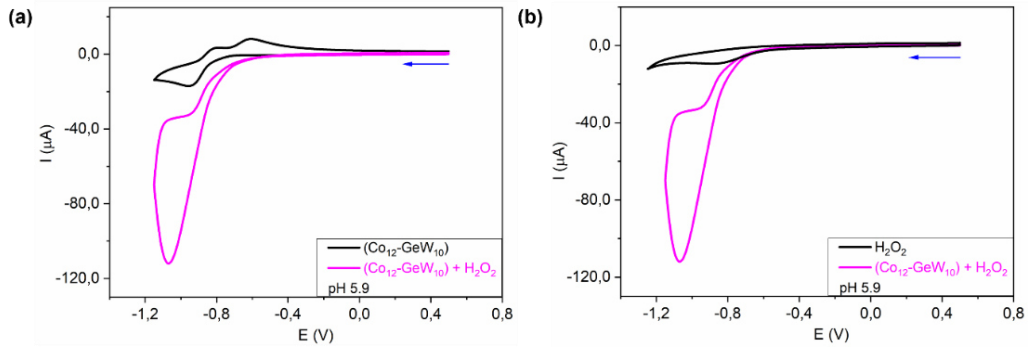


Figure 5.27 CVs recorded on an EPG electrode at scan rate 20 $mV.s^{-1}$ in 0.4M LiH_2PO_4 + LiOH / pH 5.9. **a. Co_{12}-GeW_{10}** alone (black) and **Co_{12}-GeW_{10}**+ H_2O_2 (purple). **b.** H_2O_2 alone (black) and **Co_{12}-GeW_{10}** + H_2O_2 (purple).

The catalytic properties of **Co_{12}-GeW_{10}** for reducing hydrogen peroxide in LiH_2PO_4 + LiOH at pH 5.9 were examined. While **Co_{12}-GeW_{10}** shows no effect on O_2 reduction, it demonstrates significant catalytic activity for H_2O_2 reduction. At a scan rate of 20 $mV.s^{-1}$, the catalytic current for H_2O_2 reduction is substantially higher than that of **Co_{12}-GeW_{10}** alone. As shown in Figure **5.27** at a scan rate of 100 $mV.s^{-1}$, the difference in currents provides a

clear comparison of the two CVs, with the normalised current, I_N, exceeding 500% (Figure **5.27.a** and Table **A.5.3.**). The CV of H_2O_2 reduction without POM shows similar onset potentials with or without **Co_{12}-GeW_{10}** (Figure **5.27.b**), resulting in normalised currents of 524% and 467%, respectively. A study of the scan rate could further explore whether a slower scan increases I_N.

The reduction current of H_2O_2 was studied on a bare glassy carbon (EPG) electrode at various scan rates, both with and without **Co_{12}-GeW_{10}** (Figure **A.5.5 (a)**). The catalytic effect of **Co_{12}-GeW_{10}** on H_2O_2 reduction was minimal, with noticeable differences in current responses only at scan rates of 60 $mV.s^{-1}$ or lower (Figure **A.5.5 (b)**). At a scan rate of 10 $mV.s^{-1}$, the normalised current, I_N, exceeded 10000% (Table **A.5.3**).

In conclusion, while the observations at pH 5.9 under slow scan rate conditions are promising, the electrochemical behaviour of the **Co_{12}-GeW_{10}** compound remains complex to analyse. A more comprehensive understanding of its electrocatalytic properties could be achieved by immobilising the compound onto the electrode surface and conducting studies in the heterogeneous phase.

5.4.2. Electrochemical Characterisation of the Ni_{12}-GeW_{10}

Redox behaviour

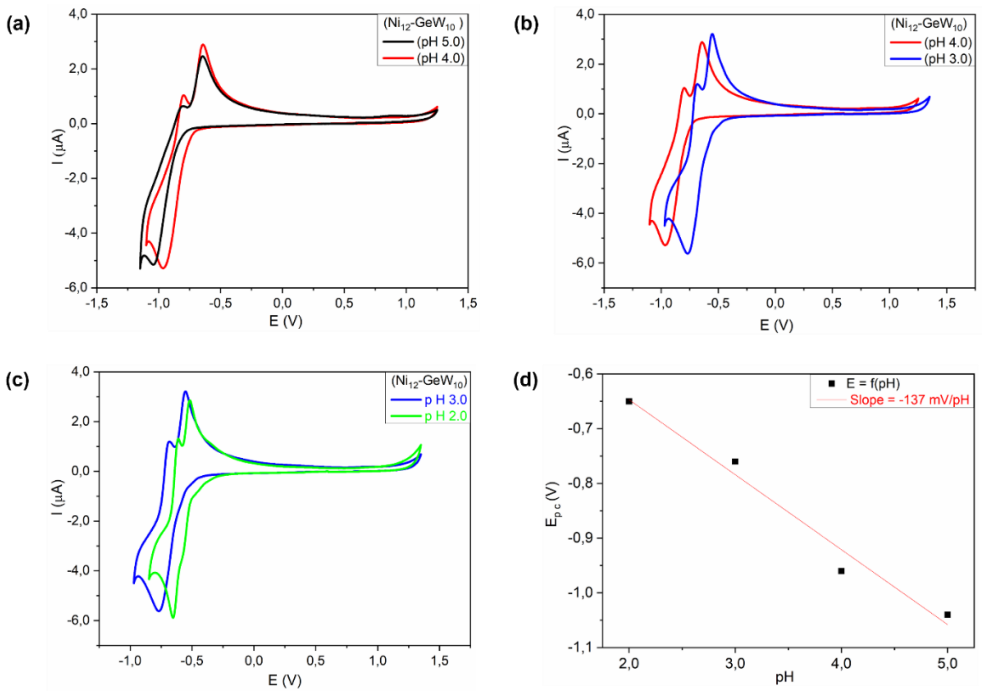


Figure 5.28 CVs recorded with an EPG working electrode, a SCE reference electrode and a Pt counter electrode at a scan rate of 10 $mV.s^{-1}$ in 0.4 M LiH_2PO_4 + LiOH. POM concentration: 0.2 mM.

a. pH 5.0 (black) and 4.0 (red). **b.** pH 4.0 (red) and 3.0 (blue). **c.** pH 3.0 (blue) and 2.0 (green). **d.** Dependence of the reduction peak potential on the pH.

Table 5.6 Reduction (E_{Pc}) and oxidation (E_{Pa}) peak potential values obtained in the medium 0.4 M LiH_2PO_4 + LiOH at 4 different pH values: 2.0, 3.0, 4.0 and 5.0, with a POM concentration of 0.2 mM.

V / SCE	pH 5.0		pH 4.0		pH 3.0		pH 2.0	
E_{Pc}	-1.04		-0.96		-0.76		-0.57	-0.65
E_{Pa}	-0.65	-0.81	-0.64	-0.80	-0.56	-0.68	-0.52	-0.61

A 0.4 M LiH_2PO_4 + LiOH medium was the only one where the compound showed both solubility and stability for CV characterisation. The catalytic activity of **Ni_{12}-GeW_{10}** was assessed for nitrite reduction in this medium, but the complex rapidly degraded, limiting studies at pH 2.0 and 3.0. At pH 5.0, the cyclic voltammogram of **Ni_{12}-GeW_{10}** showed a single-step reduction with a peak at -1.04 V vs. SCE. During the reverse scan, two re-oxidation peaks appeared at -0.65 V and -0.81 V vs. SCE (Figure **5.28.a** and Table **5.6**). As expected, electron transfer improved with lower pH. The reduction wave shifted to less negative potential from pH 5.0 to 4.0, and then from pH 4.0 to 3.0 (Figure **5.28.a**, **b** and **c**. At pH 2.0, the wave split, showing a shoulder at -0.57 V vs. SCE (Figure **A.5.6** and **A.5.7**).

Under experimental conditions with various scan rates, potential ranges, and pH values, the POM does not deposit on the working electrode, and the electron transfer process is diffusion-controlled, even at pH 3.0, where slow degradation in solutions occurs. This is supported by the peak current dependence on the scan rate (**Figure A.5.8**).

Electrocatalytic activity of the Ni_{12}-GeW_{10} compound towards the reduction of nitrite, NO_2^-

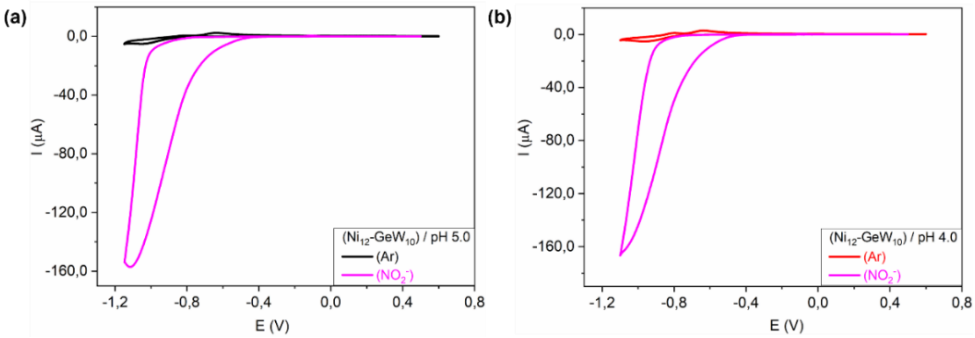


Figure 5.29 CVs recorded with an EPG working electrode, a SCE reference electrode and a Pt counter electrode at a scan rate of 10 $mV.s^{-1}$ in 0.4 M LiH_2PO_4 + LiOH. POM concentration: 0.2 mM. Nitrite concentration: 20.0 mM. **a.** pH 5.0, **Ni_{12}-GeW_{10}** alone (black) and **Ni_{12}-GeW_{10}**+ NO_2^- (purple). **b.** pH 4.0, **Ni_{12}-GeW_{10}** alone (red), **Ni_{12}-GeW_{10}**+ NO_2^- (purple).

The **Ni_{12}-GeW_{10}** demonstrates stable performance at pH 4.0 and 5.0, enabling evaluation of its catalytic activity for electrochemical reduction of nitrite ions. CVs were recorded at

scan rates from 100 to 10 $mV.s^{-1}$, with a POM concentration of 0.2 mM and sodium nitrite ($NaNO_2$) at 20.0 mM, resulting in an excess factor (γ) of 100. The catalytic efficiency (I_N) was calculated by normalising the catalytic current. Figure **5.29** shows CVs from a scan rate of 10 $mV.s^{-1}$ in both media, revealing that the reduction current response to nitrite ions was similar, with an exponential increase at low scan rates.

Influence of the scan rate on the catalytic activity

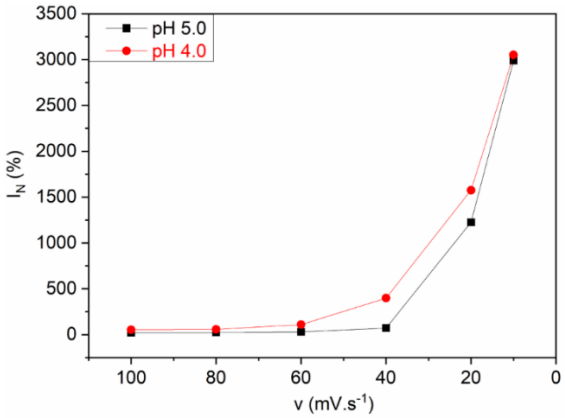


Figure 5.30 Evolution of the catalytic efficiency as a function of the scan rate at pH 5.0 (black) and 4.0 (red).

Table 5.7 Reduction current as a function of the scan rate, in the absence (I_0) and in the presence (I_x) of nitrite, and catalytic efficiency (I_N), at pH 5.0 and 4.0.

	pH 5.0			pH 4.0		
V ($mV.s^{-1}$)	**I_0 (μA)**	**I_x (μA)**	**I_N (%)**	**I_0 (μA)**	**I_x (μA)**	**I_N (%)**
100	-13.79	-16.60	20.37	-15.29	-23.50	53.70
80	-12.55	-15.50	23.51	-13.75	-21.70	57.82
60	-11.07	-14.40	30.08	-11.91	-24.90	109.07
40	-9.20	-15.80	71.74	-9.87	-49.20	398.48
20	-6.10	-80.90	1226.23	-7.19	-120.50	1575.94
10	-5.08	-157.00	2990.55	-5.29	-166.70	3051.23

At pH 5.0 and 4.0, catalytic activity was negligible at a scan rate of 100 $mV.s^{-1}$. Reducing the scan rate from 100 to 40 $mV.s^{-1}$ had little effect at pH 5.0, but between 40 and 20 $mV.s^{-1}$, the reduction current surged from 70% to over 1200%, reaching a maximum of 2990% at 10 $mV.s^{-1}$. At pH 4.0, electrocatalytic activity appears to start slightly earlier at 40 $mV.s^{-1}$ with a 398% increase, reaching maximum values similar to those at pH 5.0 at 10 $mV.s^{-1}$ (Table **5.7** and Figure **5.30**).

5.4.3. Electrochemical Characterisation of Fe_{12}-PW_{10}

Redox behaviour

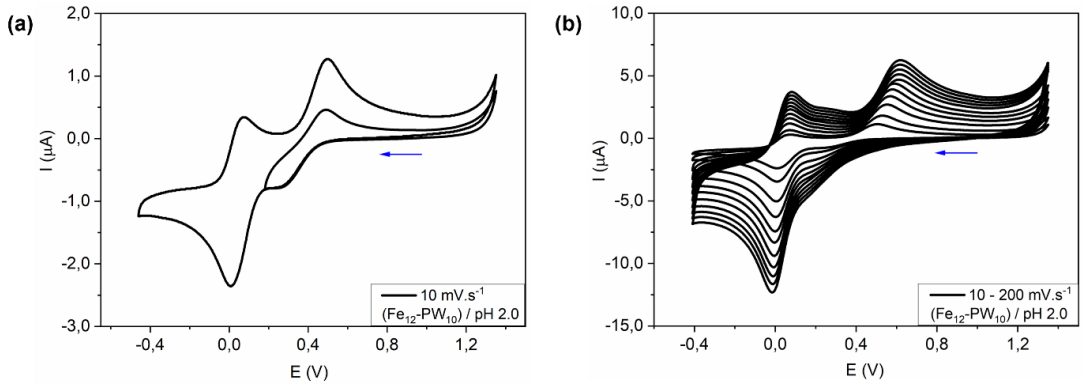


Figure 5.31 CVs of **Fe_{12}-PW_{10}** in 0.2 M Li_2SO_4 + H_2SO_4 / pH 2.0. POM concentration: 10^{-4} M. Potential scan restricted to the redox processes attributable to the Fe^{3+} centres. **a.** The two curves shown have reverse potentials at E_R = +0.18 V and -0.46 V vs. SCE. Scan rate: 10 mV.s^{-1}. **b.**The scan rate varied from 10 to 200 mV.s^{-1}. Working electrode: EPG. Auxiliary electrode: Pt. Reference electrode: SCE.

The **Fe_{12}-PW_{10}** has low solubility, necessitating a high concentration of lithium ions to facilitate its solubilisation in aqueous media. To achieve a concentration of 10^{-4} M of POM at pH levels of 2.0 and 5.0, up to 1.0 M of Li^+ ions was needed. The solubilised **Fe_{12}-PW_{10}** remains stable during electrochemical experiments.

At pH 2.0, the reduction of Fe^{3+} occurs in two quasi-reversible steps (Figure **5.31.a**), with peaks at +0.25 V and +0.01 V vs. SCE (Table **5.8**). The electron transfer was diffusion-controlled, demonstrated by the relationship between reduction peak current and the square root of the scan rate, per the Randles-Sevcik equation (Figure **5.31.b** and **Figure A.5.9**).

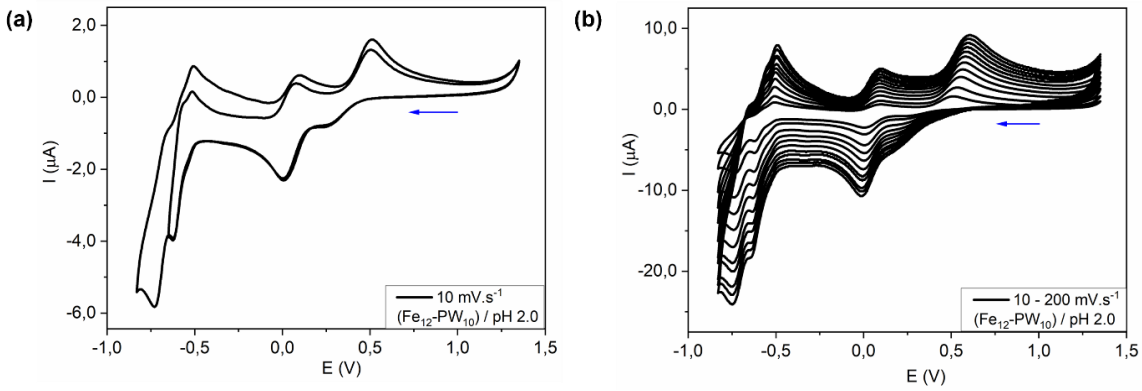


Figure 5.32 CVs of **Fe_{12}-PW_{10}** in 0.2 M Li_2SO_4 + H_2SO_4 / pH 2.0. POM concentration: 10^{-4} M. Potential scan extended to the redox processes attributable to the W^{6+} centres. **a.** The two curves shown have reverse potentials at E_R = -0.65 V and -0.83 V vs. SCE. Scan rate: 10 mV.s^{-1}. **b.** The scan rate varied from 10 to 200 mV.s^{-1}. Working electrode: EPG. Auxiliary electrode: Pt. Reference electrode: SCE.

Table 5.8 Peak potential values in the medium 0.5 M Li_2SO_4 + H_2SO_4 at pH 2.0 for **Fe_{12}-PW_{10}**. Working electrode: EPG. Auxiliary electrode: Pt. Reference electrode: SCE. Scan rate 10 $mV.s^{-1}$.

E / V vs.SCE	Fe^{3+}		W^{6+}	
E_{Pc}	0.25	0.01	-0.62	-0.73
E_{Pa}	0.49	0.07	-0.52	-0.66

By extending the scanning to more negative values, two additional reduction steps were observed at -0.62 V and -0.73 V vs. SCE, related to the W^{6+} centres (Figure **5.32**.**a**, Table **5.8**). Even at these low potentials, the working electrode surface remains unchanged, which would invalidate the linear variation of the peak current as a function of the square root of the scan rate (Figure **5.32.b** and Figure **A.5.9**).

Electrocatalytic reduction of O_2, H_2O_2 and NO_2^-

Catalytic activity of **Fe_{12}-PW_{10}** was investigated towards the reduction of O_2, H_2O_2 and NO_2.To assess the catalytic performance of **Fe_{12}-PW_{10}** for oxygen (O_2) reduction on an EPG electrode, experiments were conducted in an O_2-saturated electrolyte saturated with O_2 and maintained under a positive pressure of O_2. Two electrochemical techniques were used: (1) CV, which allowed for the measurement of the catalytic current flowing through the electrochemical circuit during the reduction of dissolved O_2, and (2) chronoamperometry, which enabled the measurement of the electrical charge consumed for O_2 reduction over a fixed period of 60 s. The catalytic currents and charges obtained under these conditions were then compared to those measured under an inert atmosphere of Ar, which served as the reference.

Figure **5.33.a** presents the CVs of **Fe_{12}-PW_{10}** in an inert atmosphere (black line) and an O_2-saturated solution (red line), showing O_2 reduction onset at -0.20 V vs. SCE. Figure **5.33.b** highlights key reduction potentials: E_1 = -0.46 V (Fe^{3+} reduction completion), E_2 = -0.65 V (first W^{6+} reduction end), and E_3 = -0.83 V (second W^{6+} reduction completion). Catalytic efficiency at these potentials was assessed using the normalised current from equation 5. 7.

$$I_N = \left[\frac{I_X - I_0}{I_0}\right] \times 100 \qquad (5.7)$$

where I_0 : the current under an inert atmosphere (Ar) and I_X: the current in the presence of O_2, the maximum values of the catalytic efficiency are reached upon reduction of the Fe^{3+} centres (Table **5.9**).

Applying equation (5.7) to the electrical charge from chronoamperometry experiments at consistent potential values over 60 s leads to equation (5.8):

$$Q_N = \left[\frac{Q_X - Q_0}{Q_0}\right] \times 100 \qquad (5.8)$$

where Q_0 : the current under an inert atmosphere (Ar) and Q_X: the current in the presence of O_2.

The comparison of normalised electrical charge values revealed that the difference between the end of Fe^{3+} reduction and the first W^{6+} reduction was smaller than expected. Additionally, advancing to the last W^{6+} reduction step led to a decrease in catalytic efficiency regarding the electrical charge used for O_2 reduction (Table **5.9** and **Figure A.5.10**).

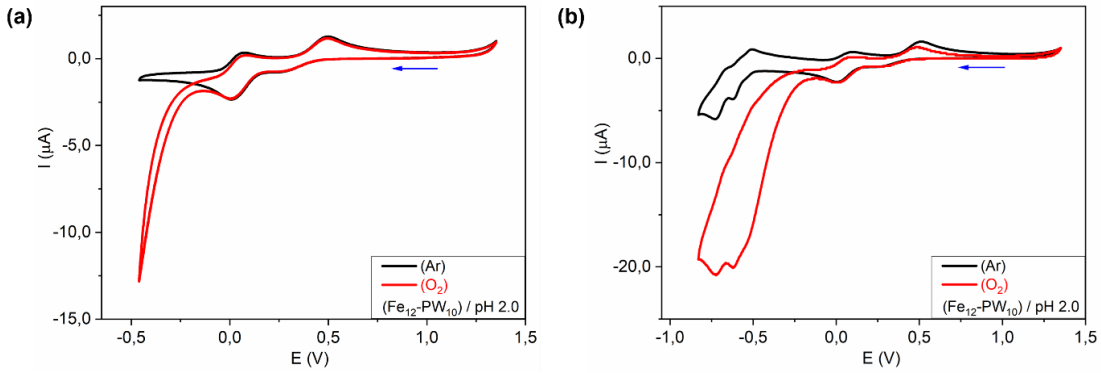


Figure 5.33 CVs of **Fe_{12}-PW_{10}** in 0.5 M Li_2SO_4 + H_2SO_4 / pH 2.0 in the absence (black) and in the presence of O_2 (red). POM concentration 10^{-4}M. **a.** Potential scan restricted to the redox processes attributable to the Fe^{3+} centres, reverse potential E_R = -0.46 V. **b.** Potential scans extended to the redox processes attributable to the W^{6+} centres, reverse potential, E_R = -0.83 V vs. SCE. Scan rate 10 $mV.s^{-1}$. Working electrode, EPG. Auxiliary electrode, Pt. Reference electrode, SCE.

Table 5.9 Normalised current and normalised electrical charge values at selected potentials for the electrocatalytic reduction of O_2 in 0.5 M Li_2SO_4 + H_2SO_4 / pH 2.0. Reference electrode: SCE. Auxiliary electrode: Pt. Working electrode: EPG. Scan rate: 10 $mV.s^{-1}$.

E / V vs. SCE	**-0.46**	**-0.65**	**-083**
I_N / %	920	391	248
Q_N / %	207	270	161

Electrocatalytic reduction of H_2O_2 was investigated using **Fe_{12}-PW_{10}** under similar conditions. CVs were recorded with increasing H_2O_2 amounts. Observations from the O_2 reduction indicate that only the first two redox steps for the Fe^{3+} centres are necessary. The preliminary observation of electrocatalytic reduction of H_2O_2 (Figure **5.34.a**) was that the reduction of H_2O_2 and the reduction of the Fe^{3+} centres began concomitantly at a very positive potential value of +0.5 V vs. SCE, a possible difference of 700 mV compared to the reduction of O_2 under the same conditions.

In Figure **5.34.b**, the reduction peaks for the second reduction step of Fe^{3+} centres, with and without H_2O_2, are around +0.01 V vs. SCE. As with O_2, catalytic efficiency will be assessed based on peak currents and electrical charges, summarised in Table **5.10** and **Figure A.5.11**.

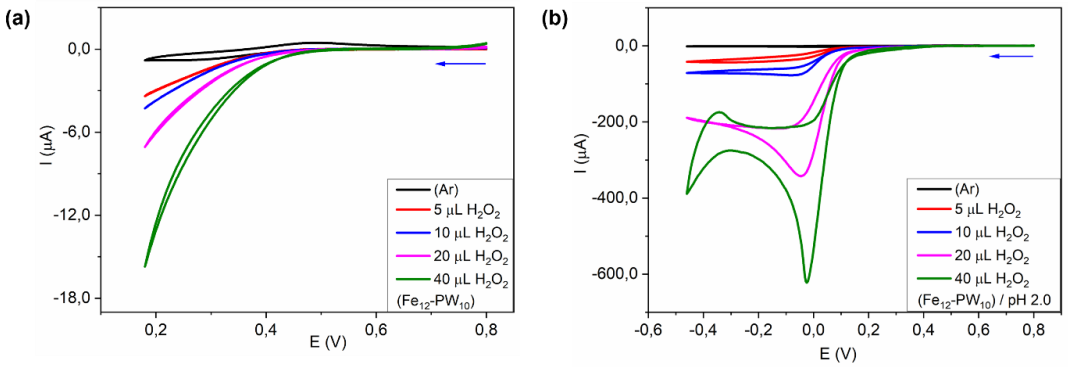


Figure 5.34 CVs of **Fe_{12}-PW_{10}** in 0.5 M Li_2SO_4 + H_2SO_4 / pH 2.0 in the absence (black) and in the presence of increasing amounts of H_2O_2. POM concentration: 10^{-4} M. **a.** Potential scan restricted to the first reduction step of the Fe^{3+} centres, reverse potential, E_R = +0.18 V. **b.** Potential scan restricted to the second reduction step of the Fe^{3+} centres, reverse potential, E_R = -0.46 V vs. SCE. Scan rate: 10 mV.s^{-1}. Working electrode: EPG. Auxiliary electrode: Pt. Reference electrode: SCE.

Table 5.10 Normalised current and normalised charge values at selected potentials in 0.5 M Li_2SO_4 + H_2SO_4 / pH 2.0 for **Fe_{12}-PW_{10}**. Reference electrode: SCE. Auxiliary electrode: Pt. Working electrode: EPG. Scan rate: 10 mV.s^{-1}. The excess factor γ is defined as the ratio of the H_2O_2 concentration to the POM concentration (5.9):

	E / V vs. SCE	70	140	280	560
I_N (%)	**+0.18**	310	416	752	1793
	-0.46	1708	3134	14251	25925
Q_N (%)	**+0.18**	179	317	1008	1799
	-0.46	1540	2749	9253	22035

$$\gamma = \frac{[H_2O_2]}{[POM]} \qquad (5.9)$$

Upon switching to a 1.0 M CH_3COOLi + CH_3COOH / pH 5.0 medium, the redox waves shifted towards negative potentials (Figure **5.35.a**. The reduction of Fe^{3+} centres, which previously occurred in two steps, now merges into a single step with a peak at -0.40 V vs. SCE, while re-oxidation shows distinct steps at +0.26 V and +0.02 V vs. SCE. Similarly, the two reduction steps of W^{6+} centres at pH 2.0 merge into one step at pH 5.0 (Figure **5.35.b**), with a reduction peak at -1.04 V and a re-oxidation peak at -0.78 V vs. SCE. A scan rate study confirms that the electron transfer is controlled by diffusion (**Figure A.5.12**).

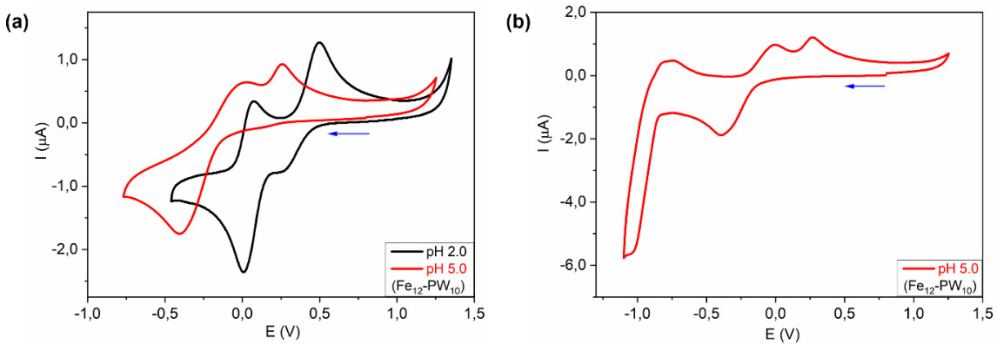


Figure 5.35 a. CVs of **Fe_{12}-PW_{10}** in 0.5 M Li_2SO_4 + H_2SO_4 / pH 2.0 (black) and 1.0 M CH_3COOLi + CH_3COOH / pH 5.0 (red). Potential scan restricted to the first reduction step of the Fe^{3+} centres, at reverse potentials E_R = -0.46 V and -0.77 V vs. SCE, respectively. **b.** Potential scan extended to the reduction of the W^{6+} centres; reverse potential, E_R = -1.10 V vs. SCE. Scan rate: 10 $mV.s^{-1}$. Working electrode: EPG. Auxiliary electrode: Pt. Reference electrode: SCE.

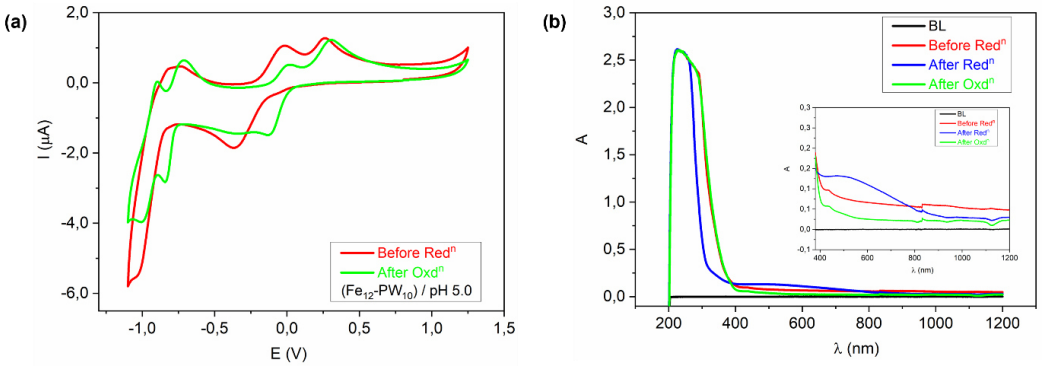


Figure 5.36 a. CVs of **Fe_{12}-PW_{10}** in 1.0 M CH_3COOLi + CH_3COOH / pH 5.0, before total reduction at -0.6 V vs. SCE (red) and after total re-oxidation at +1.0 V vs. SCE (green). Scan rate: 10 $mV.s^{-1}$. Working electrode: EPG. Auxiliary electrode: Pt. Reference electrode: SCE. **b.** UV-visible spectra of the **Fe_{12}-PW_{10}** solution before total reduction at -0.6 V vs. SCE (red), after total reduction at -0.6 V vs. SCE (blue), and after total re-oxidation at +1.0 V vs. SCE (green).

Controlled potential coulometry was conducted using a -0.6 V working electrode (1cm^2 glassy carbon plate) to assess Fe^{3+} centres in **Fe_{12}-PW_{10}**. The measurement indicated a charge of -531.29 mC, reflecting the reduction of fewer than 10 Fe^{3+} centres out of 12. During re-oxidation at +1.0 V, only 464.8 mC was recovered, which is less than 90% of the electrical charge consumed during the reduction of the **Fe_{12}-PW_{10}**. This suggests a structural rearrangement of the POM during the reduction process. Comparisons of CV before and after the reduction (at -0.6 V vs. SCE (red, Figure **5.36.a**) and re-oxidation (at +1.0 V vs. SCE (green, Figure **5.36.a**) reveal significant differences. The Fe^{3+} reduction occurs in two steps at less negative potentials (E_{C1} = -0.13 V and E_{C2} = -0.34 V), and W^{6+} centres also split into two steps (E_{C1} = -0.84 V and E_{C2} = -1.01 V). The UV-visible spectra before and after reduction and re-oxidation show an apparent change in the product (Figure **5.36.b**).

The catalytic efficiency of **Fe_{12}-PW_{10}** for reducing nitrite ions in a 1.0 M CH_3COOLi + CH_3COOH / pH 5.0 medium was evaluated. Figure **5.37.a** illustrates the CV of **Fe_{12}-PW_{10}** with (red) and without (black) an excess $NaNO_2$ (3 mM). Similar to O_2 at pH 2.0, nitrite reduction starts after the Fe^{3+} reduction, at an onset potential of -0.70 V vs. SCE. It reaches its peak, almost at the same value as the reduction peak of the W^{6+} centres, around -0.98 V vs. SCE.

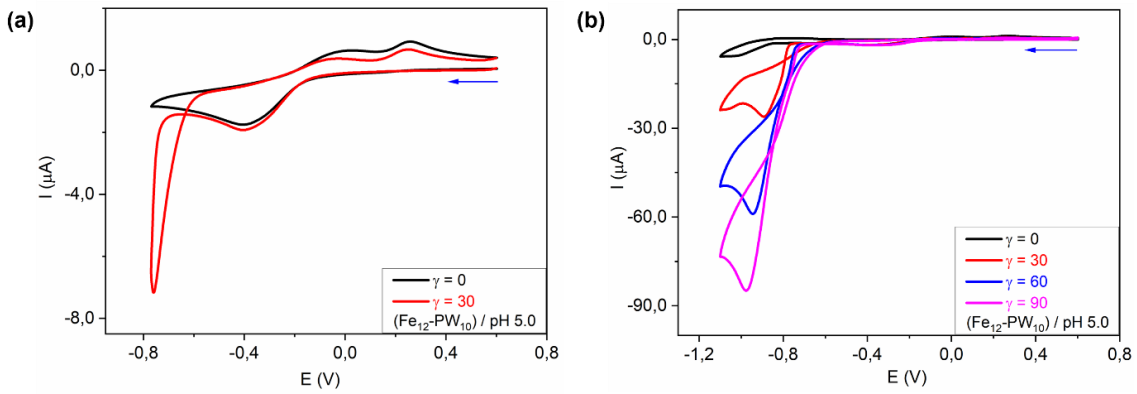


Figure 5.37 a. CVs of **Fe_{12}-PW_{10}** restricted to the redox waves of the Fe^{3+} centres in 1.0 M CH_3COOLi + CH_3COOH / pH 5.0, in the absence (black) and the presence of nitrite (red). **b.** CVs extended to the redox waves of the W^{6+} centres in the absence (black) and the presence of increasing amounts of nitrite (red, blue, and purple). Scan rate: 10 $mV.s^{-1}$. Working electrode: EPG. Auxiliary electrode: Pt. Reference electrode: SCE.

Table 5.11 Normalised current and normalised charge values at selected potentials in 1.0 M CH_3COOLi + CH_3COOH / pH 5.0 for **Fe_{12}-PW_{10}**. Reference electrode: SCE. Auxiliary electrode: Pt. Working electrode: EPG. Scan rate: 10 $mV.s^{-1}$.

γ	30	60	90
E / V vs. SCE		**I_N (%)**	
-0.98	387	999	1484
		Q_N (%)	
-0.40	12.2	24.1	12.4
-0.77	15.3	113.1	226.5
-1.10	743	2010	2136

The reduction peak current and the total charge consumed were evaluated in the presence of increasing amounts of $NaNO_2$ by CV (Figure **5.37.b**) and by chronoamperometry (**Figure A.5.13**). The excess factor γ is defined as the ratio of the $NaNO_2$ concentration to the POM concentration:

$$\gamma = \frac{[NO_2^-]}{[POM]} \qquad (5.10)$$

For each value of γ, the normalised current I_N at the reduction peak and the normalised electrical charge, Q_N, were calculated. That passed through the circuit for 60 s at E = +0.05 V, -0.40 V, -0.77 V, and -1.10 V vs. SCE, as shown in Table **5.11**.

5.4.4. Electrochemical Characterisation of Fe_4-GeW_{10}

Redox behaviour

The **Fe_4-GeW_{10}** species was dissolved in a 1.0 M $LiCH_3CO_2$ + CH_3CO_2H buffer, at either pH 4.0 or 5.0, with a high concentration of lithium ions (1 M LiCl) to enhance solubilisation. The reproducible response during experiments indicates the stability of **Fe_4-GeW_{10}** in these conditions.

At pH 5.0, two reduction waves at E_{pc} = -292 and -376 mV were attributed to Fe centres, with corresponding oxidation waves at E_{pa} = -66 and +358 mV (Figure **5.38.a** black) when the scan direction was reversed. This suggests two distinct redox couples linked to different Fe centres within the POM scaffold. A similar pattern was noted at pH 4.0 (Figure **5.38.b** black). There are, then, two types of Fe centres, and the response observed when varying the potential range in order to address them successively is rather reproducible (Figure **5**. **39**).

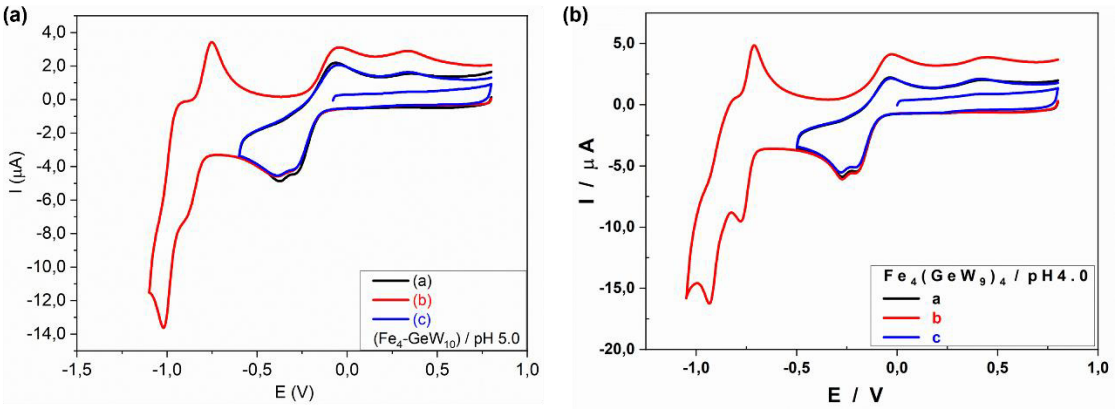


Figure 5.38 CVs of **Fe_4-GeW_{10}** in 1.0 M LiCl, 1.0 M $LiCH_3CO_2$ + CH_3CO_2H at pH 5.0 **(a)** and at pH 4.0 **(b)** POM concentration: 10^{-4} M. **a.** The Potential window is restricted to the redox processes attributable to the Fe centres, starting at +800 mV towards the negative direction. **b.** Potential window extended to the waves of the W centres. (c) Potential window restricted to the redox processes attributable to the Fe centres, starting at -80 mV **(a)** and starting at 0 mV **(b)** towards the positive direction. Scan rate: 100 $mV.s^{-1}$. Working electrode: EPG. Auxiliary electrode: Pt. Reference electrode: SCE.

When the potential window was extended to the negative side to include the W centres, reduction waves were observed at E_{pc} = -890 and -1018 mV, while oxidation waves appeared at E_{pa} = -916 and -752 mV at pH 5.0 (Figure **38.a** red). Similar behaviour was noted at pH 4.0 (Figure **38.b** red), with more defined reduction waves for the W centres. The choice of the initial potential and scan direction allowed to confirm that all the Fe atoms

in **$Fe_4(GeW_{10})_2$** are in the 3+ oxidation state. Indeed, scanning from +800 mV revealed the two previously mentioned waves attributed to the reduction of Fe^{3+} into Fe^{2+}, and the two corresponding oxidation waves upon scan reversal, as expected (Figure **38.a**). Scanning from -80 mV showed no oxidation waves, indicating the Fe centres were already at the 3+ state. Subsequent re-oxidation from Fe^{2+} to Fe^{3+} was noted after reducing Fe^{3+} to Fe^{2+} when scanning negatively (Figure **38.a** blue**)**.

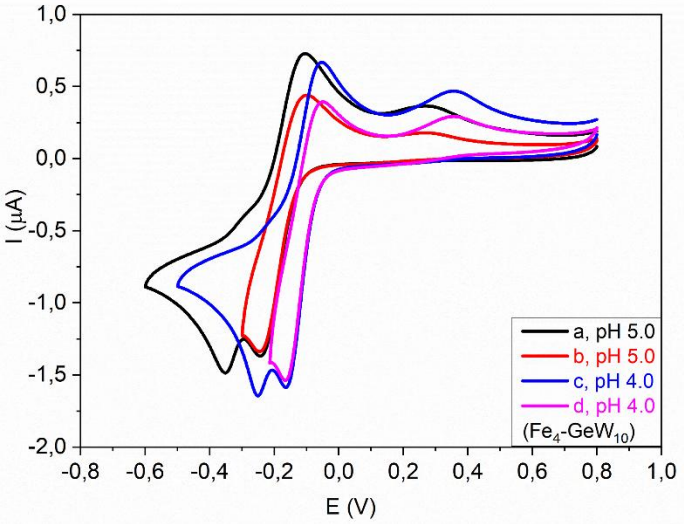


Figure 5.39 CVs of **Fe_4-GeW_{10}** in 1.0 M LiCl, 1.0 M $LiCH_3CO_2$ + CH_3CO_2H at either pH 4.0 or pH 5.0. POM concentration: 10^{-4} M. (a) and (c) Potential window including just the redox processes attributable to the Fe centres, both at pH 5.0 and 4.0, respectively. (b) and (d) Potential window restricted to the first wave attributable to the Fe centres, both at pH 5.0 and 4.0, respectively. Scan rate: 10 $mV.s^{-1}$. Working electrode: EPG. Auxiliary electrode: Pt. Reference electrode: SCE.

Table 5.12 Oxidation peak potentials (E_{pa}) and reduction peak potentials (E_{pc}), in mV vs. SCE, measured from CVs of **Fe_4-GeW_{10}** recorded at 100 $mV.s^{-1}$ in 1.0 M LiCl, 1.0 M $LiCH_3COO.2H_2O$ + CH_3COOH either at pH 4.0 or at pH 5.0. The values were taken from the curves shown in Figure 5.10 (b) and Figure 5.11 (b).

Fe centres	pH 4.0	pH 5.0	W centres	pH 4.0	pH 5.0
E_{pc1}	–208	–292	**E_{pc3}**	–778	–890
E_{pa1}	+442	+358	**E_{pa3}**	–712	–752
E_{pc2}	–272	–376	**E_{pc4}**	–934	–1018
E_{pa2}	–30	–66	**E_{pa4}**	–816[#]	–916[#]

[#] ***shoulder***

Electron transfer phenomena involving POMs, such as **$Fe_4(GeW_{10})_2$**, are accompanied by proton exchange with the medium. Proton-coupled electron transfer is evident from the shifting peak potentials of redox waves as pH changes. More protons facilitate the reduction process, causing shifts to higher potentials with decreasing pH (increasing acidity). This behaviour was observed in **$Fe_4(GeW_{10})_2$**, with waves shifting towards higher peak potentials when pH decreased from 5.0 to 4.0 (Figure **38 (a)** red, **38(b)** red , **39** and Table **5.12**).

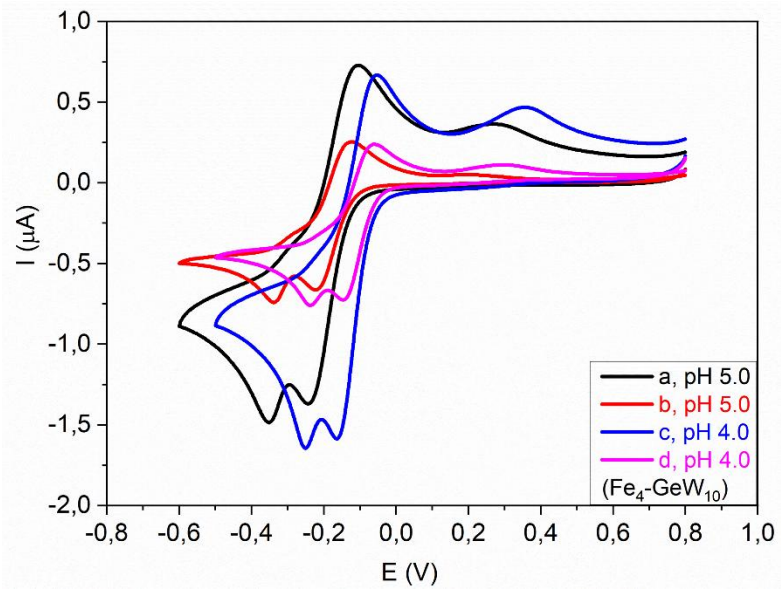


Figure 5.40 CVs of **Fe_4-GeW_{10}** in 1.0 M LiCl, 1.0 M $LiCH_3CO_2$ + CH_3CO_2H at either pH 4.0 or pH 5.0, recorded in a potential window including just the redox processes attributable to the Fe centres. POM concentration: 10^{-4} M. (**a)** and (**c**) Scan rate: 10 $mV.s^{-1}$, both at pH 5.0 and 4.0, respectively. (**b)** and (**d**) Scan rate: 2 $mV.s^{-1}$, both at pH 5.0 and 4.0, respectively. Working electrode: EPG. Auxiliary electrode: Pt. Reference electrode: SCE.

Electrocatalytic reduction of O_2 and NO_2^-

Tests were carried out at pH 5.0 to verify if **Fe_4-GeW_{10}** had a relevant electro-catalytic activity towards the reduction of either O_2 or NO_2^-. A favourable shift of about 100 mV towards less negative values concerning the onset potential of the reduction of the O_2 was measured in the presence of the POM, but hardly with a current enhancement, meaning the outcome was not promising (Figure **5.41.a**). Interestingly, **Fe_4-GeW_{10}** had a clear influence on the reduction of nitrite (Figure **5.41.b**). On the one hand, there was no influence on the onset potential (E_{onset} = –560 mV) nor the magnitude of the maximum current measured with respect to the situation in the absence of the POM. On the other hand, the steep increase in negative current observed in the presence of **Fe_4-GeW_{10}** right after the onset potential, as well as the awkward shape of the voltammogram, with the backwards and forward scan lines crossing, suggests the involvement of a mechanism more complex than just electron transfer steps between the electrode, the POM and the substrate.

The controlled potential coulometry experiment carried out at E = –500 mV, a potential more negative than the two reduction waves attributed to the Fe centres, resulted in a ratio of 4.45 electrons picked up per molecule. This is close to the expected value of 4 electrons required to reduce four Fe^{3+} into four Fe^{2+}, and is supplementary evidence that all the Fe centres in **Fe_4-GeW_{10}** are in the +3 oxidation state in the sample provided.

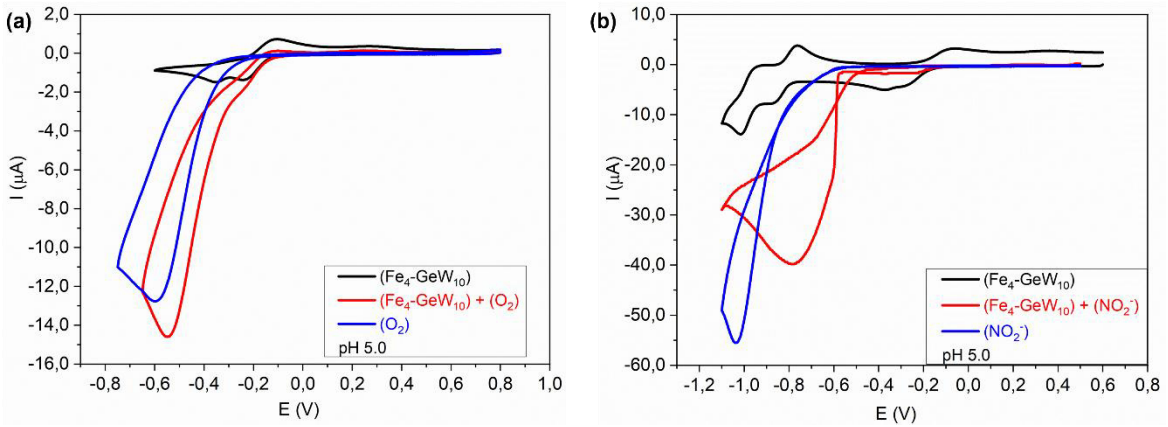


Figure 5.41 CVs of **Fe_4-GeW_{10}** in 1.0 M LiCl, 1.0 M $LiCH_3CO_2$ + CH_3CO_2H at pH 5.0, recorded in a potential window including the redox processes attributable both to the Fe and the W centres. POM concentration: 10^{-4} M. **Fe_4-GeW_{10}** in the absence (**black**) and in the presence (**red**) of O_2 (saturated solution) **(a)** (**red**) of NO_2^- **(b) (red)** at a concentration of 10^{-2} M. The **blue** curve corresponds to a blank obtained with a saturated solution of O_2 **(a)** a NO_2^- solution at the same concentration of 10^{-2} M **(b)**. Scan rate: 10 mV.s^{-1}. Working electrode: EPG. Auxiliary electrode: Pt. Reference electrode: SCE. Scan rate: 10 mV.s^{-1}. Working electrode: EPG. Auxiliary electrode: Pt. Reference electrode: SCE.

5.4.5. Electrochemical Characterisation of $Co_7Ln_xNa_{1-x}$-GeW_9

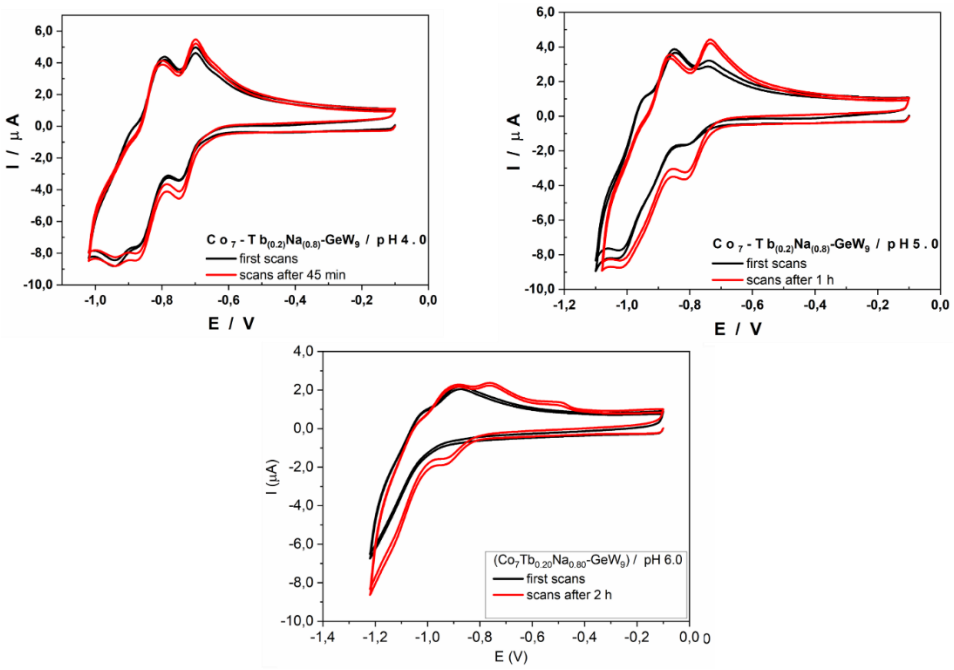


Figure 5.42 Evolution with time of the CVs of **$Co_7Tb_{0.2}Na_{0.8}$-GeW_9** recorded at a scan rate of 100 mV.s-1, in 1.0 M LiCl, 1 M $LiCH_3COO.2H_2O$ + CH_3COOH, at pH values (a) 4.0, (b) 5.0 and (c) 6.0. POM concentration: 0.1 mM. Working electrode: EPG; counter electrode: Pt; reference electrode: SCE.

Each **$Co_7Ln_xNa_{1-x}$-GeW_9**, Ln^{3+} = Dy^{3+}, Gd^{3+}, Y^{3+}, Ho^{3+}, Eu^{3+}, Tb^{3+} series of 3d-4f-POM clusters, composed of seven cobalt ions and one central lanthanide ion, exhibits positional disorder with sodium**.** Previous studies conducted on POMs containing lanthanide ions have shown that the latter are, in general, electrochemically silent in the range of potentials

explored.[329–331] The electrochemical response of Co centres in POMs depends on the nature of the POM, the former being either silent or electroactive.[332]

The POMs of the present series exhibit a very similar behaviour in cyclic voltammetry. The specific example chosen from the series, **$Co_7Tb_{0.2}Na_{0.8}$-GeW_9,** is described in detail in the main text, and the responses of the others are compiled in the appendices. The cyclic voltammograms of all the compounds in the series evolved with time before they reached a stable response. The phenomenon was observed at the three pH values used in the study (4.0, 5.0 and 6.0), and the kinetics became faster upon increasing the acidity. Hence, at pH 6.0, the reproducibility of the CV was attained 2 hours after the POM was solubilised at the beginning of the experiment, whereas it took just 1 hour at pH 5.0 and 45 minutes at pH 4.0 (as shown in Figure **5.42** for **$Co_7Tb_{0.2}Na_{0.8}$-GeW_9**).

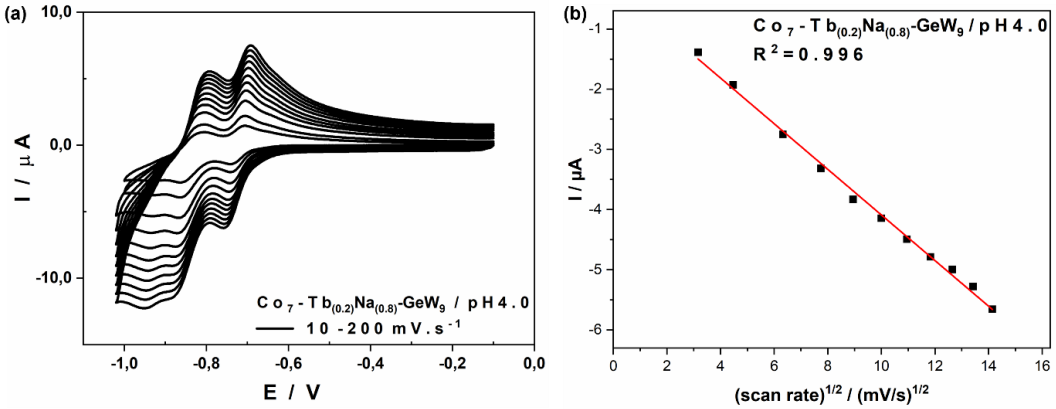


Figure 5.43 a. CVs of **$Co_7Tb_{0.2}Na_{0.8}$-GeW_9** recorded at scan rates ranging from 10 to 200 $mV.s^{-1}$, in 1.0 M LiCl, 1 M $LiCH_3COO.2H_2O$ + CH_3COOH, at pH 4.0. POM concentration: 0.1 mM. Working electrode: EPG; counter electrode: Pt; reference electrode: SCE. **b.** Linear dependence of the magnitude of the peak current (I_p) of the first reduction wave on the square root of the scan rate.

The magnitude of the peak current depends linearly on the square root of the scan rate, meaning that the electron transfer is controlled by the diffusion of the electro-active species to the working electrode surface. This is shown in Figure **5.43** for **$Co_7Tb_{0.2}Na_{0.8}$-GeW_9**, together with the sequence of CVs obtained at different scan rates. Similar graphs for all the other compounds in the **$Co_7Ln_xNa_{1-x}$-GeW_9** series and the ligand **GeW_9** are shown in Figure **A.5.14**.

Figure **5.44** shows the expected shift of the waves towards higher potentials upon decreasing the pH, indicative of the presence of proton exchange coupled to electron transfer and confirming that the species becomes easier to reduce at higher proton concentrations.[333,334] It is also clear from Figure **5.44** that the definition of the waves in the CV for **$Co_7Tb_{0.2}Na_{0.8}$-GeW_9** increases with the acidity. The same applies to all the other compounds in the series (Figure **A.5.15**). Since in the response at pH 6.0, the reduction waves observed at pH 4.0 and 5.0 merged into a poorly defined wave, and the peak currents

had lower intensities as well, the discussion will henceforth concentrate on the experiments carried out at the more acidic pH values (4.0 and 5.0). The oxidation and the reduction peak potentials of the waves attributed to the W centres for all the compounds in the series are compiled in **Table A.5.4.**

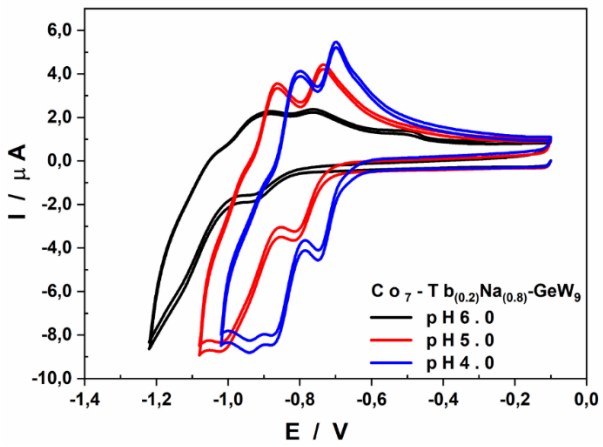


Figure 5.44 CVs of **$Co_7Tb_{0.2}Na_{0.8}$-GeW_9** recorded at a scan rate of 100 mV.s^{-1}, in 1.0 M LiCl, 1 M $LiCH_3COO.2H_2O$ + CH_3COOH, at pH values 4.0, 5.0 and 6.0. POM concentration: 0.1 mM. Working electrode: EPG; counter electrode: Pt; reference electrode: SCE.

The CVs in Figure **5.45** show the electron transfer processes at pH 5.0, attributable to the W^{6+} centres of both the GeW_9 ligand and the **$Co_7Tb_{0.2}Na_{0.8}$-GeW_9** species, the former being twice as concentrated as the latter to have an equivalent amount of the ligand in the two systems. During the scan of the potentials towards the negative values, the W centres in **GeW_9** undergo a reduction in a well-defined, single wave peaking at –1016 mV, having a pre-wave at –814 mV, whereas for **$Co_7Tb_{0.2}Na_{0.8}$-GeW_9** there are two well-defined reduction waves at –814 and –1022 mV, the latter exhibiting a shoulder at – 950 mV. The main reduction waves of the two compounds peak at the same potentials. The ligand **GeW_9** showed two oxidation waves upon reversal of the scan direction, peaking at – 890 and – 746 mV, whereas **$Co_7Tb_{0.2}Na_{0.8}$-GeW_9** exhibited a shoulder at –958 mV, followed by two well-defined waves at – 862 and –734 mV. When just the two main re-oxidation waves of each compound are considered, **$Co_7Tb_{0.2}Na_{0.8}$-GeW_9** turns out to be more difficult to re-oxidise than **GeW_9** (Figure **5.45** and Table **5.13**).

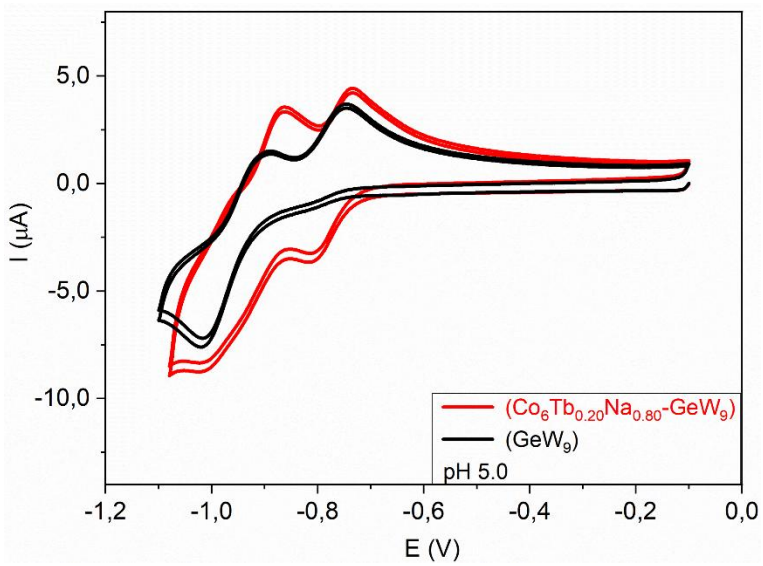


Figure 5.45 CVs of **GeW_9** and **$Co_7Tb_{0.2}Na_{0.8}$-GeW_9** recorded at a scan rate of 100 $mV.s^{-1}$, in 1.0 M LiCl, 1 M $LiCH_3COO.2H_2O$ + CH_3COOH, pH 5.0. POM concentrations: 0.2 mM for **GeW_9** and 0.1 mM for **$Co_7Tb_{0.2}Na_{0.8}$-GeW_9**. Working electrode: EPG; counter electrode: Pt; reference electrode: SCE.

Table 5.13 Oxidation peak potentials (E_{pa}) and reduction peak potentials (E_{pc}), in mV vs. SCE, of the W centres of **GeW_9** and **$Co_7Tb_{0.2}Na_{0.8}$-GeW_9**, measured from CVs recorded in 1.0 M LiCl, 1.0 M $LiCH_3COO.2H_2O$ + CH_3COOH, either at pH 4.0 or at pH 5.0.

	pH 4.0		pH 5.0	
	GeW_9	**$Co_7Tb_{0.2}Na_{0.8}$-GeW_9**	**GeW_9**	**$Co_7Tb_{0.2}Na_{0.8}$-GeW_9**
W centres				
E_{pc1}	-764*	-748	-814*	-814
E_{pa1}	-696	-700	-746	-734
E_{pc2}		-876	---	-950#
E_{pa2}		-800	---	-862
E_{pc3}	-868	-940	-1016	-1022
E_{pa3}	-806	-906#	-890	-958#

*** Pre-wave; # shoulder.**

The quest for the response of the Co centres in the POMs of the present series was not conclusive, even if some waves were observed in the expected range on the positive side of the potential scale. In the case of **$Co_7Tb_{0.2}Na_{0.8}$-GeW_9**, in a first look at the full-scale curves (Figure **5.46.a**), there was an increasing oxidation current as the potential was scanned up to +1400 mV. This is likely to be the oxidation of water, the current magnitude being higher at pH 5.0 than at pH 4.0, as expected for a process where the addition of electrons is concomitant with the uptake of protons. However, a closer look into the zoomed potential range where the Co centres are expected to respond (Figure **5.46.b**) revealed, at pH 5.0, a weak oxidation wave at +956 mV and two reduction waves at +1010 and +572

mV. This last reduction wave at +572 mV was more intense and better defined than the others, and it shifted to +708 mV at pH 4.0. The oxidation and the reduction peak potentials of the waves attributed to the Co centres for all the compounds in the series are compiled in Table **A.5.4.** The oxidation wave at +956 mV may correspond to the formation of an insoluble product, possibly a cobalt oxide, that stays adsorbed on the electrode surface and desorbs upon re-reduction at +572 mV, as its symmetrical shape seems to indicate.[335] Interestingly, the ligand **GeW_9** on its own showed, at pH 4.0, a much less intense reduction wave than the ones observed for the **$Co_7Ln_xNa_{1-x}$-GeW_9** compounds in the same potential range (Figure **A.5.16**), but the peak potential was not the same (E_{pc} at +800).

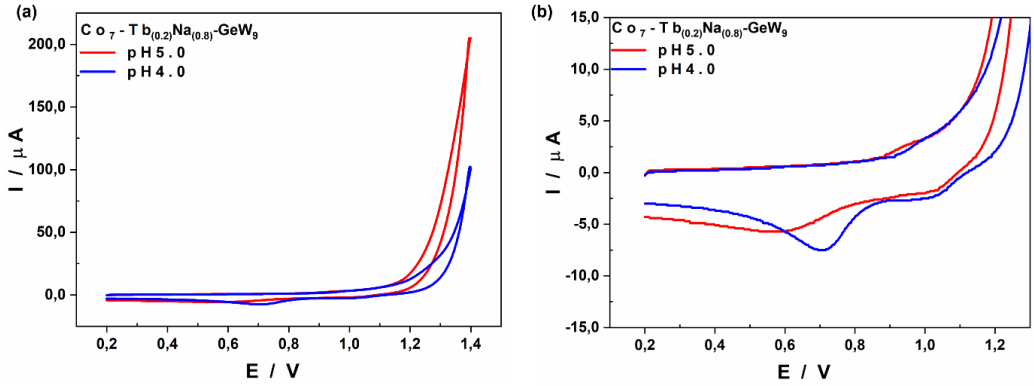


Figure 5.46 CVs recorded at a scan rate of 100 mV.s^{-1} for **$Co_7Tb_{0.2}Na_{0.8}$-GeW_9** at a POM concentration of 0.1 mM, in 1.0 M LiCl, 1.0 M $LiCH_3COO.2H_2O$ + CH_3COOH, either at pH 4.0 or at pH 5.0. **a.** Full-scale scans; **b.** Zooming on the potential range where the Co centres respond. Working electrode: EPG; counter electrode: Pt; reference electrode: SCE.

Electrocatalytic activity toward the reduction of O_2 or NO_2^-

Tests were carried out at pH 5.0 to verify if **$Co_7Ln_xNa_{1-x}$-GeW_9** had a relevant electro-catalytic activity towards the reduction of either O_2 or NO_2^-. No major influence was observed as far as O_2 was concerned, but there was a clear influence in the reduction of nitrite when **$Co_7Dy_{0.3}Na_{0.7}$-GeW_9** was used (Figure **5.47**). On the one hand, the onset potential for the electro-catalytic reduction of nitrite was less favourable in the presence of the POM (E_{onset} = –680 mV) than in its absence (E_{onset} = –560 mV), and the peak currents were similar. On the other hand, the negative current increased faster in the presence of **$Co_7Dy_{0.3}Na_{0.7}$-GeW_9** and reached its maximum value at E_{pc} = –950 mV, as compared to E_{pc} = –1036 mV in the absence of the POM. Also, the awkward shape of the voltammogram in the presence of the POM, with a steep cathodic current increase after the first wave, followed by the crossing of the backwards and forward scan lines, suggests the involvement of a mechanism more complex than just electron transfer steps between the electrode, the POM and the substrate.

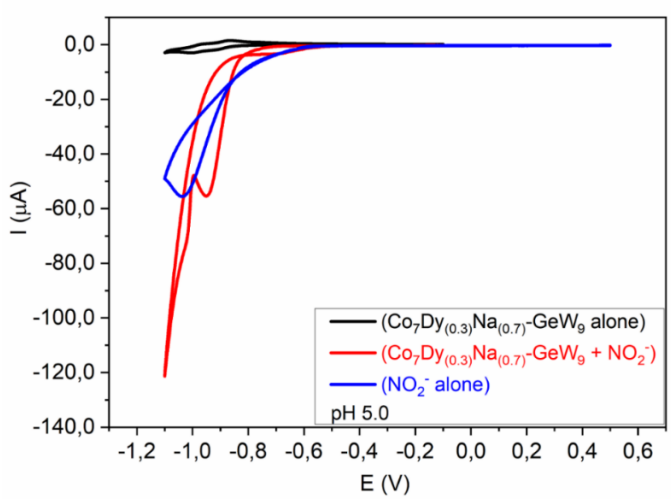


Figure 5.47 CVs of **$Co_7Dy_{0.3}Na_{0.7}$-GeW_9** in 1.0 M LiCl, 1.0 M $LiCH_3CO_2$ + CH_3CO_2H at pH 5.0, recorded in a potential window including the redox processes attributable to the W centres. POM concentration: 10^{-4} M. **$Co_7Dy_{0.3}Na_{0.7}$-GeW_9** in the absence (**black**) and in the presence (**red**) of NO_2^- at a concentration of 10^{-2} M. The **blue** curve corresponds to a blank obtained with a NO_2^- solution at the same concentration of 10^{-2} M. Scan rate: 10 $mV.s^{-1}$. Working electrode: EPG. Auxiliary electrode: Pt. Reference electrode: SCE.

5.5. Conclusion and Outlook

In conclusion, this chapter describes the electrochemical and electrocatalytic behaviour of metal-substituted polyoxometalates (POMs), specifically 3d-POMs and 3d-4f-POMs, evaluated through cyclic voltammetry (CV) experiments. The stability of the analysed POM species was investigated by CV. Their oxidative catalytic properties towards water oxidation and reductive catalytic properties for small molecules such as NO_2^-, H_2O_2, and O_2 were evaluated in a homogeneous phase.

The electrochemical characterisation of **Co_{12}-GeW_{10}** was performed across a range of pH levels (2.0, 3.0, 4.0, 5.0, and 5.9). Results revealed that the material remained stable at pH levels above 4.0. Detailed analysis showed that **Co_{12}-GeW_{10}** exhibited unique behaviour by transforming into a more stable form in solution through structural rearrangement or changes in electronic configuration. This transformed form demonstrated greater stability and distinctive redox properties compared to the parent **Co_{12}-GeW_{10}** cluster. Consequently, the redox catalytic activity was evaluated at higher pH levels. The stable form of **Co_{12}-GeW_{10}** acted as a water oxidation catalyst, indicated by a higher oxidative current and crossover current, showcasing its electrocatalytic nature. It was also observed that the modification of the working electrode with cobalt oxide facilitated water oxidation. At pH 5.9, this form exhibited a greater tendency to modify the working electrode, resulting in enhanced oxidative properties towards water oxidation. The redox catalytic properties of **Co_{12}-GeW_{10}** were evaluated for the reduction of O_2, H_2O_2, and NO_2^-. Electrocatalytic reduction was found to occur only with NO_2-, which is attributed to the W^{6+} reduction wave.

Additionally, the electrochemical characterisation and electrocatalytic studies of **Ni_{12}-GeW_{10}** were performed. The results indicated that **Ni_{12}-GeW_{10}** possesses adequate stability and demonstrates reductive catalytic properties at pH levels 4 and 5, particularly at lower scanning rates. It also showed a reduction in catalytic activity for NO_2^- reduction.

In the case of **Fe_{12}-GeW_{10}**, its sparingly soluble nature requires a higher concentration of Li^+ ions in the solution for better dissolution; however, the dissolved material remained stable during electrochemical characterisation. During reduction, Fe^{3+} displayed two quasi-reversible waves, while W^{6+} showed an additional two reduction steps. The electrocatalytic reduction properties of **Fe_{12}-GeW_{10}** towards NO_2-, H_2O_2, and O_2 were evaluated using two electrochemical techniques, CV and chronoamperometry. An increased redox current was observed after the Fe^{3+} wave, indicating the catalytic nature of **Fe_{12}-GeW_{10}** for NO_2^- reduction process.

Besides these 3d-POMs, the electrochemical catalytic properties of **Fe_4-GeW_{10}** were evaluated for NO_2^- and O_2 reduction. A clear influence on the reduction of nitrite was noted; however, the steep current increase and crossover current during the reverse scan complicated the interpretation, suggesting a more complex mechanism beyond simple electron transfer.

The 3d-4f POMs, **$Co_7Ln_xNa_{1-x}$-GeW_9**, where Ln^{3+} = Dy^{3+}, Gd^{3+}, Ho^{3+}, Eu^{3+}, Tb^{3+}, and Y^{3+}, were also evaluated through electrochemical characterisation. Even though the lanthanide ion centres exhibited some positional disorder in the crystal structure, this was deemed irrelevant for electrochemical evaluation due to their silent electrochemical nature, with response expected only from the Co ions in the crystal. During the positive scan, Co^{2+} generated an increased oxidative current; however, the possibility of water oxidation due to Co^{2+} in the cluster was not confirmed because of its asymmetrical oxidative wave upon closer inspection. These materials were further evaluated for their reduction catalytic properties towards NO_2^- and O_2, revealing a clear influence of the NO_2^- reduction reaction due to the W^{6+} wave.

To summarise, the 3d and 3d-4f metal-incorporated POM materials exhibit unique electrochemical properties and, due to these distinctive characteristics, have the potential to develop redox catalysts. A significant challenge for these materials is their instability across various pH ranges, which can potentially be addressed by immobilising the compounds onto the electrode surface and conducting studies in a heterogeneous phase.

5.6. Experimental Section

Chemicals and reagents

Pure water obtained with a Milli-Q Integral 5 purification set was used throughout. All reagents were of high-purity grade and were used as purchased without further purification. Lithium dihydrogen phosphate (LiH_2PO_4, 97%, Alfa Aesar), lithium hydroxide ($LiOH.H_2O$, R.P. Normapur, Prolabo), CH_3CO_2H (Glacial, Prolabo Normapur), $LiCH_3CO_2.2H_2O$ (Acros Organics), LiCl (Acros Organics), H_2SO_4 (Sigma Aldrich), $Li_2SO_4.H_2O$ (Acros Organics) were used to prepare the buffers.

Electrochemical experiments

Electrochemical data were obtained using an EG & G 273 A, potentiostat driven by a PC with the M270 software. A one-compartment cell with a standard three-electrode configuration was used for cyclic voltammetry experiments. The reference electrode was a saturated calomel electrode (SCE), which was separated from the bulk electrolyte solution via a fritted compartment filled with the same electrolyte, and the counter electrode was a platinum gauze of large surface area. The working electrode was a 3 mm outer diameter edge plane pyrolytic graphite (EPG) from Mersen, France. The pre-treatment of the working electrode before each experiment is adapted from a method described elsewhere [336,337] and was as follows: fine polishing using diamond pastes (DP Diamond-Struers) of decreasing grain size (3 min with a grain size of 6 µm, 3 min with a grain size of 3 µm and 6 min with a grain size of 1 µm). The electrode then underwent two successive ultrasonic washes in ethanol and Millipore water, respectively, for 5 minutes each. Before each experiment, solutions were thoroughly deaerated for at least 30 minutes with pure argon. A positive pressure of this gas was maintained during subsequent work. All cyclic voltammograms were recorded at a scan rate of 100 $mV.s^{-1,}$ and potentials are quoted against SCE unless otherwise stated. All experiments were performed at room temperature. Results were very reproducible from one experiment to another, and slight variations observed over successive runs are rather attributed to the uncertainty associated with the detection limit of our equipment (potentiostat, hardware and software) and not to the working electrode pre-treatment nor possible fluctuations in temperature.

Preparation of solutions and experimental conditions

To investigate the stability and solubility of 3d and 3d-4f POMs, various buffer solutions were employed, each with specific concentrations and pH levels. The stability of the 3d and 3d-4f POMs in buffer solution was assessed by cyclic voltammetry or UV-vis spectroscopy. Before each experiment, solutions were thoroughly deaerated for at least 30 minutes with

pure argon. A positive pressure of this gas was maintained during subsequent work. Cyclic voltammograms were recorded at different scan rates according to the experiment's purpose. All experiments were performed at room temperature, which was close to 20°C in our laboratory. The details of the buffer used for different POM molecules are discussed below.

$Na_{36}Cs_4[Cs_8(\{\alpha GeW_{10}Ni_2O_{38}\}_6)]\cdot 70H_2O$

The composition of the various media was as follows: 0.4 M LiH_2PO_4 + LiOH for pH 2.0, 3.0, 4.0 and 5.0. The polyanion concentration was 2×10^{-4} M.

$Na_{36}Cs_4[Cs_8(\{\alpha\text{-}GeW_{10}Co_2O_{38}\}_6)]\cdot 70H_2O$

The composition of the various media was as follows: 0.4 M LiH_2PO_4 + LiOH for pH 2.0, 3.0, 4.0 and 5.0. The polyanion concentration was 2×10^{-4} M.

$Na_{12}K_4[Fe_4O_4(GeW_{10}O_{37})_2]\cdot 60H_2O$

The compositions of the various media were as follows: 1.0 M LiCl, 1.0 M $LiCH_3CO_2$ + CH_3CO_2H either at pH 4.0 or at pH 5.0. The polyanion concentration was 10^{-4} M.

$Na_4K_{24}[Fe_{12}(PO_4)_4(PW_9O_{34})_4]\cdot 120\ H_2O$

The compositions of the various media were as follows: 0.2M Li_2SO_4 + H_2SO_4 for pH 2.0 and 1.0 M $LiCH_3CO_2$ + CH_3CO_2H for pH 5.0. The polyanion concentration was 10^{-4} M.

$Na_{20}Cs_3[(Co_3GeW_9)_2(PO_4)_6Dy(W_4O_{12})Co_2O_2(H_2O)_2]\cdot 100H_2O$

The composition of the media used was as follows: 1.0 M LiCl and 1 M $LiCH_3COO\cdot 2H_2O$ + CH_3COOH, at pH values 4.0, 5.0 and 6.0. The polyanion concentration was 10^{-4} M.

6. Overall Conclusion and Outlook

Through one-pot synthetic methods multinuclear 3d polyoxometalates (POMs) were synthesised, including **Co_{12}-GeW_{10}**, **Ni_{12}-GeW_{10}**, **Fe_{12}-PW_{10}**, and 3d-4f POMs such as **$Co_7Dy_{0.3}Na_{0.7}$-GeW_9**, **$Co_7Gd_{0.1}Na_{0.9}$-GeW_9**, **$Co_7Y_{0.3}Na_{0.7}$-GeW_9**, **$Co_7Eu_{0.1}Na_{0.9}$-GeW_9**, **$Co_7Ho_{0.1}Na_{0.9}$-GeW_9**, and **$Co_7Tb_{0.2}Na_{0.8}$-GeW_9** were synthesised. The reaction parameters for these syntheses were optimised, and structural characterisation (SCXRD and PXRD), as well as characterisations using ATR-FTIR, elemental analysis, and ESI-MS of the metal clusters, were performed.

^{1}H relaxometric studies of 3d-POM, 4f-POM, and 3d-4f-POM reveal that the incorporation of paramagnetic ions into the POM systems can enhance relaxivity properties, resulting in improved image contrast. Comparative studies of isostructural **Co_{16}-PW_9**, **Ni_{16}-PW_9**, and **Mn_{16}-SiW_9** demonstrate that differences in electronic relaxation times can significantly affect both longitudinal and transverse relaxivities. All 3d-POM clusters exhibited high relaxivity at low magnetic fields (20 MHz); however, beyond this point, relaxivity became field-independent, while transverse relaxivity increased with the field strength. The variation in electronic relaxation times and significant dipole-dipole contributions probably explain the higher relaxivity observed at lower magnetic fields. For the 4f-POMs, metal clusters containing Er^{3+} and Dy^{3+} show field dependency, exhibiting higher relaxation behaviour at intermediate and ultra-high magnetic fields, even though their electronic relaxation times are shorter than those of Gd^{3+}. In contrast, Gd^{3+} displays a plateau at high magnetic fields. Additional factors such as the number of unpaired electrons, magnetic moment, anisotropic characteristics of the paramagnetic ions, and size of the molecule are important for developing contrast agents for ultra-high magnetic fields. In terms of 3d-4f-POMs **$Co_7Ln_xNa_{1-x}$-GeW_9** (Ln^{3+} = Gd^{3+}, Dy^{3+}, Y^{3+}), the interpretation of relaxivity primarily depends on the details of the molecule. The SCXRD shows that these molecules form a 1D chain linked by Co/Na ions. The chains are maintained in solution according to the PRE studies; however, the ESI-MS studies can allow the fundamental building blocks of the POMs to be accurately

mainly arises from the 3d metals (Co^{2+}), whereas the influence of the lanthanide ions (Gd, Dy, Y) leads to a dramatic shift for the Gd congener compared with the Dy and Y relaxivities. Systematic studies to track the effects and understand the underlying mechanisms would help to unravel the details of the relaxivity processes. For example, data modelling and the

measurement of electronic relaxation times using EPR spectroscopy would give significant insights to enable a better understanding of the underlying mechanisms.

Electrochemical characterisation and electrochemical catalytic properties were also evaluated. Among the synthesised compounds, **Co_{12}-GeW_{10}** demonstrated significant catalytic activity for water oxidation. The 3d-4f POM metal clusters also showed water oxidation activity; however, the appearance of outlier peaks in the reduction wave after oxidation made the analysis difficult to interpret and further measurements are required to gain insight into the details of the catalytic behaviour for water oxidation. From the assessment of redox catalytic behaviour, all synthesised 3d-POM and 3d-4f POM metal clusters exhibited redox catalytic activity in terms of the reduction of NO_2. Notably, **Co_{12}-GeW_{10}** and **Fe_{12}-PW_{10}** showed catalytic activity for the reduction of H_2O_2 and O_2.

These oxidative and reductive catalytic properties suggest that POM clusters incorporating Co^{2+} can effectively function as water oxidation catalysts, while the W^{6+} centres are mainly responsible for the reduction reactions. The varying reduction behaviours of these POM metal clusters highlight the effect of variations in metal ions coordinated by lacunary POMs.

7. Experimental

Materials and Methods

The following reactions were conducted under aerobic conditions. Weather conditions may influence the material yields and crystallisation time. All chemicals used in the preparation of the materials were obtained from commercial sources (Sigma Aldrich, VWR International) and used without further purification.

Synthesis of starting materials

All mentioned starting materials (lacunary POM precursor) were prepared based on the literature and confirmed with ATR-FTIR spectroscopy.

$Na_{10}[A\text{-}\alpha\text{-}GeW_9O_{34}]\cdot 18H_2O$

A mixture of 182 g (0.55 mol) of sodium tungstate and 5.2 g (50 mmol) of germanium oxide was dissolved in 200 mL of water. The solution was stirred thoroughly, and gradually, 130 mL of 6 M hydrochloric acid was added while continuing to stir. The mixture was then heated to boiling and maintained at that temperature for 1 hour. Afterwards, the solution was concentrated to a total volume of less than 300 mL, and the silica residue was filtered out. In a separate step, 50 g of anhydrous sodium carbonate was dissolved in 50 mL of water. This sodium carbonate solution was added to the lukewarm mixture and stirred gently, which resulted in the slow precipitation of the sodium salt, $Na_{10}[A\text{-}\alpha\text{-}GeW_9O_{34}]$. The thick precipitate was then filtered using a sintered glass filter. It was successively washed with 100 mL of ethanol, followed by 100 mL of diethyl ether, and then air-dried. After complete drying, the solid material was powdered evenly and stored in a clean, dry glass container.

$Na_9[PW_9O_{34}]\cdot 7H_2O$

A mixture of 120 g (0.36 mol) of sodium tungstate dihydrate ($Na_2WO_2\cdot H_2O$) and 150 g of water was stirred in a 300 mL beaker using a magnetic stirring bar until the solid was completely dissolved. Phosphoric acid (85%) is then added dropwise while stirring, totalling 4.0 mL (0.06 mol). After all the acid had been added, the measured pH of the solution was between 8.9 and 9.0. Next, glacial acetic acid (22.5 mL, 0.40 mol) was added dropwise with vigorous stirring, which resulted in the formation of a large quantity of white precipitate during the addition. The final pH of the solution was 7.5 ± 0.3. The solution was stirred for

1 hour, after which the precipitate was collected using a medium frit and air-dried. The dried materials are finely powdered and stored in a clean glass container.

$Na_{10}[A\text{-}\alpha\text{-}SiW_9O_{34}]$

Dissolve 11 g (50 mmol) of sodium metasilicate and 182 g (0.55 mol) of sodium tungstate in 200 mL of hot water (80-100°C) while stirring. Slowly add 130 mL of HCl (6 M) dropwise over ~30 minutes, then boil until the volume reaches ~300 mL. Filter out unreacted silica. Prepare a second solution with 50 g of Na_2CO_3 in 150 mL of water and slowly add it to the first solution, stirring gently. After 1 hour, filter the slow-forming precipitate. Stir the solid with 1 L of NaCl (4 M) solution, filter, and wash with 100 mL portions of ethanol and diethyl ether, then dry under vacuum.

$Na_{12}[\alpha\text{-}P_2W_{15}O_{56}]\cdot 24H_2O$

In a 600 mL beaker, 38.5 g of $K_6[\alpha\text{-}P_2W_{18}O_{62}]\cdot 14H_2O$ is dissolved in 125 mL of water, followed by the addition of 35 g of $NaClO_4\cdot H_2O$. After stirring for 20 minutes and cooling in an ice bath, potassium perchlorate is filtered out after approximately 3 hours. A solution of 10.6 g of Na_2CO_3 in 100 mL of water is added to the filtrate, resulting in an immediate fine white precipitate. This is decanted, filtered through a medium-porosity sintered glass frit, and dried under suction for about 3 hours. The precipitate is then washed with 4 g of NaCl in 25 mL of water, dried, washed with 25 mL of ethanol, and air-dried under suction for 3 days.

Synthesis of 3d metal-containing polyoxometalates

$Na_{36}CoCs_2[Cs_8(W_{10}Co_2GeO_{38})_6]\cdot 120H_2O$ **(Co_{12}-GeW_{10})**

0.4 g (3.08mmol) of $CoCl_2\cdot 6H_2O$ was dissolved in 20 mL of 0.1 M sodium phosphate buffer. Then, 1.5 g (0.5mmol) of $Na_{10}[A\text{-}\alpha\text{-}GeW_9O_{34}]\cdot 18H_2O$ was added and stirred until dissolved. While stirring, 0.30 mL of 1M $Y(NO_3)_3\cdot 5H_2O$ (0.131g, 0.299 mmol) was added dropwise. The mixture was stirred for 5 minutes and heated at 85°C for one hour. After centrifuging to obtain a clear solution, 0.05 mL of 1 M CsCl was added. The solution was left to evaporate at room temperature. After 48 hours, purple **Co_{12}-GeW_{10}** crystals were collected and air-dried, yielding 600 mg (53% based on W). ATR-FTIR ($\tilde{\nu}$) = 932(s), 861(w), 778(w), 589(w),616(b). Elemental analysis ((%)calculated (found)) for $Na_{36}CoCs_2[Cs_8(W_{10}Co_2GeO_{38})_6]\cdot 120H_2O$; W 54.6(54.2), Co 3.79 (3.95), Ge 2.16(2.07), Na 4.10 (4.47), Cs 6.58 (6.28).

$Na_{37}Cs_3[Cs_8\{W_{10}Ni_2GeO_{38}\}_6]\cdot 160H_2O$ **(Ni_{12}-GeW_{10})**

Dissolve 0.4g (1.38 mmol) of $N_2NiO_6{\cdot}6H_2O$ in 20mL of 0.1M sodium phosphate buffer. Add 1.5g (0.5 mmol) of $Na_{10}[A\text{-}\alpha\text{-}GeW_9O_{34}]{\cdot}18H_2O$ and stir until fully dissolved. While stirring, add 0.30 mL of 1M $Y(NO_3)_3{\cdot}5H_2O$ (0.131g, 0.3420 mmol) dropwise. Stir for 5 minutes, then heat at 85°C for one hour. Centrifuge the mixture to obtain a clear solution, then add 0.05 mL of 1M CsCl. Allow to evaporate at room temperature for 4 days. Filter the pale green **Ni_{12}-GeW_{10}**crystals and let them air dry. Yield: 600 mg (53% based on W). ATR-FTIR ($\tilde{\nu}$) = 932(s),877(b),779(b), 686(b), 684(w). Elemental analysis ((%) calculated (found)) for $Na_{37}Cs_3[Cs_8\{W_{10}Ni_2GeO_{38}\}_6]{\cdot}160H_2O$; W 52.5(53.1), Co 3.35 (4.36), Ge 2.07(2.08), Na 4.05 (4.38), Cs 6.96 (5.84).

$K_{12}(OH_2)_{24}[\{W_{10}Fe_2PO_{37}\}_4\{Fe_4(PO_4)_4\}]{\cdot}30H_2O$ **(Fe_{12}-PW_{10})**

1M $FeCl_3{\cdot}6H_2O$ (1.00 mmol) was dissolved in 25 mL of 0.5 M KCl solution and stirred for 5 minutes. Then, 0.5 g (0.16mmol) of $Na_{10}[A\text{-}\alpha\text{-}GeW_9O_{34}]{\cdot}18H_2O$ was added and stirred until dissolved. The mixture was heated at 85°C for 1 hour, then cooled to room temperature. The clear yellow solution slowly evaporated, and after one week, yellow crystals of **Fe_{12}-PW_{10}** formed and were collected and air-dried. The yield 600 mg (38% based on W). ATR-FTIR ($\tilde{\nu}$) = 1612(s), 1086(sh), 1051(sh), 1032(s), 965(sh), 949(s), 862(s), 783(s), 699(w), 585(w), 499(w). Elemental analysis ((%)calculated (found)) for $K_{12}(OH_2)_{24}[\{W_{10}Fe_2PO_{37}\}_4\{Fe_4(PO_4)_4\}]{\cdot}30H_2O$; W 59.6(46.2), Fe 5.43 (4.20), P 1.54(2.01), K 3.80(7.33).

Synthesis of 3d-4f metal-containing polyoxometalates

$Na_{21.5}Cs_{1.3}[(W_9GeO_{34})_2(WO_3)_4(PO_4)_6Co_6(Dy_{0.3}/Na_{(0.7)})(Co_{0.6}/Na_{0.4})]{\cdot}75H_2O$ **($Co_7Dy_{0.3}Na_{0.7}$-GeW_9)**

0.4 g (3.08 mmol) of $CoCl_2{\cdot}6H2O$ was dissolved in 20 mL of 0.1 M sodium phosphate buffer with a pH of 8.6. Next, 1.5 g (5.45 mmol) of $Na_{10}[A\text{-}\alpha\text{-}GeW_9O_{34}]{\cdot}18H_2O$ was added to the buffer solution and stirred until fully dissolved. While stirring vigorously, 0.30 mL of 1 M $Dy(NO_3)_3{\cdot}5H_2O$ (0.131 g, 0.299 mmol) was added dropwise. The mixture was stirred for an additional 5 minutes and then heated to 85°C for one hour. Upon completion of the reaction, the turbid solution was centrifuged to obtain a clear solution. This clear solution was carefully decanted into a new vial, and 0.05 mL of 1 M CsCl was introduced. The solution was then allowed to evaporate at room temperature. After three weeks, the resulting pure purple crystals were collected and washed with ice-cold deionised water. Finally, the crystals were allowed to air dry. The yield 300 mg (3.5% based on W). ATR-FTIR ($\tilde{\nu}$) = 1037(b), 932(s), 862 (b), 667(w).

$Na_{21.7}Cs_{1.7}[(W_9GeO_{34})_2(WO_3)_4(PO_4)_6Co_6(Gd_{0.1}/Na_{0.9})(Co_{0.5}/Na_{0.5})]\cdot 75H_2O$ **($Co_7Gd_{0.1}Na_{0.9}$-GeW_9)**

0.4 g (3.08 mmol) of $CoCl_2\cdot 6H_2O$ was dissolved in 20 mL of 0.1 M sodium phosphate buffer (pH 8.6). Then, 1.5 g (5.45 mmol) of $Na_{10}[A\text{-}\alpha\text{-}GeW_9O_{34}]\cdot 18H_2O$ was added and stirred until dissolved. While stirring, 0.30 mL of 1 M $Gd(NO_3)_3\cdot 5H_2O$ (0.131 g, 0.299 mmol) was added dropwise. The mixture was stirred for 5 minutes and heated at 85°C for one hour. After centrifugation, the clear solution was decanted into a new vial, and 0.05 mL of 1 M CsCl was added. The solution evaporated at room temperature, and after three weeks, pure purple crystals were collected, washed with ice-cold deionised water, and allowed to air dry. The yield 300 mg (3.5% based on W). ATR-FTIR ($\tilde{\nu}$) = 1037(b), 934(s), 862 (b), 661(w).

$Na_{21.65}Cs_{1.5}[(W_9GeO_{34})_2(WO_3)_4(PO_4)_6Co_6(Y_{0.3}/Na_{0.7})(Co_{0.25}/Na_{0.75})]\cdot 75H_2O$ **($Co_7Y_{0.3}Na_{0.7}$-GeW_9)**

0.4 g (3.08 mmol) of $CoCl_2\cdot 6H_2O$ was dissolved in 20 mL of 0.1 M sodium phosphate buffer (pH 8.6). Then, 1.5 g (5.45 mmol) of $Na_{10}[A\text{-}\alpha\text{-}GeW_9O_{34}]\cdot 18H_2O$ was added and stirred until dissolved. While stirring, 0.30 mL of 1 M $Y(NO_3)_3\cdot 5H_2O$ (0.131 g, 0.299 mmol) was added dropwise. The mixture was stirred for 5 minutes and heated at 85°C for one hour. After centrifugation, the clear solution was decanted into a new vial, and 0.05 mL of 1 M CsCl was added. The solution evaporated at room temperature, and after three weeks, pure purple crystals were collected, washed with ice-cold deionised water, and allowed to air dry. The yield 300 mg (3.5% based on W). ATR-FTIR ($\tilde{\nu}$) = 1037(b), 922(s), 872 (b), 667(w).

$Na_{21.6}Cs_{1.7}[(W_9GeO_{34})_2(WO_3)_4(PO_4)_6Co_6(Eu_{0.1}/Na_{0.9})(Co_{0.4}/Na_{0.6})]\cdot 75H_2O$ **($Co_7Eu_{0.1}Na_{0.9}$-GeW_9)**

0.4 g (3.08 mmol) of $CoCl_2\cdot 6H_2O$ was dissolved in 20 mL of 0.1 M sodium phosphate buffer (pH 8.6). Then, 1.5 g (5.45 mmol) of $Na_{10}[A\text{-}\alpha\text{-}GeW_9O_{34}]\cdot 18H_2O$ was added and stirred until dissolved. While stirring, 0.30 mL of 1 M $Eu(NO_3)_3\cdot 5\,H_2O$ (0.131 grams, 0.299 mmol) was added dropwise. The mixture was stirred for 5 minutes and heated at 85°C for one hour. After centrifugation, the clear solution was decanted into a new vial, and 0.05 mL of 1 M CsCl was added. The solution evaporated at room temperature, and after three weeks, pure purple crystals were collected, washed with ice-cold deionised water, and allowed to air dry. The yield 300 mg (3.5% based on W). ATR-FTIR ($\tilde{\nu}$) = 1037(b), 932(s), 862 (b), 667(w).

$Na_{21.7}Cs_{1.5}[(W_9GeO_{34})_2(WO_3)_4(PO_4)_6Co_6(Ho_{0.1}/Na_{0.9}Co_{0.6}/Na_{0.4})]\cdot 75H_2O$ **($Co_7Ho_{0.1}Na_{0.9}$-GeW_9)**

0.4 g (3.08 mmol) of $CoCl_2 \cdot 6H_2O$ was dissolved in 20 mL of 0.1 M sodium phosphate buffer (pH 8.6). Then, 1.5 g (5.45 mmol) of $Na_{10}[A\text{-}\alpha\text{-}GeW_9O_{34}] \cdot 18H_2O$ was added and stirred until dissolved. While stirring, 0.30 mL of 1 M $Ho(NO_3)_3 \cdot 5\,H_2O$ (0.131 grams, 0.299 mmol) was added dropwise. The mixture was stirred for 5 minutes and heated at 85°C for one hour. After centrifugation, the clear solution was decanted into a new vial, and 0.05 mL of 1 M CsCl was added. The solution evaporated at room temperature, and after three weeks, pure purple crystals were collected, washed with ice-cold deionised water, and allowed to air dry. Yield: 0 mg (per cent yield to be determined).The yield 300 mg (3.5% based on W). ATR-FTIR ($\tilde{\nu}$) = 1027(b), 932(s), 862 (b), 657(w).

$Na_{21.6}Cs_{1.5}[(W_9PO_{34})_2Co_6(PO_4)_6(WO_3)_4(Tb_{0.2}/Na_{0.8})(Co_{0.5}/Na_{0.5})] \cdot 75H_2O$ **($Co_7Tb_{0.2}Na_{0.8}$-GeW_9)**

0.4 g (3.08 mmol) of $CoCl_2 \cdot 6H_2O$ was dissolved in 20 mL of 0.1 M sodium phosphate buffer (pH 8.6). Then, 1.5 g (5.45 mmol) of $Na_{10}[A\text{-}\alpha\text{-}GeW_9O_{34}] \cdot 18H_2O$ was added and stirred until dissolved. While stirring, 0.30 mL of 1 M $Tb(NO_3)_3 \cdot 5\,H_2O$ (0.131 grams, 0.299 mmol) was added dropwise. The mixture was stirred for 5 minutes and heated at 85°C for one hour. After centrifugation, the clear solution was decanted into a new vial, and 0.05 mL of 1 M CsCl was added. The solution evaporated at room temperature, and after three weeks, pure purple crystals were collected, washed with ice-cold deionised water, and allowed to air dry. Yield: 0 mg (per cent yield to be determined).The yield 300 mg (3.5% based on W). ATR-FTIR ($\tilde{\nu}$) = 1033(b), 934(s), 862 (b), 667(w).

Synthesis of paramagnetic metal-containing polyoxometalates used for NMR relaxometry

$(NH_2Me_2)_{13}Na_3[\{Er(H_2O)(CH_3COO)(P_2W_{17}O_{61})\}_2] \cdot 40\,H_2O$ **(Er_2-W_{34})**

$Na_{12}[P_2W_{15}O_{56}] \cdot 18H_2O$ (0.88 g, 0.20 mmol) was dissolved in 20 mL of a 1 M lithium acetate/acetic acid buffer (pH 4.8). Next, 0.30 g (0.65 mmol) of $Er(NO_3)_3 \cdot 6H_2O$ was added, resulting in a light pink solution. The mixture was heated at 90 °C for one hour. After heating, the solution was filtered, and then 0.05 mL of a 1 M dimethylammonium chloride $(CH_3)_2NH_2Cl$ solution was added to the clear filtrate. The solution was allowed to evaporate slowly, leading to the formation of light pink crystals after approximately two weeks. These crystals were then isolated by filtration and dried in air.

$K_5[Dy(H_2O)_4GeW_{11}O_{39}] \cdot 16H_2O$ **($Dy\text{-}W_{11}$)**

$K_8[GeW_{10}O_{36}]\cdot 6H_2O$ (0.58 g, 0.20 mmol) was dissolved in 20 mL of a 1 M lithium acetate buffer at pH 4.8. $DyCl_3\cdot 6H_2O$ (0.23 g, 0.61 mmol) was then added to this solution in small portions while stirring. The resulting turbid, colourless solution was stirred and heated at 70 °C for one hour. Afterwards, the solution was filtered and allowed to evaporate slowly at room temperature. Colourless crystals were obtained after approximately two weeks.

$K_5[Er(H_2O)_3GeW_{11}O_{39}]\cdot 16H_2O$ **(Er-W_{11})**

$K_8[GeW_{10}O_{36}]\cdot 6H_2O$ (0.58 g, 0.20 mmol) was dissolved in 20 mL of a 1 M lithium acetate buffer at pH 4.8. $ErCl_3\cdot 6H_2O$ (0.23 g, 0.61 mmol) was then added to this solution in small portions while stirring. The resulting turbid, colourless solution was stirred and heated at 70 °C for one hour. Afterwards, the solution was filtered and allowed to evaporate slowly at room temperature. Colourless crystals were obtained after approximately two weeks.

$Na_4K_8[\{Gd(CH_3COO)GeW_{11}O_{39}(H_2O)\}_2]\cdot 20H_2O$ **(Gd-W_{22})**

A sample of $Na_{10}(GeW_9O_{34})$ weighing 0.526 g (0.15 mmol) was added under stirring to a solution of 0.193 g (0.45 mmol) $Gd(NO_3)_3\cdot 6H_2O$ in 25 mL of a 1 M CH_3COOH – CH_3COOK buffer at pH 4.7. The solution was heated to 50 °C for 30 minutes and then filtered. The colourless filtrate was subjected to slow evaporation at room temperature, resulting in a colourless crystalline product after four weeks.

$Na_4K_8[\{Dy(CH_3COO)GeW_{11}O_{39}(H_2O)\}_2]\cdot 20H_2O$ **(Dy-W_{22})**

A sample of $Na_{10}(GeW_9O_{34})$ weighing 0.526 g (0.15 mmol) was added under stirring to a solution of 0.193 g (0.45 mmol) $Dy(NO_3)_3\cdot 6H_2O$ in 25 mL of a 1 M CH_3COOH – CH_3COOK buffer at pH 4.7. The solution was heated to 50 °C for 30 minutes and then filtered. The colourless filtrate was subjected to slow evaporation at room temperature, resulting in a colourless crystalline product after four weeks.

$Na_4K_8[\{Er(CH_3COO)GeW_{11}O_{39}(H_2O)\}_2]\cdot 20H_2O$ **(Er-W_{22})**

A sample of $Na_{10}(GeW_9O_{34})$ weighing 0.526 g (0.15 mmol) was added under stirring to a solution of 0.193 g (0.45 mmol) $Er(NO_3)_3\cdot 6H_2O$ in 25 mL of a 1 M CH_3COOH – CH_3COOK buffer at pH 4.7. The solution was heated to 50 °C for 30 minutes and then filtered. The colourless filtrate was subjected to slow evaporation at room temperature, resulting in a colourless crystalline product after four weeks.

$[Gd_8O_4(H_2O)_3(PW_{10}O_{37})_4(W_3O_{12})]^{26-}$ (**Gd_8-PW_{10}**)

Dissolve 0.5 g (0.1 mmol) of $Na_9[PW_9O_{34}]\cdot 7H_2O$ and 0.131 g (0.299 mmol) of $Gd(NO_3)_3\cdot 6H_2O$ in 25 ml of 0.5 M KCl solution. Heated the mixture to 80°C for 1 hour, then centrifuged it. Kept the clear solution for evaporation. After 24 hours, white needle-like crystals appeared.

$[Y_8O_4(H_2O)_3(PW_{10}O_{37})_4(W_3O_{12})]^{26-}$ (**Y_8-PW_{10}**)

Dissolve 0.5 g (0.1 mmol) of $Na_9[PW_9O_{34}]\cdot 7H2O$ and 0.131 g (0.299 mmol) of $Y(NO_3)_3\cdot 6H_2O$ in 25 ml of 0.5 M KCl solution. Heated the mixture to 80°C for 1 hour, then centrifuged it. Kept the clear solution for evaporation. After 24 hours, white needle-like crystals appeared.

$[Mn^{2+}_{12}Mn^{3+}_4\{(OH)_3PO_4\}_4(PW_9O_{34})_4]^{28-}$ (**Mn_{16}-PW_9**)

$MnCl_2\cdot 4H_2O$ (0.24 g, 1.21 mmol) was dissolved in 20 mL of water. Subsequently, Na_{10}[A-α-$SiW_9O_{34}]\cdot 23H_2O$ (0.50 g, 0.17 mmol) was added to the solution. The pH was adjusted to 9 by adding solid Na_3PO_4. The resulting dark brown solution was stirred for 1 hour at room temperature. After filtration, 3 to 4 drops of 1.0 M RbCl solution were added to the filtrate, which was then allowed to evaporate in an open vial at room temperature. Dark brown crystals began to appear after one week, and these were collected by filtration and air-dried.

$[Co_{16}\{(OH)_3PO_4\}_4(PW_9O_{34})_4]^{28-}$(**$Co_{16}$-$PW_9$**)

$CoCl_2\cdot 6H_2O$ (0.39 g, 1.63 mmol) was dissolved in 20 mL of H_2O. Na_9[A-a-$PW_9O_{34}]\cdot 7H_2O$ (0.58 g, 0.20 mmol) was added, and the mixture was stirred until a clear, purple solution formed. Na_3PO_4 (0.50 g, 3.0 mmol) was added in portions, maintaining a pH of 8 with HCl. After stirring for 1 hour, the purple precipitate settled and was filtered out. A 1.0 M RbCl solution (0.55 mL) was added to the filtrate, resulting in another precipitate, which was also filtered after 10 minutes at 30°C. The clear, dark purple filtrate was left to evaporate in an open vial. After a week, dark purple crystals appeared, and once half the solvent evaporated, the solid was filtered and air-dried.

$[Ni_{16}\{(OH)_3PO_4\}_4(PW_9O_{34})_4]^{28-}$(**$Ni_{16}$-$PW_9$**)

This material is obtained from PD. Dr. Masooma Ibrahim.

Synthesis of 3d metal-containing polyoxometalates used for electrocatalysis

$K_{14}[Fe^{3+}4(\mu\text{-}O)_2(\mu\text{-}OH)_2\{W_{10}GeO_{37}\}_2]\cdot 34H_2O$ **(Fe_4-GeW_{10})**

1M $FeCl_3\cdot 6H_2O$ (1.00 mmol) was dissolved in 25 mL of 0.5 M KCl and stirred for 5 minutes. Then, 0.5 g of Na_{10}[A-α-$GeW_9O_{34}]\cdot 18H_2O$ was added and stirred until fully dissolved. The mixture was heated at 85°C for 1 hour, then cooled to room temperature. After centrifugation, the clear brown-yellow solution was left to evaporate. After one week, a

yellow precipitate formed, followed by shiny orange crystals the next week. The crystals were collected, washed, and air-dried.

Instrumentation

Attenuated Total Reflectance Fourier Transform Infrared Spectroscopy (ATR-FTIR)

(ATR-FTIR) were measured on a Nicolet iS50 FTIR spectrometer operating between 400-4000 cm^{-1} using the OMNIC software. (ATR-FTIR). The following abbreviations indicate the peak intensities: s= strong, m= medium, sh= shoulder and w= weak.

Powder X-ray Diffraction (PXRD)

X-ray powder diffraction was performed on a STOE STADI-P diffractometer with Cu-Ka radiation (λ= 1.544 Å) and interpreted using WinXPOW.The PXRD patterns were simulated using Mercury 2022.2.0.

Mass Spectrometry

Mass spectrometry (MS), specifically Electron Spray Ionisation (ESI) MS, is useful in determining the intact POM core as it generally possesses a high inherent negative charge. Mass spectra were taken on a SYNAPT G2-S ion mobility mass spectrometer from Waters in the negative ion mode. The clusters were dissolved in a 1:1 mixture of acetonitrile and water and injected into an electrospray ionisation (ESI) source at a flow rate of 180 µl/h. The capillary voltage of the ESI source was held at -2 kV, and the voltage of the sampling cone was 0 V. The flow of the desolvation gas was set to 400 l/h, and the nebuliser gas was set to 2.5 bar. The desolvation temperature was held at 150°C, and the ESI source temperature was set to 100°C. Isotopologue distributions were calculated with MATLAB R2024b by using its *isotopicdist* function.

Single crystal X-ray diffraction (SC-XRD)

Single crystal X-ray diffraction was performed on a STADIVARI by STOE using Mo-Kα radiation with a characteristic wavelength of 0.71073 Å, on a STADIVARI by STOE with Ga-Jet X-ray source by Excilium using Ga-Kα radiation with a wavelength of 1.3143 Å and on an IPDS II by STOE with Mo-Kα radiation. Additionally, measurements were performed on an Agilent SuperNova diffractometer using Cu-Kα radiation. The structures were solved and

refined by full-matrix least squares using ShelXT and ShelXL in the Olex2-1.5 program. *(Sheldrick, G. M. SHELXTL 6.12; Bruker AXS, 2003; Dolomanov, O. V.; Bourhis, L. J.; Gildea, R. J.; Howard, J. A. K.; Puschmann, H. J. Appl. Cryst. 2009, 42, 339)*

NMR spectroscopy

^{31}P NMR spectroscopy was performed on a Bruker Avance III 500 MHz located at the Institute for Nanotechnology (INT, KIT)

Dynamic Light Scattering (DLS) measurements

DLS measurements were performed by using a Malvern ZetaSizer nano device. Prior to measurement, samples were filtered through a syringe filter (0.22 µm, polypropylene membrane). The intensity of the scattered light was measured at a fixed angle (173°), while the laser light wavelength for the scattering experiments was *λ*=633 nm. The refractive index for POMs was 1.55. Data analysis was performed according to standard procedures by using the Malvern software. Briefly, the decay rates were determined by the following relationship, where *η* is the viscosity of the medium (water), *D*h is the hydrodynamic diameter, and θ is the scattering angle. $\Gamma = D_h \,.\, \left(\frac{4\pi\eta}{\lambda} \,.\, sin\left(\frac{\theta}{2}\right)\right)$

To fit the autocorrelation function, the non-negatively constrained least squares (NNLS) algorithm built into the software was used, which allows for the determination of the diffusion coefficient (*d*), from which the hydrodynamic diameter of the particles is calculated by using the Stokes-Einstein equation (see below), where kb is the Boltzmann constant, *T* is the temperature, and *η* is the viscosity of the medium (water). $D_h = \frac{K_b \,.T}{3 \,.\, \pi \,.\, \eta \,.\, d}$

Zeta-potential measurements were performed by using the Malvern ZetaSizer nanodevice and analysed according to standard procedures using Malvern software.

Elemental analysis

Elemental analysis was performed by triplicate determination of the samples. The samples were dissolved with acid in a graphite oven. Afterwards, the elements were analysed using ICP-OES and ICP-MS located at the Institute for Applied Materials-Energy Storage Systems (IAM-ESS), Karlsruhe Institute of Technology.

References

1. Pope, M. T.; Sadakane, M.; Kortz, U. Celebrating Polyoxometalate Chemistry. *Eur. J. Inorg. Chem.*, **2019**, 340–342.
2. Long, D. L.; Tsunashima, R.; Cronin, L. Polyoxometalates: Building Blocks for Functional Nanoscale Systems. *Angew. Chem. Int. Ed.*, **2010**, 1736–1758.
3. Müller, A.; Bögge, H.; Henry, M. Coordination Chemistry under Confined Conditions: A Simplified Illustrative View. *CR CHIM.,* **2005**, *8* (1), 47–56.
4. Pope, M. T. Mattes - Heteropoly and Isopoly Oxometalates. *Angew. Chem.*, **1984** Springer-Verlag Berlin.
5. Gao, Y.; Choudhari, M.; Such, G. K.; Ritchie, C. Polyoxometalates as Chemically and Structurally Versatile Components in Self-Assembled Materials. *Chem Sci.,* **2022**, *13* (9), 2510–2527.
6. Pope, M. T.; Müller, A. Polyoxometalate Chemistry: An Old Field with New Dimensions in Several Disciplines. *Angew. Chem. Int. Ed.,***1991**, *30* (1), 34–48.
7. Ammam, M. Polyoxometalates: Formation, Structures, Principal Properties, Main Deposition Methods and Application in Sensing. *J Mater Chem A Mater.,* **2013**, *1* (21), 629.
8. Xiao, W.; Li, S.; Zhao, Y.; Ma, Y.; Li, N.; Zhang, J.; Chen, X. Multinuclear Transition Metal-Containing Polyoxometalates Constructed from Nb/W Mixed-Addendum Precursors: Synthesis, Structures and Catalytic Performance. *Dalton Trans.,***2021**, *50* (25), 8690–8695.
9. Gumerova, N. I.; Rompel, A. Synthesis, Structures and Applications of Electron-Rich Polyoxometalates. *Nat Rev Chem.,* **2018**, *2* (2).
10. Oms, O.; Dolbecq, A.; Mialane, P. Diversity in Structures and Properties of 3d-Incorporating Polyoxotungstates. *Chem Soc Rev.,* **2012**, *41* (22), 7497–7536.
11. Berzelius, J. J. Beitrag Zur Näheren Kenntniss Des Molybdäns. *Ann Phys.,* **1826**, *82* (4), 369–392.
12. Pope, M. T.; Müller, A. Polyoxometalate Chemistry: An Old Field with New Dimensions in Several Disciplines. *Angew. Chem. Int. Ed*., **1991**,34–48.
13. Lunk, H. J.; Hartl, H. The Fascinating Polyoxometalates. *ChemTexts.,* **2021**,*7* (4).
14. J. F. Keggin. Structure of the Molecule of 12-Phosphotungstic Acid. *Nature,* **1933**.
15. Howard T. Evans Jr. The crystal structure of ammonium and potassium molybdotellurates. *J Am Chem Soc.,* **1948**, *70* (3).
16. J. Stuart Anderson. Constitution of the Poly-Acids. *Nature,* **1937**, *140*, 850.
17. Nowicka, D.; Vadra, N.; Wieczorek-Szweda, E.; Patroniak, V.; Gorczyński, A. Overview of Wells-Dawson Polyoxometalates: From Structure and Functionalization to Application. *Coord. Chem. Rev.,* **2024**.

18. Hale, G. E.; Astrophy, • J. *Structure of the Crystals of 12-Phosphotungstic Acid Measurement of Frequency of Longitudinal Vibration of a Steel Wire by Magneto-Striction Effect*; **1929**; Vol. 70.
19. John B. Moffat. Structure and Bulk Properties. In: Metal-Oxygen Clusters. Fundamental and Applied Catalysis. In *Metal-Oxygen Clusters The Surface and Catalytic Properties of Heteropoly Oxometalates*; **2002**.
20. H.N. Miras, D.-L. L. L. C. Chapter One - Exploring Self-Assembly and the Self-Organization of Nanoscale Inorganic Polyoxometalate clusters. *Adv. Inorg. Chem*., **2017**, Vol. 69.
21. Vilà-Nadal, L.; Cronin, L. Design and Synthesis of Polyoxometalate-Framework Materials from Cluster Precursors. *Nat Rev Mater.,* **2017**, *2*.
22. Raabe, J. C.; Jameel, F.; Stein, M.; Albert, J.; Poller, M. J. Heteroelements in Polyoxometalates: A Study on the Influence of Different Group 15 Elements on Polyoxometalate Formation. *Dalton Trans.,* **2023**, *53* (2), 454–466.
23. Ammam, M. Polyoxometalates: Formation, Structures, Principal Properties, Main Deposition Methods and Application in Sensing. *J Mater Chem A Mater*.,**2013**, *1* (21), 6291–6312.
24. Ivanova, S. Hybrid Organic-Inorganic Materials Based on Polyoxometalates and Ionic Liquids and Their Application in Catalysis. *ISRN Chemical Engineering* **2014**, 1–13.
25. Mioc, U. B.; Nedić, Z. P. Keggin Structure. In *Encyclopedia of Membranes*; Springer Berlin Heidelberg, **2014**,1–3.
26. Baker, L. C. W. & F. J. S. *A New Fundamental Type of Inorganic Complex: Hybrid between Heteropoly and Conventional Coordination Complexes. Possibilities for Geometrical Isomerisms in 11-, 12-, 17-, and 18-Heteropoly Derivatives*; **1970**, Vol. 73.
27. Simic, M.; Neta, P.; Hayon, E. *A New Fundamental Type of Inorganic Complex: Hybrid between Heteropoly and Conventional Coordination Complexes. Possibilities for Geometrical Isomerisms in 11-, 12-, 17-, and 18-Heteropoly Derivatives*; **1969**, Vol. 73.
28. Sartzi, H.; Miras, H. N.; Vilà-Nadal, L.; Long, D.; Cronin, L. Trapping the δ Isomer of the Polyoxometalate-Based Keggin Cluster with a Tripodal Ligand. *Angew. Chem. Int. Ed.,***2015**, *127* (51), 15708–15712.
29. RENÉ THOUVENOT, M. F. R. F. and C. R.-D. Vibrational Investigations of Polyoxometalates. 3. Isomerism in Molybdenum(VI) and Tungsten(VI) Compounds Related to the Keggin Structure. *Inorg. Chem.,* **1984**.
30. Malmir, M.; Heravi, M. M.; Yekke-Ghasemi, Z.; Mirzaei, M. Incorporating Heterogeneous Lacunary Keggin Anions as Efficient Catalysts for Solvent-Free Cyanosilylation of Aldehydes and Ketones. *Sci Rep.,* **2022**, *12* (1).
31. Jacqueline Canny Andre Teze Rene Thouvenot Gilbert Herve. Disubstituted Tungstosilicates. 1. Synthesis, Stability, and Structure of the Lacunary Precursor Polyanion of a Tungstosilicate. Gamma.-$SiW_{10}O_{368}$. *Inorg Chem.,* **1986**, *25* (13).
32. Yoshihito Hayashi. Coordination Chemistry of Polyoxovanadates as Inorganic Ligands. *BJSCC.,***2015**.

33. Nsouli, N. H.; Bassil, B. S.; Dickman, M. H.; Kortz, U.; Keita, B.; Nadjo, L. Synthesis and Structure of Dilacunary Decatungstogermanate, [γ-$GeW_{10}O_{36}$]$^{8-}$. *Inorg Chem.,* **2006**, *45* (10), 3858–3860.
34. Petrehele, A. I. G.; Duteanu, N.; Morgovan, M. C.; Filip, S. M.; Ciocan, S.; Marian, E. Synthesis and Characterisation of Monolacunary Keggin Monovanado-Deca-Tungstophosphate and Its Complexes with Transition Metal Cations. *Materials,* **2023**, *16* (2).
35. Malmir, M.; Heravi, M. M.; Yekke-Ghasemi, Z.; Mirzaei, M. Incorporating Heterogeneous Lacunary Keggin Anions as Efficient Catalysts for Solvent-Free Cyanosilylation of Aldehydes and Ketones. *Sci Rep.,* **2022**, *12* (1).
36. Lu-Lu Liu a, L. W. a, X.-Y. X. a, P. Y. a, J. Z. b, U. K. c. Structural Overview and Evolution Paths of Lacunary Polyoxometalates. *Coord Chem Rev.,* **2024**, *506*.
37. Louis C. W. BakerDiana C. Glick. Present General Status of Understanding of Heteropoly Electrolytes and a Tracing of Some Major Highlights in the History of Their Elucidation. *Chem Rev.,* **1998**, *98* (1).
38. Long, D. L.; Tsunashima, R.; Cronin, L. Polyoxometalates: Building Blocks for Functional Nanoscale Systems. *Angew. Chem. Int. Ed*., **2010**, 1736–1758.
39. Vivek Das, R. K. F. H. Heterometallic 3d-4f Polyoxometalates: An Emerging Field with Structural Diversity to Multiple Applications. *Coord Chem Rev.,* **2020**, *413*, 213271.
40. Oms, O.; Dolbecq, A.; Mialane, P. Diversity in Structures and Properties of 3d-Incorporating Polyoxotungstates. *Chem Soc Rev*., **2012**, *41* (22), 7497–7536.
41. Proust, A.; Thouvenot, R.; Gouzerh, P. Functionalization of Polyoxometalates: Towards Advanced Applications in Catalysis and Materials Science. *ChemComm.,* **2008**, 1837–1852.
42. Zhang, J.; Xiao, F.; Hao, J.; Wei, Y. The Chemistry of Organoimido Derivatives of Polyoxometalates. *Dalton Trans*., **2012**, 3599–3615.
43. Merkel, M. P.; Anson, C. E.; Kostakis, G. E.; Powell, A. K. Taking the Third Route for Construction of POMOFs: The First Use of Carboxylate-Functionalized MnIIIAnderson-Evans POM-Hybrid Linkers and Lanthanide Nodes. *Cryst Growth Des.,* **2021**, *21* (6), 3179–3190.
44. Luo, J.; Huang, Y.; Ding, B.; Wang, P.; Geng, X.; Zhang, J.; Wei, Y. Single-Atom Mn Active Site in a Triol-Stabilized β-Anderson Manganohexamolybdate for Enhanced Catalytic Activity towards Adipic Acid Production. *Catalysts.,* **2018**, *8* (3).
45. Zhang, J.; Luo, J.; Wang, P.; Ding, B.; Huang, Y.; Zhao, Z.; Zhang, J.; Wei, Y. Step-by-Step Strategy from Achiral Precursors to Polyoxometalates-Based Chiral Organic-Inorganic Hybrids. *Inorg Chem.,* **2015**, *54* (6), 2551–2559.
46. Traustason, H.; Bell, N. L.; Caranto, K.; Auld, D. C.; Lockey, D. T.; Kokot, A.; Szymanowski, J. E. S.; Cronin, L.; Burns, P. C. Reactivity, Formation, and Solubility of Polyoxometalates Probed by Calorimetry. *J Am Chem Soc.,* **2020**, *142* (48), 20463–20469.
47. C. L. HILL and C. M. PROSSER-McCARTHA., In *Photosensitization and Photocatalysis Using Inorganic and Organometallic Compounds*; Kluwer Academic Publishers., **1993**.

48. Gumerova, N. I.; Rompel, A. Polyoxometalates in Solution: Speciation under Spotlight. *Chem. Soc. Rev.*, **2020,** 7568–7601.
49. Ždrnja, M.; Gumerova, N. I.; Rompel, A. Exploring Polyoxometalate Speciation: The Interplay of Concentration, Ionic Strength, and Buffer Composition. *Front. Chem. Biol.,* **2024**, *3*.
50. Misra, A.; Kozma, K.; Streb, C.; Nyman, M. Jenseits von Ladungsausgleich: Gegenkationen in Der Polyoxometallat-Chemie. *Angew. Chem.***2020**, *132* (2), 606–623.
51. Hong, C. Bin; Wang, T.; Liu, H. Insights into the Structure of Keggin-Type Polyoxometalate-Based Organic-Inorganic Hybrid Materials: The Actual Ratio of Organic Cations to Heteropolyanions. *Inorg Chem.,* **2023**, *62* (10), 4054–4065.
52. Gumerova, N. I.; Rompel, A. Synthesis, Structures and Applications of Electron-Rich Polyoxometalates. *Nat. Rev. Chem*., **2018**.
53. Wang, H.; Hamanaka, S.; Nishimoto, Y.; Irle, S.; Yokoyama, T.; Yoshikawa, H.; Awaga, K. In Operando X-Ray Absorption Fine Structure Studies of Polyoxometalate Molecular Cluster Batteries: Polyoxometalates as Electron Sponges. *J Am Chem Soc.,* **2012**, *134* (10), 4918–4924.
54. Casañ-Pastor, N.; Gomez-Romero, P.; Jameson, G. B.; Baker, L. C. W. *Crystal Structures of A-[ConW$_{12}$O$_{40}$]$^{6-}$ and Its Heteropoly Blue 2e Reduction Product, a-[ConW$_{12}$O$_{40}$]$^{8-}$. Structural, Electronic, and Chemical Consequences of Electron Delocalization in a Multiatom Mixed-Valence System*; **1991**; Vol. 113.
55. Ahmad, W.; Ahmad, N.; Wang, K.; Aftab, S.; Hou, Y.; Wan, Z.; Yan, B. B.; Pan, Z.; Gao, H. L.; Peung, C.; Junke, Y.; Liang, C.; Lu, Z.; Yan, W.; Ling, M. Electron-Sponge Nature of Polyoxometalates for Next-Generation Electrocatalytic Water Splitting and Nonvolatile Neuromorphic Devices. *Adv. Sci.*, **2024**.
56. Zhang, Y.; Li, Y.; Guo, H.; Guo, Y.; Song, R. Recent Advances in Polyoxometalate-Based Materials and Their Derivatives for Electrocatalysis and Energy Storage. *Mater. Chem. Front.*, **2023**, 732–768.
57. Kortz, U.; Müller, A.; van Slageren, J.; Schnack, J.; Dalal, N. S.; Dressel, M. Polyoxometalates: Fascinating Structures, Unique Magnetic Properties. *Coord. Chem. Rev.,* **2009**, 2315–2327.
58. AlDamen, M. A.; Clemente-Juan, J. M.; Coronado, E.; Martí-Gastaldo, C.; Gaita-Ariño, A. Mononuclear Lanthanide Single-Molecule Magnets Based on Polyoxometalates. *J Am Chem Soc.,* **2008**, *130* (28), 8874–8875.
59. Clemente-Juan, J. M.; Coronado, E.; Gaita-Ariñoa, A. Magnetic Polyoxometalates: From Molecular Magnetism to Molecular Spintronics and Quantum Computing. *Chem Soc Rev.,* **2012**, *41* (22), 7464–7478.
60. Boskovic, C. Rare Earth Polyoxometalates. *Acc Chem Res.,* **2017**, *50* (9), 2205–2214.
61. Ibrahim, M.; Lan, Y.; Bassil, B. S.; Xiang, Y.; Suchopar, A.; Powell, A. K.; Kortz, U. Hexadecacobalt(II)-Containing Polyoxometalate-Based Single-Molecule Magnet. *Angew. Chem. Int. Ed.,* **2011**, *50* (20), 4708–4711.

62. Ibrahim, M.; Mereacre, V.; Leblanc, N.; Wernsdorfer, W.; Anson, C. E.; Powell, A. K. Self-Assembly of a Giant Tetrahedral 3 d-4 f Single-Molecule Magnet within a Polyoxometalate System. *Angew. Chem. Int. Ed.,* **2015**, *54* (51), 15574–15578.
63. Mousavi, S. M.; Hashemi, S. A.; Mazraedoost, S.; Chiang, W. H.; Yousefi, K.; Arjmand, O.; Ghahramani, Y.; Gholami, A.; Omidifar, N.; Pynadathu Rumjit, N.; Salari, M.; Sadrmousavi-Dizaj, A. Anticancer, Antimicrobial and Biomedical Features of Polyoxometalate as Advanced Materials: A Review Study. *Inorg. Chem. Commun.*, **2022.**
64. Cla, P.; And, Y.; Dormont, D. Polyoxometalates III AIDS Therapy; Pope, M. T. , M. A., Ed.; **1994**.
65. Moskovitz, B. L. *Clinical Trial of Tolerance of HPA-23 in Patients with Acquired Immune Deficiency Syndrome*; **1988**; Vol. 32
66. Lentink, S.; Salazar Marcano, D. E.; Moussawi, M. A.; Parac-Vogt, T. N. Exploiting Interactions between Polyoxometalates and Proteins for Applications in (Bio)Chemistry and Medicine. *Angew. Chem. Int. Ed*., **2023.**
67. Bijelic, A.; Aureliano, M.; Rompel, A. Im Kampf Gegen Krebs: Polyoxometallate Als Nächste Generation Metallhaltiger Medikamente. *Angew. Chem.,***2019**, *131* (10), 3008–3029.
68. Wang, S. S.; Yang, G. Y. Recent Advances in Polyoxometalate-Catalyzed Reactions. *Chem. Rev.,* **2015**, 4893–4962.
69. Yu-Feng Liu a, C.-W. H. b, G.-P. Y. a. Recent Advances in Polyoxometalates Acid-Catalyzed Organic Reactions. *Chin. Chem. Lett.,* **2023**.
70. Hu, Q.; Li, K.; Chen, X.; Liu, Y.; Yang, G. Polyoxometalate Catalysts for the Synthesis of N-Heterocycles. *Polyoxometalates* **2024**, *3* (1), 9140048.
71. TOSHIO OKUHARA, A. K. N. H. M. M. Catalysis by Heteropoly Compounds. VI. The Role of the Bulk Acid in Catalytic Reactions over Na,H3-XPW120401. *J Catal* **1983**, *83.*
72. Das, V.; Kaushik, R.; Hussain, F. Heterometallic 3d-4f Polyoxometalates: An Emerging Field with Structural Diversity to Multiple Applications. *Coord. Chem. Rev.*, **2020**.
73. Zhang, Y.; Li, Y.; Guo, H.; Guo, Y.; Song, R. Recent Advances in Polyoxometalate-Based Materials and Their Derivatives for Electrocatalysis and Energy Storage. *Mater. Chem. Front.*, **2023**, 732–768.
74. Sadakane, M.; Steckhan, E. *Electrochemical Properties of Polyoxometalates as Electrocatalysts*; **1998**.
75. Qiushi Yin; Jeffrey Miles Tan; Claire Besson; Djamaladdin G. Musaev; Aleksey E. Kuznetsov, Z. L. C. L. H. A Fast Soluble Carbon-Free Molecular Oxidation Catalyst Based on Abundant Metals. *Phosphorus Sulfur Silicon Relat Elem.,* **2010**, *185* (5–6), 1068–1076.
76. Han, X. B.; Li, Y. G.; Zhang, Z. M.; Tan, H. Q.; Lu, Y.; Wang, E. B. Polyoxometalate-Based Nickel Clusters as Visible Light-Driven Water Oxidation Catalysts. *J Am Chem Soc.* **2015**, *137* (16), 5486–5493.
77. Bassil, B. S.; Ibrahim, M.; Al-Oweini, R.; Asano, M.; Wang, Z.; Van Tol, J.; Dalal, N. S.; Choi, K. Y.; Ngo Biboum, R.; Keita, B.; Nadjo, L.; Kortz, U. A Planar $\{Mn_{19}(OH)_{12}\}^{26+}$ Unit

Incorporated in a 60-Tungsto-6-Silicate Polyanion. *Angew. Chem. Int. Ed.* **2011**, *50* (26), 5961–5964.

78. Godin, B.; Chen, Y.; Vaissermann, J.; Ruhlmann, L.; Verdaguer, M.; Gouzerh, P. Coordination Chemistry of the Hexavacant Tungstophosphate [H 2 P 2 W 12 O 48] 12− with Fe III Ions: Towards Original Structures of Increasing Size and Complexity. *Angew. Chem.* **2005**, *117* (20), 3132–3135.
79. Zhan, C.; Cameron, J. M.; Gao, J.; Purcell, J. W.; Long, D.; Cronin, L. Time-Resolved Assembly of Cluster-in-Cluster {Ag12 }-in-{W76 } Polyoxometalates under Supramolecular Control . *Angew. Chem. Int. Ed.* **2014**, *53* (39), 10362–10366.
80. Huang, L.; Wang, S. S.; Zhao, J. W.; Cheng, L.; Yang, G. Y. Synergistic Combination of Multi-ZrIV Cations and Lacunary Keggin Germanotungstates Leading to a Gigantic Zr_{24}-Cluster-Substituted Polyoxometalate. *J Am Chem Soc.* **2014**, *136* (21), 7637–7642.
81. Mal, S. S.; Kortz, U. The Wheel-Shaped Cu_{20} Tungstophosphate $[Cu_{20}Cl(OH)_{24}(H_2O)_{12}(P_8W_{48}O_{184})]^{25-}$ Ion. *Angew. Chem. Int. Ed.* **2005**, *44* (24), 3777–3780.
82. Ibrahim, M.; Lan, Y.; Bassil, B. S.; Xiang, Y.; Suchopar, A.; Powell, A. K.; Kortz, U. Hexadecacobalt(II)-Containing Polyoxometalate-Based Single-Molecule Magnet. *Angew. Chem. Int. Ed.* **2011**, *50* (20), 4708–4711.
83. Oliveira, P. De; Nadjo, L. Cobalt-Containing Silicotungstate Sandwich Dimer. *Inorg. Chem*. **2005**, *44* (25), 9360–9368.
84. Lisnard, L.; Mialane, P.; Dolbecq, A.; Marrot, J.; Clemente-Juan, J. M.; Coronado, E.; Keita, B.; De Oliveira, P.; Nadjo, L.; Sécheresse, F. Effect of Cyanato, Azido, Carboxylato, and Carbonato Ligands on the Formation of Cobalt(II) Polyoxometalates: Characterization, Magnetic, and Electrochemical Studies of Multinuclear Cobalt Clusters. *Chem. Eur. J.* **2007**, *13* (12), 3525–3536.
85. Rehan, K.; Asma, M.; McMillen, C. D.; Sokolov, A.; Sohail, M.; Sher, M.; Shafique, M. A.; Bukhari, N.; Tirmizi, S. A. Synthesis, Structure, and Properties of the Multinuclear Cobalt Core POM $Na_{14}[Co_3O(H_2O)(A\text{-}\alpha\text{-}PW_9O_{34})_2]\cdot\sim 29.5H_2O$. *Inorganica Chim Acta.* **2020**.
86. Zhang, Z.; Wang, E.; Li, Y.; An, H.; Qi, Y.; Xu, L. Synthesis, Characterization, and Crystal Structures of Two 6-Cobalt-Containing Dimeric Polyoxoanions: $[Co_2(H_2O)_{10}Co_4(H_2O)_2(B\text{-}\alpha\text{-}XW_9O_{34})_2]^{8-}$ (X = Ge and Si). *J Mol Struct.* **2008**, *872* (2–3), 176–181.
87. Duan, Y.; Clemente-Juan, J. M.; Giménez-Saiz, C.; Coronado, E. Large Magnetic Polyoxometalates Containing the Cobalt Cubane "$[Co^{III}Co_3^{II}(OH)_3(H_2O)_{6-m}(PW_9O_{34})]^{3-}$" (m = 3 or 5) as a Subunit. *Front Chem.* **2018.**
88. Haider, A.; Bassil, B. S.; Soriano-López, J.; Qasim, H. M.; Sáenz De Pipaón, C.; Ibrahim, M.; Dutta, D.; Koo, Y. S.; Carbó, J. J.; Poblet, J. M.; Galán-Mascarós, J. R.; Kortz, U. 9-Cobalt(II)-Containing 27-Tungsto-3-Germanate(IV): Synthesis, Structure, Computational Modeling, and Heterogeneous Water Oxidation Catalysis. *Inorg Chem.* **2019**, *58* (17), 11622–11629.
89. Soriano-López, J.; Goberna-Ferrón, S.; Vigara, L.; Carbó, J. J.; Poblet, J. M.; Galán-Mascarós, J. R. Cobalt Polyoxometalates as Heterogeneous Water Oxidation Catalysts. *Inorg Chem.* **2013**, *52* (9), 4753–4755.

90. Bassil, B. S.; Nellutla, S.; Kortz, U.; Stowe, A. C.; Tol, J. Van; Dalal, N. S.; Keita, B.; Nadjo, L. The Satellite-Shaped Co-15 Polyoxotungstate. *Inorg Chem.* **2005**, *44* (8), 2659–2665.
91. Ibrahim, M.; Lan, Y.; Bassil, B. S.; Xiang, Y.; Suchopar, A.; Powell, A. K.; Kortz, U. Hexadecacobalt(II)-Containing Polyoxometalate-Based Single-Molecule Magnet. *Angew. Chem. Int. Ed.* **2011**, *50* (20), 4708–4711.
92. Ibrahim, M.; Haider, A.; Lan, Y.; Bassil, B. S.; Carey, A. M.; Liu, R.; Zhang, G.; Keita, B.; Li, W.; Kostakis, G. E.; Powell, A. K.; Kortz, U. Multinuclear Cobalt(II)-Containing Heteropolytungstates: Structure, Magnetism, and Electrochemistry. . *Inorg Chem.* **2014.**
93. Liu, Z. Z.; Huang, S. L.; Yang, G. Y. High-Nuclear Co-Added Polyoxometalate-Based Chain: Electrocatalytic Oxygen Production. *Inorg Chem.* **2024**, *63* (28), 12803–12809.
94. Shi, D.; Cui, C. J.; Sun, C. X.; Du, J. P.; Liu, C. Sen. A New $[Co_{21}(H_2O)_4(OH)_{12}]^{30+}$unit-Incorporating Polyoxotungstate for Sensitive Detection of Dichlorvos. *New J. Chem.* **2020**, *44* (26), 11336–11341.
95. Zhao, Q.; Li, X.; Wang, Y.; Lv, H.; Yang, G. A Hexadecanuclear Cobalt-Added Tungstogermanate Containing Counter Cobalt Hydrates: Synthesis, Structure and Photocatalytic Properties. *Nanomaterials.* **2023**, *13* (13).
96. Zhang, Z.; Li, Y.; Wang, E.; Wang, X.; Qin, C.; An, H. Synthesis, Characterization, and Crystal Structures of Two Novel High-Nuclear Nickel-Substituted Dimeric Polyoxometalates. *Inorg Chem*. **2006**, *45* (11), 4313–4315.
97. Yao, S.; Zhang, Z.; Li, Y.; Wang, E. Two Hexa-TM-Containing (TM = Co^{2+} and Ni^{2+}) {P_2W_{12}}-Based Trimeric Tungstophosphates. *Dalton Trans.* **2010**, *39* (16), 3884–3889.
98. Z. Zhang.; E. Wang.; Y. Qi; Y. Li; B. Ma; Z. Su.; Synthesis, Characterization, and Crystal Structures of Double-Cubane-Substituted and Asymmetric Penta-Ni-Substituted. *Cryst. Growth Des*. **2007** Vol. 7, No. 7.
99. Pichon, C.; Mialane, P.; Dolbecq, A.; Marrot, J.; Rivière, E.; Bassil, B. S.; Kortz, U.; Keita, B.; Nadjo, L.; Sécheresse, F. Octa- and Nonanuclear Nickel(II) Polyoxometalate Clusters: Synthesis and Electrochemical and Magnetic Characterizations. *Inorg Chem.* **2008**, *47* (23), 11120–11128.
100. Clemente-Juan, J. M.; Coronado, E.; Galán-Mascarós, J. R.; Gómez-García, C. J. G. Increasing the Nuclearity of Magnetic Polyoxometalates. Syntheses, Structures, and Magnetic Properties of Salts of the Heteropoly Complexes $[Ni_3(H_2O)_3(PW_{10}O_{39})H_2O]^{7-}$, $[Ni_4(H_2O)_2(PW_9O_{34})_2]^{10-}$, and $[Ni_9(OH)_3(H_2O)_6(HPO_4)_2(PW_9O_{34})_3]^{16-}$. *Inorg. Chem.* **1999**, *38* (1), 55–63.
101. Zhang, H. M.; Li, Y. G.; Lu, Y.; Clérac, R.; Zhang, Z. M.; Wu, Q.; Feng, X. J.; Wang, E. B. A New Ni_{12} Cluster Based on Polyoxometalate Ligands. *Inorg Chem.* **2009**, *48* (23), 10889–10891.
102. Han, X. B.; Li, Y. G.; Zhang, Z. M.; Tan, H. Q.; Lu, Y.; Wang, E. B. Polyoxometalate-Based Nickel Clusters as Visible Light-Driven Water Oxidation Catalysts. *J Am Chem Soc.* **2015**, *137* (16), 5486–5493.

103. Ibrahim, M.; Xiang, Y.; Bassil, B. S.; Lan, Y.; Powell, A. K.; Oliveira, P. De; Keita, B.; Kortz, U. Synthesis, Magnetism, and Electrochemistry of the Ni_{14}- and Ni_5-Containing Heteropolytungstates $[Ni_{14}(OH)_6(H_2O)_{10}(HPO_4)_4(P_2W_{15}O_{56})_4]^{34-}$ and $[Ni_5(OH)_4(H_2O)_4(\beta\text{-}GeW_9O_{34})(\beta\text{-}GeW_8O_{30}(OH))]^{13-}$. *Inorg.Chem.* **2013**, *14*.

104. Lv, H.; Chi, Y.; Van Leusen, J.; Kögerler, P.; Chen, Z.; Bacsa, J.; Geletii, Y. V.; Guo, W.; Lian, T.; Hill, C. L. 28-: A New Polyoxometalate Structural Family with Catalytic Hydrogen Evolution Activity. *Chem. Eur. J.* **2015**, *21* (48), 17363–17370.

105. Wang, Y.; Xin, X.; Feng, Y.; Chi, M.; Wang, R.; Liu, T.; Lv, H. Structurally-New Hexadecanuclear Ni-Containing Silicotungstate with Catalytic Hydrogen Generation Activity. *Molecules* **2023**, *28* (5).

106. Goura, J.; Bassil, B. S.; Ma, X.; Rajan, A.; Moreno-Pineda, E.; Schnack, J.; Ibrahim, M.; Powell, A. K.; Ruben, M.; Wang, J.; Ruhlmann, L.; Kortz, U. Ni^{II}_{36}-Containing 54-Tungsto-6-Silicate: Synthesis, Structure, Magnetic and Electrochemical Studies. *Chem. Eur. J.* **2021**, *27* (61), 15080–15084.

107. Limanski, E. M.; Piepenbrink, M.; Droste, E.; Burgemeister, K.; Krebs, B. Syntheses and X-Ray Characterization of Novel $[M_4(H_2O)_2(XW_9O_{34})_2]^{N-}$ (M=Cu^{II} , X=Cu^{II} ; and M=Fe^{III} , X=Fe^{III}) Polyoxotungstates; **2002**; Vol. 13.

108. Andersen, T. M.; Neiwert, W. A.; Hardcastle, K. I.; Hill, C. L. Multi-Iron Silicotungstates: Synthesis, Characterization, and Stability Studies of Polyoxometalate Dimers. *Inorg Chem.* **2004**, *43* (23), 7353–7358.

109. Bi, L. H.; Kortz, U.; Nellutla, S.; Stowe, A. C.; Van Tol, J.; Dalal, N. S.; Keita, B.; Nadjo, L. Structure, Electrochemistry, and Magnetism of the Iron(III)-Substituted Keggin Dimer, $[Fe_6(OH)_3(A\text{-}\alpha\text{-}GeW_9O_{34}(OH)_3)_2]^{11-}$. *Inorg Chem.* **2005**, *44* (4), 896–903.

110. Barats, D.; Leitus, G.; Popovitz-Biro, R.; Shimon, L. J. W.; Neumann, R. A Stable “End-on” Iron(III)-Hydroperoxo Complex in Water Derived from a Multi-Iron(II)-Substituted Polyoxometalate and Molecular Oxygen. *Angew. Chem. Int. Ed.* **2008**, *47* (51), 9908–9912.

111. Compain, J. D.; Mialane, P.; Dolbecq, A.; Mbomekallé, I. M.; Marrot, J.; Sécheresse, F.; Riviére, E.; Rogez, G.; Wernsdorfer, W. Iron Polyoxometalate Single-Molecule Magnets. *Angew. Chem. Int. Ed.* **2009**, *48* (17), 3077–3081.

112. Chen, W. C.; Qin, C.; Wang, X. L.; Li, Y. G.; Zang, H. Y.; Jiao, Y. Q.; Huang, P.; Shao, K. Z.; Su, Z. M.; Wang, E. B. Assembly of Fe-Substituted Dawson-Type Nanoscale Selenotungstate Clusters with Photocatalytic H2 Evolution Activity. *ChemComm.* **2014**, *50* (87), 13265–13267.

113. Godin, B.; Chen, Y. G.; Vaissermann, J.; Ruhlmann, L.; Verdaguer, M.; Gouzerh, P. Coordination Chemistry of the Hexavacant Tungstophosphate $[H_2P_2W_{12}O_{48}]^{12-}$ with Fe^{III} Ions: Towards Original Structures of Increasing Size and Complexity. *Angew. Chem. Int. Ed.* **2005**, *44* (20), 3072–3075.

114. Singh, V.; Chen, Z.; Ma, P.; Zhang, D.; Drew, M. G. B.; Niu, J.; Wang, J. Unprecedented $\{Fe_{14}\}/\{Fe_{10}\}$ Polyoxotungstate-Based Nanoclusters with Efficient Photocatalytic H2Evolution

Activity: Synthesis, Structure, Magnetism, and Electrochemistry. *Chem. Eur. J.* **2016**, *22* (31), 10983–10989.

115. Du, X.; Zhao, J.; Mi, J.; Ding, Y.; Zhou, P.; Ma, B.; Zhao, J.; Song, J. Efficient Photocatalytic H_2 Evolution Catalyzed by an Unprecedented Robust Molecular Semiconductor {Fe11} Nanocluster without Cocatalysts at Neutral Conditions. *Nano Energy.* **2015**, *16*, 247–255.
116. Pradeep, C. P.; Long, D. L.; Kögerler, P.; Cronin, L. Controlled Assembly and Solution Observation of a 2.6 Nm Polyoxometalate "super" Tetrahedron Cluster: $[KFe_{12}(OH)_{18}(\alpha\text{-}1,2,3\text{-}P_2W_{15}O_{56})_4]^{29-}$. *ChemComm.* **2007**, No. 41, 4254–4256.
117. Molina, P. I.; Miras, H. N.; Long, D. L.; Cronin, L. Assembly and Core Transformation Properties of Two Tetrahedral Clusters: $[Fe^{III}_{13}P_8W_{60}O_{227}(OH)_{15}(H_2O)_2]^{30-}$ and $[Fe^{III}_{13}P_8W_{60}O_{224}(OH)_{12}(PO_4)_4]^{33-}$. *Dalton Trans.* **2014**, *43* (13), 5190–5199.
118. Ibrahim, M.; Haider, A.; Xiang, Y.; Bassil, B. S.; Carey, A. M.; Rullik, L.; Jameson, G. B.; Doungmene, F.; Mbomekallé, I. M.; De Oliveira, P.; Mereacre, V.; Kostakis, G. E.; Powell, A. K.; Kortz, U. Tetradecanuclear Iron(III)-Oxo Nanoclusters Stabilized by Trilacunary Heteropolyanions. *Inorg Chem.* **2015**, *54* (13), 6136–6146.
119. Cui, T.; Qin, L.; Fu, F.; Xin, X.; Li, H.; Fang, X.; Lv, H. Pentadecanuclear Fe-Containing Polyoxometalate Catalyst for Visible-Light-Driven Generation of Hydrogen. *Inorg Chem.* **2021**, *60* (6), 4124–4132.
120. Mal, S. S.; Dickman, M. H.; Kortz, U.; Todea, A. M.; Merca, A.; Bögge, H.; Glaser, T.; Müller, A.; Nellutla, S.; Kaur, N.; Van Tol, J.; Dalal, N. S.; Keita, B.; Nadjo, L. Nucleation Process in the Cavity of a 48-Tungstophosphate Wheel Resulting in a 16-Metal-Centre Iron Oxide Nanocluster. *Chem. Eur. J.* **2008**, *14* (4), 1186–1195.
121. Godin, B.; Chen, Y.; Vaissermann, J.; Ruhlmann, L.; Verdaguer, M.; Gouzerh, P. Coordination Chemistry of the Hexavacant Tungstophosphate $[H_2P_2W_{12}O_{48}]^{12-}$ with Fe^{III} Ions: Towards Original Structures of Increasing Size and Complexity . *Angew. Chem.* **2005**, *117* (20), 3132–3135.
122. Todea, A. M.; Merca, A.; Bögge, H.; Glaser, T.; Pigga, J. M.; Langston, M. L. K.; Liu, T.; Prozorov, R.; Luban, M.; Schröder, C.; Casey, W. H.; Müller, A. Porous Capsules $\{(M)M_5\}_{12}Fe^{III}_{30}$ ($M=Mo^{VI}$, W^{VI}): Sphere Surface Supramolecular Chemistry with 20 Ammonium Ions, Related Solution Properties, and Tuning of Magnetic Exchange Interactions . *Angew. Chem.* **2010**, *122* (3), 524–529.
123. Goura, J.; Bassil, B. S.; Bindra, J. K.; Rutkowska, I. A.; Kulesza, P. J.; Dalal, N. S.; Kortz, U. FeIII48-Containing 96-Tungsto-16-Phosphate: Synthesis, Structure, Magnetism and Electrochemistry. *Chem. Eur. J.* **2020**, *26* (68), 15821–15824.
124. Zheng, S. T.; Yuan, D. Q.; Jia, H. P.; Zhang, J.; Yang, G. Y. Combination between Lacunary Polyoxometalates and High-Nuclear Transition Metal Clusters under Hydrothermal Conditions: I. From Isolated Cluster to 1-D Chain. *ChemComm.***2007**, No. 18, 1858–1860.
125. Zhao, J. W.; Zhang, J.; Zheng, S. T.; Yang, G. Y. Combination between Lacunary Polyoxometalates and High-Nuclear Transition Metal Clusters under Hydrothermal Conditions: First (3,6)-Connected Framework Constructed from Sandwich-Type

Polyoxometalate Building Blocks Containing a Novel {Cu_8} Cluster. *ChemComm.* **2002**, *8* (5), 570–572.

126. Li, H. Lou; Lian, C.; Yang, G. Y. {Ti_6}/{Ti_{10}} Wheel Cluster Substituted Silicotungstate Aggregates. *Inorg Chem.* **2021**, *60* (21), 16852–16859.
127. Souza, J. R. C.; Torres, J. A.; Ribeiro, L. S.; Filho, J. B. G.; Santos, F. L.; Malgioglio, N.; Gorup, L. F.; Pinto, A. H.; Nogueira, A. E. The Facile Microwave-Assisted Coprecipitation Route to Obtain Polyoxoniobate ($Na_7(H_3O)Nb_6O_{19}{\cdot}14H_2O$) Nanorods Modified with Copper for CO_2 Photoreduction. *AppliedChem.* **2023**, *3* (2), 320–333.
128. Spillane, S.; Sharma, R.; Zavras, A.; Mulder, R.; Ohlin, C. A.; Goerigk, L.; O'Hair, R. A. J.; Ritchie, C. Nichtwässrige Mikrowellengestützte Synthesen von Deca- Und Hexamolybdovanadaten. *Angew. Chem.* **2017**, *129* (29), 8691–8695.
129. Lian, C.; Li, H. Lou; Yang, G. Y. High-Nuclear Ni-Substituted Poly(Polyoxometalate) Containing an Anderson-like {Cs_7} Cluster. *Inorg Chem.* **2022**, *61* (29), 11335–11341.
130. Zheng, S. T.; Zhang, J.; Li, X. X.; Fang, W. H.; Yang, G. Y. Cubic Polyoxometalate-Organic Molecular Cage. *J Am Chem Soc.* **2010**, *132* (43), 15102–15103.
131. Li, D.; Ma, P.; Niu, J.; Wang, J. Recent Advances in Transition-Metal-Containing Keggin-Type Polyoxometalate-Based Coordination Polymers. *Coord. Chem. Rev.* 2019, 49–80.
132. Crossley, S.; Faria, J.; Shen, M.; Resasco, D. E. Solid Nanoparticles That Catalyze Biofuel Upgrade Reactions at the Water/Oil Interface. *Science(1979)* **2010**, *327* (5961), 68–72.
133. Bassil, B. S.; Kortz, U. Recent Advances in Lanthanide-Containing Polyoxotungstates. *Z Anorg Allg Chem.* **2010**, *636* (12), 2222–2231.
134. Das, V.; Kaushik, R.; Hussain, F. Heterometallic 3d-4f Polyoxometalates: An Emerging Field with Structural Diversity to Multiple Applications. *Coord. Chem. Rev.* **2020**.
135. Ritchie, C.; Moore, E. G.; Speldrich, M.; Kögerler, P.; Boskovic, C. Terbium Polyoxometalate Organic Complexes: Correlation of Structure with Luminescence Properties. *Angew. Chem.* **2010**, *122* (42), 7868–7871.
136. Hussain, F.; Conrad, F.; Patzke, G. R. Ein Gadolinium-verbrückter Polywolframarsenat(III)-Nanocluster: $[Gd_8As_{12}W_{124}O_{432}(H_2O)_{22}]^{60-}$. *Angew. Chem.* **2009**, *121* (48), 9252–9255.
137. Thomas, J. A. Metal Ion Directed Self-Assembly of Sensors for Ions, Molecules and Biomolecules. *Dalton Trans.* 2011, 12005–12016.
138. Ibrahim, M.; Mereacre, V.; Leblanc, N.; Wernsdorfer, W.; Anson, C. E.; Powell, A. K. Selbstorganisation Eines Riesigen Tetraedrischen 3d-4f-Einzelmolekülmagneten Innerhalb Eines Polyoxometallatsystems. *Angew. Chem.* **2015**, *127* (51), 15795–15799.
139. Chen, W.; Li, Y.; Wang, Y.; Wang, E.; Zhang, Z. A New Polyoxometalate-Based 3d–4f Heterometallic Aggregate: A Model for the Design and Synthesis of New Heterometallic Clusters. *J. Chem. Soc., Dalton Trans.* **2007**, No. 7, 865–867
140. Fang, X.; Kögerler, P. PO43--Mediated Polyoxometalate Supercluster Assembly. *Angew. Chem. Int. Ed.* **2008**, *47* (42), 8123–8126.
141. Reinoso, S.; Galán-Mascarós, J. R. Heterometallic 3d-4f Polyoxometalate Derived from the Weakley-Type Dimeric Structure. *Inorg Chem.* **2010**, *49* (2), 377–379.

142. Reinoso, S.; Galán-Mascarós, J. R.; Lezama, L. New Type of Heterometallic 3d-4f Rhomblike Core in Weakley-like Polyoxometalates. *Inorg Chem.* **2011**, *50* (19), 9587–9593.
143. Zhang, Z. M.; Li, Y. G.; Yao, S.; Wang, E. B. Hexameric Polyoxometalates Decorated by Six 3d-4f Heterometallic Clusters. *Dalton Trans.***2011**, *40* (24), 6475–6479.
144. Ismail, A. H.; Bassil, B. S.; Yassin, G. H.; Keita, B.; Kortz, U. {W 48} Ring Opening: Fe 16-Containing, Ln 4-Stabilized 49-Tungsto-8-Phosphate Open Wheel $[Fe_{16}O_2(OH)_{23}(H_2O)_9(P_8W_{49}O_{189})Ln_4(H_2O)_{20}]^{11-}$. *Chem. Eur. J.* **2012**, *18* (20), 6163–6166.
145. Wu, H. H.; Yao, S.; Zhang, Z. M.; Li, Y. G.; Song, Y.; Liu, Z. J.; Han, X. B.; Wang, E. B. Heterometallic Appended $\{MMn^{III}_4\}$ Cubanes Encapsulated by Lacunary Polytungstate Ligands. *Dalton Trans.* **2013**, *42* (2), 342–346.
146. Shurong Li a, Z. W. a, L. J. a, R. W. b, H. S. a, L. L. a, L. Z. a, X. K. a. A Series of Heterometallic 3d-4f Polyoxometalates as Single-Molecule Magnets. *Chin. Chem. Lett.* **2023**, *34* (3), 107251.
147. Das, V.; Khan, I.; Hussain, F.; Sadakane, M.; Tsunoji, N.; Ichihashi, K.; Kato, C.; Inoue, K.; Nishihara, S. Single-Molecule Magnetic, Catalytic and Photoluminescence Properties of Heterometallic 3d–4f $[Ln\{PZn_2W_{10}O_{38}(H_2O)_2\}_2]^{11-}$ Tungstophosphate Nanoclusters. *Eur J Inorg Chem.* **2021**, *2021* (37), 3819–3831.
148. Li, S. R.; Wang, H. Y.; Su, H. F.; Chen, H. J.; Du, M. H.; Long, L. S.; Kong, X. J.; Zheng, L. S. A Giant 3d-4f Polyoxometalate Super-Tetrahedron with High Proton Conductivity. *Small Methods.* **2021**, *5* (3).
149. Cai, J.; Ye, R.; Liu, X.; Guo, L.; Qiao, X. Ionic Strength Effect on Regulating the Synthetic Assembly of Polyoxometalate Clusters with Slow Magnetic Relaxation Behavior. *Dalton Trans.* **2020**, *49* (46), 16954–16961.
150. Gu, Y. N.; Yu, H.; Lin, L. D.; Wu, Y. L.; Li, Z.; Pan, W. Y.; He, J.; Chen, L.; Li, Q.; Li, X. X. Two Rare Cr-Ln (Ln = Dy, Tb) Heterometallic Cluster Substituted Polyoxometalates Featuring Hexameric Aggregates: Hydrothermal Syntheses, Crystal Structures and Magnetic Studies. *New J. Chem.* **2019**, *43* (7), 3011–3016.
151. Das, V.; Khan, I.; Hussain, F.; Sadakane, M.; Hageo, K.; Ichihashi, K.; Inoue, K.; Nishihara, S. A Self-Assembled Heterometallic $\{Co_7–Ho_1\}$ Nanocluster: 3d-4f Trimeric Keggin-Type Silicotungstate $[HoCo_7Si_3W_{29}O_{108}(OH)_5(H_2O)_4]^{18–}$ and Its Catalytic and Magnetic Applications. *Eur J Inorg Chem*. **2019**, *2019* (3), 430–436.
152. Ibrahim, M.; Moreno-Pineda, E.; Bergfeldt, T.; Anson, C. E.; Powell, A. K. Synthesis and Characterization of a Heterometallic Extended Architecture Based on a Manganese (II)-Substituted Sandwich-Type Polyoxotungstate. *Materials.* **2018**, *11* (1).
153. Cai, J.; Zheng, X. Y.; Xie, J.; Yan, Z. H.; Kong, X. J.; Ren, Y. P.; Long, L. S.; Zheng, L. S. Anion-Dependent Assembly of Heterometallic 3d-4f Clusters Based on a Lacunary Polyoxometalate. *Inorg Chem* **2017**, *56* (14), 8439–8445.
154. Xue, G.; Liu, B.; Hu, H.; Yang, J.; Wang, J.; Fu, F. Large Heteropolymetalate Complexes Formed from Lanthanide (Y, Ce, Pr, Nd, Sm, Eu, Gd), Nickel Cations and Cryptate

$[As_4W_{40}O_{140}]^{28-}$: Synthesis and Structure Characterization. *J Mol Struct.* **2004**, *690* (1–3), 95–103.

155. Merca, A.; Müller, A.; Van Slageren, J.; Läge, M.; Krebs, B. Systematic Study of the Interaction between VIV Centres and Lanthanide Ions M^{III} in Well Defined $\{V^{IV}_2M^{III}\}\{As^{III}W_9O_{33}\}_2$ Sandwich Type Clusters: Part 1. *J Clust Sci.* **2007**, *18* (3), 711–719.
156. Yao, S.; Zhang, Z.; Li, Y.; Lu, Y.; Wang, E.; Su, Z. Two Heterometallic Aggregates Constructed from the {P2W 12}-Based Trimeric Polyoxotungstates and 3d-4f Heterometals. *Cryst Growth Des.* **2010**, *10* (1), 135–139.
157. Gupta, R.; Hussain, F.; Sadakane, M.; Kato, C.; Inoue, K.; Nishihara, S. Lanthanoid Template Isolation of the α-1,5 Isomer of Dicobalt(II)-Substituted Keggin Type Phosphotungstates: Syntheses, Characterization, and Magnetic Properties. *Inorg Chem.* **2016**, *55* (17), 8292–8300.
158. Cai, J.; Zheng, X. Y.; Xie, J.; Yan, Z. H.; Kong, X. J.; Ren, Y. P.; Long, L. S.; Zheng, L. S. Anion-Dependent Assembly of Heterometallic 3d-4f Clusters Based on a Lacunary Polyoxometalate. *Inorg Chem.* **2017**, *56* (14), 8439–8445.
159. Das, V.; Khan, I.; Hussain, F.; Sadakane, M.; Hageo, K.; Ichihashi, K.; Inoue, K.; Nishihara, S. A Self-Assembled Heterometallic $\{Co_7–Ho_1\}$ Nanocluster: 3d-4f Trimeric Keggin-Type Silicotungstate $[HoCo_7Si_3W_{29}O_{108}(O_H)_5\ (H_2O)_4]^{18–}$ and Its Catalytic and Magnetic Applications. *Eur J Inorg Chem.* **2019**, *2019* (3), 430–436.
160. Gu, Y. N.; Yu, H.; Lin, L. D.; Wu, Y. L.; Li, Z.; Pan, W. Y.; He, J.; Chen, L.; Li, Q.; Li, X. X. Two Rare Cr-Ln (Ln = Dy, Tb) Heterometallic Cluster Substituted Polyoxometalates Featuring Hexameric Aggregates: Hydrothermal Syntheses, Crystal Structures and Magnetic Studies. *New J. Chem.* **2019**, *43* (7), 3011–3016.
161. Bassil, B. S.; Dickman, M. H.; Römer, I.; Von Der Kammer, B.; Kortz, U. The Tungstogermanate $[Ce_{20}Ge_{10}W_{100}O_{376}(OH)_4(H_2O)_{30}]^{56-}$: A Polyoxometalate Containing 20 Cerium (III) Atoms. *Angew. Chem. Int. Ed.* **2007**, *46* (32), 6192–6195.
162. Liu, L. L.; Wang, L.; Xiao, X. Y.; Yang, P.; Zhao, J.; Kortz, U. Structural Overview and Evolution Paths of Lacunary Polyoxometalates. *Coord. Chem. Rev.* **2024**.
163. Zhang, C.; Howell, R. C.; Scotland, K. B.; Perez, F. G.; Todaro, L.; Francesconi, L. C. Aqueous Speciation Studies of Europium (III) Phosphotungstate. *Inorg Chem* **2004**, *43* (24), 7691–7701.
164. Liu, Y.; Shang, J.; Xue, G.; Hu, H.; Fu, F.; Wang, J. A Dimeric Fe(III)-Substituted α-Keggin Tungstogermanate: $([\alpha\text{-}GeFe_2W_{10}O_{38}(OH)]_2)^{14-}$. *J Clust Sci.* **2007**, *18* (1), 205–216.
165. Ruizhan, T.; Chen, L.; Liu, Y.; Liu, B.; Xue, G.; Hu, H.; Fu, F.; Wang, J. A New Multi-Cobalt-Substituted C-Shaped Polyoxotungstogermanate, $[((CoOH_2)Co_2GeW_9O_{34})_2(GeW_6O_{26})]^{20-}$. *Inorg Chem Commun.* **2010**, *13* (1), 98–100.
166. H Levitt. Spin Dynamics: Basics of Nuclear Magnetic Resonance. **2008**.
167. Nagel, S. M.; Strangfeld, C.; Kruschwitz, S. Application of ^{1}H Proton NMR Relaxometry to Building Materials – A Review. *J Magn Reson Open.* **2021**, *6–7*.
168. Keeler, J. H. *Understanding NMR Spectroscopy*.

169. E. L. Hahn. Nuclear Induction Due to Free Larmor Precession. *Phys. Rev.* **1950**, *77*, 297.
170. Rabenstein, D. L.; Millis, K. K.; Strauss, E. J. Proton NMR Spectroscopy of Human Mood Plasma.
171. Chou, C. Y.; Abdesselem, M.; Bouzigues, C.; Chu, M.; Guiga, A.; Huang, T. H.; Ferrage, F.; Gacoin, T.; Alexandrou, A.; Sakellariou, D. Ultra-Wide Range Field-Dependent Measurements of the Relaxivity of Gd1-x Eux VO_4 Nanoparticle Contrast Agents Using a Mechanical Sample-Shuttling Relaxometer. *Sci Rep* **2017**, *7*.
172. Bottrill, M.; Kwok, L.; Long, N. J. Lanthanides in Magnetic Resonance Imaging. *Chem Soc Rev*. **2006**, *35* (6), 557–571.
173. Aime, S.; Botta, M.; Fasano, M.; Terreno, E. *Lanthanide(III) Chelates for NMR Biomedical Applications*.
174. Helm, L. Relaxivity in Paramagnetic Systems: Theory and Mechanisms. *Progress in Nuclear Magnetic Resonance Spectroscopy*. **2006**, 45–64.
175. Sharp, R.; Lohr, L.; Miller, J. *Paramagnetic NMR Relaxation Enhancement: Recent Advances in Theory*.*Chem. Soc. Rev.* **1998**, 27, 19-29.
176. Caravan, P.; Greenfield, M. T.; Bulte, J. W. M. Molecular Factors That Determine Curie Spin Relaxation in Dysprosium Complexes. *Magn Reson Med.* **2001**, *46* (5), 917–922.
177. Harris, M.; Biju, S.; Parac-Vogt, T. N. High-Field MRI Contrast Agents and Their Synergy with Optical Imaging: The Evolution from Single Molecule Probes towards Nano-Architectures. *Chem. Eur. J.***2019**,13838–13847.
178. Schork, N.; Ibrahim, M.; Baksi, A.; Krämer, S.; Powell, A. K.; Guthausen, G. NMR Relaxivities of Paramagnetic, Ultra-High Spin Heterometallic Clusters within Polyoxometalate Matrix as a Function of Solvent and Metal Ion. *ChemPhysChem*. **2022**
179. Hermann, P.; Kotek, J.; Kubíček, V.; Lukeš, I. Gadolinium(III) Complexes as MRI Contrast Agents: Ligand Design and Properties of the Complexes. *Dalton Trans.* **2008**, No. 23, 3027–3047.
180. Randall B. Lauffer. Paramagnetic Metal Complexes as Water Proton Relaxation Agents for NMR Imaging: Theory and Design. C*hem. Rev.* **1987**, *47* (5), 901–927.
181. Hermann, P.; Kotek, J.; Kubíček, V.; Lukeš, I. Gadolinium(III) Complexes as MRI Contrast Agents: Ligand Design and Properties of the Complexes. *Dalton Trans.***2008**, No. 23, 3027–3047.
182. Lanir, A. Electron Spin Relaxation Time of Fe (III) in High Spin Heme Protiens.; ***BBA General Subjects***. **1977**; Vol. 497.
183. Nasser Din, R.; Venu, A. C.; Rudszuck, T.; Vallet, A.; Favier, A.; Powell, A. K.; Guthausen, G.; Ibrahim, M.; Krämer, S. Longitudinal and Transverse ^{1}H Nuclear Magnetic Resonance Relaxivities of Lanthanide Ions in Aqueous Solution up to 1.4 GHz/33 T. *Molecules* **2024**, *29* (20), 4956.
184. Ibrahim, M.; Rudszuck, T.; Kerdi, B.; Krämer, S.; Guthausen, G.; Powell, A. K. Comparative NMR Relaxivity Study of Polyoxometalate-Based Clusters $[Mn_4(H_2O)_2(P_2W_{15}O_{56})_2]^{16-}$ and

[{Dy(H_2O)$_6$}$_2$Mn$_4$(H_2O)$_2$(P2W$_{15}$O$_{56}$)$_2$]$^{10-}$ from 20 MHz to 1.2 GHz. *Appl Magn Reson.* **2020**, *51* (11), 1295–1305.

185. Gustavo A. ; Mercier Jr. *Enhancing the relaxivity of paramagnetic coordination complexes through the optimization of the molecular electrostatic potential.* Mag. Res. Img. **1998**.
186. Mercier Jr. ;Gustavo A. *Enhancing the relaxivity of paramagnetic coordination complexes through the optimization of the molecular electrostatic potential.* Mag. Res. Img. **1998**.
187. Rashid, H. U.; Martines, M. A. U.; Jorge, J.; de Moraes, P. M.; Umar, M. N.; Khan, K.; Rehman, H. U. Cyclen-Based Gd^{3+}complexes as MRI Contrast Agents: Relaxivity Enhancement and Ligand Design. *Bioorg. Med. Chem*. **2016**, 5663–5684.
188. Schork, N.; Ibrahim, M.; Baksi, A.; Krämer, S.; Powell, A. K.; Guthausen, G. NMR Relaxivities of Paramagnetic, Ultra-High Spin Heterometallic Clusters within Polyoxometalate Matrix as a Function of Solvent and Metal Ion. *ChemPhysChem*. **2022.**
189. Fries, P. H.; Belorizky, E. Electronic Relaxation of Paramagnetic Metal Ions and NMR Relaxivity in Solution: Critical Analysis of Various Approaches and Application to a Gd(III)-Based Contrast Agent. *J.Chem. Phy.***2005**, *123* (12).
190. Borel, A.; Bean, J. F.; Clarkson, R. B.; Helm, L.; Moriggi, L.; Sherry, A. D.; Woods, M. Towards the Rational Design of MRI Contrast Agents: Electron Spin Relaxation Is Largely Unaffected by the Coordination Geometry of Gadolinium(III)-DOTA-Type Complexes. *Chem. Eur. J.* **2008**, *14* (9), 2658–2667.
191. Benmelouka, M.; Borel, A.; Moriggi, L.; Helm, L.; Merbach, A. E. Design of Gd(III)-Based Magnetic Resonance Imaging Contrast Agents: Static and Transient Zero-Field Splitting Contributions to the Electronic Relaxation and Their Impact on Relaxivity. *J. Phys. Chem. B.* **2007**, *111* (4), 832–840.
192. Sharp, R.; Lohr, L.; Miller, J. *Paramagnetic NMR Relaxation Enhancement: Recent Advances in Theory*.*Progress in Nuclear Magnetic Resonance Spectroscopy.* **2001**.
193. De Haën, C. Conception of the First Magnetic Resonance Imaging Contrast Agents: A Brief History. *Topics in Magnetic Resonance Imaging* **2001**, *12* (4), 221–230.
194. Caravan, P.; Ellison, J. J.; McMurry, T. J.; Lauffer, R. B. Gadolinium(III) Chelates as MRI Contrast Agents: Structure, Dynamics, and Applications. *Chem Rev* **1999**, *99* (9), 2293–2352.
195. Kagawa, T.; Yoshida, S.; Shiraishi, T.; Hashimoto, M.; Inadomi, D.; Sato, M.; Tsuzuki, T.; Miwa, K.; Yuasa, K. Basic Principles of Magnetic Resonance Imaging for Beginner Oral and Maxillofacial Radiologists. *Oral Radiology*. 2017.
196. Library, K. I. T.; Core, C. MRI Physics – Basic Principles. **2009**, 200–201.
197. Le Bihan, D. Looking into the Functional Architecture of the Brain with Diffusion MRI. *Nat Rev Neurosci.* **2003**, *4* (6), 469–480.
198. Grover, V. P. B.; Tognarelli, J. M.; Crossey, M. M. E.; Cox, I. J.; Taylor-Robinson, S. D.; McPhail, M. J. W. Magnetic Resonance Imaging: Principles and Techniques: Lessons for Clinicians. *J Clin Exp Hepatol* **2015**, *5* (3), 246–255.

199. Feng, J.; Li, X.; Pei, F.; Sun, G.; Zhang, X.; Liu, M. An Evaluation of Gadolinium Polyoxometalates as Possible MRI Contrast Agent. *Magn Reson Imaging.* **2002**, *20* (5), 407–412.
200. Xinyu Li.; Xiaojing Li.; Shanrong Zhang.; Fengkui Pei. NMR Relaxation Studies of GdDTPA in Human Serum Albumin Solution. *Polyhedron*. **1999**.
201. Feng, J.; Sun, G.; Pei, F.; Liu, M. Comparison between GdDTPA and Two Gadolinium Polyoxometalates as Potential MRI Contrast Agents. *J. Inorg. Biochem.* **2002**, *92* (3–4), 193–199.
202. Sun, G.; Feng, J.; Wu, H.; Pei, F.; Fang, K.; Lei, H. Investigation of Sandwiched Gadolinium (III) Complexes with Tungstosilicates as Potential MRI Contrast Agents. *Magn Reson Imaging.* **2004**, *22* (3), 421–426.
203. Sun, G.; Feng, J.; Wu, H.; Pei, F.; Fang, K.; Lei, H. Gadolinium Heteropoly Complex $K_{17}[Gd(P_2W_{17}O_{61})_2]$ as a Potential MRI Contrast Agent. *J Magn Magn Mater.* **2004**, *281* (2–3), 405–409.
204. Li, Z.; Li, W.; Li, X.; Pei, F.; Li, Y.; Lei, H. The Gadolinium Complexes with Polyoxometalates as Potential MRI Contrast Agents. *Magn Reson Imaging.* **2007**, *25* (3), 412–417.
205. Li, Z.; Li, W.; Li, X.; Pei, F.; Wang, X.; Lei, H. Mn(II)-Monosubstituted Polyoxometalates as Candidates for Contrast Agents in Magnetic Resonance Imaging. *J Inorg Biochem.* **2007**, *101* (7), 1036–1042.
206. Kong, D. liang; Wei, B.; Zhou, S. yan; Yang, H. shan; Jiang, Y. Volume-Related Efficiency of Gadolinium Polyoxometalates as MRI Contrast Agents. *Chem Res Chin Univ.* **2013**, *29* (6), 1055–1058.
207. Dan, K.; Fujinami, K.; Sumitomo, H.; Ogiwara, Y.; Suhara, S.; Konno, Y.; Sawada, M.; Soga, Y.; Takada, A.; Takanashi, K.; Watanabe, K.; Shinozuka, T. Application of Antiviral Polyoxometalates to Living Environments—Antiviral Moist Hand Towels and Stationery Items. *Applied Sciences.* **2020**, *10* (22).
208. Boulmier, A.; Feng, X.; Oms, O.; Mialane, P.; Rivière, E.; Shin, C. J.; Yao, J.; Kubo, T.; Furuta, T.; Oldfield, E.; Dolbecq, A. Anticancer Activity of Polyoxometalate-Bisphosphonate Complexes: Synthesis, Characterization, in Vitro and in Vivo Results. *Inorg Chem*. **2017**, *56* (13), 7558–7565.
209. Bijelic, A.; Aureliano, M.; Rompel, A. Polyoxometalates as Potential Next-Generation Metallodrugs in the Combat Against Cancer. *Angew. Chem., Int. Ed.* **2019**, *58* (10), 2980–2999.
210. Gumerova, N. I.; Rompel, A. Polyoxometalates in Solution: Speciation under Spotlight. *Chem Soc Rev.* **2020**, *49* (21), 7568–7601.
211. Gumerova, N. I.; Rompel, A. Interweaving Disciplines to Advance Chemistry: Applying Polyoxometalates in Biology. *Inorg Chem.* **2021**, *60* (9), 6109–6114.
212. Bijelic, A.; Aureliano, M.; Rompel, A. Polyoxometalates as Potential Next-Generation Metallodrugs in the Combat Against Cancer. *Angew.Chem.Int.Ed.* **2019**, *58* (10), 2980–2999.

213. Ogata, A.; Yanagie, H.; Ishikawa, E.; Morishita, Y.; Mitsui, S.; Yamashita, A.; Hasumi, K.; Takamoto, S.; Yamase, T.; Eriguchi, M. Antitumour Effect of Polyoxomolybdates: Induction of Apoptotic Cell Death and Autophagy in in Vitro and in Vivo Models. *Br J Cancer.* **2008**, *98* (2), 399–409.

214. Huang, Y.; Hu, H.; Li, R. Q.; Yu, B.; Xu, F. J. Versatile Types of MRI-Visible Cationic Nanoparticles Involving Pullulan Polysaccharides for Multifunctional Gene Carriers. *ACS Appl Mater Interfaces.* **2016**, *8* (6), 3919–3927.

215. Ly, J.; Li, Y.; Vu, M. N.; Moffat, B. A.; Jack, K. S.; Quinn, J. F.; Whittaker, M. R.; Davis, T. P. Nano-Assemblies of Cationic MPEG Brush Block Copolymers with Gadolinium Polyoxotungstate $[Gd(W_5O_{18})_2]^{9-}$ Form Stable, High Relaxivity MRI Contrast Agents. *Nanoscale.* **2018**, *10* (15), 7270–7280.

216. Chai, W.; Wang, S.; Zhao, H.; Liu, G.; Fischer, K.; Li, H.; Wu, L.; Schmidt, M. Hybrid Assemblies Based on a Gadolinium-Containing Polyoxometalate and a Cationic Polymer with Spermine Side Chains for Enhanced MRI Contrast Agents. *Chem. Eur. J.* **2013**, *19* (40), 13317–13321.

217. Hermann, P.; Kotek, J.; Kubíček, V.; Lukeš, I. Gadolinium(III) Complexes as MRI Contrast Agents: Ligand Design and Properties of the Complexes. *Dalton Trans.* **2008**, *9226* (23), 3027–3047.

218. Liu, L. L.; Wang, L.; Xiao, X. Y.; Yang, P.; Zhao, J.; Kortz, U. Structural Overview and Evolution Paths of Lacunary Polyoxometalates. *Coord. Chem. Rev.* 2024.

219. Britton, M. M. MRI of Chemical Reactions and Processes. *Progress in Nuclear Magnetic Resonance Spectroscopy*. **2017**,51–70.

220. Britton, M. M. Magnetic Resonance Imaging of Chemistry. *Chem Soc Rev.* **2010**, *39* (11), 4036–4043.

221. Hall, L.D.; Carpenter, T. A. Magnetic Imaging: A New Window into Industrial Processing. **1992**; Vol.10.

222. Feindel, K. W. Spatially Resolved Chemical Reaction Monitoring Using Magnetic Resonance Imaging. *Magnetic Resonance in Chemistry*. **2016**, 429–436.

223. Davenport, A. J.; Forsyth, M.; Britton, M. M. Visualisation of Chemical Processes during Corrosion of Zinc Using Magnetic Resonance Imaging. *Electrochem Commun.* **2010**, *12* (1), 44–47.

224. Harris, M.; Biju, S.; Parac-Vogt, T. N. High-Field MRI Contrast Agents and Their Synergy with Optical Imaging: The Evolution from Single Molecule Probes towards Nano-Architectures. *Chem. Eur. J.* **2019**, *25* (61), 13838–13847.

225. Moser, E.; Laistler, E.; Schmitt, F.; Kontaxis, G. Ultra-High Field NMR and MRI-the Role of Magnet Technology to Increase Sensitivity and Specificity. *Front Phys.***2017**, 1–15.

226. Giovannetti, G.; Guerrini, A.; Salvadori, P. A. Magnetic Resonance Spectroscopy and Imaging for the Study of Fossils. *Magn Reson Imaging.* **2016**, *34* (6), 730–742.

227. Britton, M. M. MRI of Chemical Reactions and Processes. *Prog Nucl Magn Reson Spectrosc.* **2017**, *101*, 51–70.

228. Banerjee, A.; Blasiak, B.; Dash, A.; Tomanek, B.; van Veggel, F. C. J. M.; Trudel, S. High-Field Magnetic Resonance Imaging: Challenges, Advantages, and Opportunities for Novel Contrast Agents. *CPR.* **2022**, *3* (1), 011304.
229. Bottrill, M.; Kwok, L.; Long, N. J. Lanthanides in Magnetic Resonance Imaging. *Chem Soc Rev.* **2006**, *35* (6), 557–571.
230. Ibrahim, M.; Mereacre, V.; Leblanc, N.; Wernsdorfer, W.; Anson, C. E.; Powell, A. K. Self-Assembly of a Giant Tetrahedral 3 d-4 f Single-Molecule Magnet within a Polyoxometalate System. *Angew. Chem. Int. Ed.* **2015**, *54* (51), 15574–15578.
231. Ibrahim, M.; Rudszuck, T.; Kerdi, B.; Krämer, S.; Guthausen, G.; Powell, A. K. Comparative NMR Relaxivity Study of Polyoxometalate-Based Clusters $[Mn_4(H_2O)_2(P_2W_{15}O_{56})_2]^{16-}$ and $[\{Dy(H_2O)_6\}_2Mn_4(H_2O)_2(P_2W_{15}O_{56})_2]^{10-}$ from 20 MHz to 1.2 GHz. *Appl Magn Reson.* **2020**, *51* (11), 1295–1305.
232. Haider, A.; Ibrahim, M.; Bassil, B. S.; Carey, A. M.; Viet, A. N.; Xing, X.; Ayass, W. W.; Miñambres, J. F.; Liu, R.; Zhang, G.; Keita, B.; Mereacre, V.; Powell, A. K.; Balinski, K.; N'Diaye, A. T.; Küpper, K.; Chen, H. Y.; Stimming, U.; Kortz, U. Mixed-Valent Mn16-Containing Heteropolyanions: Tuning of Oxidation State and Associated Physicochemical Properties. *Inorg Chem.* **2016**, *55* (6), 2755–2764.
233. Kruk, D.; Nilsson, T.; Kowalewski, J. Outer-Sphere Nuclear Spin Relaxation in Paramagnetic Systems: A Low-Field Theory. *Mol Phys.* **2001**, *99* (17), 1435–1445.
234. Ivano Bertini. *NMR of Paramagnetic Molecules Applications to Metallobiomolecules and Models*; **2015**.
235. Henoumont, C.; Devreux, M.; Laurent, S. Mn-Based MRI Contrast Agents: An Overview. *Molecules*. **2023**.
236. Pan, D.; Schmieder, A. H.; Wickline, S. A.; Lanza, G. M. Manganese-Based MRI Contrast Agents: Past, Present, and Future. *Tetrahedron*. **2011**, 8431–8444.
237. Caravan, P.; Farrar, C. T.; Frullano, L.; Uppal, R. Influence of Molecular Parameters and Increasing Magnetic Field Strength on Relaxivity of Gadolinium- and Manganese-Based T_1 Contrast Agents. *Contrast Media Mol Imaging.* **2009**, *4* (2),
238. Ivano Bertini, C. L. G. P. E. R. *Https://Doi.Org/10.1016/C2013-0-18690-4*, 2nd ed.; Copyright © **2015** Elsevier B.V. All rights reserved.
239. Bonnet, C. S.; Fries, P. H.; Crouzy, S.; Delangle, P. Outer-Sphere Investigation of MRI Relaxation Contrast Agents. Example of a Cyclodecapeptide Gadolinium Complex with Second-Sphere Water. *Journal of Physical Chemistry B*. **2010**, *114* (26), 8770–8781.
240. Helm, L. Relaxivity in Paramagnetic Systems: Theory and Mechanisms. *Progress in Nuclear Magnetic Resonance Spectroscopy*. **2006**, 45–64.
241. Ibrahim, M.; Mbomekallé, I. M.; De Oliveira, P.; Baksi, A.; Carter, A. B.; Peng, Y.; Bergfeldt, T.; Malik, S.; Anson, C. E. Syntheses, Crystal Structure, Electrocatalytic, and Magnetic Properties of the Monolanthanide-Containing Germanotungstates $[Ln(H_2O)\ NGeW_{11}O_{39}]^{5-}$ (Ln = Dy, Er, n = 4,3). *ACS Omega.* **2019**, *4* (26), 21873–21882.

242. Ibrahim, M.; Baksi, A.; Peng, Y.; Al-Zeidaneen, F. K.; Mbomekallé, I. M.; de Oliveira, P.; Anson, C. E. Synthesis, Characterization, Electrochemistry, Photoluminescence and Magnetic Properties of a Dinuclear Erbium(III)-Containing Monolacunary Dawson-Type Tungstophosphate: $[\{Er(H_2O)(CH_3COO)(P_2W_{17}O_{61})\}_2]^{16-}$. *Molecules* **2020**, *25* (18).

243. Venu, A. C.; Din, R. N.; Rudszuck, T.; Picchetti, P.; Chakraborty, P.; Powell, A. K.; Krämer, S.; Guthausen, G.; Ibrahim, M. Nmr Relaxivities of Paramagnetic Lanthanide-Containing Polyoxometalates. *Molecules* **2021**, *26* (24).

244. Hussain, F.; Sandriesser, S.; Speldrich, M.; Patzke, G. R. A New Series of Lanthanoid Containing Keggin-Type Germanotungstates with Acetate Chelators: $[\{Ln(CH_3COO)GeW_{11}O_{39}(H_2O)\}_2]^{12-}$ {Ln=Eu^{III}, Gd ^{III}, Tb^{III}, Dy^{III}, Ho^{III}, Er ^{III}, Tm^{III}, and Yb^{III}}. *J Solid State Chem.* **2011**, *184* (1), 214–219.

245. Funk, A. M.; Harvey, P.; Finney, K. L. N. A.; Fox, M. A.; Kenwright, A. M.; Rogers, N. J.; Senanayake, P. K.; Parker, D. Challenging Lanthanide Relaxation Theory: Erbium and Thulium Complexes That Show NMR Relaxation Rates Faster than Dysprosium and Terbium Analogues. P*hys. Chem. Chem. Phys.***2015**, *17* (25), 16507–16511.

246. Nasser Din, R.; Venu, A. C.; Rudszuck, T.; Vallet, A.; Favier, A.; Powell, A. K.; Guthausen, G.; Ibrahim, M.; Krämer, S. Longitudinal and Transverse 1H Nuclear Magnetic Resonance Relaxivities of Lanthanide Ions in Aqueous Solution up to 1.4 GHz/33 T. *Molecules.* **2024**, *29* (20), 4956.

247. Machado, J. R.; Baniodeh, A.; Powell, A. K.; Luy, B.; Krämer, S.; Guthausen, G. Nuclear Magnetic Resonance Relaxivities: Investigations of Ultrahigh-Spin Lanthanide Clusters from 10 MHz to 1.4 GHz. *ChemPhysChem.* **2014**, *15* (16), 3608–3613.

248. Ibrahim, M.; Krämer, S.; Schork, N.; Guthausen, G. Polyoxometalate-Based High-Spin Cluster Systems: A NMR Relaxivity Study up to 1.4 GHz/33 T. *Dalton Trans.* **2019**, *48* (41), 15597–15604.

249. Nasser Din, R.; Venu, A. C.; Rudszuck, T.; Vallet, A.; Favier, A.; Powell, A. K.; Guthausen, G.; Ibrahim, M.; Krämer, S. Longitudinal and Transverse 1H Nuclear Magnetic Resonance Relaxivities of Lanthanide Ions in Aqueous Solution up to 1.4 GHz/33 T. *Molecules* **2024**, *29* (20).

250. Gupta, R.; Saini, M. K.; Hussain, F. Syntheses, Crystal Structures and Solid-State Properties of the Lanthanoid-Containing Nanoclusters $[(Ln_2PW_{10}O_{38})_4(W_3O_8)(OH)_4(H_2O)_2]^{26-}$. *Eur J Inorg Chem.* **2014**, *2014* (35), 6031–6038.

251. Pope, M. *Heteropoly and Isopoly Oxometalates*; **1983**.

252. Gumerova, N. I.; Rompel, A. Polyoxometalates in Solution: Speciation under Spotlight. *Chem. Soc. Rev.* **2020,** 7568–7601.

253. Maksimovskaya, R. I.; Maksimov, G. M. ^{31}P NMR Studies of Hydrolytic Conversions of 12-Tungstophosphoric Heteropolyacid. *Coord. Chem. Rev.* **2019**, 81–99.

254. Sadakane, M.; Steckhan, E. Electrochemical Properties of Polyoxometalates as Electrocatalysts, **1998**.

255. A. MuÈ ller, S. Q. N. S. H. B. gge & M. S. Molecular Growth Froma to A Mo_{248} Cluster. *Nature* **1999**.

256. Şuteu, R.; Raţ, C. I.; Silvestru, C.; Simion, A.; Candu, N.; Pârvulescu, V. I.; Silvestru, A. Hypercoordinated Diorganoantimony(III) Compounds of Types $[2\text{-}(Me_2NCH_2)C_6H_4]_2SbL$ and $[PhCH_2N(CH_2C_6H_4)_2]SbL$ (L = Cl, ONO_2, OSO_2CF_3). Synthesis, Structure and Catalytic Behaviour in the Henry Reaction. *Appl Organomet Chem.* **2020**, *34* (4).

257. Proust, A.; Matt, B.; Villanneau, R.; Guillemot, G.; Gouzerh, P.; Izzet, G. Functionalization and Post-Functionalization: A Step towards Polyoxometalate-Based Materials. *Chem Soc Rev.* **2012**, *41* (22), 7605–7622.

258. Wang, S.; Xie, W.; Wu, P.; Lin, G.; Cui, Y.; Tao, J.; Zeng, G.; Deng, Y.; Qiu, H. Soft Nanobrush-Directed Multifunctional MOF Nanoarrays. *Nat Commun.* **2022**, *13* (1).

259. Du, D. Y.; Qin, J. S.; Li, S. L.; Su, Z. M.; Lan, Y. Q. Recent Advances in Porous Polyoxometalate-Based Metal-Organic Framework Materials. *Chem Soc Rev.*July 7, **2014**, 4615–4632.

260. Liebhafsky, H. A.; Cairns, E. J.; Grubb, W. T.; Mckee, D. W.; Niedrach, L. W. *Specific Acetylcholine Acyl-Hydrolases of Sheep Brain*, **1940**, Vol. 31.

261. Banoth, P.; Kandula, C.; Kollu, P. Introduction to Electrocatalysts. In *ACS Symposium Series*; ACS, **2022**; Vol. 1432, pp 1–37

262. Pletcher, D. *Electrocatalysis: Present and Future*; **1984**,Vol. 14.

263. Bandarenka, A. S.; Ventosa, E.; Maljusch, A.; Masa, J.; Schuhmann, W. Techniques and Methodologies in Modern Electrocatalysis: Evaluation of Activity, Selectivity and Stability of Catalytic Materials. *Analyst* **2014**, *139* (6), 1274–1291.

264. Banoth, P.; Kandula, C.; Kollu, P. Introduction to Electrocatalysts. In *ACS Symposium Series*, ACS. **2022**; Vol. 1432,1–37.

265. Maheshwari, S.; Li, Y.; Agrawal, N.; Janik, M. J. Density Functional Theory Models for Electrocatalytic Reactions; *Adv. Catal*. **2018**, Vol. 63, 117–167.

266. Zhang, M. K.; Chen, W.; Xu, M. Le; Wei, Z.; Zhou, D.; Cai, J.; Chen, Y. X. How Buffers Resist Electrochemical Reaction-Induced PH Shift under a Rotating Disk Electrode Configuration. *Anal Chem.* **2021**, *93* (4), 1976–1983.

267. Blasco-Ahicart, M.; Soriano-Lopez, J.; Carbo, J. J.; Poblet, J. M.; Galan-Mascaros, J. R. Polyoxometalate Electrocatalysts Based on Earthabundant Metals for Efficient Water Oxidation in Acidic Media. *Nat Chem.* **2018**, *10* (1), 24–30.

268. Gouzerh, P.; Proust, A. *Main-Group Element, Organic, and Organometallic Derivatives of Polyoxometalates*; **1998**.

269. Li, S.; Zhao, Z.; Ma, T.; Pachfule, P.; Thomas, A. Superstructures of Organic–Polyoxometalate Co-Crystals as Precursors for Hydrogen Evolution Electrocatalysts. *Angew. Chem. Int. Ed.***2022**, *61* (3).

270. Keita, B.; Nadjo, L. Polyoxometalate-Based Homogeneous Catalysis of Electrode Reactions: Recent Achievements. *J Mol Catal A Chem.* **2007**, *262* (1–2), 190–215.

271. Yang, L.; Lei, J.; Fan, J. M.; Yuan, R. M.; Zheng, M. Sen; Chen, J. J.; Dong, Q. F. The Intrinsic Charge Carrier Behaviors and Applications of Polyoxometalate Clusters Based Materials. *Adv. Mater.* **2021**.

272. Freire, C.; Fernandes, D. M.; Nunes, M.; Abdelkader, V. K. POM & MOF-Based Electrocatalysts for Energy-Related Reactions. *ChemCatChem*. 24, **2018**,1703–1730.

273. Zhang, L. N.; Li, R.; Zang, H. Y.; Tan, H. Q.; Kang, Z. H.; Wang, Y. H.; Li, Y. G. Advanced Hydrogen Evolution Electrocatalysts Promising Sustainable Hydrogen and Chlor-Alkali Co-Production. *Energy Environ. Sci.* **2021**, 6191–6210.

274. Zhang, B.; Wu, Z.; Shao, W.; Gao, Y.; Wang, W.; Ma, T.; Ma, L.; Li, S.; Cheng, C.; Zhao, C. Interfacial Atom-Substitution Engineered Transition-Metal Hydroxide Nanofibers with High-Valence Fe for Efficient Electrochemical Water Oxidation. *Angew. Chem. Int. Ed.* **2022**, *61* (13).

275. Xu, W.; Zhou, B.; Wang, Q.; Xu, G.; Li, N.; Liu, W.; Zhang, Z. C. Energy-Efficient Electrochemical Hydrogen Production Combined with Biomass Oxidation Using Polyoxometalate and Metal Salts. *ChemCatChem.* **2023**, *15* (15).

276. Vetter, K. M.; Aring da Silva Ramos Mauro, C.; Reinisch, D.; Reichbauer, T.; Martić, N.; Jandl, C.; Hinrichsen, O.; Schmid, G. Stability Evaluation of Earth-Abundant Metal-Based Polyoxometalate Electrocatalysts for Oxygen Evolution Reaction towards Industrial PEM Electrolysis at High Current Densities. *Electrochem. Sci. Adv.* **2022**, *2* (3).

277. Ahsan, H.; Saeed, M.; Ahmad, W.; Rehman, A.; Haseeb Bashir, A.; Aiman, V.; Irshad, T.; Irtza, T.; Zahid, U. Polyoxometalates for Carbon Dioxide Activation: Current Progress and Perspective. *J. Chin. Chem. Soc.* **2024**, 526–549.

278. Kawakami, K.; Yabe, T.; Amano, F.; Yamaguchi, K.; Suzuki, K. Pd-Incorporated Polyoxometalate Catalysts for Electrochemical CO_2 Reduction. *Chem Sci.* **2024**.

279. Aresta, M.; Dibenedetto, A.; Angelini, A. Catalysis for the Valorisation of Exhaust Carbon: From CO_2 to Chemicals, Materials, and Fuels. Technological Use of CO2. *Chemical Reviews*.**2014**,1709–1742.

280. Vasileff, A.; Zheng, Y.; Qiao, S. Z. Carbon Solving Carbon's Problems: Recent Progress of Nanostructured Carbon-Based Catalysts for the Electrochemical Reduction of CO2. *Adv. Energy Mater.* **2017**.

281. Khalil, I. E.; Xue, C.; Liu, W.; Li, X.; Shen, Y.; Li, S.; Zhang, W.; Huo, F. The Role of Defects in Metal–Organic Frameworks for Nitrogen Reduction Reaction: When Defects Switch to Features. *Adv. Funct. Mater*. **2021**.

282. Ma, T.; Yan, R.; Wu, X.; Wang, M.; Yin, B.; Li, S.; Cheng, C.; Thomas, A. Polyoxometalate-Structured Materials: Molecular Fundamentals and Electrocatalytic Roles in Energy Conversion. *Adv. Mater.* **2024**.

283. Qiushi Yin, 1 Jeffrey Miles Tan,1 Claire Besson,1,2 Yurii V. Geletii,1 Djamaladdin G. Musaev,1 Aleksey E. Kuznetsov,1 Zhen Luo,1 Ken I. Hardcastle,1 Craig L. Hill1*. A Fast Soluble Carbon-Free Molecular Oxidation Catalyst Based on Abundant Metals. *Science (1979)* **2010**, *185* (5–6), 1068–1076.

284. Zhu, G.; Glass, E. N.; Zhao, C.; Lv, H.; Vickers, J. W.; Geletii, Y. V.; Musaev, D. G.; Song, J.; Hill, C. L. A Nickel Containing Polyoxometalate Water Oxidation Catalyst. *Dalton Trans.***2012**, *41* (42), 13043–13049.
285. Blasco-Ahicart, M.; Soriano-Lopez, J.; Carbo, J. J.; Poblet, J. M.; Galan-Mascaros, J. R. Polyoxometalate Electrocatalysts Based on Earthabundant Metals for Efficient Water Oxidation in Acidic Media. *Nat Chem* **2018**, *10* (1), 24–30.
286. Han, Q.; Ding, Y. Recent Advances in the Field of Light-Driven Water Oxidation Catalyzed by Transition-Metal Substituted Polyoxometalates. *Dalton Trans.* **2018**, *47* (25), 8180–8188.
287. Geletii, Y. V.; Yin, Q.; Hou, Y.; Huang, Z.; Ma, H.; Song, J.; Besson, C.; Luo, Z.; Cao, R.; O'Halloran, K. P.; Zhu, G.; Zhao, C.; Vickers, J. W.; Ding, Y.; Mohebbi, S.; Kuznetsov, A. E.; Musaev, D. G.; Lian, T.; Hill, C. L. Polyoxometalates in the Design of Effective and Tunable Water Oxidation Catalysts. *Isr. J. Chem.* **2011**, 238–246.
288. Han, X. B.; Li, Y. G.; Zhang, Z. M.; Tan, H. Q.; Lu, Y.; Wang, E. B. Polyoxometalate-Based Nickel Clusters as Visible Light-Driven Water Oxidation Catalysts. *J. Am. Chem Soc.* **2015**, *137* (16), 5486–5493.
289. Geletii, Y. V.; Botar, B.; Kögerler, P.; Hillesheim, D. A.; Musaev, D. G.; Hill, C. L. An All-Inorganic, Stable, and Highly Active Tetraruthenium Homogeneous Catalyst for Water Oxidation. *Angew. Chem. Int. Ed.* **2008**, *47* (21), 3896–3899.
290. Teillout, A. L.; de Oliveira, P.; Marrot, J.; Howell, R. C.; Vilà, N.; Walcarius, A.; Mbomekallé, I. M. Synthesis, Crystal Structure, Electrochemistry and Electro-Catalytic Properties of the Manganese-Containing Polyoxotungstate, $[(Mn(H_2O)_3)_2(H_2W_{12}O_{42})]^{6-}$. *Inorganics (Basel).* **2019**, *7* (2).
291. Yu, L.; Ding, Y.; Zheng, M. Polyoxometalate-Based Manganese Clusters as Catalysts for Efficient Photocatalytic and Electrochemical Water Oxidation. *Appl. Catal. B.* **2017**, *209*, 45–52.
292. Al-Oweini, R.; Sartorel, A.; Bassil, B. S.; Natali, M.; Berardi, S.; Scandola, F.; Kortz, U.; Bonchio, M. Photocatalytic Water Oxidation by a Mixed-Valent MnIII3MnIVO3 Manganese Oxo Core That Mimics the Natural Oxygen-Evolving Center. *Angew. Chem. Int. Ed.* **2014**, *53* (42), 11182–11185.
293. Wu, Y.; Pei, J.; Yu, X.; Bi, L. Study on Catalytic Water Oxidation Properties of Polynuclear Manganese Containing Polyoxometalates. *Catalysts.* **2022**, *12* (2).
294. Du, X.; Ding, Y.; Song, F.; Ma, B.; Zhao, J.; Song, J. Efficient Photocatalytic Water Oxidation Catalyzed by Polyoxometalate [Fe11(H2O)14(OH)2(W3O10)2(α-SbW9O33)6]27- Based on Abundant Metals. *Chem. Commun.* **2015**, *51* (73), 13925–13928.
295. Cui, T.; Qin, L.; Fu, F.; Xin, X.; Li, H.; Fang, X.; Lv, H. Pentadecanuclear Fe-Containing Polyoxometalate Catalyst for Visible-Light-Driven Generation of Hydrogen. *Inorg Chem.* **2021**, *60* (6), 4124–4132.
296. Chen, W. C.; Wang, X. L.; Qin, C.; Shao, K. Z.; Su, Z. M.; Wang, E. B. A Carbon-Free Polyoxometalate Molecular Catalyst with a Cobalt-Arsenic Core for Visible Light-Driven Water Oxidation. *Chem. Commun.* **2016**, *52* (61), 9514–9517.

297. Soriano-López, J.; Goberna-Ferrón, S.; Vigara, L.; Carbó, J. J.; Poblet, J. M.; Galán-Mascarós, J. R. Cobalt Polyoxometalates as Heterogeneous Water Oxidation Catalysts. *Inorg Chem.* **2013**, *52* (9), 4753–4755.

298. Han, X. B.; Zhang, Z. M.; Zhang, T.; Li, Y. G.; Lin, W.; You, W.; Su, Z. M.; Wang, E. B. Polyoxometalate-Based Cobalt-Phosphate Molecular Catalysts for Visible Light-Driven Water Oxidation. *J. Am. Chem. Soc.* **2014**, *136* (14), 5359–5366.

299. Yu, L.; Ding, Y.; Zheng, M.; Chen, H.; Zhao, J. $[\{\beta\text{-}SiNi_2W_{10}O_{36}(OH)_2(H_2O)\}_4]^{24-}$: A New Robust Visible Light-Driven Water Oxidation Catalyst Based on Nickel-Containing Polyoxometalate. *Chem. Commun.* **2016**, *52* (100), 14494–14497.

300. Zhu, G.; Glass, E. N.; Zhao, C.; Lv, H.; Vickers, J. W.; Geletii, Y. V.; Musaev, D. G.; Song, J.; Hill, C. L. A Nickel Containing Polyoxometalate Water Oxidation CatalystDalton Trans. **2012**, *41* (42), 13043–13049.

301. Han, X. B.; Li, Y. G.; Zhang, Z. M.; Tan, H. Q.; Lu, Y.; Wang, E. B. Polyoxometalate-Based Nickel Clusters as Visible Light-Driven Water Oxidation Catalysts. *J.Am. Chem. Soc.* **2015**, *137* (16), 5486–5493.

302. Yu, L.; Du, X.; Ding, Y.; Chen, H.; Zhou, P. Efficient Visible Light-Driven Water Oxidation Catalyzed by an All-Inorganic Copper-Containing Polyoxometalate. *Chem. Commun.* **2015**, *51* (98), 17443–17446.

303. Quirós-Huerta, J.; Troya, J.; Clemente-León, M.; Clemente-Juan, J. M.; Coronado, E.; Soriano-López, J. A Novel Banana-Shaped Mixed-Metal Co/Fe Polyoxometalate Cluster. *Chempluschem.* **2024**.

304. Ruhlmann, L.; Costa-Coquelard, C.; Canny, J.; Thouvenot, R. Electrochemical and Electrocatalytical Investigations on the Trimanganese Sandwich Complex $[NaMn_3(H_2O)_2(P_2W_{15}O_{56})_2]^{17-}$. *Journal of Electroanalytical Chemistry* **2007**, *603* (2), 260–268.

305. Toth, J. E.; Anson, F. C.; J Electroanal Chem, F. C.; Heteropoly, T.; Oxometallates, I. Elec-Troanal. Chem. 1986, 208, 343. (i) Keita, B.; Nadjo, L. *J. Chem. Soc., Faraday Trans. 1* **1966**, *88* (4), 5876.

306. Ammam, M.; Mbomekalle, I. M.; Keita, B.; Nadjo, L.; Anderson, T. M.; Zhang, X.; Hardcastle, K. I.; Hill, C. L.; Fransaer, J. Electrochemical Behavior and Electrocatalytic Properties towards Hydrogen Peroxide, Dioxygen and Nitrate of the Polyanions $[(Ni^{II}OH_2)_2(Fe^{III})_2(X_2W_{15}O_{56})_2]^{14-}$ ($X = P^V$ or As^V): A Comparative Study. *J. Electroanal. Chem.* **2010**, *647* (2), 97–102.

307. Keita, B.; Martyr Mbomekalle, I.; Nadjo, L.; Contant, R. $[H_4AsW_{18}O_{62}]^{7-}$, A Novel Dawson Heteropolyanion and Two of Its Sandwich-Type Derivatives$[Zn_4(H_2O)_2(H_4AsW_{15}O_{56})_2]^{18-}$, $[Cu_4(H_2O)_2(H_4AsW_{15}O_{56})_2]^{18-}$: Cyclic Voltammetry and Electrocatalytic Properties towards Nitrite and Nitrate. *Electrochem. Commun.***2001**, Vol.3, 267-273

308. Jiang, Y.; Chen, C.; Li, K.; Cui, L.-P.; Chen, J. Polyoxometalates for the Catalytic Reduction of Nitrogen Oxide and Derivatives: From Novel Structures to Functional Applications. *ChemComm.* **2025**.

309. Jabbour, D.; Keita, B.; Nadjo, L.; Kortz, U.; Mal, S. S. The Wheel-Shaped Cu20-Tungstophosphate [Cu20Cl(OH) 24(H2O)12(P8W48O 184)]25-, Redox and Electrocatalytic Properties. *Electrochem. Commun.* **2005**, *7* (8), 841–847.
310. Mbomekalle, I. M.; Cao, R.; Hardcastle, K. I.; Hill, C. L.; Ammam, M.; Keita, B.; Nadjo, L.; Anderson, T. M. Synthesis, Structural Characterization, and Electrocatalytic Studies of Aββα-$(Zn^{II}OH_2)_2$ $(Fe^{III})_2(X_2W_{15}O_{56})^{214-}$ (X = P or As). *CR CHIM.***2005**, *8* ,1077–1086.
311. Ibrahim, M.; Mbomekallé, I. M.; De Oliveira, P.; Baksi, A.; Carter, A. B.; Peng, Y.; Bergfeldt, T.; Malik, S.; Anson, C. E. Syntheses, Crystal Structure, Electrocatalytic, and Magnetic Properties of the Monolanthanide-Containing Germanotungstates $[Ln(H_2O)\ NGeW_{11}O_{39}]^{5-}$ (Ln = Dy, Er, n = 4,3). *ACS Omega* **2019**, *4* (26), 21873–21882.
312. Zhou, Y.; Sun, J.; Gallet, S.; Raya, J.; Boudon, C.; Bonnefont, A.; Ruhlmann, L.; Badets, V. Nitrite Electroreduction Enhanced by Hybrid Compounds of Keggin Polyoxometalates and 1-Butyl-3-Vinylimidazolium. *ChemCatChem* **2024**.
313. Zhang, S.; Wu, J.; Zheng, M.; Jin, X.; Shen, Z.; Li, Z.; Wang, Y.; Wang, Q.; Wang, X.; Wei, H.; Zhang, J.; Wang, P.; Zhang, S.; Yu, L.; Dong, L.; Zhu, Q.; Zhang, H.; Lu, J. Fe/Cu Diatomic Catalysts for Electrochemical Nitrate Reduction to Ammonia. *Nat Commun* **2023**, 14 (1).
314. Jiang, Y.; Chen, C.; Li, K.; Cui, L.-P.; Chen, J. Polyoxometalates for the Catalytic Reduction of Nitrogen Oxide and Derivatives: From Novel Structures to Functional Applications. *Chem Commun* **2025**.
315. S. Hörold, K.-D. V. T. T. a, M. S. b. Development of Catalysts for a Selective Nitrate and Nitrite Removal from Drinking Water. *Catalysis Today* **1993**, 17, 21–30.
316. Moore, J. M.; Miller, T. J.; Mu, M.; Peñas-Defrutos, M. N.; Gullett, K. L.; Elford, L. S.; Quintero, S.; García-Melchor, M.; Fout, A. R. Selective Stepwise Reduction of Nitrate and Nitrite to Dinitrogen or Ammonia. *J Am Chem Soc.* **2025**.
317. Liang, X.; Zhu, H.; Yang, X.; Xue, S.; Liang, Z.; Ren, X.; Liu, A.; Wu, G. Recent Advances in Designing Efficient Electrocatalysts for Electrochemical Nitrate Reduction to Ammonia. *Small Structures*. **2023**.
318. Rousseau, G.; Zhang, S.; Oms, O.; Dolbecq, A.; Marrot, J.; Liu, R.; Shang, X.; Zhang, G.; Keita, B.; Mialane, P. Sequential Synthesis of 3d-3d, 3d-4d, and 3d-5d Hybrid Polyoxometalates and Application to the Electrocatalytic Oxygen Reduction Reactions. *Chem. Eur. J.* **2015**, *21* (34), 12153–12160.
319. Novais, H. C.; Jarrais, B.; Mbomekallé, I. M.; Teillout, A. L.; de Oliveira, P.; Freire, C.; Fernandes, D. M. Enhanced Oxygen Reduction Reaction Activity of the Wells-Dawson Polyoxometalate P2W12Mo6 Immobilised in Nitrogen and Sulphur-Doped Carbon Nanomaterials. *ChemElectroChem.* **2024**, *11* (4).
320. Keita, B.; Nadjo, L. *Prdiminarynote Catalytic Synthesis of Hydrogen Peroxide: An Attractive electrochemical and Photoelectrochemical route to the reduction of oxygen.* Elsevier Sequoia S.A, **1983**; Vol. 145.

321. Keita, B.; Bena, M.; ıssa, ı; Nadjo, L.; Contant, R. *Dioxygen and Hydrogen Peroxide Electrocatalytic Reduction: Evidence for a Cooperativity of Mo and Cu Centres in Substituted Heteropolyanions*. www.elsevier.com/locate/elecom.
322. Farsani, M. R.; Yadollahi, B.; Rudbari, H. A.; Amini, A.; Caradoc-Davis, T.; Price, J. R. First Stable Nitrate-Encapsulated Sandwich Type Polyoxometalate: Synthesis, Structural Characterization, and Catalytic Performance. *Inorg Chem Commun.* **2014**, *43*, 39–44.
323. Hooe, S. L.; Rheingold, A. L.; MacHan, C. W. Electrocatalytic Reduction of Dioxygen to Hydrogen Peroxide by a Molecular Manganese Complex with a Bipyridine-Containing Schiff Base Ligand. *J Am Chem Soc.* **2018**, *140* (9), 3232–3241.
324. Novais, H. C.; Jarrais, B.; Mbomekallé, I. M.; Teillout, A. L.; de Oliveira, P.; Freire, C.; Fernandes, D. M. Enhanced Oxygen Reduction Reaction Activity of the Wells-Dawson Polyoxometalate P2W12Mo6 Immobilised in Nitrogen and Sulphur-Doped Carbon Nanomaterials. *ChemElectroChem.* **2024**, *11* (4).
325. Zhang, S.; Oms, O.; Hao, L.; Liu, R.; Wang, M.; Zhang, Y.; He, H. Y.; Dolbecq, A.; Marrot, J.; Keita, B.; Zhi, L.; Mialane, P.; Li, B.; Zhang, G. High Oxygen Reduction Reaction Performances of Cathode Materials Combining Polyoxometalates, Coordination Complexes, and Carboneous Supports. *ACS Appl Mater Interfaces.* **2017**, *9* (44), 38486–38498.
326. Mbomekallé, I. M.; López, X.; Poblet, J. M.; Sécheresse, F.; Keita, B.; Nadjo, L. Influence of the Heteroatom Size on the Redox Potentials of Selected Polyoxoanions. *Inorg Chem.* **2010**, *49* (15), 7001–7006.
327. Ayingone Mezui, C. S.; De Oliveira, P.; Teillout, A. L.; Marrot, J.; Berthet, P.; Lebrini, M.; Mbomekallé, I. M. Synthesis, Structure, and Magnetic Electrochemical Properties of a Family of Tungstoarsenates Containing Just CoII Centers or Both CoII and FeIII Centers. *Inorg Chem.* **2017**, *56* (4), 1999–2012.
328. Snir, O.; Wang, Y.; Weinstock, I. A. The Reduction of Dioxygen by Keggin Heteropolytungstates. *Isr. J. Chem.* **2011,** 247–258.
329. Khan, I.; Das, V.; Teillout, A. L.; Mbomekallé, I. M.; de Oliveira, P.; Sahoo, S. C.; Hussain, F. Tetrameric Lanthanide-Substituted Silicotungstate {$Ln_8Si_4W_{40}$} Nanoclusters: Synthesis, Structural Characterization, Electrochemistry, and Catalytic Application for Oxidation of Thioethers. *Eur J Inorg Chem.* **2021**, *2021* (11), 1071–1081.
330. Ibrahim, M.; Mbomekallé, I. M.; De Oliveira, P.; Baksi, A.; Carter, A. B.; Peng, Y.; Bergfeldt, T.; Malik, S.; Anson, C. E. Syntheses, Crystal Structure, Electrocatalytic, and Magnetic Properties of the Monolanthanide-Containing Germanotungstates $[Ln(H_2O)\ NGeW_{11}O_{39}]^{5-}$ (Ln = Dy, Er, n = 4,3). *ACS Omega.* **2019**, *4* (26), 21873–21882.
331. Khan, I.; Kaushik, R.; Tiwari, R. K.; Mbomekallé, I.; Oliveira, P. de; Matono, T.; Ooyama, H. E.; Sadakane, M.; Hussain, F. Self-Assembled Tetrameric Lanthanide-Containing Germanotungstates $[(Ln_2GeW_{10}O_{38})_4(W_3O_8)(OH)_4(H_2O)_2]^{26-}$: Syntheses, Crystal Structure, Photoluminescence and Electrochemical Properties. *ChemistrySelect* **2019**, *4* (43), 12668–12675.

332. Lisnard, L.; Mialane, P.; Dolbecq, A.; Marrot, J.; Clemente-Juan, J. M.; Coronado, E.; Keita, B.; De Oliveira, P.; Nadjo, L.; Sécheresse, F. Effect of Cyanato, Azido, Carboxylato, and Carbonato Ligands on the Formation of Cobalt(II) Polyoxometalates: Characterization, Magnetic, and Electrochemical Studies of Multinuclear Cobalt Clusters. *Chem. Eur. J.* **2007**, *13* (12), 3525–3536.

333. Bineta KeitaLouis Nadjo. *Electrochemistry of Isopoly and Heteropoly Oxometalates*; **2007**.

334. Weinstock, I. A. Homogeneous-Phase Electron-Transfer Reactions of Polyoxometalates*.*

335. Bard, A. J. .; Faulkner, L. R. . *Electrochemical Methods : Fundamentals and Applications*; John Wiley & Sons, Inc.,**2001**.

336. Vilà, N.; Aparicio, P. A.; Sécheresse, F.; Poblet, J. M.; López, X.; Mbomekallé, I. M. Electrochemical Behavior of α 1/α 2- $[Fe(H_2O)P_2W_{17}O_{61}]^{7-}$ Isomers in Solution: Experimental and DFT Studies. *Inorg Chem.* **2012**, *51* (11),6129–6138.

337. Teillout, A. L.; de Oliveira, P.; Marrot, J.; Howell, R. C.; Vilà, N.; Walcarius, A.; Mbomekallé, I. M. Synthesis, Crystal Structure, Electrochemistry and Electro-Catalytic Properties of the Manganese-Containing Polyoxotungstate, $[(Mn(H_2O)_3)_2(H_2W_{12}O_{42})]^{6-}$. *Inorganics (Basel)* **2019**,*7* (2).

Additional Information

Chapter 3: Crystallographic data

Short Name	Co_{12}-GeW_{10}	Ni_{12}-GeW_{10}
Formula	$Co_{13}H_{240}Cs_{10}Ge_6Na_{36}O_{348}W_{60}$	$Cs_{11}H_{320}Ge_6Na_{37}Ni_{12}O_{388}W_{60}$
Formula Weight / g mol^{-1}	20199.28	21014.24
Crystal System	triclinic	tetragonal
Space Group	P -1	I 41/a
***a* / Å**	23.4195(5)	23.3165(3)
***b* / Å**	23.6461(4)	23.3165(3)
***c* / Å**	31.7940(6)	69.4954(14)
α / °	83.848(2)	90
β / °	86.980(2)	90
ϒ / °	83.673(2)	90
***V* / Å^3**	17384.0(6)	37781.8(12)
Z	2	4
T / K	180	180
***F*(000)**	17906	37616
***D_c* / Mg m^{-3}**	3.859	3.694
μ / mm^{-1}	35.230	20.444
Crystal description	Needle	Needle
Crystal colour	violet	light green
Wavelength	1.34143	0.71073
Data Measured	261080	246020
Unique Data	69955	319453
R_{int}	0.0675	0.0640
Unique Data with I ≥ 2σ(I)	36016	73713
Parameters/Restraints	2487/0	1006/0
***wR_2*, (all data)**	0.1802	0.1504
***S* (all data)**	0.935	1.081
***R_1* [I≥2σ(I)]**	0.0586	0.0458
Biggest diff. peak/hole	4.333 -4.935	3.322 -2.393

Short Name	**Fe_4-GeW_{10}**	**Fe_{12}-PW_{10}**
Formula	$Fe_4H_{70}Ge_2K_{14}O_{112}W_{20}$	$Fe_{12}H_{108}K_{12}O_{218}P_8W_{40}$
Formula Weight / g mol^{-1}	6455.54	12338.02
Crystal System	monoclinic	cubic
Space Group	P 1 21/c 1	I -4 3 m
***a* / Å**	20.5042(11)	20.9899(2)
***b* / Å**	15.4416(5)	20.9899(2)
***c* / Å**	17.9724(9)	20.9899(2)
α / °	90	90
β / °	114.825(4)	90
Ɣ / °	90	90
***V* / Å^3**	5164.6(4)	9247.6(3)
Z	2	2
T / K	150	180
***F*(000)**	5760	10944
***D_c* / Mg m^{-3}**	4.151	4.431
μ / mm^{-1}	35.028	38.556
Crystal description	Plate	Block
Crystal colour	yellow	yellow
Wavelength	1.34143	1.34143
Data Measured	47134	66388
Unique Data	11535	2085
R_{int}	0.0733	0.0415
Unique Data with I ≥ 2σ(I)	7959	2072
Parameters/Restraints	404/0	125/32
***wR_2*, (all data)**	0.1557	0.1501
***S* (all data)**	1.004	1.175
***R_1* [I≥2σ(I)]**	0.0563	0.0516
Biggest diff. peak/hole	5.415/-3.520	2.888/-1.750

Short Name	$Co_7Tb_{(0.2)}Na_{(0.8)}$-GeW_9	$Co_7Y_{(0.3)}Na_{(0.7)}$-GeW_9
Formula	$Co_{6.50}H_{150}Cs_{1.50}Ge_2Na_{22.90}O_{179}P_6Tb_{0.20}W_{22}$	$Co_{6.25}H_{150}Cs_{1.50}Ge_2Na_{23.10}O_{179}P_6W_{22}Y_{0.30}$
Formula Weight / g mol^{-1}	8531.56	8516.31
Crystal System	monoclinic	monoclinic
Space Group	C 1 2/c 1	C 1 2/c 1
***a* / Å**	33.5226(4)	33.6383(5)
***b* / Å**	21.7805(2)	21.9467(3)
***c* / Å**	22.4670(3)	22.5134(3)
α / °	90	90
β / °	118.0650(10)	118.177(1)
Ɣ / °	90	90
***V* / Å^3**	14475.1(3)	14650.9(4)
Z	4	4
T / K	180	180.15
***F*(000)**	15548	15524
***D$_c$* / Mg m^{-3}**	3.915	3.861
μ / mm^{-1}	30.060	29.658
Crystal description	Block	----
Crystal colour	pink	----
Wavelength	1.34143	1.34143
Data Measured	95022	108773
Unique Data	17463	18205
R$_{int}$	0.0238	0.0551
Unique Data with I ≥ 2σ(I)	15748	17402
Parameters/Restraints	912/0	883/0
***wR$_2$*, (all data)**	0.1373	0.1402
***S* (all data)**	1.030	1.137
***R$_1$* [I≥2σ(I)]**	0.0496	0.0529
Biggest diff. peak/hole	4.709/-5.072	3.086/-2.237

Short Name	**$Co_7Dy_{(0.3)}Na_{(0.7)}$-GeW_9**	**$Co_7Eu_{(0.1)}Na_{(0.9)}$-GeW_9**
Formula	$Co_{6.60}H_{150}Cs_{1.30}Dy_{0.30}Ge_2Na_{22.60}O_{179}P_6W_{22}$	$Co_{6.40}H_{150}Cs_{1.70}Eu_{0.10}Ge_2Na_{23.10}O_{179}P_6W_{22}$
Formula Weight / g mol^{-1}	8520.94	8540.26
Crystal System	monoclinic	monoclinic
Space Group	C 1 2/c 1	C 1 2/c 1
***a* / Å**	33.5513(5)	33.4073(8)
***b* / Å**	21.7248(4)	21.7811(4)
***c* / Å**	22.4999(4)	22.4224(5)
α / °	90	90
β / °	118.2240(10)	118.165(2)
ϒ / °	90	90
***V* / Å^3**	14450.2(4)	14383.7(6)
Z	4	4
T / K	300	180.15
***F*(000)**	15528	15563
***D_c* / Mg m^{-3}**	3.917	3.944
μ / mm^{-1}	30.192	30.690
Crystal description	block	----
Crystal colour	pink	----
Wavelength	1.34143	1.34143
Data Measured	85720	68662
Unique Data	17405	17170
R_{int}	0.0237	0.0273
Unique Data with I ≥ 2σ(I)	14340	16142
Parameters/Restraints	903/ 0	872/ 0
***wR_2*, (all data)**	0.1511	0.2636
***S* (all data)**	1.027	1.091
***R_1* [I≥2σ(I)]**	0.0525	0.0938
Biggest diff. peak/hole	2.778/ -2.388	5.172/ -3.161

Short Name	$Co_7Gd_{(0.1)}Na_{(0.9)}$-GeW_9	$Co_7Ho_{(0.1)}Na_{(0.9)}$-GeW_9
Formula	$Co_{6.50}H_{150}Cs_{1.70}Gd_{0.10}Ge_2Na_{23}O_{179}P_6W_{22}$	$Co_{6.60}Cs1_{.50}Ge_2Ho_{0.10}Na_{23}O_{179}P_6W_{22}$
Formula Weight / g mol^{-1}	8544.38	8373.27
Crystal System	monoclinic	monoclinic
Space Group	C 1 2/c 1	C 1 2/c 1
***a* / Å**	33.3290(11)	33.4664(3)
***b* / Å**	21.5872(6)	21.7032(3)
***c* / Å**	22.4404(7)	22.4719(2)
α / °	90	90
β / °	117.878(2)	118.0200(10)
ϒ / °	90	90
***V* / Å^3**	14271.7(8)	14408.8(3)
Z	4	4
T / K	150	180
***F*(000)**	15570	14938
***D$_c$* / Mg m^{-3}**	3.977	3.860
μ / mm^{-1}	31.004	30.504
Crystal description	block	block
Crystal colour	aubergine	pink
Wavelength	1.34143	1.34143
Data Measured	83410	102339
Unique Data	14787	16195
R$_{int}$	0.0838	0.0568
Unique Data with I ≥ 2σ(I)	9217	14690
Parameters/Restraints	822/ 35	857/ 27
***wR$_2$*, (all data)**	0.3288	0.2387
***S* (all data)**	1.061	1.036
***R$_1$* [I≥2σ(I)]**	0.1157	0.0928
Biggest diff. peak/hole	6.974/-8.002	17.829/-10.843

Chapter 4: NMR Relaxivities of Paramagnetic Metal Ions Containing POMS

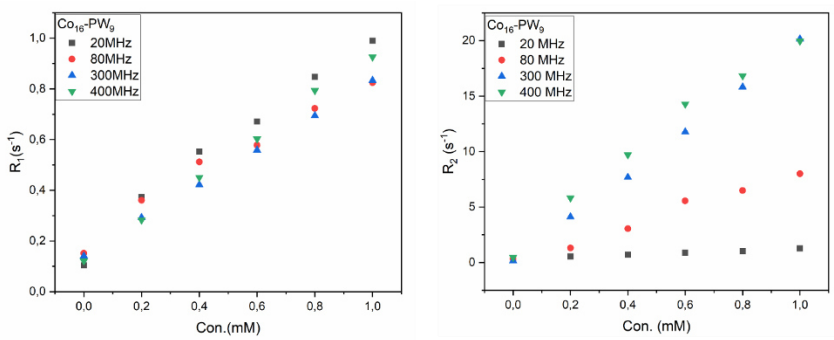


Figure **A.4.1** Relaxation rates of R_1 and R_2 as a function of the concentration of **Co_{16}-PW_9** clusters. R_1 shows a linear dependence on the concentration in all magnetic fields. The value of the slope is dependent on the magnetic field (left) R_2 shows linear dependence with the magnetic field, and the slope increases with increasing magnetic field up to 400 MHz (right).

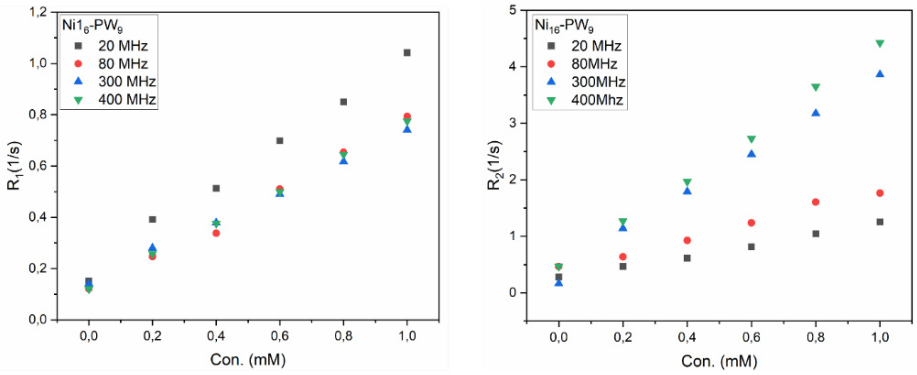


Figure **A.4.2** Relaxation rates of R_1 and R_2 as a function of the concentration of **Ni_{16}-PW_9** clusters. R_1 shows a linear dependence on the concentration in all magnetic fields. The value of the slope is dependent on the magnetic field (left) R_2 shows linear dependence with the magnetic field, and the slope increases with increasing magnetic field up to 400 MHz (right).

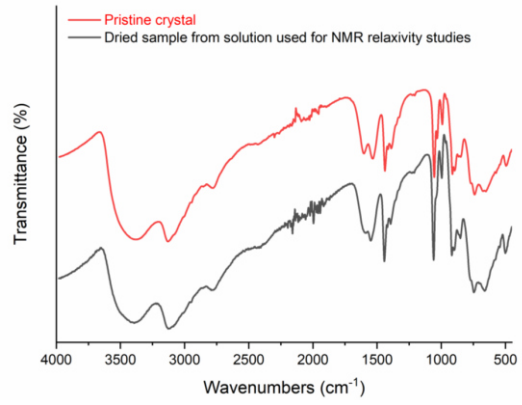


Figure A.4.3. Comparison of ATR-FTIR spectra of **Er_2-W_{34}:** Pristine crystals (red) and the dried sample obtained from the solution used for NMR relaxivity measurement (black).

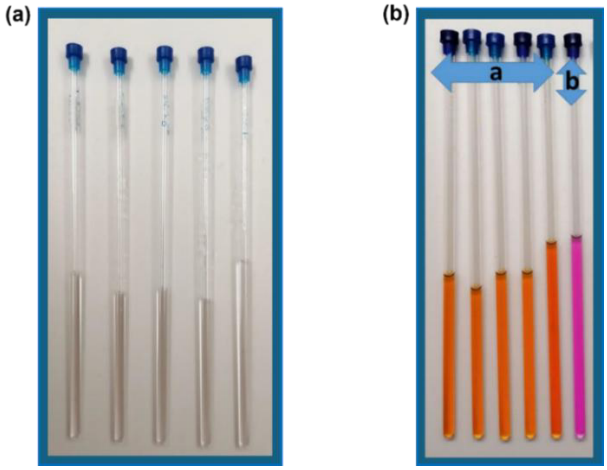


Figure (A.4.4) (a) NMR tubes containing the **Er_2-W_{34}** solution after completion of the NMR relaxivity studies. (b) Pictures of NMR Tubes: Addition of Xylenol Orange Solution to **Er_2-W_{34}** Solution After NMR Relaxivity Studies (a) Addition of Xylenol Orange solution to the **Er_2-W_{34}** solution containing approximately 0.2 mg of $Er(NO_3)_3 \cdot 6H_2O$.

Table 1: Parameters affecting the proton relaxivity behaviour of transition metal ions.

Metal ion	Electronic configuration	S	L	τ_e
Ti^{3+}	$3d^1$	1/2		$10^{-10} – 10^{-11}$
VO^{4+}	$3d^1$	1/2	7/2	10^{-8a}
Cr^{3+}	$3d^3$	3/2		$5\times10^{-9} - 5\times10^{-10}$
Mn^{2+}	$3d^5$	5/2	5/2	10^{-8a}
Fe^{3+}(HS)	$3d^5$	5/2		$10^{-9} – 10^{-10}$
Fe^{2+}(HS)	$3d^6$	2		$10^{-12} – 10^{-13}$
Co^{2+}	$3d^7$	3/2	7/2	10^{-10}
Ni^{2+}	$3d^8$	1		10^{-10}
Cu^{2+}	$3d^9$	1/2	3/2	10^{-9}

Table 2: The experimental values of $r1$ and $r2$ of **M_{16}-POM.**

$f_{0(MHz)}$	$r1$ ($s^{-1}mM^{-1}$)			$r2$ ($s^{-1}mM^{-1}$)		
	(Mn_{16}-SiW_9)	**(Co_{16}-PW_9)**	**(Ni_{16}-PW_9)**	**(Mn_{16}-SiW_9)**	**(Co_{16}-PW_9)**	**(Ni_{16}-PW_9)**
20	13.1655	0.85318	0.85918	13.1655	0.93835	0.97573
80	8.19127	0.64547	0.67929	8.19127	8.05173	1.38566
300	7.85308	0.68676	0.5892	7.85308	19.549	3.6049
400	7.93287	0.81568	0.65098	7.93287	19.30087	3.95544
860	10.27919	----	----	----	----	----
1020	11.5226	----	----	----	----	----
1200	11.78862	----	----	----	----	----
1400	11.30778	----	----	----	----	----

Table 3: The experimental values of $r1$ of Ln-POMs.

f_0 (MHz)	$r_1(Gd_2\text{-}W_{22})$ ($s^{-1}mM^{-1}L$	$r_1(Dy_2\text{-}W_{22})$	$r_1(Er_2\text{-}W_{22})$	$r_1(Er_2\text{-}W_{34})$	$r_1(Dy\text{-}W_{11})$	$r_1(Er\text{-}W_{11})$	$r_1(Dy\text{-}PW_{22})$
20	23.52843	0.58447	0.45007	0.60726	0.28277	0.19968	0.12071
80	27.18237	0.61683	0.46321	0.7283	0.40753	0.28616	0.1726
300	29.03231	0.98777	0.69871	1.08193	0.60001	0.38846	0.30003
400	26.98044	1.34933	0.93064	1.41807	0.75024	0.49351	0.34826
860	19.24401	2.93076	2.0067	2.59569	1.6882	0.97826	0.61807
1020	19.00888	3.69378	2.54752	2.9761	2.08994	1.23424	0.76428
1200	16.25358	4.38944	3.00863	3.09972	1.98801	1.38129	0.8342
1400	15.88719	5.12005	3.41667	3.23967	2.32956	1.53502	0.75531

Table 4: The experimental values of r_2 of Ln-POMs.

f_0 (MHz)	$r_2(Gd_2\text{-}W_{22})$ ($s^{-1}mM^{-1}L$	$r_2(Dy_2\text{-}W_{22})$	$r_2(Er_2\text{-}W_{22})$	$r_2(Er_2\text{-}W_{34})$	$r_2(Dy\text{-}W_{11})$	$r_2(Er\text{-}W_{11})$	$r_2(Dy\text{-}PW_{22})$
20	24.37705	0.46533	0.44076	0.54221	0.34899	0.17334	0.04603
80	31.44013	0.59314	0.41402	0.59592	0.41981	0.2291	-0.01106
300	35.56705	1.32883	0.9315	1.07667	0.69535	0.53508	0.11151
400	35.1962	1.69759	0.93064	1.46272	0.80718	0.66284	0.19125

Chapter 5: Electrochemistry and electrocatalytic behaviour of POMs

Electrochemical characterisation of the Co_{12}-GeW_{10}

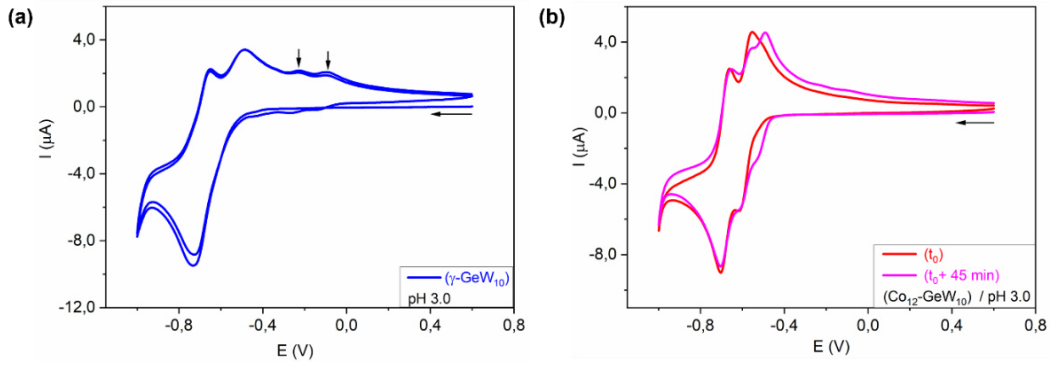


Figure A.5.1 CVs of **a.** γ-GeW_{10} (blue) and **b.** Co_{12}-GeW_{10} (red and violet) recorded on an EPG electrode at a scan rate of 20 $mV.s^{-1}$ in 0.4 M LiH_2PO_4 + LiOH / pH 3.0. The concentrations of both compounds are adjusted to facilitate comparison: 0.2 mM for Co_{12}-GeW_{10} and 1.2 mM for γ-GeW_{10}. Potential scan towards negative potentials, down to -1.0 V vs. SCE.

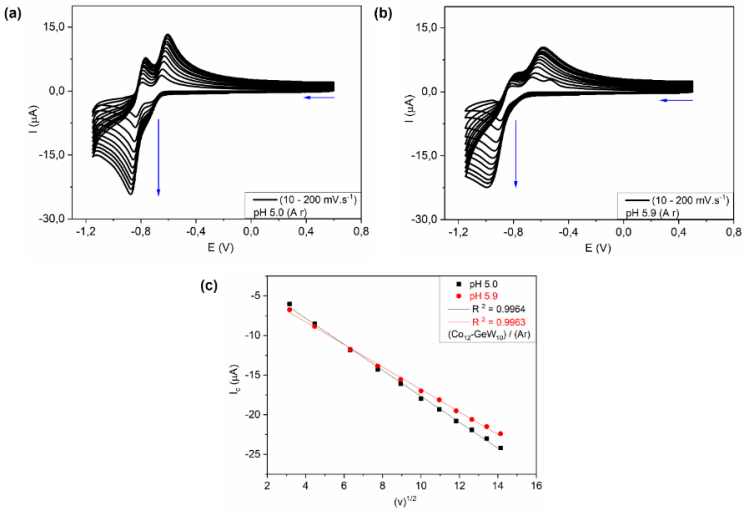


Figure A.5.2 CVs of **Co_{12}-GeW_{10}** recorded on an EPG electrode at varying scan rates from 10 to 200 mV.s^{-1} in 0.4M LiH_2PO_4 + LiOH. Potential scan towards the negative direction and the positive direction. **a.** pH 5.0. **b.** pH 5.9. **c.** Reduction peak potential as a function of the square root of the scan rate at pH 5.0 (black) and at pH 5.9 (red).

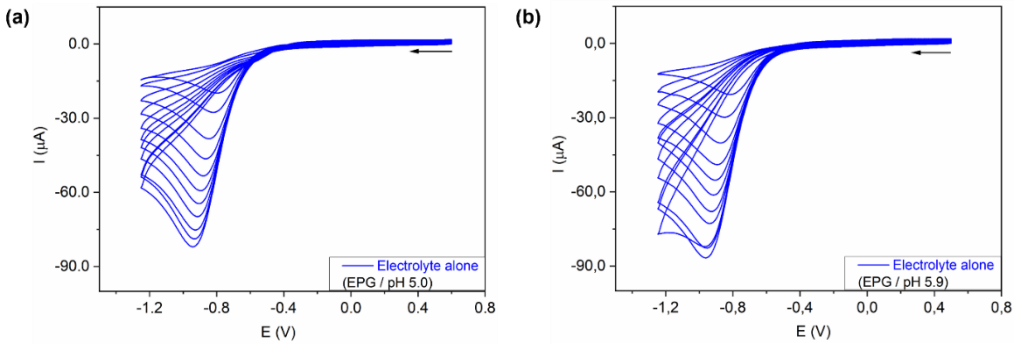


Figure A.5.3 CVs in an O_2-saturated solution under a positive pressure of O_2, on an EPG electrode in 0.4 M LiH_2PO_4 + LiOH. **a.** pH 5.0 at varying scan rates from 10 to 200 mV.s^{-1}. **b.** pH 5.9 at varying scan rates from 10 to 200 mV.s^{-1}. Potential scan towards the negative direction in the first place.

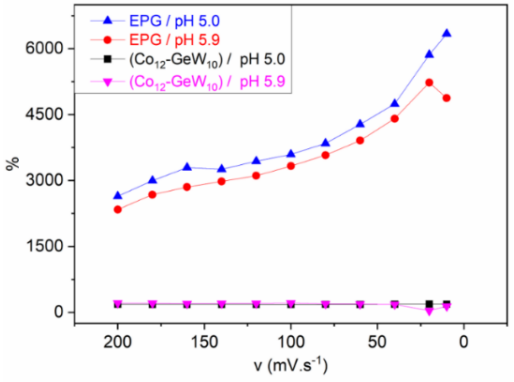


Figure A.5.4 Evolution of the normalised current, $\mathbf{I_N}$, of the electrochemical reduction of O_2 at pH 5.0 and pH 5.9 as a function of the scan rate, both in the presence of **Co_{12}-GeW_{10}** and in the absence of **Co_{12}-GeW_{10}** (bare EPG).

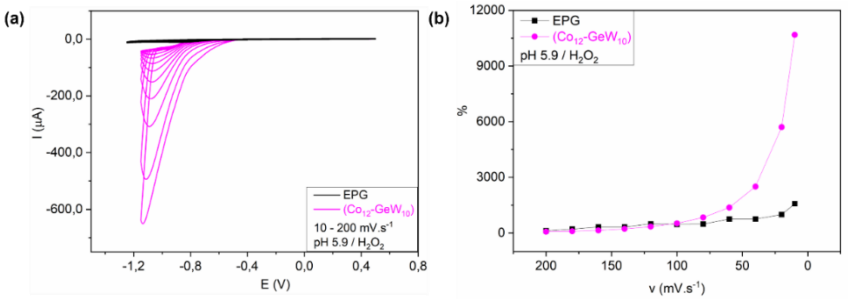


Figure A.5.5 a. CV responses of hydrogen peroxide reduction in an aqueous solution of 0.4 M LiH_2PO_4 + LiOH at pH 5.9, obtained at an EPG electrode using potential scan rates ranging from 200 to 10 $mV.s^{-1}$. Black curves represent the voltammograms recorded in the absence of **Co_{12}-GeW_{10}**, while purple curves correspond to those obtained in the presence of **Co_{12}-GeW_{10}** at a molar ratio of 100. **b.** Evolution of the normalised current, **I_N**, as a function of the potential scan rate.

Electrochemistry of Ni_{12}-GeW_{10}

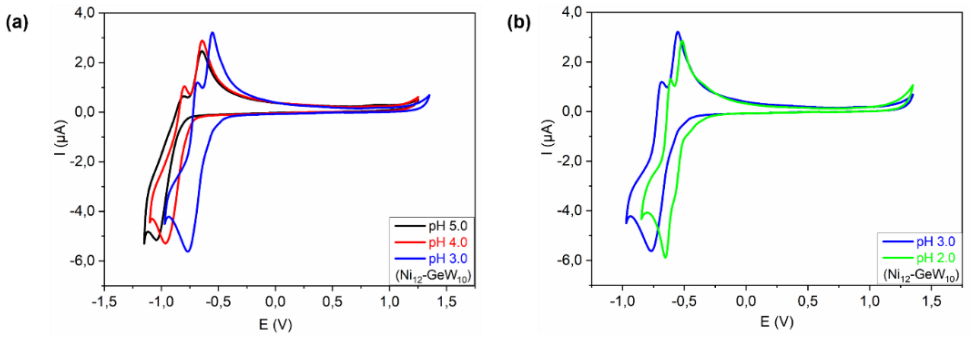


Figure A.5.6 Comparison of the CVs obtained with the **Ni_{12}-GeW_{10}** at different pH values (from 5.0 to 2.0)

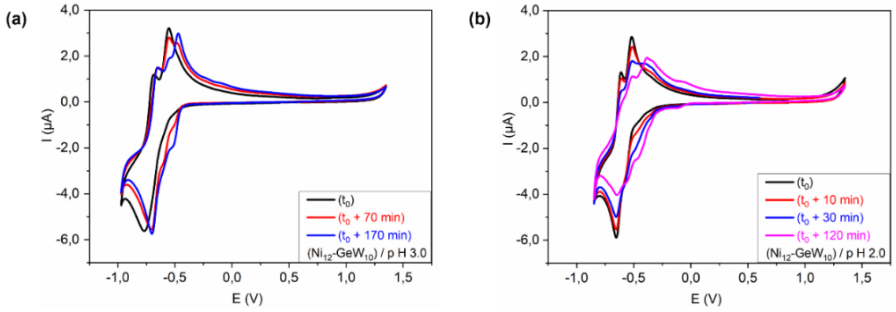


Figure A.5.7 Evolution of the CVs showing the decay of the **Ni_{12}-GeW_{10}** at pH 3.0 and at pH 2.0 with time.

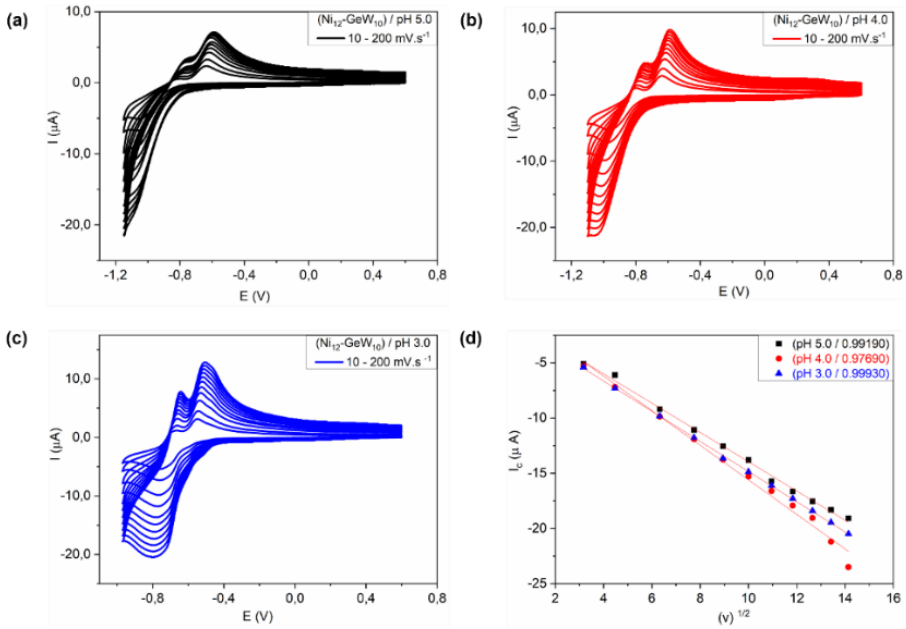


Figure A.5.8 CVs recorded with an EPG working electrode, a SCE reference electrode and a Pt counter electrode at scan rates ranging from 10 to 200 mV.s^{-1} in 0.4 M LiH_2PO_4 + LiOH. POM concentration: 0.2 mM. **a.** pH 5.0 (black). **b.** pH 4.0 (red). **c.** pH 3.0 (blue). **d.** Dependence of the reduction peak potential on the square root of the scan rate.

Electrochemistry of Fe_{12}-PW_{10}

Figure A.5.9 Influence of scan rate in 0.5 M Li_2SO_4 + H_2SO_4 at pH 2.0. The linear relationship observed between the reduction current and the square root of the scan rate confirms that the electron transfer process is diffusion-controlled within the explored potential range.

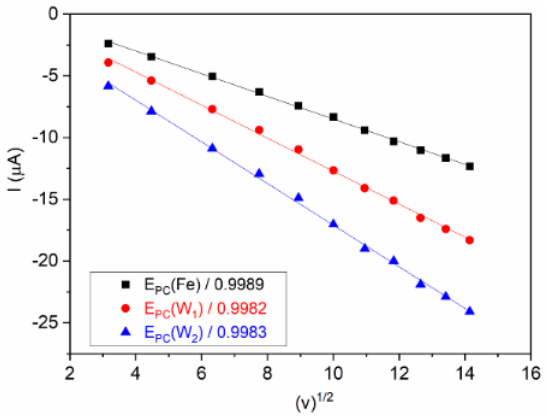


Figure A.5.9 Evolution of the reduction peak current as a function of the square root of the scan rate. Values recorded from CVs at scan rates ranging from 10 to 200 mV.s^{-1}. Working electrode: EPG. Auxiliary electrode: Pt. Reference electrode: SCE. Electrolyte: 0.2M Li_2SO_4 + H_2SO_4 / pH 2.0.

Figure A.5.10 Chronoamperometry experiments are performed at selected potential values under an inert atmosphere (Ar) and then in an O_2-saturated solution under positive O_2 pressure. The figures below show the plots of integrated charge versus time.

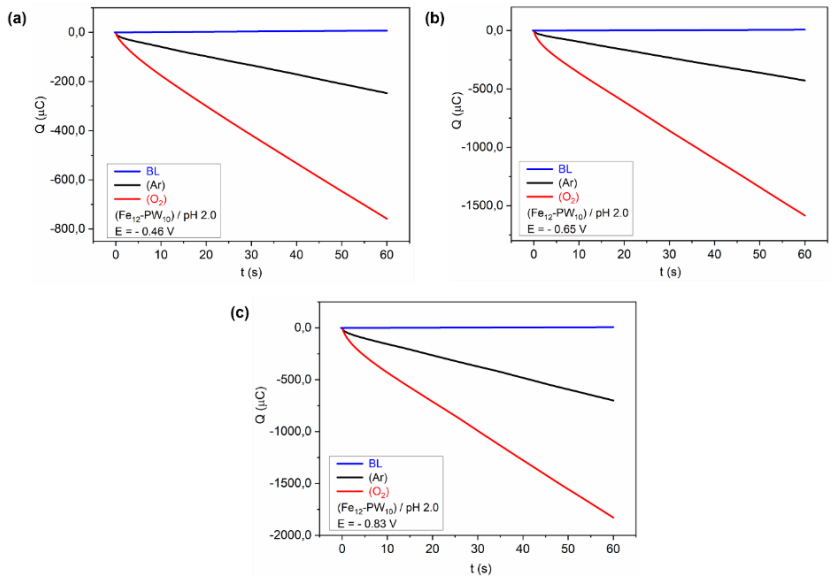


Figure A.5.10 Integrated charge curves obtained by chronoamperometry over a 60 s period at the following potential values: -0.46 V **a.**; -0.65 V **b.**; and -0.83 V **c.**. Ar (black), O_2 (red). Working electrode: EPG. Auxiliary electrode: Pt. Reference electrode: SCE. Electrolyte: 0.2M Li_2SO_4 + H_2SO_4 / pH 2.0.

Figure A.5.11 Chronoamperometry experiments are performed at selected potential values under an inert atmosphere (Ar) and with increasing amounts of H_2O_2. The figures below show the plots of integrated charge versus time.

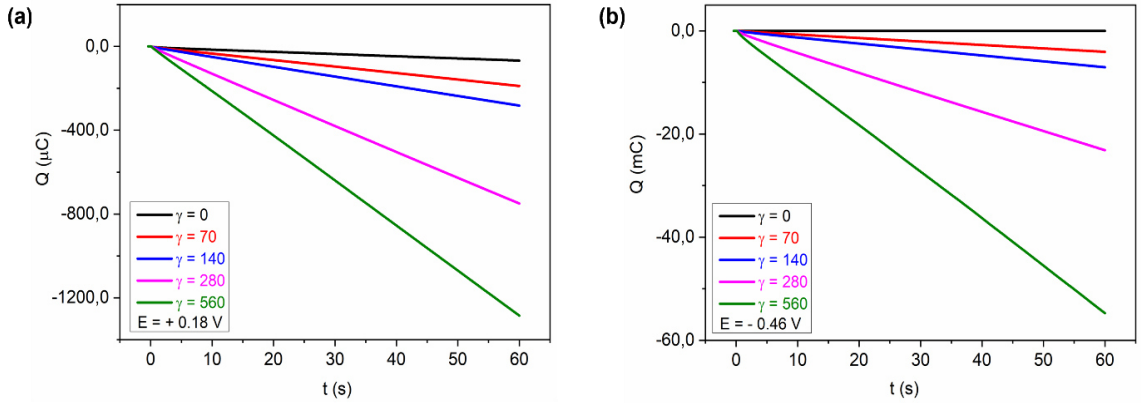


Figure A.5.11 Integrated charge curves from 60 s chronoamperometry experiments at +0.18 V **a.** and -0.46 V **b.** in Ar (black) with increasing H_2O_2 concentrations. Working electrode: EPG; auxiliary electrode: Pt; reference electrode: SCE; electrolyte: 0.2M Li_2SO_4 + H_2SO_4 / pH 2.0.

Figure A.5.12 The effect of scan rate was investigated in 1.0 M CH_3COOLi + CH_3COOH / pH 5.0. The observed linear relationship between the peak current and the square root of the scan rate indicates that the electron transfer process is diffusion-controlled within the studied potential window.

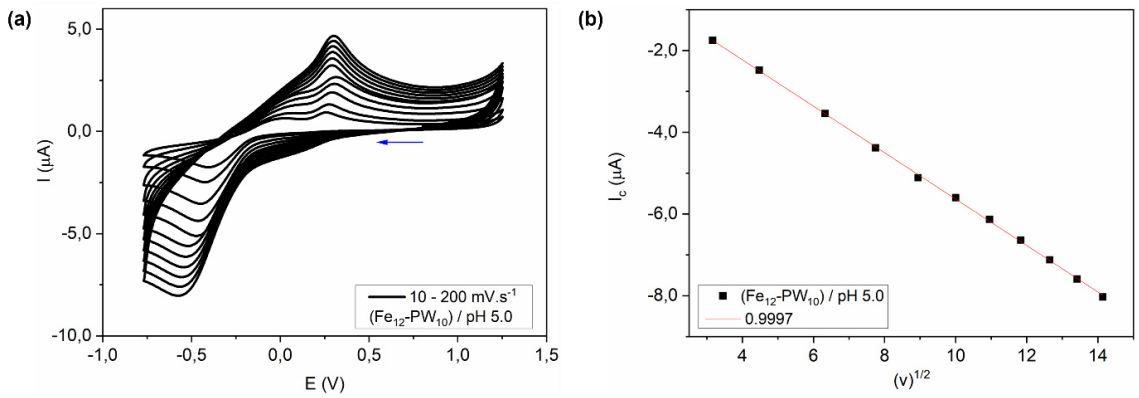


Figure A.5.12 CVs were recorded for **Fe_{12}-PW_{10}** at a concentration of 10^{-4} M in a 1.0 M CH_3COOLi + CH_3COOH solution at pH 5.0. The potential scan was restricted to the potential range where redox processes attributable to the Fe^{3+} centres occur. The reverse potential (E_R) was -0.77 V vs. SCE. **a.** CVs were obtained at scan rates ranging from 10 to 200 $mV.s^{-1}$. **b.**The relationship between the reduction peak current and the square root of the scan rate is shown. The working electrode was an EPG, the auxiliary electrode was Pt, and the reference electrode was SCE.

Figure A.5.13 Chronoamperometric measurements were conducted at various potential values under an inert atmosphere (Ar) and with successive additions of NO_2^-. The following figures present the integrated charge as a function of time.

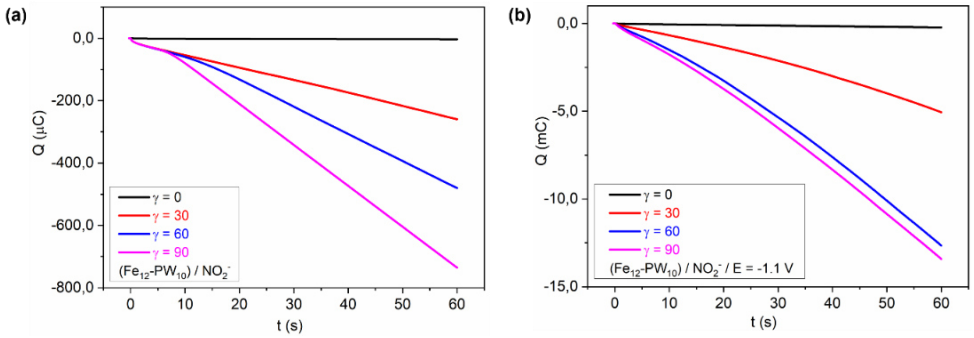


Figure A.5.13 Integrated charge curves from 60 s chronoamperometry experiments at -0.77 V **a.** and -1.10 V **b.** in Ar (black) with increasing NO_2^- concentrations. Working electrode: EPG; auxiliary electrode: Pt; reference electrode: SCE; electrolyte: 1.0 M CH_3COOLi + CH_3COOH / pH 5.0.

Electrochemistry of $Co_7Ln_xNa_{1-x}$-GeW_9 (Ln = Dy, Eu, Gd, Ho, Y)

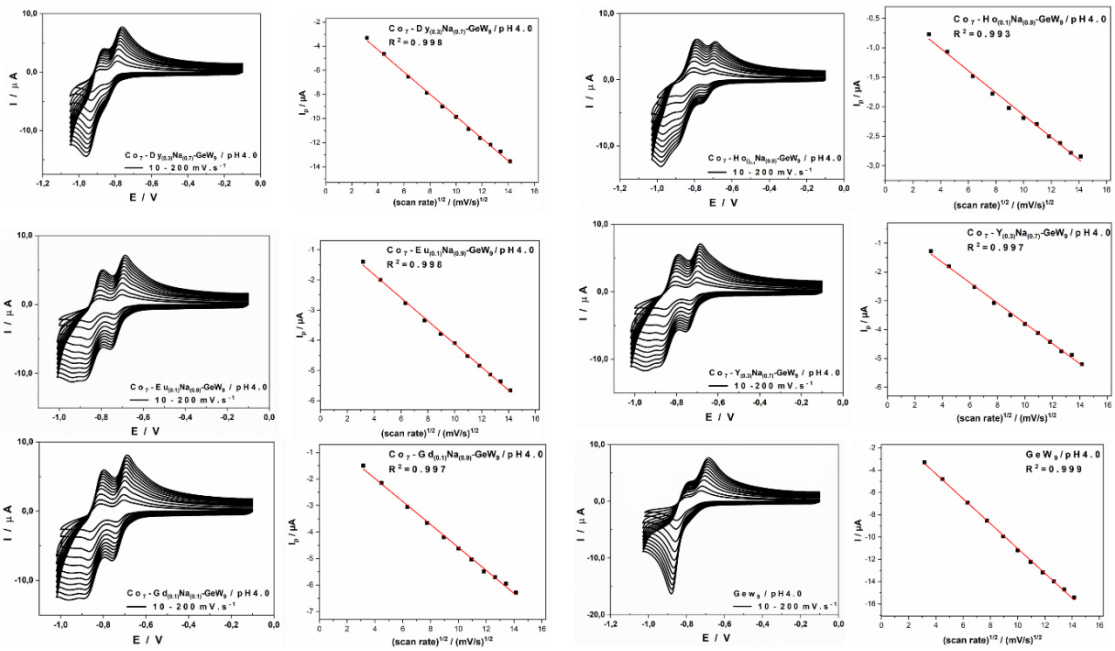


Figure A.5.14 CVs of **$Co_7Ln_xNa_{1-x}$-GeW_9** (Ln = Dy, Eu, Gd, Ho, Y) and **GeW_9** recorded at scan rates ranging from 10 to 200 mV.s^{-1}, in 1.0 M LiCl, 1 M $LiCH_3COO.2H_2O$ + CH_3COOH, at pH 4.0. POM concentrations: 0.1 mM for **$Co_7Ln_xNa_{1-x}$-GeW_9** and 0.2 mM for **GeW_9**. Working electrode: EPG; counter electrode: Pt; reference electrode: SCE. Linear dependence of the magnitude of the peak current (I_p) of the first well-defined reduction wave on the square root of the scan rate.

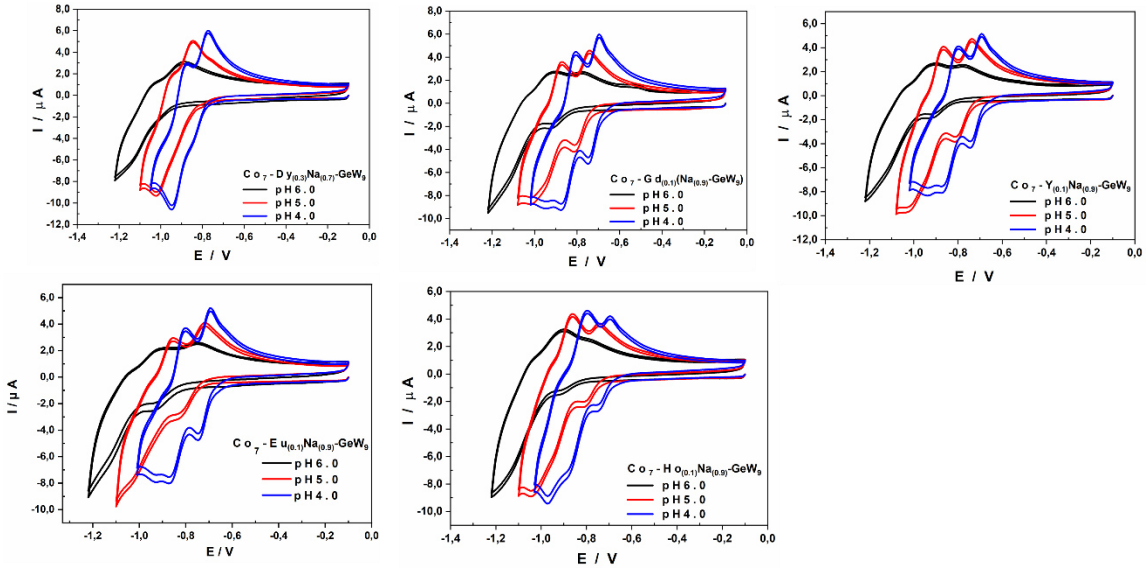


Figure A.5.15 CVs of **$Co_7Ln_xNa_{1-x}$-GeW_9** (Ln = Dy, Eu, Gd, Ho, Y) recorded at a scan rate of 100 mV.s^{-1}, in 1.0 M LiCl, 1 M $LiCH_3COO.2H_2O$ + CH_3COOH, at pH values 4.0, 5.0 and 6.0. POM concentration: 0.1 mM. Working electrode: EPG; counter electrode: Pt; reference electrode: SCE.

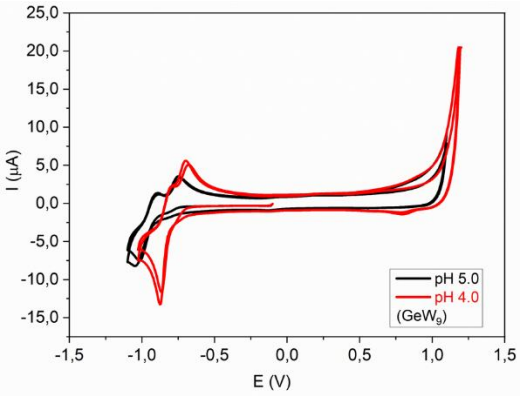


Figure A.5.16 CVs of **GeW_9** recorded at a scan rate of 100 $mV.s^{-1}$ in 1.0 M LiCl, 1.0 M $LiCH_3COO.2H_2O$ + CH_3COOH, at pH 4.0 and 5.0. POM concentration: 0.2 mM. Working electrode: EPG; counter electrode: Pt; reference electrode: SCE.

Table A.5.1 Peak potential values in the media 0.4 M LiH_2PO_4 + LiOH at pH 2.0 and 3.0 for **Co_{12}-GeW_{10}** and **γ-GeW_{10}**. Reference electrode: SCE. Auxiliary electrode: Pt. Working electrode: EPG. Scan rate 20 $mV.s^{-1}$.

	Co_{12}-GeW_{10}		**γ-GeW_{10}**	
V / SCE	E_{Pc}	E_{Pa}	E_{Pc}	E_{Pa}
pH 2.0	-0.50	-0.46	----	
	-0.58	-0.54		
pH 3.0	-0.62	-0.55	-0.75	----
	-0.70	-0.66	-0.47	-0.65

Table A.5.2 Peak potential values in the media 0.4 M LiH_2PO_4 + LiOH at pH 4.0, 5.0 and 5.9 for **Co_{12}-GeW_{10}** and **γ-GeW_{10}**. Reference electrode: SCE. Auxiliary electrode: Pt. Working electrode: EPG. Scan rate 20 $mV.s^{-1}$.

	Co_{12}-GeW_{10}		**γ-GeW_{10}**	
V / SCE	**E_{Pc}**	**E_{Pa}**	**E_{Pc}**	**E_{Pa}**
pH 4.0	-0.94	-0.65	-0.91	-0.60
	---	-0.80	---	-0.70
	---	---	---	-0.80
pH 5.0	-1.00	-0.68	-0.99	-0.67
	---	-0.84	---	-0.86
pH 5.9	-1.15	-0.65*	-1.07	-0.69
	---	---	---	-0.90

**** There is no longer a need to observe two oxidation steps; only one is now present.***

Table A.5.3. Summary of normalised current values, I_N, obtained for the electrocatalytic reduction of NO_2^- in solutions at pH 5.0 and of H_2O_2 in solutions at pH 5.9. Data were calculated from cyclic voltammograms recorded at potential scan rates between 200 and 10 $mV.s^{-1}$.

v / $mV.s^{-1}$	**200**	**180**	**160**	**140**	**120**	**100**	**80**	**60**	**40**	**20**	**10**
pH 5.0 / NO_2^-											
(Co_{12}-GeW_{10}) / %	5	6	5	13	36	49	82	120	185	388	1300
EPG / %	25	26	23	27	23	28	24	29	31	42	33
pH 5.9 / H_2O_2											
(Co_{12}-GeW_{10}) / %	73	92	144	221	344	524	837	1372	2506	5705	10680
EPG / %	125	213	329	328	492	467	484	750	754	996	1578

Table A.57.4. Oxidation peak potentials (E_{pa}) and reduction peak potentials (E_{pc}), in mV *vs.* SCE, measured from CVs recorded in 1.0 M LiCl, 1.0 M $LiCH_3COO.2H_2O$ + CH_3COOH either at pH 4.0 or at pH 5.0 for the POMs in the **$Co_7Ln_xNa_{1-x}$-GeW_9** series, with Ln = Dy, Eu, Gd, Ho, Tb, Y.

	pH 4.0					
	Dy	**Eu**	**Gd**	**Ho**	**Tb**	**Y**
W centres						
E_{pc1}	-850	-746	-748	-748	-748	-746
E_{pa1}	-772	-694	-696	-696	-700	-694
E_{pc2}	-946	-872	-876	-882#	-876	-872
E_{pa2}	-874	-800	-806	-796	-800	-798
E_{pc3}	---	-930	-944	-970	-940	-936
E_{pa3}	---	-900#	-910#	-922#	-906#	-900#
Co centres						
E_{pa4}	---	---	---	---	988#	---
E_{pc4}	?	1000	1000	994	998	1010
E_{pa5}	---	---	---	---	---	---
E_{pc5}	698	704	698	674	708	706

 # Shoulder

	pH 5.0					
	Dy	**Eu**	**Gd**	**Ho**	**Tb**	**Y**
W centres						
E_{pc1} / mV	-790	-834	-814	-808	-816	-806
E_{pa1} / mV	-750	-718	-742	-746	-734	-744
E_{pc2} / mV	-924#	?	-960#	-950#	-950#	-946#
E_{pa2} / mV	-846	-856	-872	-860	-862	-848
E_{pc3} / mV	-1022	-1026#	-1018	-1044	-1022	-1040
E_{pa3} / mV	-948	-962#	-966#	-958#	-958#	-948#
Co centres						
E_{pa4} / mV	---	---	---	952#	956#	956#
E_{pc4} / mV	980	984	1012	1000#	1010#	1024#
E_{pa5} / mV	---	---	---	---	---	---
E_{pc5} / mV	600	598	586	568	572	556

Shoulder

Curriculum Vitae

Education

Since 2020,	PhD Scholar under the supervision of Prof. Annie K. Powell, Karlsruhe Institute of Technology, Karlsruhe, Germany. Association with Project B4 of the CRC 1573 “4f for Future” (4f4f) (From Jan1st 2025).
2018	M.Tech. Industrial Catalysis, Cochin University of Science and Technology, Cochin, Kerala, India.
2013	M.Sc. Applied Chemistry, Cochin University of Science and Technology, Cochin, Kerala, India.
2010	B.Sc. Chemistry, Vimala College, Thrissur, Kerala, India.
2006	St. Therese Higher Secondary School, Shornur, Kerala, India.
2004	Govt. Girls High School, Wadakkanchery, Kerala, India.

Previous work and research experience

2018	National Chemical Laboratory (NCL), Pune, India. M.Tech. Internship 1 year.
2016	Orientation Program in Catalysis, NCCR, IIT Madras, India.
2012	CSIR, Central Leather Research Institute (CLRI), Chennai, India. M.Sc. Master's Thesis - 6 months.
2011	Department of Inorganic and Physical Chemistry (IPC), Indian Institute of Science (IISc), Bangalore, India. M.Sc. Summer Internship - 2 months.

Previous Employment

2019	Chemistry Specialist, Sigma Aldrich, Merck, Bangalore, India.
2014	Chemistry tutor for 12th-grade students, specialising in competitive exam preparation at leading private institutes, Kerala, India.

Grants obtained during PhD work for the scientific collaboration

2021	Two-week stay at LNCMI Grenoble, France, for the high-field magnetic field experiments funded by LNCMI-CNRS.
2023	Two-week stay at LNCMI Grenoble, France, for the high-field magnetic field experiments funded by LNCMI-CNRS.
2024	One-month stay at LNCMI Grenoble, France. Funded by the EMFL/ISABEL exchange program.
2024	Three-month stay at Équipe d’Electrochimie et de Photo-électrochimie, Institut de Chimie Physique, Université Paris-Saclay,France. Funded by the KHYS Travel grant.

Conferences Attended

2025	Oral contribution, 4f4f CRC Spring Seminar Days at Haus Saron, Wildberg.
2024	Poster presentation, Innovative Minds & Inclusive Science, Birthday Symposium dedicated to Prof. Dr. Annie K. Powell on the occasion of her 65th Birthday, member of the organising committee.
2024	Poster presentation, NANOMAT Conference at Vienna, Austria.

2023 Olex2 workshop at Karlsruhe Institute of Technology, Karlsruhe, Germany.

2023 Poster presentation, MSE Day at Geesthacht, Germany.

2022 Online Workshop on NMR Relaxometry for Dairy Products.

Collaborations

- Dr. Papri Chakraborty and Dr. Marco Neumaier (Prof. Dr. Manfred Kappes) - ESI-MS, Institute for Nanotechnology, Karlsruhe Institute of Technologie, Karlsruhe, Germany.
- Dr. Pierre Picchetti - DLS studies, Institute for Nanotechnology, Karlsruhe Institute of Technologie, Karlsruhe, Germany.
- Dr. Thomas Bergfeldt - Elemental analysis, Institut für Angewandte Materialien Angewandte Werkstoffphysik, IAM-AWP, Karlsruhe Institute of Technologie, Karlsruhe, Germany.
- Prof. Dr. Gisela Guthausen - NMR experiments, Institute of Mechanical Process Engineering and Mechanics, Karlsruhe Institute of Technology, 76131 Karlsruhe, Germany.
- Dr Steffen Krämer - High field NMR experiments, LNCMI-EMFL, CNRS, INSA-T and UPS, Université Grenoble Alpes, Boîte Postale 166, CEDEX 9, 38042 Grenoble, France.
- Prof. Pedro de Oliveira and Dr. Israël Martyr Mbomekalle - Electrochemical studies. Equipe d'Electrochimie et de Photo-électrochimie, Institut deChimie Physique, Université Paris-Saclay, UMR 8000 CNRS, Orsay F-91405, France.

List of Publications

- Ramasamy Indumathy, Perunninakulath S. Parameswaran, C.V. Aiswarya, Balachandran Unni Nair “Bibenzimidazole containing mixed ligand cobalt (III) complex as a selective receptor for iodide” *Polyhedron*, Volume 75, **2014**, Pages 22-29

- Aiswarya Chalikunnath Venu, Rami Nasser Din, Thomas Rudszuck, Pierre Picchetti, Papri Chakraborty, Annie K. Powell, Steffen Krämer, Gisela Guthausen and Masooma Ibrahim.“NMR Relaxivities of Paramagnetic Lanthanide-Containing Polyoxometalates” *Molecules***, 2021**, 26, 7481.

- Rami Nasser Din, Aiswarya Chalikunnath Venu, Thomas Rudszuck, Alicia Vallet, Adrien Favier, Annie K. Powell, Gisela Guthausen, Masooma Ibrahim and Steffen Krämer.“Longitudinal and Transverse 1H Nuclear Magnetic Resonance Relaxivities of Lanthanide Ions in Aqueous Solution up to 1.4 GHz/33 T” *Molecules*, **2024**, 29, 4956.

- Aiswarya Chalikunnath Venu, Masooma Ibrahim, Israël M. Mbomekallé, Anne-Lucie Teillout, Papri Chakraborty, Christopher E. Anson, Thomas Bergfeldt, Pedro de Oliveira, Annie K Powell. *Inorg. Chem* “Structural characterisation and electrocatalytic properties of redox active Co(II) and Ni(II) complexes with dilacunary Keggin polyoxometalate ligands: the devil is in the detail”, **To be submitted**

- Aiswarya Chalikunnath Venu, Kliment Bozov,Rami Nasser Din, Annie K. Powell, Steffen Krämer, Gisela Guthausen and Masooma Ibrahim. Study of Paramagnetic relaxation Enhancement (PRE) for Paramagnetic Lanthanide-Containing Polyoxometalates up to 1.4 GHz/33, **In preparation**.

- Aiswarya Chalikunnath Venu, Masooma Ibrahim, Rami Nasser Din, Annie K. Powell, Steffen Krämer, Gisela Guthausen, Israël M. Mbomekallé, Anne-Lucie Teillout, Papri Chakraborty, Christopher E. Anson, Thomas Bergfeldt, Pedro de Oliveira, Annie K Powell. Structural characterisation, electrochemical properties and NMR relaxometric properties of novel 3d-4f POMs, **In preparation**.

- Aiswarya Chalikunnath Venu, Masooma Ibrahim, Israël M. Mbomekallé, Anne-Lucie Teillout, Papri Chakraborty, Christopher E. Anson, Thomas Bergfeldt, Pedro de Oliveira, Annie K. Powell.Structural characterisation, electrochemical properties and of novel Fe^{III}_{12} POMs, **In preparation**

- Aiswarya Chalikunnath Venu, Rami Nasser Din, Annie K. Powell, Steffen Krämer, Gisela Guthausen and Masooma Ibrahim. Study of Paramagnetic relaxation Enhancement (PRE) for Paramagnetic Transition metal-Containing Polyoxometalates up to 1.4 GHz/33, **In preparation**.

Acknowledgments

I want to express my heartfelt gratitude to my supervisor, Prof. Dr. Annie K. Powell, for the opportunity to pursue my PhD in her research group. I greatly appreciate the support and guidance she provided throughout my research journey, especially in encouraging me to attend conferences, apply for grants, and engage in numerous valuable experiences. Your suggestions and assistance have been crucial to my overall development and have significantly alleviated the stress associated with my research. I have genuinely enjoyed spending time with you, as it has inspired me both in my scientific endeavours and in my personal growth. Thank you for everything.

I had a wonderful experience working with PD Dr. Masooma Ibrahim, the POM queen of KIT. She offered unwavering support from my very first day at INT and throughout my research journey. Thanks to her, I was able to engage in numerous great scientific collaborations. She was always available to discuss both my research challenges and personal struggles. I am genuinely grateful for her patience and guidance throughout my PhD experience. Thank you for being there for me every step of the way.

I would like to thank Dr. Christopher Anson, our crystal expert, for his assistance in refining the crystallographic data. His advice and suggestions have been invaluable. He remained exceptionally calm and helpful when I approached him with my disordered structure and kindly explained various methods to help me understand and visualise the crystal structures better.

I would like to express my gratitude to Prof. Dr. Dieter Fenske and Dr. Olaf Fuhr for their assistance in collecting single-crystal data for all my crystal structures. I especially appreciate Dieter’s willingness to measure the crystals quickly, despite his busy schedule.

Special thanks to Gertraud Amschlinger and Isabella Vogelbacher for their assistance in organising and managing all the paperwork promptly. I also appreciate Weber Cornalia for helping me with the contract extension.

I would like to express my gratitude to Daniel Seufert for his assistance with translations and to Dr. Jonas Brun for his help whenever I need it. I would also like to thank Kliment, who accompanied me during one of the NMR studies in Grenoble, and Dr. Aravind and Vani Krishna, my colleagues in the office next door; it was nice to converse with them in Malayalam. I am especially grateful to all the members of the Powell group, both past and present, for their valuable feedback during my presentations and for their understanding and support throughout my research journey.

Furthermore, I would like to thank Dr. Papri Chakraborty and Dr. Marco Neumaier from Prof. Dr. Manfred Kappes' group for performing the ESI-MS measurements. I also appreciate Dr. Pierre Picchetti for the rapid DLS measurements of POM samples for publication, and Dr. Thomas Bergfeldt for the elemental analysis of my samples.

I would like to express my heartfelt gratitude to Prof. Dr. Gisela Guthausen for her patience in teaching me how to use the NMR instruments and conduct measurements. I sincerely appreciate your kindness and support during the corrections of my thesis, as well as the time you dedicated to our discussions, which helped me deepen my understanding of the concepts. I also want to thank Dr. Lena Trapp and Dr. Thomas Rudszuck for their assistance in the NMR lab whenever I needed help.

Furthermore, I would like to express my gratitude to Dr. Steffen Krämer, who hosted me in Grenoble and guided several scientific missions at LNCMI involving the use of the resistive magnet. His clear explanations about both the magnet and the various facilities at LNCMI were extremely valuable. I am thankful to Dr. Rami Nasser Din for his involvement in the NMR experiments and for his company during my stay in Grenoble. I feel truly grateful to be part of the inspiring “POM-NMR” team, where excellent discussions, regular Zoom meetings, and collaborative efforts have led to such fruitful results.

Additionally, I would like to thank Prof. Pedro de Oliveira and Dr. Israël Martyr Mbomekalle for their collaboration on the electrochemical studies of POM samples. Their help was instrumental in enhancing my understanding of this technique and significantly contributed to the development of my thesis report. I especially want to thank Pedro for hosting me at Université Paris-Saclay and for teaching me about the electrochemistry setup. It was also a pleasure to meet Prof. Dr. Anne-Lucie Teillout at Université Paris-Saclay, and I appreciate her valuable insights during our discussions.

I am grateful to KIT for the initial funding and to the CRC 1573 initiative “4f for Future” (4f4f) for supporting my ongoing research at KIT, Germany. I also want to thank LNCMI-CNRS for providing financial support for my two scientific missions at LNCMI in Grenoble, as well as the EMFL/ISABEL project for funding my one-month secondment program at LNCMI. Additionally, I would like to thank KHYS for awarding the travel grant for junior researchers, which enabled me to spend three months at Université Paris-Saclay.

Finally, I would like to express my heartfelt gratitude to my loving husband, Dr. Girish Karadka Shankara, for his unwavering support and constant encouragement in helping me pursue my dreams. I am also deeply thankful to my parents, brother, and in-laws for their love and support throughout this journey. A special note of gratitude goes to my parents and brother for lovingly taking care of my daughter while I was completing my PhD.